LBL-34908
UC-404

Lawrence Berkeley Laboratory
UNIVERSITY OF CALIFORNIA

Materials Sciences Division

Computer Simulation of Martensitic Transformations

P. Xu
(Ph.D. Thesis)

November 1993

Prepared for the U.S. Department of Energy under Contract Number DE-AC03-76SF00098

DISCLAIMER

LBL 34908

Computer Simulation of Martensitic Transformations

Ping Xu

Ph.D. Dissertation

Department of Materials Science and Mineral Engineering
University of California

and

Center for Advanced Materials
Materials Sciences Division
Lawrence Berkeley Laboratory
University of California
Berkeley, CA 94720

November 1993

This work was supported by the Director, Office of Energy Research, Office of Basic Energy Science, Materials Science Division of the U.S. Department of Energy under Contract No. DE-AC03-76F00098

Computer Simulation of Martensitic Transformations

Ping Xu

Ph..D. Dissertation

ABSTRACT

The characteristics of martensitic transformations in solids are largely determined by the elastic strain that develops as martensite particles grow and interact. To study the development of microstructure, a finite-element computer simulation model was constructed to mimic the transformation process. The transformation is athermal and simulated at each incremental step by transforming the cell which maximizes the decrease in the free energy. To determine the free energy change, the elastic energy developed during martensite growth is calculated from the theory of linear elasticity for elastically homogeneous media, and updated as the transformation proceeds.

The computer model is in good agreement with the linear elastic analytic solution, especially when the latter predicts single-variant martensite or twinned martensite with nearly equal fractions of the two variants. The model also generates "butterfly martensite" which has been observed experimentally. The development of similar complex, multivariant microstructures is seen to be promoted by geometric constrains on the transforming crystal, and is strongly affected by applied stress. Either constraint or applied stress increases the thermal resistance to the transformation, as measured by the difference between the M_s and M_f temperatures. When the transformation is made reversible, phenomena such as thermoelasticity, pseudoelasticity and the shape memory effect naturally appear. The fundamental understanding of thermal and stress-strain hysteresis is made possible by calculating the elastic energy developed during the transformation. When plastic deformation and frictional resistance are absent, thermal or stress-strain hysteresis exists because of the absence of equilibrium between the driving force and the elastic energy resistance. This non-equilibrium effect, which is also the source of energy dissipation, is due to the elastic relaxation caused by elastic interaction and accommodation between martensite particles of like and different variants. When the computer model is applied to partially-stabilized-zirconia systems, it simulates the transformation from cubic to monoclinic structure and generates twinned microstructures that have {100} habit planes. Analysis shows that the twinning occurs not to achieve an invariant plane, but to cancel the shear components in the transformation strain. The twinning is also promoted by the constraint of the untransformed matrix.

dedicate to

my parents

and

my husband

TABLE OF CONTENTS

LIST OF TABLES

ACKNOWLEDGEMENTS

I would like to express my deepest appreciation to my research advisor, Professor J.W. Morris, Jr. Without his guidance and support, this dissertation work would not have been possible. I would also like to express my gratitude to Professor A.G. Khachaturyan, Rutgers University, for helpful discussions; to my dissertation committee members, Professors R.Gronsky and H.R. Wenk, for reading and approving my dissertation and for their helpful suggestions and encouraging comments; to my qualifying examination committee members, Professors G. Thomas, R.O. Ritchie, T. Devine and H.R. Wenk, for giving me tough but good time during the examination.

I 'd like to say thanks to all members in Morris group, past and present, for giving me encouragement and help in learning American culture and the English language. Special thanks to Jin Chan, Peter Chou, David Chu, Rusty Cinque, Julia F. Goldstein, Heidi Linch, Chris Krenn, and Peter Skarpelos for proof reading this dissertation.

I cannot give enough thanks to my dear husband, Zequn Mei, for always being ready to help, emotionally and academically. It is his love, understanding, encouragement, and belief in my ability that made it possible for me to overcome the many difficult obstacles which I confronted during my graduate studies.

I would like especially to thank my parents for their encouragement and support; their high expectations were the underlying reason for my success. I will always remember their love. I hope my receiving a Ph.D. from Berkeley will give them joy and, perhaps, some peace of mind.

This work is supported by the Director, Office of Energy Research, Office of Basic Energy Sciences, Materials Sciences Division of the United States Department of Energy under Contract No. DE-AC03-76SF00098.

CHAPTER 1

INTRODUCTION

1.1. Martensite and Martensitic Transformation

The significant increase in the strength of steels obtained through quenching was first discovered in the 19th century. The product of quenched steels was named "martensite" in honor A. Martens, a German metallographer who was among the first to study the correlation between the microstructures and properties of quenched steels. Since then the mechanism responsible for producing martensite is known as the "martensitic transformation".

The martensitic transformation is one of the principal processes responsible for structural or phase transitions in crystalline materials, and it produces a wide variety of microstructures with desirable properties. Martensitic transformations have been used to strengthen structural steels, as well as to increase the fracture toughness of steels and ceramics. They are also the sources of phenomena involving thermoelasticity, pseudoelasticity and shape memory effects in many non-ferrous and ferrous alloys.

As defined by Cohen, Olson and Clapp [1] most recently, "A martensitic transformation can be considered to be a first-order solid-state structural change which is (a) displacive, (b) diffusionless, and (c) dominated in kinetics and morphology by the strain energy arising from shear-like displacements." During a martensitic transformation, a parent lattice changes into a product lattice by coordinated movements of a large numbers of atoms. This mechanical distortion of the parent lattice induces a substantial local elastic strain. Accommodation of the transformation-induced strain determines the transformation kinetics and makes the martensite phase grow in a pattern that keeps the elastic strain energy at a minimum or a tolerable level, resulting in complex microstructures in the martensite, including twins and dislocations.

The crystallography of martensite was first studied in 1924 by Bain [2]. He showed that a body-centered cubic (bcc) structure can be produced from a face-centered cubic (fcc) structure by a contraction of approximately 17 percent in one cubic direction of the fcc lattice and an expansion of 12 percent in the other two directions perpendicular to it. This process of generating a bcc structure from a fcc structure involves considerably less distortion or strain than any of the other processes which generate such structure change, and the strain, named "Bain strain", became the fundamental basis for studying the crystallography of the martensitic transformations. Similar mechanisms were also proposed for martensitic transformations between other crystal structures. The Bain strain is an essential ingredient of the martensite crystallographic theory, developed later in the 1950's, and the linear elastic theory, formulated in the 1970's.

The crystallographic theory of the martensitic transformation was developed by Wechsler, Lieberman and Read [3] to predict the crystallographic habit plane and twin fraction of a twinned martensite plate. Bowles and Mackenzie [4] developed an equivalent version of the crystallographic theory from a different approach almost simultaneously. The method identifies an undistorted "invariant plane" of the transformation on which the martensite and matrix structures fit without distortion, so that a martensite plate parallel to this plane is nearly strain-free (local strains associated with twinning in the plate are ignored). The crystallographic theory has been particularly useful for predicting the habits and twin fractions of twinned martensite in steels and other alloys [5 - 7].

Despite its success, the crystallographic theory confines the martensitic transformation as a phase transition to achieve an invariant-plane strain. The theory does not provide direct linkage of the strain energy to the transformation kinetics, nor to the morphology of the martensitic transformation. The theory cannot explain the complex microstructure produced by the martensitic transformations that do not have an invariant plane, for example, the twinning that occurs during the tetragonal to monoclinic martensitic transformation in partially-stabilized-zirconia systems [8]. Unlike the crystallographic

theory, the linear elastic theory, which is a new approach that emerged by the end of the 1970's, directly relates the morphology of martensite to the elastic energy induced during the transformation, providing a new tool for theoretical studies of the martensitic transformation.

1.2. The Linear Elastic Theory

The application of linear elastic theory for studying martensitic transformation requires computation of the elastic energy associated with the product of a transformation in a linear elastic matrix. Eshelby [9,10] developed such a solution for an isotropic elastic medium with an ellipsoidal inclusion undergoing any given transformation strain. By employing the Fourier transformation, Khachaturyan extended Eshelby's solution to compute the elastic energy of a particle of any shape, or particles of an arbitrary distribution [11 - 13]. The fundamental basis of these calculations is the fact that in some solid state transformations, such as coherent precipitations and martensitic transformations, new phases remain coherent with the matrix. The tendency towards decreasing the elastic energy plays an essential role in the formation of multiphase structures that develop in the process of transformations.

There are limitations to the linear elastic theory. It linearizes the transformation strain, which is often appreciable, and it ignores the rotational component of the finite strain, which alters the crystallographic habit. On the other hand, it has several compensating advantages that avoid some of the shortcomings of the crystallographic theory. The linear elastic model is not restricted to "invariant plane" transformations. It can treat particles with intermediate shapes that might be assumed during growth. The model yields a value for the elastic energy than can be used to measure the energetic stability of the preferred habit and can be summed with the surface energy to predict the preferred shape, habit and composite state as a function of volume. The most valuable aspect of the linear

elastic theory is that, it is straightforward to compute the elastic energy of an arbitrary distribution of particles, provided that the difference between the elastic moduli of the particle and the matrix phases is ignored [12, 13]. It is this advantage that makes the linear elastic theory an elegant theoretical tool for studying the relationship between the morphology of martensite and the elastic energy, or strain energy, arising from the martensitic transformation.

The last advantage of the linear elastic theory makes it possible to construct computationally simple models in which a martensitic transformation is allowed to develop spontaneously, revealing the factors that determine the progress of the transformation and the microstructural patterns that result. Although the analytical solutions have been obtained to predict the habits, shape and composite structures in the martensitic transformations [13-16], they provide no information about the paths that lead to these states and the possible metastable states along the paths. To study the development of microstructure of martensitic transformations, a computer simulation can be used to mimic the process. A model of this type was proposed by Wen, Khachaturyan and Morris (WKM) [17]. They simulated a two-dimensional martensitic transformation by dividing a plane into a grid of elementary square cells with periodic boundary conditions.

This simulation method produced transformation paths and final microstructures that were encouragingly realistic. However, the simulation was done by using the "point approximation", in which the finite volume or shape of the elementary cell was not taken into account but was treated as an equivalent point [13,17,18]. This approximation introduces error in the elastic energy interaction that becomes increasingly significant for near neighbor terms, and has limited the further extension and development of the model.

1.3. Objectives

In this investigation, the WKM model for computer simulation was modified to include the effect of the volume and shape of the elementary cell. The new model was then tested in two- and three-dimensional spaces for the stress-free condition under which the original WKM model was used. The results of the simulation using the new model were found to be significantly different from those using the original model, but were in a good agreement with those predicted by analytical solutions of the linear elastic theory.

Secondly, the effects of boundary conditions on the microstructural development of the martensitic transformation were studied. In addition to the stress-free condition, the constrained boundary condition was introduced, in which the martensitic transformation occurs in a crystal that is constrained by untransformed matrix. The function of the matrix constraint was found to be remarkably important to the microstructural development and thermal resistance to the martensitic transformation, as well as to the reversible martensitic transformation. The transformations in the constrained crystal under external monotonic or cyclic stress were also simulated. Thirdly, the reversible martensitic transformation was simulated, and the phenomena of thermoelasticity, pseudoelasticity and the shape memory effect were studied. Finally, the model was applied to partially-stabilized-zirconia systems to simulate the martensitic transformation from a cubic to monoclinic structure.

There are nine chapters in this dissertation. Chapter 2 presents the analytical solutions for the preferred habit planes and composite structure of martensite particles using the linear elastic theory. A comprehensive description of the computer simulation model is included in Chapter 3. In Chapter 4, the computer model is tested by using it to simulate the cases which can be solved exactly by the linear elastic theory shown in Chapter 2. Chapter 5 presents the results of simulation of martensitic transformations under constraint and external stresses. The results of simulations and investigation of the reversible transformations and their related phenomena - thermoelasticity, pseudoelasticity and the

shape memory effects are described in Chapters 6 and 7. Chapter 8 presents the results of the simulation of the transformation in partially-stabilized-zirconia systems. The summary of the work and the discussion of the possibilities of further developments of the computer model are included in Chapter 9.

CHAPTER 2

THE SHAPE, HABIT AND COMPOSITE STRUCTURE OF AN ELASTIC INCLUSION

In this chapter, the linear elastic theory developed by Eshelby and modified by Khachaturyan is used to predict the shapes, habits, and composite structures of coherent inclusions, such as small volumes that have undergone martensitic transformations. The predictions will be used to compare with the results from the computer simulation (Chapter 4).

2.1. The Elastic Energy of a Homogeneous, Coherent Inclusion

The linear elastic theory predicts that the preferred shape of a martensitic particle is ordinarily a thin plate parallel to a particular habit plane. It then shows that the preferred internal state of the particle falls into one of three cases: (1) A thin, single-variant plate of martensite can fit into the parent matrix without strain. In this case the preferred state is a single-variant particle on the plane of perfect match (the habit plane). (2) A single-variant plate cannot fit into the matrix without strain, but a composite plate of two alternating variants can. If the two variants share a common crystallographic plane (usually a twin plane) then the preferred state is a thin, composite plate on the plane of perfect match. (3) Neither a single-variant nor a composite plate can fit into the matrix without distortion. In this case the preferred state is a thin plate with a definite habit, but the system is strained. The result is ordinarily a complex microstructure that includes several crystallographic variants with compensating strains.

To show these results mathematically, let a homogeneous, coherent inclusion form within an elastic matrix. Neglecting the difference between the elastic constants of the in-

clusion and the matrix, and assuming linear elasticity, the elastic energy of the inclusion can be written as the Fourier integral [13]

$$E_e = \frac{1}{2}\int_{\mathbf{k}} B(\mathbf{e})|\theta(\mathbf{k})|^2 \frac{d^3k}{(2\pi)^3} \tag{2.1}$$

In this equation, $\theta(\mathbf{k})$ is the *shape function* of the inclusion,

$$\theta(\mathbf{k}) = \int_{\mathbf{k}} \theta(\mathbf{r}) e^{i\mathbf{k}\bullet\mathbf{r}} \frac{d^3k}{(2\pi)^3} \tag{2.2}$$

where $\theta(\mathbf{r})$ has the value 1 if the position, $\mathbf{r}$, is inside the inclusion and is zero otherwise, and $B(\mathbf{e})$ is the *elastic intensity* in the direction, $\mathbf{e} = \mathbf{k}/|\mathbf{k}|$,

$$\begin{aligned} B(\mathbf{e}) &= \lambda_{ijkl}\varepsilon^0_{ij}\varepsilon^0_{kl} - e_i\sigma^0_{ij}\Omega_{jk}(\mathbf{e})\sigma^0_{kl}e_l \\ &= \lambda_{ijkl}\varepsilon^0_{ij}\varepsilon^0_{kl} - B'(\mathbf{e}) \end{aligned} \tag{2.3}$$

In Eq. (2.3), λ is the fourth-order tensor of elastic moduli, ε^0 is the *transformation strain* tensor, the strain that would result if the matrix were transformed into the inclusion under stress-free conditions, σ^0 is the *transformation stress* tensor,

$$\sigma^0_{ij} = \lambda_{ijkl}\varepsilon^0_{kl} \tag{2.4}$$

the tensor, $\Omega(\mathbf{e})$ is defined by its inverse, the *Green's tensor*

$$\Omega^{-1}_{ij}(\mathbf{e}) = \lambda_{ijkl}e_je_k \tag{2.5}$$

and $B'(\mathbf{e})$ is the *relaxation function*, a function of the direction, $\mathbf{e}$.

2.2. The Preferred Shape and Habit

When the inclusion volume is large or the surface tension is relatively small, the elastic energy is large compared to the surface energy, and the preferred state of the inclusion is that which minimizes the elastic energy. Several important conclusions about the behavior of such inclusions can be extracted from Eq. (2.1) without solving it. First, the preferred shape of an isolated inclusion is ordinarily a thin plate with a definite habit. When the inclusion is a thin plate with normal vector, $\mathbf{n}$, the shape function reduces to a Dirac δ-function in the direction of $\mathbf{n}$, and the elastic energy is

$$E_e = \frac{1}{2} V_p B(\mathbf{n}) \tag{2.6}$$

where V_p is the volume of the inclusion. If $B(\mathbf{e})$ has a discrete minimum for a particular direction, $\mathbf{e} = \mathbf{n}_0$, as it ordinarily does, then the elastic energy is minimized if the inclusion is a thin plate perpendicular to the direction, $\mathbf{n}_0$, which defines its habit plane.

Secondly, the elastic energy vanishes entirely if the transformation has an invariant plane and the inclusion has the form of an arbitrarily thin plate that lies in that plane, since the inclusion and matrix fit together on that plane without distortion. In infinitesimal elasticity the transformation strain, $\boldsymbol{\varepsilon}^0$, has an invariant plane if and only if it can be written in the dyadic form

$$\boldsymbol{\varepsilon}^0 = \frac{1}{2}(\mathbf{ln} + \mathbf{nl}) \tag{2.7}$$

where $\mathbf{l}$ and $\mathbf{n}$ are vectors, and $\mathbf{n}$ can be taken to be a unit vector without loss of generality. Eq. (2.7) can be written in matrix form

$$\boldsymbol{\varepsilon}^0 = \frac{1}{2}\begin{bmatrix} 2n_1l_1 & n_1l_2+l_1n_2 & n_1l_3+l_1n_3 \\ n_1l_2+l_1n_2 & 2n_2l_2 & n_2l_3+l_2n_3 \\ n_1l_3+l_1n_3 & n_2l_3+l_2n_3 & 2n_3l_3 \end{bmatrix} \tag{2.8}$$

A dyadic strain, ε^0, has invariant planes perpendicular to the dyad vectors, **l** and **n**. As can be shown by substitution into Eqs. (2.3) and (2.4), when ε^0 is dyadic,

$$B(\mathbf{n}) = B(\mathbf{l}) = 0 \tag{2.9}$$

so that the elastic energy vanishes for thin plates in the habits **n** or **l**. This relation provides the connection between the "elastic" and "crystallographic" theories of the habit plane; however, as Christian has emphasized, finite deformation ordinarily removes the degeneracy between **n** and **l**, so there is only one invariant plane in the crystallographic theory. We shall let this be the plane **n**.

2.3. Dyadic Transformation Strains

It is relatively easy to determine whether a particular transformation strain, ε^0, has dyadic form. In a coordinate system chosen so that the coordinate direction $\mathbf{e}_3$ lies perpendicular to both of the dyad vectors, **n** and **l**, the strain component, $\varepsilon^0_{ij} = 0$ whenever i or j = 3. Then from Eq. (2.8), ε^0 becomes

$$\varepsilon^0 = \frac{1}{2}\begin{bmatrix} 2n_1l_1 & n_1l_2+l_1n_2 & 0 \\ n_1l_2+l_1n_2 & 2n_2l_2 & 0 \\ 0 & 0 & 0 \end{bmatrix} \tag{2.10}$$

If the tensor is then referred to its principal axes in the (**nxl**) plane, its form is

$$\varepsilon^0 = \begin{bmatrix} \lambda_1 & 0 & 0 \\ 0 & \lambda_2 & 0 \\ 0 & 0 & 0 \end{bmatrix} \tag{2.11}$$

where λ_1 and λ_2 are the principal strains. Comparing Eq. (2.10) with Eq. (2.11) and using the relations $n_1 l_1 = \lambda_1$, $n_2 l_2 = \lambda_2$, $n_1 l_2 + l_1 n_2 = 0$, the vectors $\mathbf{n}$ and $\mathbf{l}$ have components along the principal axes:

$$\mathbf{n} = \left[\sqrt{\frac{\lambda_1}{(\lambda_1-\lambda_2)}}, \sqrt{\frac{-\lambda_2}{(\lambda_1-\lambda_2)}}, 0\right]$$

$$\mathbf{l} = \left[\frac{\lambda_1}{n_1}, \frac{\lambda_2}{n_2}, 0\right] \tag{2.12}$$

The vector, $\mathbf{n}$, is imaginary unless the principal strains, λ_1 and λ_2, have opposite signs. Hence $\boldsymbol{\varepsilon}^0$ is dyadic if and only if one of its principal strains vanishes and the other two are opposite in sign.

In general, the transformation strain is not dyadic. However, it is still often possible to form a composite particle that has a dyadic net transformation strain by alternating thin strips of two different crystallographic variants of the transformation product, and joining them internally along a plane of perfect crystallographic match, such as a twin plane, to achieve a strain-free junction. If such a composite particle forms as a thin plate on an invariant plane of the net transformation strain, its elastic energy is very small. The elastic energy is not quite zero since the individual elements of the composite strain the surrounding matrix. However, since the strain fields of the different variants that make up the particle cancel one another at distances much greater than their domain size, the strain associated with such a particle is localized along its interface [13] and acts like a surface energy.

The linear elastic theory of composite particles is particularly simple when the transformation strain is orthorhombic or tetragonal, as, for example, is the tetragonal Bain strain that governs the martensitic transformation in steel. An orthorhombic strain referred to its principal axes has the form

$$\varepsilon^0 = \begin{bmatrix} \varepsilon_{11} & 0 & 0 \\ 0 & \varepsilon_{22} & 0 \\ 0 & 0 & \varepsilon_{33} \end{bmatrix} \tag{2.13}$$

where the ε_{ii} are the principal strains. ε^0 is tetragonal if two of the principal strains are equal. If the parent matrix is cubic and the principal axes of the strain parallel the cubic axes, there are three distinct crystallographic variants. These are obtained by interchanging the three principal strains. Let a composite plate be made by alternating the variant described by (2.13) with that whose transformation strain interchanges ε_{11} and ε_{33}, and let the fraction of the second variant be f. Then the net transformation strain is

$$\varepsilon^0 = (1\text{-}f)\begin{bmatrix} \varepsilon_{11} & 0 & 0 \\ 0 & \varepsilon_{22} & 0 \\ 0 & 0 & \varepsilon_{33} \end{bmatrix} + f\begin{bmatrix} \varepsilon_{33} & 0 & 0 \\ 0 & \varepsilon_{22} & 0 \\ 0 & 0 & \varepsilon_{11} \end{bmatrix} \tag{2.14}$$

In order that ε^0 have dyadic form we must have

$$f = \frac{\varepsilon_{33}}{\varepsilon_{33} - \varepsilon_{11}} \tag{2.15}$$

in which case the net principal strains are

$$\lambda_1 = \varepsilon_{11} + \varepsilon_{33} \qquad \lambda_2 = \varepsilon_{22} \qquad \lambda_3 = 0 \tag{2.16}$$

But, since $0 \le f \le 1$, a solution exists only if ε_{11} and ε_{33} have opposite signs, and Eq. (2.12) can only be satisfied if the sign of $(\varepsilon_{11} + \varepsilon_{33})$ is opposite to that of ε_{22}. Assuming ε_{11} has a sign which is opposite to that of ε_{22} and ε_{33}, an invariant plane exists if $|\varepsilon_{11}| > |\varepsilon_{33}|$. Any symmetric strain tensor can be diagonalized to have an orthorhombic form. Therefore, Eq. (2.16) and the above condition can be used for any symmetric strain to determine whether or not it is a dyadic strain. In the case of a tetragonal strain ($\varepsilon_{22} = \varepsilon_{33}$), an invariant plane exists if and only if ε_{11} and ε_{22} have opposite signs, and $|\varepsilon_{11}| > |\varepsilon_{22}|$. The familiar Bain strain has this form.

It follows that the linear elastic theory distinguishes three cases. (1) The transformation strain is dyadic. In this case the preferred configuration is a single-variant particle on the invariant plane. (2) The transformation strain is not dyadic, but there exists a composite particle whose net strain is dyadic. In this case the preferred configuration is a composite particle on the invariant plane of the net dyadic strain. (3) The transformation strain is not dyadic and cannot be made so. In this case no invariant plane exists. The preferred configuration is a thin plate on the plane that minimizes the elastic energy.

2.4. The Two-dimensional Case

It is important to note that case (2) is lost in the two-dimensional case (plane strain). When a two-dimensional transformation strain is referred to its principal axes in the plane it always takes the form:

$$\boldsymbol{\varepsilon}^0 = \begin{bmatrix} \varepsilon_{11} & 0 & 0 \\ 0 & \varepsilon_{22} & 0 \\ 0 & 0 & 0 \end{bmatrix} \tag{2.16}$$

which is dyadic if the principal strains have opposite signs and is non-dyadic otherwise. Hence two-dimensional models of the martensitic transformation are inherently limited. They cannot reproduce the case in which a particle develops as a composite to create an invariant plane. The single-variant particle either has an invariant plane or it does not.

Despite this limitation, two-dimensional simulations of the martensitic transformation can be interesting and informative, as it will be shown below. They are computationally simple, and do illustrate the development of multivariant microstructures to minimize the overall elastic energy. The development of microtwinned particles can be simulated by assuming that the elementary transformation step creates a microtwinned particle with a net transformation strain given by Eq. (2.16). Then the normal to the invariant plane lies in the $\mathbf{e}_1$, $\mathbf{e}_2$ plane of the simulation, and there are two variants of the

microtwinned particle in the plane, whose strains are related by the interchange of ε_{11} and ε_{22}. When a three-dimension strain is dyadic, it is reduced to a two-dimension or plane strain like that in Eq. (2.16). Therefore, the simulation using the dyadic strain in two-dimension case does not loose its generality but represents the transformation with a branch of transformation strain in three-dimension space.

CHAPTER 3

COMPUTER SIMULATION MODEL OF THE MARTENSITE TRANSFORMATIONS

In this Chapter, the computer simulation model of the martensitic transformation is constructed. It also includes the descriptions of several extensions of the model for simulating the martensitic transformation in a constrained, under external stress conditions (Chapter 5), the reversible transformations during a thermal (cooling-heating) cycle (Chapter 6) and during a mechanical (loading-unloading) cycle (Chapter 7).

3.1. The Computer Model

The body that undergoes the transformation is represented by an (n x n x n) cubic grid in three-dimensional space, or an (n x n) square grid in two-dimensional space. The cubic or the square grid is repeated periodically across each of its boundaries to fill the three or two-dimensional space. Each small cube or square is an elementary cell that is the minimum element that can undergo the martensitic transformation. For the purposes of this paper the body is assumed to have a free boundary with no external stress.

To describe the configuration of martensite in a partially transformed body, each cell is labeled by its position vector, $\mathbf{R}$, and define the function $\zeta_p(\mathbf{R})$, which has the value 1 if the cell at $\mathbf{R}$ is filled by martensite of variant, p, and is zero otherwise. Given periodic boundary conditions, $\zeta_p(\mathbf{R}+\mathbf{R}_L) = \zeta_p(\mathbf{R})$, where $\mathbf{R}_L$ is any translation vector of the repeated grid. If there are α distinct variants of the martensite, the configuration is specified by the α distribution functions, $\zeta_p(\mathbf{R})$, $p = 1,...,\alpha$.

To simulate the constraint imposed when the transformation occurs within a restricted region of a larger body, the transformation is confined to an (m x m) subarea in the center of the (n x n) array. Mathematically, $\zeta_p(\mathbf{R})$ is constrained to the value, 0, unless $\mathbf{R}$

is within the (m x m) subarea. The thick, untransformed border acts as a buffer that provides mechanical constraint during the transformation. This boundary condition provides a direct simulation for the transformation of isolated particles within a non-transforming matrix. It also provides a rough model for the transformation of a restricted region within a larger body, for example, the transformation of a single grain within a polygranular body. If m = n, the situation is reduced to the unconstrained condition.

3.2. The Transformation Strains

For simplicity we assume that the parent phase is cubic and the three-dimensional transformation strain is tetragonal. The most general tetragonal strain can be written as the sum of a pure dilation, of magnitude ε_d, and a pure shear, of magnitude ε_s. If the tetragonal axis lies in the [100] direction, the transformation strain is

$$\boldsymbol{\varepsilon}^0(1) = \varepsilon_d \begin{bmatrix} 1 & 0 & 0 \\ 0 & 1 & 0 \\ 0 & 0 & 1 \end{bmatrix} + \varepsilon_s \begin{bmatrix} 2 & 0 & 0 \\ 0 & -1 & 0 \\ 0 & 0 & -1 \end{bmatrix} = \varepsilon_s \begin{bmatrix} R+2 & 0 & 0 \\ 0 & R-1 & 0 \\ 0 & 0 & R-1 \end{bmatrix} \qquad (3.1)$$

where $R = \varepsilon_d/\varepsilon_s$ is the ratio of dilation to shear, the *dilation ratio.* The transformation strain (16) admits two other crystallographic variants which differ in the orientation of the tetragonal axis. If the tetragonal axis parallels [010] the transformation strain, $\boldsymbol{\varepsilon}^0(2)$, has $\varepsilon_{11} = \varepsilon_{33} = R-1$, $\varepsilon_{22} = R+2$. A tetragonal axis parallel to [001] leads to $\boldsymbol{\varepsilon}^0(3)$, with $\varepsilon_{11} = \varepsilon_{22} = R-1$, $\varepsilon_{33} = R+2$.

If the principal axes of a two-dimensional (plane) transformation strain parallel those of the parent cubic crystal the strain tensors of the two variants can be written

$$\boldsymbol{\varepsilon}^0(1) = \varepsilon_s \begin{bmatrix} R+1 & 0 \\ 0 & R-1 \end{bmatrix} \qquad \boldsymbol{\varepsilon}^0(2) = \varepsilon_s \begin{bmatrix} R-1 & 0 \\ 0 & R+1 \end{bmatrix} \qquad (3.2)$$

where ε_s is the shear in the plane and the dilation ratio, $R = \varepsilon_a/\varepsilon_s$, is the ratio of the areal expansion, ε_a, to the shear.

3.3. The Elastic Energy

To compute the energy of an arbitrary distribution of transformed cells, specified by the α distribution functions, $\zeta_p(\mathbf{R})$, we must generalize Eq. (2.1) to the case in which many different inclusions are simultaneously present. This was done by Khachaturyan and Shatalov [12] (see also Khachaturyan [13]). In the special case in which the inclusions are transformed cells of volume, υ, in an array of volume, $V = N\upsilon$, with periodic boundary conditions, the Khachaturyan-Shatalov equation can be written as the simple sum [13]

$$E_{elast} = \frac{V}{2}\sum_{p}\lambda_{ijkl}\varepsilon^0_{ij}(p)\varepsilon^0_{kl}(p)\zeta_p - \frac{V}{2}\sum_{p,q}\lambda_{ijkl}\,\varepsilon^0_{ij}(p)\varepsilon^0_{kl}(q)\zeta_p\zeta_q$$

$$+\frac{1}{2}\sum_{p,q}\sum_{\mathbf{R},\mathbf{R}'}W_{pq}(\mathbf{R}-\mathbf{R}')\zeta_p(\mathbf{R})\zeta_q(\mathbf{R}') \qquad (3.3)$$

where the summation is taken over all possible variants and over all cells, $\mathbf{R}$, in V. In this expression $\boldsymbol{\varepsilon}^0(p)$ is the transformation strain of the p^{th} variant and ζ_p is the volume fraction of the p^{th} variant. The two-body potential, $W_{pq}(\mathbf{R}-\mathbf{R}')$, is given by the Fourier sum

$$W_{pq}(\mathbf{R}-\mathbf{R}') = -\frac{1}{V}\sum_{\mathbf{k}}{}'\left[e_i\sigma^0_{ij}(p)\Omega_{jk}(\mathbf{e})\sigma^0_{kl}(q)e_l\right]\frac{|\eta_0(\mathbf{k})|^2}{\upsilon}\,e^{i\mathbf{k}\cdot(\mathbf{R}-\mathbf{R}')} \qquad (3.4)$$

where $\boldsymbol{\sigma}^0(p)$ is the transformation stress of the p^{th} variant, $\mathbf{e}$ is the unit vector in the direction of $\mathbf{k}$, $\eta_0(\mathbf{k})$ is the shape function of the cell,

$$\eta_0(\mathbf{k}) = \int_{\upsilon} e^{i\mathbf{k}\cdot\mathbf{r}} d^3r = \frac{\sin(k_1L/2)}{k_1/2}\frac{\sin(k_2L/2)}{k_2/2}\frac{\sin(k_3L/2)}{k_3/2} \tag{3.5}$$

where L is the edge length of the cubic elementary cell, and the summation is taken over the permissible values of $\mathbf{k}$, $k_i = \frac{2\pi i}{n}$, where i = 1,2,3, j is any integer and $n = N^{1/3}$ is the number of cells along the edge of the volume V. The prime on the summation indicates that the origin, $\mathbf{k} = \mathbf{0}$, is eliminated from the sum.

The same formulae hold in the two-dimensional case, with $\upsilon = a = L^2$, the area of a square cell of edge length, L, and

$$\eta_0(\mathbf{k}) = \frac{\sin(k_1L/2)}{k_1/2}\frac{\sin(k_2L/2)}{k_2/2} \tag{3.6}$$

Figure 3.1 shows a quadrant of $|\eta_0(\mathbf{k})|^2$, plotted using Eq. (3.6), which extends into 5th Brillouin zone in two-dimensional space.

To solve for the interparticle interaction, Eq. (3.4), it is necessary to calculate the Fourier sum on the right hand side. Since the bracketed term in Eq. (3.4) is independent of the magnitude of $\mathbf{k}$, and $\eta_0(\mathbf{k})$ decreases rapidly with $|\mathbf{k}|$, it is only necessary to consider the terms that lie in the first few Brillouin zones about the origin. However, to evaluate the term in brackets we require the transformation strain tensor, $\boldsymbol{\sigma}^0(p)$, for each variant, and the matrix elastic tensor, $\boldsymbol{\Omega}(\mathbf{e})$. For the three-dimensional case we assume the tetragonal transformation strain given in Eq. (3.1), which permits three variants that differ in the choice of the tetragonal axis. We further assume that the matrix is elastically isotropic with shear modulus, μ, and Poisson's ratio, ν (which we approximate as 1/3). The transformation stress of the variant with tetragonal axis along $\mathbf{e}_1$ is

$$\boldsymbol{\sigma}^0(1) = 2\mu\varepsilon_s\left\{\frac{1+\nu}{1-2\nu}\begin{bmatrix} R & 0 & 0 \\ 0 & R & 0 \\ 0 & 0 & R \end{bmatrix} + \begin{bmatrix} 2 & 0 & 0 \\ 0 & -1 & 0 \\ 0 & 0 & -1 \end{bmatrix}\right\} \equiv 2\mu\varepsilon_s\begin{bmatrix} 4R+2 & 0 & 0 \\ 0 & 4R-1 & 0 \\ 0 & 0 & 4R-1 \end{bmatrix} \tag{3.7}$$

The two-dimensional form of Eq. (3.7) is

$$\sigma^0(1) = 2\mu\varepsilon_s \left\{ \frac{R}{1-2\nu} \begin{bmatrix} 1 & 0 \\ 0 & 1 \end{bmatrix} + \begin{bmatrix} 1 & 0 \\ 0 & -1 \end{bmatrix} \right\} \equiv 2\mu\varepsilon_s \begin{bmatrix} 3R+1 & 0 \\ 0 & 3R-1 \end{bmatrix} \tag{3.8}$$

In both cases the matrix elastic tensor can be written

$$\Omega_{ij}(\mathbf{e}) = \frac{1}{\mu}\delta_{ij} - \frac{1}{2\mu(1-\nu)} e_i e_j \tag{3.9}$$

When Eqs. (3.7) or (3.8) and (3.9) are substituted into Eq. (3.4), the shear strain, ε_s, and shear modulus, μ, are gathered into the multiplicative factor, $\mu\varepsilon_s^2$, which has units of energy. If we take this term to define the unit of energy, then $W_{pq}(\mathbf{R})$ depends only on the dilation ratio, R. The dilation ratio is the single material variable that determines the pattern of transformation under a given set of conditions.

As an illustration of the results, Figure 3.2 shows a plot of the function $W_{11}(\mathbf{R}-\mathbf{R}')$, the interaction between like particles, for a two-dimensional case in which the transformation strain is a pure shear (R = 0). Figure 3.3 and Figure 3.4 show the plots of $W_{11}(\mathbf{R}-\mathbf{R}')$ for the dilation ratio R = 0.25 and R = 1.0 respectively. In the pure shear case, $W_{11}(\mathbf{R}-\mathbf{R}')$ has a four-fold symmetry. The dilation disturbs the four-fold symmetry, and the interaction between near neighbor increases with the value of R.

3.4. The Free Energy

When the boundary of the solid is diathermal and deformable its equilibrium is governed by the Gibbs free energy. When there is no traction on the boundary the elastic contribution to the Gibbs free energy is the elastic energy given by Eq. (3.3). If a matrix cell at position **R** is transformed to a martensite particle of variant, p, the elastic part of the Gibbs free energy changes by the amount

$$\Delta G_e(p,R) = \frac{\upsilon}{2}\lambda_{ijkl}\varepsilon^0_{ij}(p)\varepsilon^0_{kl}(p) - \upsilon\sum_q \lambda_{ijkl}\varepsilon^0_{ij}(p)\varepsilon^0_{kl}(q)\zeta_q + \sum_{q,R'} W_{pq}(R-R')\zeta_q(R') \quad (3.10)$$

The total change in the free energy when the cell at R transforms to variant p is the sum of chemical and elastic terms when the external stress is missing and the other resistance (e.g., surface energy) are neglected:

$$\Delta G(T, p,R) = \upsilon\Delta G_\upsilon(T) + \Delta G_e(p,R) \quad (3.11)$$

where $\Delta G_\upsilon(T)$ is the chemical free energy change per unit volume in a stress-free transformation. $\Delta G_\upsilon(T)$ is approximately linear in temperature for T near T_0, the equilibrium transformation temperature:

$$\Delta G_\upsilon(T) \cong \Delta H°(T_0-T) \quad (3.12)$$

It follows that a plot of the fraction transformed against $\Delta G_\upsilon(T)$ approximates the TT curve of the transformation, to within the scale factor, $\Delta H°$ (which is measured in units of E_0).

3.5. External Stress

An external stress, σ^e, changes the Gibbs free energy by the term

$$G_S = - V\sigma^e_{ij}\bar{\varepsilon}_{ij} = - V\sum_p \zeta_p\sigma^e_{ij}\varepsilon^0_{ij}(p) \quad (3.13)$$

where $\bar{\varepsilon}$ is the macroscopic strain induced by the transformation,

$$\bar{\varepsilon}_{ij} = \sum_p \zeta_p\varepsilon^0_{ij}(p) \quad (3.14)$$

The formation of a martensite particle with variant, p, changes G_s by the amount

$$\Delta G_s(p) = - \upsilon \sigma^e_{ij} \varepsilon^0_{ij}(p) \tag{3.15}$$

which ordinarily depends on the variant, p, but is independent of the position, **R**. If we measure the magnitude of the external stress in units of $\mu\varepsilon_s$, and measure ΔG_s in units of $E_0 = (\upsilon/2)\mu\varepsilon_s^2$, then $\Delta G_s(p)$ depends only on the dimensionless stress and the dilation ratio, R.

The total change in the free energy for the transformation of the element (p, **R**) under a stress, σ^e, at a fixed temperature, T, is:

$$\Delta G(T, p, R) = \upsilon \Delta G_\upsilon(T) + \Delta G_e(p,R) + \Delta G_i(\sigma^e, p) \tag{3.16}$$

when the other resistance are neglected.

3.6. Frictional resistance and Plastic Relaxation

In the ideal case the cell at **R** would transform spontaneously if the free energy change, $\Delta G(T, p, R)$, is negative. However, to approach the experimental situation more closely we wish to include the possibility that the transformation is opposed by a frictional resistance that may be associated with nucleation barriers, restrictions on interface mobility, plastic deformation, or interactions with internal defects. To phrase the simplest possible model, the frictional resistance, ΔG_r, is assumed a constant, independent of temperature, particle type, or particle configuration.

The second effect we wish to include in the model is the possibility that some part of the elastic strain that is stored during the transformation is relaxed by plastic

deformation. The relaxed part of the elastic energy does not oppose further transformation (unless it changes its form and becomes a part of the frictional resistance), and the elastic interaction between the particles decreases because of the reduced elastic energy at each position. In this case, a particle of type p, at position **R**, stores only a fraction, $f_f(p,\mathbf{R},T)$, of the elastic energy, $\Delta G_e(p,\mathbf{R})$, associated with the forward transformation. The simplest model is used and f_f, *plastic relaxation factor*, is set at the constant value. In the limit, $f_f = 1$, there is no lost in the elastic energy by the plastic deformation. In the limit, $f_f = 0$, the elastic energy is fully relaxed.

With these assumptions, the free energy that must be supplied to transform a cell at **R** to the variant, p, is

$$\Delta G(T,\ p,\mathbf{R}) = \upsilon\Delta G_\upsilon(T) + f_f\,\Delta G_e(p,\mathbf{R}) + \Delta G_i(\sigma^e,p) + \Delta G_r \qquad (3.17)$$

3.7. Reverse Transformation and Reversibility

When the transformation is reversed, the part of the elastic energy relaxed by plastic deformation cannot be recovered. In this case, the reversion of a particle of type p, at position **R**, releases only a fraction, $f_r(p,\mathbf{R},T)$, of the elastic energy, $\Delta G_e(p,\mathbf{R})$, associated with the forward transformation. Again, for the simplicity, $f_r(p,\mathbf{R},T)$ is set at the constant value f_r, which is the *reversibility of the elastic energy*. In the limit, $f_r = 1$, all of the elastic energy is recovered; in the limit, $f_r = 0$, no elastic energy can be recovered during the reverse transformation.

The total free energy change for the reverse transformation, of the element (p,**R**) at temperature, T, is, then

$$\Delta G'(T,\ p,\mathbf{R}) = \upsilon\Delta G'_\upsilon(T) + f_r\,(\Delta G'_e(p,\mathbf{R}) + \Delta G'_i(\sigma^e,p)) + \Delta G'_r \qquad (3.18)$$

where $\Delta G_v^{'}(T)$ is the chemical free energy change per unit volume for the reverse transformation of martensite to parent phase, and $\Delta G_v^{'}(T) = -\Delta G_v(T)$ at the same temperature; $\Delta G_e^{'}(p,R)$ is the part of the Gibbs free energy change when a martensite particle of variant p at position R is reverse to a matrix cell, and $\Delta G_e^{'}(p,R) = -\Delta G_e(p,R)$ if the configurations of martensite are the same when the forward and reverse transformations of the element (p,R) take place; $\Delta G_i^{'}(\sigma^e,p)$ is the free energy change due to the external stress, σ^e, when a martensite particle p is reversed to a matrix cell; $\Delta G_r^{'}$ is the frictional resistance of reverse transformation, a constant for all martensite particles.

3.8. The Transformation Path

The martensitic transformation modeled here is athermal. The athermal character of the transformation has the consequence that an elementary cell within the array can transform only if the free energy change is negative.

3.8.1. Irreversible transformation

To simulate a martensitic transformation of the two or three-dimensional bodies defined above we introduce one or more martensite nuclei, which are taken to be cells that have previously transformed. Given $W_{pq}(\mathbf{R})$, which can be tabulated once and for all in a computer, $\Delta G_e(p,R)$ can be found for all untransformed cells that lie in the subarray in which transformation is permitted. The chemical driving force, ΔG_v, is then set at the value that is just sufficient to make $\Delta G(T,p,R)$ negative for at least one cell. This cell is transformed; mathematically, $\zeta_p(R)$ is set equal to one for the position R, and variant p, of the transformed particle. The transformation of the first cell usually causes several cells to have negative $\Delta G(p,R)$. The cell that does transform (R_t) and its variant (p) are chosen to maximize the decrease in free energy. $\Delta G_e(p,R)$ is then recomputed, and the remaining

untransformed cells are surveyed to identify the preferred site for the next element of the transformation. This process is iterated until either all cells have transformed or all remaining cells yield positive values of ΔG. Since $\Delta G_0(T)$ is the same for every cell, this procedure automatically chooses the transformation path that minimizes the increment to the elastic energy in each step.

3.8.2. Reversible transformation

Similar to the forward transformation, the reverse transformation occurs only if the free energy change, $\Delta G'(T,p,\mathbf{R})$, is negative. In the simulation of reversible transformation, the reverse transformation is allowed during cooling or loading, if the internal elastic strain is sufficient to drive it, and the forward transformation is also allowed during heating or unloading. This means that the forward transformation and reverse transformation compete with one another at each step. However, for simplicity, the reverse transformation is confined to the transformation from martensite to parent phase. A direct transition between martensite variants is not permitted

At each step of transformation, $\Delta G'(T,p,\mathbf{R})$ can be computed for all transformed cells. Then the smallest $\Delta G(T,p,\mathbf{R})$ and $\Delta G'(T,p,\mathbf{R})$ are compared to see which is smaller when both are negative. If $\Delta G'(T,p,\mathbf{R})$ is more negative, the variant p martensite particle at the location $\mathbf{R}$ is reversed to the matrix cell; $\zeta_p(\mathbf{R})$ is reset to zero. This process is iterated until neither can forward transformation nor reverse transformation continue and then the driving force (chemical free energy or stress) must be increased (for cooling or loading process) or decreased (for heating or unloading process). The transformation path that is simulated by this procedure is the *minimum energy path*, the path that provides the maximum decrease in free energy for each incremental step. The simulation results are generated by using the minimum energy path throughout, except otherwise indicated.

3.8.3. Temperature-Transformation (TT) curve

To determine the form of the TT curve for the cooling process, $\Delta G_v(T)$ is first given the value that is just sufficient to initiate the transformation from the pre-existing seed. This simulates a situation in which the sample is cooled ($\Delta G_v(T)$ is decreased) until the transformation initiates. The transformation is then continued until it either reaches completion, or arrives at a configuration in which any further transformation would increase the free energy ($\Delta G(T, p,\mathbf{R}) > 0$ and $\Delta G'(T, p,\mathbf{R}) > 0$ for every possible incremental step). If the transformation stops before completion, the value of $\Delta G_v(T)$ is decreased to a value that is just sufficient to continue the transformation, and the simulation is continued. This procedure generates a plot of the fraction transformed vs. $\Delta G_v(T)$ for the cooling process, which gives the TT curve to within the scale factor that relates $\Delta G_v(T)$ and T. The TT curve for a heating process can be determined by the similar way. $\Delta G_v(T)$ is increased to where the reverse transformation starts. If the reverse transformation stops before the all martensite particles transform to the matrix or before a desired remaining volume percentage martensite is reached, the value of $\Delta G_v(T)$ is increased again to a value just sufficient to continue the reverse transformation.

CHAPTER 4

COMPUTER SIMULATION OF MARTENSITIC TRANSFORMATION IN STRESS-FREE SOLIDS

In this chapter, the simulation results of irreversible martensitic transformation in stress-free solids are presented, and the shapes, habits and microstructures obtained from the simulation are compared with the analytical results predicted by the linear elastic theory in Chapter 2. The Gibbs free energy change includes only the chemical and elastic terms (Eq. (3. 11))

4.1. Simulated Transformations in Three Dimensions

The three-dimensional simulations were done on an 21x21x21 array. Six different tetragonal transformation strains were used. All were of the form given in Eq. (3.1); the dilation ratio, R, was varied to change the preferred state of the martensite particle. The examples were chosen to include a dyadic transformation strain, two different non-dyadic strains, and three intermediate cases leading to various types of composite particle. In all cases the transformation was initiated by transforming a single cell in the center of the array.

The results are shown in Figures 4.1 through 4.6. A tetragonal transformation strain leads to three distinct variants (Eq. (3.1)) which are labelled 1,2,3 according to the orientation of the tetragonal axis of the strain. In the figures, untransformed material is represented by an empty cell, variant (1) by a thin, horizontal bar, variant (2) by a short, thick vertical bar, and variant (3) by a thin, vertical bar. The origin of the transformation, which is always a particle of variant (1), is represented by a dark square. The figures show both intermediate configurations and the final configuration of the transformed body on typical (100), (010) and (001) sections.

(1) R = 1: dyadic transformation strain. In this case the transformation strains have the simple dyadic form:

$$\boldsymbol{\varepsilon}^0(1) = 3\varepsilon_s \begin{bmatrix} 1 & 0 & 0 \\ 0 & 0 & 0 \\ 0 & 0 & 0 \end{bmatrix} \qquad \boldsymbol{\varepsilon}^0(2) = 3\varepsilon_s \begin{bmatrix} 0 & 0 & 0 \\ 0 & 1 & 0 \\ 0 & 0 & 0 \end{bmatrix} \qquad \boldsymbol{\varepsilon}^0(3) = 3\varepsilon_s \begin{bmatrix} 0 & 0 & 0 \\ 0 & 0 & 0 \\ 0 & 0 & 1 \end{bmatrix} \tag{4.1}$$

The minimum energy configuration for an isolated particle is a single-variant plate with a {100} habit. As shown in Figure 4.1, this is the morphology produced by the simulation. A seed of variant (1) develops into a thin plate in the (100) plane, which gradually thickens until the whole body is transformed into a single-variant martensite.

(2) R = - 0.5: composite dyadic strain. In this case the three transformation strains are:

$$\boldsymbol{\varepsilon}^0(1) = \frac{3}{2}\varepsilon_s \begin{bmatrix} 1 & 0 & 0 \\ 0 & \bar{1} & 0 \\ 0 & 0 & \bar{1} \end{bmatrix} \qquad \boldsymbol{\varepsilon}^0(2) = \frac{3}{2}\varepsilon_s \begin{bmatrix} \bar{1} & 0 & 0 \\ 0 & 1 & 0 \\ 0 & 0 & \bar{1} \end{bmatrix} \qquad \boldsymbol{\varepsilon}^0(3) = \frac{3}{2}\varepsilon_s \begin{bmatrix} \bar{1} & 0 & 0 \\ 0 & \bar{1} & 0 \\ 0 & 0 & 1 \end{bmatrix} \tag{4.2}$$

A composite particle with a dyadic transformation strain can be made by mixing two variants in equal proportions; for example, equal fractions of variants (1) and (2) give

$$\bar{\boldsymbol{\varepsilon}} = \frac{1}{2}\boldsymbol{\varepsilon}^0(1) + \frac{1}{2}\boldsymbol{\varepsilon}^0(2) = \frac{3}{2}\varepsilon_s \begin{bmatrix} 0 & 0 & 0 \\ 0 & 0 & 0 \\ 0 & 0 & 1 \end{bmatrix} \tag{4.3}$$

The composite transformation strain is best accommodated by a thin plate with habit (001). The results of the computer simulation are shown in Figure 4.2. As expected, the simulated transformation generates a composite plate with an (001) habit in which two variants alternate. This plate gradually thickens to complete the transformation.

(3) R = 2; non-dyadic strain. In this case the three transformation strains are:

$$\boldsymbol{\varepsilon}^0(1) = \varepsilon_s \begin{bmatrix} 4 & 0 & 0 \\ 0 & 1 & 0 \\ 0 & 0 & 1 \end{bmatrix} \qquad \boldsymbol{\varepsilon}^0(2) = \varepsilon_s \begin{bmatrix} 1 & 0 & 0 \\ 0 & 4 & 0 \\ 0 & 0 & 1 \end{bmatrix} \qquad \boldsymbol{\varepsilon}^0(3) = \varepsilon_s \begin{bmatrix} 1 & 0 & 0 \\ 0 & 1 & 0 \\ 0 & 0 & 4 \end{bmatrix} \tag{4.4}$$

Since all of the principal strains are positive, these variants cannot be averaged into a dyadic strain. We are left with three separate variants, each of which has minimal energy when it is in the form of a plate with a habit of type {100}. The results of the computer simulation of this case are shown in Figure 4.3. The seed is a variant of type (1), which grows into a thin plate of variant (1) with a (100) habit. After that plate has extended through the array, a second plate of variant (2) nucleates and grows with a (010) habit. After the original plate has thickened somewhat, a plate of variant (3) nucleates and grows. These plates then thicken and new plates nucleate and grow to produce a composite microstructure in which all three variants appear. The structure is a macrocomposite of single-variant plates; the plates themselves are not composite.

(4) R = -2; non-dyadic strain giving rod-shaped particles. In this case the transformation strains are:

$$\boldsymbol{\varepsilon}^0(1) = -3\varepsilon_s \begin{bmatrix} 0 & 0 & 0 \\ 0 & 1 & 0 \\ 0 & 0 & 1 \end{bmatrix} \qquad \boldsymbol{\varepsilon}^0(2) = -3\varepsilon_s \begin{bmatrix} 1 & 0 & 0 \\ 0 & 0 & 0 \\ 0 & 0 & 1 \end{bmatrix} \qquad \boldsymbol{\varepsilon}^0(3) = -3\varepsilon_s \begin{bmatrix} 1 & 0 & 0 \\ 0 & 1 & 0 \\ 0 & 0 & 0 \end{bmatrix} \tag{4.5}$$

Since the principal strains have the same sign, no dyadic composite strain can be constructed. The elastic theory predicts single-variant particles. However, it can be shown that in an isotropic solid the energy of a particle with a transformation strain like $\boldsymbol{\varepsilon}^0(1)$ is minimized when the particle has the shape of a rod with a [100] axis [13]. (The transformed particle fits the matrix perfectly in the [100] direction, and concentrates strain in the isotropic (100) perpendicular plane.) The computer simulation of this case is illustrated in Figure 4.4. A seed of variant (1) grows into a rod in the [100] direction, as predicted. Once the rod has extended across the array, rods of the other two variants form and grow, as shown in the figure. The final microstructure consists of a complex mixture of all three variants.

Examples (3) and (4) illustrate the tendency for non-dyadic transformation strains to generate macrocomposite microstructures that mix discrete particles of several different

variants. The reason is the elastic strain that accumulates in the system as such particles grow. Particles of other variants nucleate and grow to relieve the strain.

Examples (1)-(4) illustrate the different types of behavior predicted by the elastic theory, and show that the computer simulation can reproduce them. However, the simulation is less successful in matching the theory when the minimum energy configuration is a composite particle with a preponderance of one variant, as illustrated by the following two examples.

(5) R = 0; simple shear. In this case the transformation strains are pure shears of the form

$$\varepsilon^0(1) = \varepsilon_s \begin{bmatrix} 2 & 0 & 0 \\ 0 & \bar{1} & 0 \\ 0 & 0 & \bar{1} \end{bmatrix} \tag{4.6}$$

Two pure shears of this type, for example, variants (1) and (2), can be joined to produce a dyadic composite particle by adding them in the mixture:

$$\bar{\varepsilon} = \frac{1}{3}\varepsilon^0(1) + \frac{2}{3}\varepsilon^0(2) = \varepsilon_s \begin{bmatrix} 0 & 0 & 0 \\ 0 & 1 & 0 \\ 0 & 0 & \bar{1} \end{bmatrix} \tag{4.7}$$

This particle is a composite of 1/3 variant (1) and 2/3 variant (2) that fits the matrix perfectly when it is a thin plate on the habit plane $(01\bar{1})$. A total of six symmetrically equivalent composite particles can be made in this way, whose preferred habits are the six {110} planes. The results of computer simulation of a transformation with this strain are shown in Figure 4.5. The transformation begins from a seed of type (1), and develops initially as a thick composite plate that generally follows $(01\bar{1})$. However, the fractions of the two variants are not quite right; they are near 0.5. After some growth the transformed particle develops into a mixture of all three variants that develops a complex microstructure.

(6) R = 0.2; butterfly martensite. When R = 0.2 the transformation strains have the form

$$\varepsilon^0(1) = \varepsilon_s \begin{bmatrix} 2.2 & 0 & 0 \\ 0 & .\overline{8} & 0 \\ 0 & 0 & .\overline{8} \end{bmatrix} \tag{4.8}$$

A composite particle with a dyadic strain can be made from two variants of this type in a nearly 3:1 proportion:

$$\bar{\varepsilon} = 0.73\varepsilon^0(1) + 0.27\varepsilon^0(2) = \varepsilon_s \begin{bmatrix} 1.4 & 0 & 0 \\ 0 & 0 & 0 \\ 0 & 0 & .\overline{8} \end{bmatrix} \tag{4.9}$$

This particle fits perfectly in the matrix if it has the form of a thin plate on the $(40\overline{3})$ plane. However, computer simulation of transformation from a single seed shows a different morphology (Figure 4.6). The initial particle grows as a mixture of two variants that join along a twin plane and diverge from one another to create a "butterfly" pattern. Eventually, the third variant also appears, creating a complex final microstructure.

The failure of the simulation to reproduce the minimum energy configuration suggested by the theory is a result of three factors whose contributions are difficult to separate. First, the simulated transformation proceeds one finite step at a time. Since each step is a single variant, the transformation cannot grow in increments that contain the proportions that appear in the most favorable composite plate. This does not present a problem when the variant fraction is near 0.5, since variants can alternate. However, the preferred composite structure is difficult to achieve when the fractions differ significantly from 0.5. Second, a dyadic transformation strain only produces a perfect match with the matrix when the transformed particle has the form of a thin plate. In the simulation the nucleus is cubic in cross-section, and necessarily remains a relatively thick particle in its early stages of growth. Third, the array is finite and relatively small. The growing particle is repeated periodically across the array boundaries, and begins to interact with its neighbors at a fairly early stage in the transformation. (The effect of array size was studied by doing simulations in a smaller array, 11x11x11, and in a larger array, 41x41x41. The results are

quantitatively different, but qualitatively the same; all particles grew with the same initial morphology and habit in the arrays of two different sizes.)

While these three problems are exaggerated in the computer simulation, they also affect martensitic transformations in real systems. Elementary volumes transform into single variant particles that, given surface tension, have finite size. The martensite particles initially have finite thickness and, hence, do not satisfy the assumptions of the crystallographic theory. Moreover, martensite particles tend to form from separate nuclei, often in separate grains, and interact with one another at an early stage. There may, therefore, be useful information in the details of single particle growth in the simulation. For example, "butterfly martensite", which is a common morphology in the computer simulation, is also observed in real systems [19], and has been difficult to interpret theoretically.

4.2. Simulated Transformations in Two Dimensions

The simulations of two-dimensional martensitic transformations used a 41x41 array of square cells with periodic boundary conditions. In the part of the work reported here, the matrix was assumed to be elastically isotropic and to have square symmetry in the plane. The principal axes of the transformation strain were taken to lie parallel to the cell edges. The transformation strain for these conditions was given in Eq. (3.2). The two variants are

$$\boldsymbol{\varepsilon}^0(1) = \varepsilon_s \begin{bmatrix} R+1 & 0 \\ 0 & R-1 \end{bmatrix} \qquad \boldsymbol{\varepsilon}^0(2) = \varepsilon_s \begin{bmatrix} R-1 & 0 \\ 0 & R+1 \end{bmatrix} \tag{4.10}$$

When $-1 \le R \le 1$ the transformation strain is dyadic, and the preferred state of a single martensite particle is a thin plate (line in two-dimensions) with the habit plane normal

$$\mathbf{n}(1) = \left[\sqrt{\frac{R+1}{2}}, \sqrt{\frac{1-R}{2}}\right] \qquad \mathbf{n}(2) = \left[\sqrt{\frac{1-R}{2}}, \sqrt{\frac{R+1}{2}}\right] \tag{4.11}$$

When $R > 1$ or $R < -1$ the transformation strain is not dyadic, and cannot be made so by making a composite of the two variants. The preferred state of a single particle is a thin plate (line) with the habit that maximizes the elastic relaxation energy.

As in the three-dimensional case, when the transformation strain is dyadic and the transformed material forms as a thin plate along its preferred habit, the elastic energy is zero; after an unconstrained transformation the body should contain a single variant of martensite. When the transformation strain is not dyadic, or when the particle does not form in its preferred shape and habit, strain accumulates in the body as the transformation proceeds. In this case even an unconstrained transformation will ordinarily produce a microstructure that is a complex mixture of martensite variants.

This behavior is illustrated by the results of the computer simulation studies presented in Figures 4.7 and 4.8. Figure 4.7 shows the appearance of the initial martensite plate that grows from a seed of variant (1), as the dilatation ratio, R, is varied from 0 (pure shear) to 1. As predicted, the transformation product is a single-variant plate with a definite habit. The predicted habit plane normal varies from [1,1] to [1,0] as R increases from 0 to 1. Table 4.1 compares the predicted and observed habit planes. The prediction is obeyed reasonably well, although the observed habit plane rotates toward [1,0] as R increases somewhat more quickly than the theory predicts. As in the three-dimensional case, the discrepancy has two sources: the granular structure of the computer model, which restricts the transformation path, and the finite thickness of the initial particle, which changes the preferred habit plane. If the martensite transformation is continued beyond the point shown in Figure 4.7, the plates thicken monotonically until the whole plane is transformed into a single variant of martensite.

Figure 4.8 shows the results of a simulated transformation with $R = 1.5$. In this case the predicted particle morphology is a thin, single-variant plate (line) with the normal [1,0] (variant (1)), or [0,1] (variant (2)). Growth from a seed of variant (1) produces a

single-variant plate with normal [1,0]. When this plate has grown across the array, the accumulated elastic strain triggers the formation of a plate of variant (2) that grows normal to [0,1]. the final microstructure is a mixture of plates of the two variants. Figure 4.8(b) illustrates an intermediate stage in the transformation. Note that plates of the two variants do not simply thicken; new plates tend to nucleate and grow at some distance from those that are already present.

Finally, we contrast the results obtained here with those presented in the earlier work of Wen, Khachaturyan and Morris [17], in which the two-dimensional transformation produced microtwinned plates (lines) along which the two transformation variants alternated. The reason for the difference is that Wen, et al. [17] used an approximation (point approximation) to the two-particle interaction function, $W_{pq}(\mathbf{R}-\mathbf{R}')$ (Eq. (3.4). The approximation is made by replacing the shape function of the cell, $\eta_0(\mathbf{k})$ (Eq. 3.6), by a constant such that $|\eta_0(\mathbf{k})|^2 = L^2$ (the area of the cell) when $\mathbf{k}$ is in the first Brillouin zone and zero otherwise. Figure 4.9 compares the shape function $|\eta_0(\mathbf{k})|^2$ and the approximation of it (step function) when $\mathbf{k}$ is a one dimensional variable (at (10) direction in Figure 3.1). This "point approximation" simplifies the calculation of $W_{pq}(\mathbf{R}-\mathbf{R}')$, but it exaggerates the interaction between unlike variants. Microtwinned particles appear to maximize the number of unlike neighbors. Figure 4.10 is the microstructure obtained from the simulation using the point approximation.

4.3. Discussion and Conclusion

The results presented above show that one can use the linear elastic theory to construct a tractable computer simulation model of the martensitic transformation that produces transformation patterns like those observed in real systems. The simulation was tested by comparing the shape and constitution of the initial martensite particles formed to the analytic predictions of the elastic theory. The results are generally encouraging.

In the three-dimensional case the elastic theory distinguishes three cases, depending on the nature of the transformation strain: (1) If the transformation strain is dyadic, the preferred transformation product should be a single-variant, thin-plate particle with a definite habit. (2) If the strain is not dyadic, but can be made so by constructing a composite of two variants, the preferred product should be a composite plate with a definite habit. (3) If the strain is not dyadic and cannot be made so by forming a composite particle, the initial product should be a thin plate (or rod) with the habit that minimizes the elastic energy. The computer simulation is in qualitative agreement with the theory for cases (1) and (3). In case (2), the three-dimensional computer simulation produces a properly twinned martensite when the predicted composite plate has equal fractions of two variants, but yields mixtures of thicker, single variant domains when the predicted fractions of the two variants differ significantly from 0.5. The difference between theory and simulation is not entirely due to shortcomings of the model. The theory assumes that the martensite particle forms as an arbitrarily thin plate with the correct internal constitution. The finite thickness of real martensite embryos changes both the habit and internal state. In fact, the simulation generates unusual patterns, such as "butterfly martensite", that are observed in real systems.

In the two-dimensional case the theory never predicts microcomposite particles. The two-dimensional transformation strain is either dyadic, leading to case (1), or inherently non-dyadic, leading to case (3). In both cases the initial transformation particle should be a thin plate (line in two dimensions) with a predictable habit. In agreement, the two-dimensional computer simulation yields thin, single-variant particles with habit planes that are close to those predicted. Microtwinned particles are not observed.

The microstructures that result when the simulated transformation is taken to completion are also in general agreement with theory. In cases (1) and (2) an arbitrarily thin martensite plate does not strain the matrix. Once the plate extends through the whole body, it can simply thicken until the body transforms completely. This is the behavior produced by the computer simulation in case (1) and in case (2), when the simulation leads to a mi-

crotwinned particle. In case (3), on the other hand, a growing particle produces elastic strains in the matrix. These can ordinarily be compensated if particles of different variants appear, creating a microstructure that is a macrocomposite of two or more variants. The computer simulation always produces a microstructure of this type in case (3), and also does so in examples of case (2) that do not form the favored microtwinned particle.

These results show that a martensitic microstructure is obtained only when the martensitic plate cannot adopt a strain-free form, or when its effort to do so is frustrated. In the simple model used here frustration happens when the plate has a composite microstructure that is difficult to achieve under the conditions imposed by the model. The growth of a strain-free dyadic particle can also be frustrated by physical constraints that appear naturally when the transformation occurs in a constrained or polygranular microstructure, when multiple nucleation sites are active and give rise to interacting particles, or when external stress modify the energetics of the transformation. These effects have been simulated, and will be discussed in the next chapter.

Table 4.1. The predicted and observed (in computer simulation) habit plane normals

R	$n = [n_1, n_2]$		n_1/n_2	
	predicted	observed	predicted	observed
0	[1,1]	[1,1]	1	1
0.180	[6,5]	[1,1]	1.2	1
0.219	[5,4]	[4,3]	1.25	1.33
0.3	[4,3]	[2,1]	1.36	2
0.6	[2,1]	[1,0]	2.0	∞
1.0	[1,0]	[1,0]	∞	∞

CHAPTER 5

COMPUTER SIMULATION OF MARTENSITIC TRANSFORMATIONS IN CONSTRAINED, TWO-DIMENSIONAL CRYSTALS UNDER EXTERNAL STRESS

5.1. Introduction

In previous chapters the linear elastic theory is used to predict the preferred configuration of a martensite particle and constructed a computer simulation model to study the microstructures that develop in simple situations. While the linear theory is only approximate, it does lead to a tractable model that reveals some of the factors that govern microstructure.

An analysis of the microstructures produced in computer simulated transformations of cases (2) and (3) (Chapter 4), where the transformation strain is not dyadic, suggests that external constraints play an important role. To explore this role, the transformations in crystals with constrained boundaries and in crystals that are subjected to external stress are simulated. In these simulations it is assumed that the transformation strain is dyadic (Case (1), $R < 1$ in Eq. (3.2)) so that any microstructure that appears is a consequence of the constraint. As it has been pointed out in Chapter 2, when a three-dimension strain is dyadic, it is reduced to a two-dimension or plane strain like those in Eq. (3.2), and the simulation in two-dimension case does not loose its generality but represents the transformation with a branch of transformation strain in three-dimension space. Simulations in two-dimension also minimizes computer time and simplify the visual presentation of the results.

As shown in Chapter 4, a dyadic transformation in an unconstrained crystal is accomplished by the growth and thickening of a single-variant plate. There is, therefore, no microstructure. Multivariant microstructures appear when geometric constraints prevent

relaxation of the shear stresses produced by the transformation. These can be relaxed, at least in part, by forming other variants that have compensating strains. In a real crystal the transformation is constrained by stable matrix phases, grain boundaries or other internal defects that limit the growth of a single plate, by plastic deformation of the untransformed matrix, and by the growth of plates that nucleate separately and interfere with one another. In this paper we shall consider only the first of these, and study the development of the martensitic transformation in an element of material that is embedded in an untransformed matrix.

A second qualitative feature of a dyadic transformation in a stress-free crystal is that the thermodynamic driving force (temperature or external stress) that is sufficient to nucleate the transformation is almost sufficient to complete it. The martensite start (M_s) and finish (M_f) temperatures are very close to one another. When the crystal is constrained, on the other hand, the accumulation of the transformation stress has the consequence that the transformation becomes more difficult as it proceeds. In this case the M_s and M_f temperatures are different. It is interesting to see and understand how the TT curve (fractional transformation versus temperature) of an athermal martensitic transformation depends on the transformation strain and the imposed constraints.

The external stress has an important effect on transformations that would ordinarily lead to multivariant microstructures. The deviatoric parts of the applied stress and the transformation strain ordinarily couple so that one martensite variant is preferred to the others. The applied stress affects the transformation path, the microstructure and the TT curve. The coupling between the applied stress and the martensitic transformation significantly affects the fracture and fatigue of metastable structural materials. The role of the stress is only partly understood.

These issues are explored below in the context of the computer simulation model described in Chapter 3. The transformation is irreversible, and the Gibb's free energy

includes the chemical free energy, elastic terms caused by the martensitic transformation and external stress (Eq.(3.16)).

5.2. Transformation in a Stress-Free Solid

5.2.1. The Microstructure Produced by a Pure Shear Transformation

First, let the transformation strain be a pure shear (R = 0), and let the transformation initiate from a single seed of type (1). When the transforming solid is unconstrained, the transformation proceeds through the growth of a single-variant plate along the (11) line, as described in Chapter 4. The plate extends until it touches the boundaries of the array. The plate then thickens until the whole array is transformed into a single-variant product. However, when the transformation is constrained by its surrounding the microstructure changes to a multivariant microstructure like that illustrated in Figure 5.1, which shows the transformation of a 41x41 region of a 101x101 array. The two variants form alternating bands on (11) that have almost equal areal fractions.

The source of this microstructure is straightforward. A plate of variant (1) grows across the array and thickens. However, since the growing plate is constrained by its surroundings, its shear gradually accumulates into a net shear stress that opposes further transformation. Eventually the internal stress becomes great enough to force the nucleation of plates of variant (2) along the sides of the original plate. As these grow, they first relax the shear due to the excess of variant (1), and then continue to grow until their accumulated strain forces the re-nucleation of plates of variant (1). In this way the transformation gradually builds up a microstructure of parallel plates of alternate variants.

The single-variant plates in this microstructure thin as the constraint increases since the back-stress that opposes continued growth increases more rapidly as the constraint is made more severe. This behavior is illustrated in Figure 5.2, which shows the results of

simulations in which the transforming region is fixed in size (41x41) while the array is expanded to provide a progressively larger untransformed buffer. As can be seen in the figure, the plate thickness decreases rapidly with array size, and asymptotes at a thickness of about 5 elementary cells when the array size is 80x80 or more.

Note that the microtwinning observed in this case does not develop to achieve an invariant plane strain in the sense of the "crystallographic theory" of martensite [3,4]. Each variant already has an invariant plane strain (see Chapter 3). The twins form to reduce energy by eliminating long-range shear strains in the matrix. A particularly clear experimental example is found in the microstructure of small, embedded particles of zirconia (ZrO_2) that have transformed from a tetragonal to a monoclinic structure [20].

5.2.2. The Influence of a Dilation on the Microstructure

A dilation ($R \neq 0$) affects the transformation path in two ways. First, R affects the crystallographic habit. As described and illustrated in Chapter 4, the preferred habit of a growing plate rotates as R increases from a (11) habit for $R = 0$ toward the {10} habit that is preferred when $|R|$ is large. Moreover, when $R \neq 0$ the preferred habits of the two variants differ; if the habit of variant (1) is (hk), that of variant (2) is (kh). Second, when $R \neq 0$ the transformation stress has a hydrostatic component that is the same for both variants. The hydrostatic component cannot be relaxed by forming multiple variants, and produces long-range stresses in the matrix that oppose the transformation.

The microstructural consequences of these effects are illustrated in Figure 5.3, which shows partly completed transformations for two values of the dilation ratio. In all cases the transformation begins with the growth of a thin plate of variant (1), the variant of the pre-existing seed. However, if the dilation is moderate to large ($|R| > 0.2$) this plate grows only a short distance before particles of variant (2) nucleate. Afterward the two variants grow simultaneously. Two growth morphologies have been observed. The first,

and most common, is the "butterfly" morphology that is shown in Figure 5.3(a). It closely resembles the martensite morphology that has been characterized experimentally by Tamura, Maki and coworkers (see, for example, Reference [19]). The transformation that creates this morphology begins as a twinned plate that grows along the (11) plane. However, the preferred habits of the two variants differ from one another and differ from (11) by angles that are mirror images of one another. As the twinned plate thickens, it splits into two single-variant "wings", each of which grows in a direction close to its preferred habit. As R increases the preferred habits differ farther from (11), and the "butterfly wings" spread. The second intermediate microstructure (Figure 5.3(b)) is the "cross" morphology in which the single variant plates grow out from the seed in their preferred planes and thicken to form a x-shape.

The simulations presented in Figures 5.1 through 5.3 assumed elastic isotropy. Simulations have also been done in anisotropic media. The results show that elastic anisotropy does not affect the qualitative results described above. Its major consequence is to change the preferred habit for given transformation strain.

5.2.3. The TT Curve for Stress-Free Transformations

If we assume a driving force (ΔG_v) that is just sufficient to start the transformation from a pre-existing seed, then an athermal transformation can continue only so long as there is an elementary transformation (p,**R**) such that

$$\Delta G_v + \min[\Delta G_e(p,\mathbf{R})] < 0 \qquad (5.1)$$

If the configuration is such that the smallest value of $\Delta G_e(p,\mathbf{R}) > |\Delta G_v|$ then the transformation stops, and will not begin again until ΔG_v is lowered to achieve condition (5.1). Simulated transformations in constrained systems often pass through a sequence of

metastable configurations that violate condition (5.1). Each metastable state requires a further decrease in ΔG_v to continue the transformation. The result is that the transformation develops in a series of bursts as ΔG_v is lowered. A plot of the fraction transformed against ΔG_v is roughly equivalent to a TT curve for the athermal transformation that extends from the martensite start (M_s) to the martensite finish (M_f) temperature.

When the transforming solid is unconstrained and the transformation is dyadic there is very little thermal resistance to the transformation. Under some conditions a metastable state is achieved when the first martensitic plate completes its growth to the boundaries of the array, requiring a small increase in the driving force, but it is essentially true that the whole body bursts into a single variant martensite once the applied driving force reaches the critical initiation value. The M_s and M_f temperatures are nearly the same, and the TT curve is essentially a vertical step at M_f.

The situation is very different for a transformation in a constrained solid, as is illustrated by the TT curves shown in Figure 5.4. Even when the transformation strain is a pure shear (R = 0) it is difficult to eliminate the last few particles of the untransformed phase, and ΔG_v must be lowered significantly to accomplish that. The microstructure at $\Delta G_v = -1.42E_0$, after the main burst of transformation, is shown in Figure 5.5(a); the residual phase is located at points of high stress where different variants impinge on one another and on the array boundary. The TT curve spreads significantly as the dilational contribution to the transformation (R) increases. This is partly because the dilation produces a hydrostatic stress that increases monotonically as the martensite fraction increases, and partly because transformation at high R creates a complex multivariant microstructure that contains many sites where internal stress fields interfere to create unfavorable conditions. The latter effect is apparent in the microstructures shown in Figure 5.5, which show the transformation at $\Delta G_v = -1.42E_0$ for various values of R.

(It should be noted that the numerical values of ΔG_v at which transformation starts (M_s) for the various values of R shown in Figure 5.4 are not strictly comparable because of

the way the simulation is done. In all cases the transformation initiates at a pre-existing seed of variant (1). This seed carries the transformation strain, which is different for the different values of R. This difference affects M_s, but has a negligible effect on the TT curve below M_s.)

5.3. Transformation under External Stress

It is always possible to divide an external stress into its hydrostatic and deviatoric components. These couple individually to the dilation and shear of the transformation strain. Since the martensite variants differ only in their shear, it is the deviatoric component of the stress that makes a qualitative change in the transformation. To illustrate and study this effect we have investigated three aspects of the influence of external stress: the effect of the load geometry on the martensite start temperature (M_s); the effect of uniaxial load on the microstructure and TT curve; and the influence of cyclic load on the martensite fraction and microstructure.

5.3.1. The Influence of Load Geometry on M_s

Let the solid be subject to a two-dimensional stress whose principal axes are parallel to the axes of the array. We consider three conditions: a uniaxial tensile stress along the y-axis ($\sigma^e_{22} > 0, \sigma^e_{11} = 0$), a uniaxial compressive stress along the y-axis ($\sigma^e_{22} < 0, \sigma^e_{11} = 0$), and a two-dimensional hydrostatic stress ($\sigma^e_{22} = \sigma^e_{11} < 0$). The first two stress tensors have a large deviatoric component; the third does not.

If we measure the stress in units of $\mu\varepsilon_s$,

$$\sigma^e_{22} = \sigma^* \mu\varepsilon_s \tag{5.2}$$

then, according to Eq. (3.15), the stress adds the factor

$$\Delta G_i(1) = - 2\sigma^* (R - 1) E_0 \tag{5.3}$$

$$\Delta G_i(2) = - 2\sigma^* (R + 1) E_0 \tag{5.4}$$

to the free energy changes on forming variants (1) and (2), where $E_0 = \frac{\upsilon}{2} \mu \varepsilon_s^2$. A two-dimensional hydrostatic stress

$$\sigma_{11}^e = \sigma_{22}^e = \sigma^* \mu \varepsilon_s \tag{5.5}$$

has the same effect on each variant

$$\Delta G_i(1) = \Delta G_i(2) = - 4\sigma^* R E_0 \tag{5.6}$$

The influence of the external stress on the driving force necessary to start the transformation (M_S) can be predicted from eqs. (5.3)-(5.6). A uniaxial load affects the two variants differently. Assuming nucleation sites for both variants, M_S is controlled by the variant that is favored by the external stress: variant (2) when $\sigma^* > 0$ (tension), variant (1) when $\sigma^* < 0$ (compression). Given uniaxial tension, M_S should rise with σ^* if $R > -1$, and fall if $R < -1$. Given uniaxial compression, M_S should increase with σ^* when $R < 1$, decrease when $R > 1$. Given hydrostatic stress, M_S increases with σ^* if R is positive, decreases if R is negative; that is, a hydrostatic tension promotes a transformation that increases volume while a hydrostatic compression promotes a transformation that decreases it.

These relations are illustrated by the data shown in Figure 5.6, which plots the value of ΔG_υ needed to initiate the simulated transformation in a constrained solid as a function of the applied load. The simulations tested the three load geometries for two

different transformation strains: a pure shear, R = 0 (Figure 5.6(a)) and a positive volume change, R = 0.22 (Figure 5.6(b)). When the transformation is a pure shear, hydrostatic stress has no effect, while a uniaxial load raises ΔG_v by the same amount whether the load is tensile or compressive. The only difference is that uniaxial tension nucleates variant (2) while uniaxial compression nucleates variant (1). When R = 0.22 a hydrostatic pressure lowers M_s (ΔG_v) while a uniaxial load raises it. However, note the asymmetry between tensile and compressive loading. A uniaxial tension induces a hydrostatic tension that promotes the transformation while a uniaxial compression induces a hydrostatic compression that opposes it. Hence the uniaxial tension is more effective in raising M_s. The behavior shown in Figure 5.6(b) is like that found experimentally by Patel and Cohen [21].

Note also that a sufficiently large and favorable stress initiates the transformation at a positive value of ΔG_v, which corresponds to $M_s > T_0$, the equilibrium transformation temperature. This corresponds the situation where the applied stress is so large that it provides an amount of negative free energy change which not only overcomes the positive free energy change caused by the martensitic transformation but also balance out the positive chemical energy change.

5.3.2. The Influence of External Stress on the Microstructure and the TT Curve

Computer simulated transformations were done and studied for all the cases included in Figure 5.6, that is, for a range of loads in uniaxial tension, compression and hydrostatic stress, using both pure shear (R = 0) and dilational (R = 0.22) transformation strains.

Hydrostatic stress is relatively uninteresting. Since a hydrostatic stress affects both variants in the same way, it only affects the M_s; it does not change the microstructure, and simply shifts the TT curve to higher temperature. In contrast, uniaxial stresses bias the

transformation towards a particular variant, and have profound qualitative effects. These are revealed in the sequence of simulations that modeled a transformation with R = 0.2 under uniaxial tension. In these simulations the transformation was done within a 41x41 array embedded in a 101x101 array, which should be large enough to eliminate the dependence of the constraint on the array size (Figure 5.2).

Figure 5.7 is a plot of the fraction transformed as a function of the driving force (ΔG_v) for loads that vary from $\sigma^* = 0$ to $\sigma^* = 1.2$. The data have three features that are particularly striking. First, the TT curve spreads monotonically as the load is increased from $\sigma^* = 0$ to $\sigma^* = 0.8$. The spread results primarily from an increase in M_s; there is very little change in M_f. Second, the behavior near M_s is almost identical for $\sigma^* \geq 0.4$. Third, the shape of the TT curve becomes independent of the load when $\sigma^* \geq 1.0$. The appearance of the curves suggests that there is a characteristic "low-stress" behavior that is exemplified by the behavior at $\sigma^* = 0.2$ and a characteristic "high-stress" behavior that appears clearly at $\sigma^* = 1.0$. As the load is increased from 0.2 to 1.0, an increasing fraction of the transformation exhibits "high-stress" characteristics.

To see why this is the case, and understand the microstructures that develop, it is useful to begin by examining the low- and high-stress limits. The stress-free transformation ($\sigma^* = 0$) for R = 0.2 was discussed earlier in the paper. The TT curve contains an initial step that is due to the growth of the initial, single-variant plate across the array (this initial step appears at all values of the stress). It goes to completion when the driving force is sufficient to nucleate the thickening of the initial plate. It contains equal fractions of the two variants, which appear in parallel bands along (11). The microstructure at almost complete transformation is shown in Figure 5.5(a). The alternation of the two variants largely cancels the shear developed during the transformation; only the dilation distorts the matrix. When R = 0.2 the shear is more important than the dilation, and its cancellation allows the transformation to proceed to completion relatively easily.

A high-stress uniaxial tension changes the behavior in two ways. First, a uniaxial stress in the y-direction significantly lowers the free energy required to form a particle of variant (2) (Eq. (16)), so the M_S temperature rises significantly. Second, the stress raises the free energy required to form variant (1). In the high-stress limit this variant does not form at all; the final microstructure contains only variant (2). However, the absence of variant (1) means that the shear component of the transformation strain is not compensated. It accumulates in the matrix, producing a back-stress that opposes the transformation and requires an increasing driving force to sustain it. The accumulation of the uncompensated shear strain is responsible for the large spread in the TT curve in the high-stress limit. Once the high-stress limit has been reached (at $\sigma^* \approx 1.0$ in this case), the transformation path becomes independent of the stress. The shape of the curve is fixed; it is simply translated to higher temperatures as σ^* increases.

While the final microstructure in the high-stress limit is uninteresting, there are many metastable intermediate microstructures. The pattern is illustrated in Figure 5.8. In the first stage of the transformation a plate of variant (2) nucleates, grows across the array, and thickens to create the metastable microstructure shown in Figure 5.8(a). The preferred habit of variant (2) is (34), so the plate is tilted slightly with respect to (11). In the next stage of growth the plate thickens further, but because of the increasing resistance of the matrix the driving force must be almost continuously increased. The thickening stage ends at point (b) on the transformation curve (Figure 5.8(d)). At this point a second plate of variant (2) nucleates and grows in a direction that is almost perpendicular to the original plate, creating the microstructure shown in Figure 5.8(b) at point (c) on the transformation curve. The crossing plate forms because its aggregate strain partly compensates the shear of the original plate. As the transformation continues the crossed plates thicken and the region between them is gradually filled with particles of variant (2). A late-stage metastable microstructure is shown in Figure 5.8(c). The transformation is opposed by the

accumulating strain in the matrix, and the thermodynamic driving force must be continuously increased to sustain it.

At intermediate values of the stress the transformation begins in the high-stress pattern, but changes to one that more closely resembles the low-stress pattern. The reason is that the back-stress that develops with the accumulated strain eventually becomes sufficient to overcome the bias toward the favored martensite variant. At this point the second variant appears, and the two variants alternate for the remainder of the transformation. The sequence is illustrated by the transformation at $\sigma^* = 0.4$ (Figure 5.9). The first stages of the transformation are just like those in the high-stress limit. A plate of variant (2) grows spontaneously on a plane near (34) and thickens until it reaches the metastable configuration shown in Figure 5.9(a). If the driving force is steadily increased (Figure 5.9(h)) the plate thickens until it reaches the metastable configuration shown in Figure 5.9(b). At this point a plate of variant (1) nucleates along the side of the original plate (Figure 5.9(c)). Since the preferred habit of variant (1) is (43) rather than (34), the variant (1) plate branches slightly away to leave a band of untransformed material along the interface. With a further increase in driving force parallel plates with alternating variants form to produce the microstructure in Figure 5.9(d). Additional driving force leads to the formation of a crossing plate that is a composite of the two variants, as shown in Figure 5.9(e). At this point almost 80% of the sample has transformed. The remaining transformation requires a continual increase in the driving force, and passes through metastable configurations like that shown in Figure 5.9(f). Note the untransformed material along the variant interfaces, which is due to the fact that the two variants prefer slightly different habits. The final microstructure, below M_f, is shown in Figure 5.9(g). It contains parallel plates of the two variants along (11). The last material to transform removes all signs of the relative tilt between the two variants that appears in Figures 5.9(c) through 5.9(f). The final microstructure contains a preponderance of the preferred variant (2), which is $\approx$ 73% by area. Most of the excess is due to the thick plate of variant (2) which formed at the be-

ginning of the transformation. By the time the second variant forms, the accumulated shear strain has overcome the preference for variant (2); the two variants are almost equally represented in the subsequent transformation.

Figure 5.10 shows selected metastable configurations from the transformation at $\sigma^* = 0.6$. Since the applied stress is higher than in the example shown in Figure 5.9, we expect the transformation to proceed further along the high-stress path before the second variant intrudes. This happens. While the second variant appears in the metastable configuration at point (c) on the transformation curve in Figure 5.9(h) ($\sigma^* = 0.4$), only one variant is present at the equivalent point at $\sigma^* = 0.6$ (Figure 5.10(b)). The transformation follows the high-stress path to point (c) by nucleating a crossing plate of the same variant. However, the second variant does appear in the transition from points (b) to (c) on the transformation curve (Figure 5.10(c)). By point (c), which corresponds to about 80% transformation, the microstructure bears a strong qualitative resemblance to that found at the corresponding point of the transformation at $\sigma^* = 0.4$ (Figure 5.9(c)), and is very similar in its subsequent behavior. The final microstructure consists of parallel plates on (11). The microstructure contains about 78% variant (2), with most of the excess in the single-variant plates that formed first.

An analysis of the microstructures of samples transformed at intermediate stresses between $\sigma^* = 0.2$ and $\sigma^* = 0.8$ shows that the unfavored variant appears at almost identical values of ΔG_v, between -0.54 and $-0.69E_0$. The transformation behavior at values of ΔG_v below this range, specifically including the value of M_f, is almost independent of the load. These phenomena reflect the fact that the unfavored variant forms only after accumulated strain has overcome the bias against it from the external stress. The subsequent behavior is similar because the two variants are equally favored for the remainder of the transformation.

5.3.3. Transformation under Cyclic Load

To study the influence of a cyclic load on the extent of martensitic transformation and the resulting microstructure we again assumed a transformation strain of R = 0.2, set ΔG_v at $-0.265E_0$, and imposed a uniaxial stress that was cycled in one of two saw-tooth patterns: between $\sigma^* = 0.5$ and $\sigma^* = -0.5$, and between $\sigma^* = 0.5$ and $\sigma^* = 0$. The load was raised and lowered in equal increments that were varied from 1/4 to 1/10 of the maximum. The results were insensitive to the value of the increment.

Raising the load from $\sigma^* = 0$ to $\sigma^* = 0.5$ causes a stress-induced transformation that creates the thick band of variant (2) martensite shown in Figure 5.11(a), which is almost identical to Figure 5.8(a). The fraction transformed is ≈ 30%. However, decreasing the load causes additional transformation; a decrease to $\sigma^* = 0$ produces the bands of variant (1) shown in Figure 5.11(b), and these bands grow significantly when the load is further decreased to $\sigma^* = -0.5$ (Figure 5.11(c)). Still more martensite forms if the cycle is repeated. The microstructure asymptotes to that shown in Figure 5.11(d) after several cycles. The final martensite fraction is 94%, more than three times the amount formed in the original excursion to $\sigma^* = 0.5$.

A similar result is obtained when the cycle is confined to the range $0 \le \sigma^* \le 0.5$. The asymptotic fraction of martensite is 64%, which is less than in the fully reversed cycle, but is still more than twice the fraction formed under a monotonic load of $\sigma^* = 0.5$.

The reason that cyclic loads promote the transformation is apparent from the microstructures shown in Figure 5.11. Loading the body to $\sigma^* = 0.5$ creates a variant (2) plate that is compatible with the temperature and the external load. Since the martensite transformation cannot be reversed, the body is subjected to a residual stress when the tensile load is relaxed. The residual stress is sufficient to induce the formation of a significant amount of variant (1), which removes part of its shear component. Subsequently loading the body to $\sigma^* = -0.5$ induces further transformation to variant (1),

which is favored by the compressive stress. When the load is removed, this creates an unbalanced internal stress that promotes the formation of variant (2). The transformation continues on further cycling until the only untransformed elements that are left are so highly loaded by the accumulated internal stress that neither maximum load is sufficient to trigger their transformation. Experimental observations of martensitic transformation at the tip of a growing fatigue crack [22] suggest that this mechanism is pertinent to many systems.

5.4. Discussion and Conclusion

The model assumes an athermal, irreversible martensite transformation that has a dyadic transformation strain and occurs in a crystal that is embedded in an untransformed body. It neglects interfacial tension and the difference between the elastic constants of the martensite and the matrix. The results illustrate the influence of the constraint and the imposed stress on the microstructure and the thermal resistance to the transformation ($\Delta M = M_s - M_f$).

The matrix constraint causes complex, multivariant microstructures and separates M_s and M_f. The reason is that the constraint prevents relaxation of the transformation strain at the crystal boundary. The shear strain is relaxed by introducing multiple variants that compensate one another. However, the compensation is incomplete, so the thermal resistance to the transformation increases. The dilational part of the transformation has two effects. It changes the habits of the martensite variants and produces interesting microstructures, such as "butterfly martensite" in partially transformed crystals. It also increases ΔM since it produces a hydrostatic stress that cannot be compensated by introducing other variants.

The applied stress can be divided into its hydrostatic and deviatoric components. The hydrostatic component affects all variants the same. If the transformation strain is partly dilational, a hydrostatic stress changes M_s without altering the microstructure or the

thermal resistance (ΔM). The deviatoric stress couples to the shear part of the transformation strain, and, hence, changes the relative energies of the variants. This increases M_S for transformation to the favored variant and produces a microstructure that is rich in the favored variant. It also increases M_S-M_f, since single-variant transformations must be sustained against an accumulating, uncompensated shear. The transformation can be regarded as a mixture of a high-stress, single-variant mode and a low-stress, multivariant mode. The former dominates the early stages of the transformation. The latter becomes dominant in the late stages of the transformation, since the accumulating internal shear eventually eliminates the energy difference between the two variants. The thermal resistance (ΔM) increases with the magnitude of the deviatoric stress until the high-stress limit is reached and only one variant appears. The microstructure is most complex at intermediate stress where both variants develop in a complex internal stress field.

When the applied stress is cyclic the crystal undergoes a progressive transformation during successive stress cycles; a high fraction is transformed even when the peak stress is relatively low. The reason is that the martensite that has already formed becomes a source of intense internal stress when the stress is reversed, promoting further transformation.

CHAPTER 6

COMPUTER SIMULATION OF REVERSIBLE MARTENSITIC TRANSFORMATIONS -- PART I: THERMAL HYSTERESIS AND THERMOELASTICITY

6.1. Introduction

In Chapter 4 and Chapter 5, the linear elastic theory was used to construct a computer simulation model for martensitic transformations in simple solids. The model helps to show how the elastic energy that develops during the transformation controls the microstructure and determines the thermal resistance to the transformation, which is measured by the difference (ΔM) between the martensite start and finish temperatures (M_s and M_f). For simplicity, the transformation was assumed irreversible; once an element of martensite formed, it could neither revert to the parent phase nor change its crystallographic variant.

While it is often reasonable to assume irreversibility in the treatment of a martensitic transformation during continuous cooling, the transformation can always be reversed by heating, and, in many cases, it can also be reversed by an applied stress. The characteristics of the reverse martensite transformation are both scientifically interesting and technologically important. They govern the thermal hysteresis of the reverse transformation on heating, and are responsible for such phenomena as thermoelasticity, pseudoelasticity, and the shape memory effect. They may also influence the microstructure that results from the transformation. In this and the next chapter, therefore, the computer simulation model is extended to reversible transformations. The simulations presented in this chapter are done in the absence of external stress, and the discussion is concerned primarily with thermoelasticity.

6.2. Background

6.2.1. Thermal Resistance and Thermal Hysteresis

The thermal resistance to an athermal martensitic transformation affects both the transformation and its reverse. Experimental observations show that on cooling, the transformation initiates at a martensite start temperature, M_s, and is only completed when the material is cooled to below the martensite finish temperature, M_f. When the transformation is reversed by heating, reversion begins at a temperature $A_s \geq M_f$, and is completed at the temperature $A_f \geq M_s$. In practice, $A_s > M_f$ and $A_f > M_s$, so there is a thermal hysteresis associated with the reverse transformation.

Two generic mechanisms contribute to thermal resistance: elastic strain due to the misfit between the parent and product phases, and frictional resistance. The elastic strain that accumulates as the transformation proceeds opposes its continuation and promotes reversion, since the elastic energy stored into the system can be the part of driving force for reverse transformation if the reversion does happen. However, the elastic strain can be relaxed in either of two ways: by displacement at free surfaces, and by plastic deformation within the crystal. Relaxation of the elastic strain reduces the thermal resistance of the transformation. On the other hand, relaxation of the elastic strain may increase thermal resistance if it increases the value of frictional resistance, that is, if the elastic energy changes its form into irreversible energy. The frictional resistance opposes the transformation in either direction (though the frictional resistance to the forward and reverse transformations will, generally, differ). There are three possible sources of friction: activation barriers that restrict the mobility of the martensite-matrix interface, nucleation barriers that oppose the formation of new particles, and dissipative processes, such as a plastic deformation of the matrix.

The computer simulation results presented in Chapter 5 show that the thermal resistance is also affected by the boundary conditions under which the transformation takes place. When the transformation occurs under the unconstrained condition, the M_s and M_f temperature are essentially the same and the TT curve is a vertical line. When the transforming body is constrained by its surroundings, the transformation stops after a fraction of the body has transformed and continues only when temperature is further reduced. The thermal resistance of the reverse transformation and thermal hysteresis must also be influenced by the boundary conditions, since the unconstrained body and the constrained body have different elastic strain conditions after the transformations are complete. As will be discussed later, the final strain condition determines the characteristics of reverse transformation, and therefore, determines whether or not the transformation is thermoelastic.

6.2.2. Thermoelasticity and Reversible Transformations

Thermoelastic martensite was originally defined to describe "thermoelastic equilibrium" achieved during a martensitic transformation in which the chemical driving force is balanced by the elastic resistance. At the thermoelastic equilibrium, the transformation stops, leaving the material in a partially transformed condition. A decrease in temperature leads to the growth of the martensite, and an increase in temperature leads to the shrinkage of the martensite - a reverse transformation. The elastic energy stored into the system is the part of driving force for the reverse transformation when the transformation temperature is above the chemical equilibrium temperature, T_0, of two phases (when martensite is low temperature phase), and is the only source of driving force for the reverse transformation when the transformation temperature is below the T_0.

Thermoelastic martensite was first documented by Kurdjumov and Khandros [23] in 1949 shortly after Kurdjumov [24] predicted it. Since then, thermoelastic martensitic

transformations have been observed and studied in many alloys. Among them, noble-metal based alloys such as Au-Cd, Ag-Cd, Cu-Zn, Cu-Zn-Al and Cu-Al-Ni have been studied most intensively. Thermoelasticity in the martensitic transformation of an iron-based alloy was first reported by Dunne and Wayman [25] in 1973 for an ordered Fe-Pt alloy with a composition near Fe_3Pt. Materials that are experimentally recognized as thermoelastic have relatively small temperature hysteresis; the M_s and A_f temperatures are close to one another. Moreover, the transformation path is approximately reversible; the last martensite particle to form tends to be the first to disappear.

The reverse transformation in thermoelastic martensite is different from the traditional reverse transformation in which the high-temperature phase must be nucleated if the transformation is reversed by heating. Systems that exhibit this behavior are called *non-thermoelastic*. In this case there is no residual elastic strain to assist the reverse transformation since the transformation strain is fully relaxed by free surface or plastic deformation. Most Fe-based alloys are of this type; transformations in these materials tend to have relatively large temperature hysteresis ($A_f >> M_s$) and transformation paths that do not reverse.

6.2.3. The Problems to be Solved

In the study of thermoelastic martensitic transformations, the experimental observations have left many problems which are still unsolved, and have generated considerable discussion in the literature.

A. The origin of thermal hysteresis

The thermal hysteresis (or temperature hysteresis) exists in thermoelastic transformations although it is relatively small compared with that in non-thermoelastic

transformations. Energy dissipation is observed during the thermal cycle of the transformation and reversion. The origin of the thermal hysteresis as well as its related dissipating effect has not been fully established. A number of investigators, including Deng and Ansell [26], believe that the primary cause of thermal hysteresis is the frictional resistance to the motion of martensite boundaries. The mechanisms of the frictional resistance are associated with the movements of interphase, interplate and twin boundaries, as reviewed by Krishnan, et al.[27]. Further, Ortin and Planes pointed out [28] that the thermal hysteresis is due to not only the frictional resistance to the motion of martensite boundaries but also due to other kinds of irreversible energy changes, such as interfacial energy and the effect of plastic accommodation. However, Olson and Cohen [29] argued that there will be a small residual hysteresis even in the absence of frictional effects. They concluded that the martensitic nucleation and initial growth as well as the final reversion occur away from the thermoelastic equilibrium. In a recent symposium, Ortin and Planes [30] pointed out that the accommodation of elastic strain energy by forming different variants of martensite particles should be considered as a contribution to the thermal hysteresis and energy dissipation in thermally-induced transformations. But so far no theoretical analysis or experimental work has been done to clarify the issue.

B. Relations between the characteristic temperatures

This problem concerns the location of the M_s, M_f, A_s and A_f temperatures with respect to the equilibrium temperature, T_0, the temperature at which $\Delta G_c^{P->M} = 0$, where $\Delta G_c^{P->M}$ is the chemical free energy change for the martensitic transformation. If the transformation is ideally non-thermoelastic and the nucleation barriers opposing the forward and reverse transformations are approximately the same, then $A_s > T_0 > M_s$, and T_0 should be approximately bracketed by the two temperatures:

$$T_0 = \frac{1}{2}(M_s + A_s) \tag{6.1}$$

Kauffman and Cohen [31] have shown that this relation holds for many Fe-based alloys. On the other hand, thermoelastic effects tend to depress A_s and A_f with respect to T_0. Dunne and Wayman [25] noted that A_s may fall below M_s, and divided thermoelastic transformations into two classes: Class I ($A_s > M_s$), and Class II ($M_s > A_s$). However, it is not clear whether this classification is mechanistically meaningful. In their effort to solve the contradiction between Eq. (6.1) and Class II thermoelastic transformation in which $M_s > A_s$, Tong and Wayman [32] defined another characteristic temperature, T_0', at which $\Delta G_c^{M->P} + \Delta G_{nc}^{M->P} = 0$ where $\Delta G_c^{M->P}$ and $\Delta G_{nc}^{M->P}$ are the chemical free energy change and non-chemical free energy change for the reverse martensitic transformation respectively, and proposed the following relations:

$$A_f > T_0 > M_s \tag{6.2}$$

and

$$A_s > T_0' > M_f \tag{6.3}$$

for both Class I and Class II transformations. In Tong and Wayman's analysis, the Eqs. (6.2) and (6.3) were obtained by neglecting the influence of elastic strain energy on the formation of a first isolated plate at M_s and its reversion at A_f. They concluded that, in any case, $A_f > T_0$. On the other hand, Olson and Cohen [29,33] argued that A_f lies below T_0 in an ideal thermoelastic transformation; their argument is trivially correct if there is no thermal hysteresis since, in this case, $A_f = M_s < T_0$.

C. Reversibility of the transformation path

Dunne and Wayman [25] and Tong and Wayman [32] have published sequential metallographic analyses of the growth and shrinkage of martensite plates during thermoelastic transformations. Their photographs (see particularly Figure 2 of reference [25]) illustrate a transformation path that is very nearly reversed; nonetheless, there are noticeable differences between the paths taken on heating and on cooling. During cooling, the thickening of the first few martensite plates is favored more than the nucleation and growth of the other plates. While during heating, all plates thin and shrink at roughly the same speed and the thickness of these plates is more uniform. It is not clear whether these differences are natural features of thermoelastic martensite, or whether they necessarily reflect deviations from ideality. No attention has been paid to the path differences among the investigations of thermoelastic martensitic transformations, and it has been widely accepted that the reversible transformation path is a characteristic of the thermoelastic transformation. The reason is probably due to the small thermal hysteresis observed in the most thermoelastic transformations. Questions that arise from this issue are: (1) What is the thermodynamic criterion of the path differences? (2) What is the relationship between the thermal hysteresis and the reversibility of the transformation paths taken on heating and on cooling? For example, if the transformation and reverse paths are exactly reversed, will thermal hysteresis still exist?

The above three problems are representative of the unanswered questions in the study of thermoelastic martensitic transformation. The bottom line of these questions is: what are the characteristics of thermoelasticity? The other features which are traditionally considered as the characteristics of thermoelasticity are: a small chemical driving force, a small transformation shape deformation, a matrix with a high flow stress, and no burst or spontaneous transformations, etc. It is apparent that understanding of the mechanism of

thermal hysteresis is the key to the other features, and therefore it will be the one on which our discussion concentrates in this chapter.

6.2.4. The Approach of Present Chapter

In this chapter, the computer simulation model and the procedure developed for the reverse transformation (described in Chapter 3) are used to study the thermal hysteresis and the reversibility of the transformation path during martensitic transformations, as well as the effects of the relaxation of the elastic strain by plastic deformation, the reversibility of the elastic strain energy, and frictional resistance. The simulations are done in two-dimensional space, and the transformation strains used are dyadic. The free energy changes for the martensitic transformation and reversion are shown in Eqs. (3.17) and (3.18), provided that the changes caused by external stresses are omitted:

$$\Delta G(T, p,\mathbf{R}) = \upsilon\Delta G_{\upsilon}(T) + f_f\, \Delta G_e(p,\mathbf{R}) + \Delta G_r \tag{6.4}$$

$$\Delta G'(T, p,\mathbf{R}) = \upsilon\Delta G'_{\upsilon}(T) + f_r\, \Delta G'_e(p,\mathbf{R}) + \Delta G'_r \tag{6.5}$$

Martensitic transformations under both unconstrained and constrained conditions are simulated. To simulate the transformation under the constraint imposed by an untransformed matrix, the transformation is confined to an array of 41 x 41 cells in a 101 x 101 grid that is repeated periodically. To simulate the transformation under the unconstrained condition, the transformation occurs in an array of 41 x 41 cells which is the same size as the array of the grid. The transformation is initiated from a single seed in the center of the array. The simulation is then specified by five variables: the dilation ratio, R, which has a value of 0.2 - 0.25, the relaxation factor, f_f ($0 \le f_f \le 1$), the reversibility factor

f_r ($0 \le f_r \le 1$), the transformation and reverse frictional resistance, ΔG_r and $\Delta G_r'$, which can have any value.

The model used here is simple and is idealized, but does permit a reasonably accurate treatment of the elastic energy developed during the transformation and a clean separation between the effects of elastic resistance, relaxation and reversibility of elastic strain, frictional resistance and geometric constraint on thermal hysteresis and on the reversibility of the transformation path. Therefore, the results of the computer simulation may provide some physical insights to the phenomena which are difficult to obtain from experimental observations.

6.3. Simulation Results and Discussion

In most of the results presented below, the forward transformation (parent phase to martensite) and reverse transformation (martensite to parent phase) compete with one another at each step, that is, the forward and reverse transformations are *reversible* at each step of the thermal cycle. However, for the reference, we first consider how the relaxation factor, f_f, and forward frictional resistance, ΔG_r, influence a transformation that cannot be reversed, that is, a transformation in which the reversion of the martensite is not allowed during cooling. Then the effect of f_f is ignored in reversible transformations (i.e., f_f is always equal to 1).

6.3.1. The Influence of Relaxation and Friction on an Irreversible Transformation

In Chapter 5, we studied the microstructure and thermal resistance of an irreversible transformation in a constrained crystal. The change of Gibbs free energy includes the chemical free energy and elastic energy caused by the martensitic transformation only (Eq. (3.11)), and the effects of f_f and ΔG_r were not considered ($f_f = 1$, $\Delta G_r = 0$). When the

transformation strain is a pure shear (R = 0) , the microstructure is simple: the bands of two martensite variants alternate along (11) planes, which are the preferred habit planes for this value of R. When the dilation in the transformation strain is non-zero ($R \neq 0$), however, the preferred habits of the two variants rotate in opposite directions from (11), with the consequence that the crystal develops complex two-variant patterns, described as "butterflies" and "crosses", in the early stages of the transformation. Since the transformation is irreversible, these patterns are retained. Subsequent martensite particles fill a matrix that is perturbed by these patterns, with the consequence that the final microstructure is a complex, two-variant mixture (not well arranged twinned bands) with a relatively high elastic energy. Figure 6.1 is the sequence (or path) of the irreversible transformation with R = 0.25. The chemical driving force, $|\Delta G_v|$ must be raised significantly to complete the transformation, so the thermal resistance, $\Delta M = M_f - M_s$ increase monotonically with the magnitude of R (Figure 5.4).

When the relaxation factor, f_f, and the frictional resistance, ΔG_r, are included in the Gibb's free energy, the simulation results show that, for irreversible transformations, the sequence of transformation is fixed by the value of R; it is not changed by f_f or ΔG_r. However, the difficulty of accomplishing each transformation step is affected. Increasing ΔG_r simply translates the TT curve to lower temperatures; M_s and M_f are lowered by the same amount. Decreasing f_f raises both M_s and M_f, but has a much stronger effect on M_f, and narrows the TT curve. The reason is that, as f_f decreases, less elastic strain is accumulated to oppose the transformation. Figure 6.2 illustrates the effect of f_f on TT curves.

6.3.2. Reversible Transformation of a Constrained Crystal during Cooling

The possibility of martensite reversion during cooling should simplify the microstructure (shown, for example, in Figure 6.1) and decrease the thermal resistance,

since it creates the additional freedom to reduce the elastic energy and to eliminate undesirable configurations that form during the forward transformation.

First, let us consider the reversible transformation with $f_f = f_r = 1$ and $\Delta G_r = \Delta G_r^{'} = 0$. Figure 6.3 illustrates the growth of the martensite on cooling when R = 0.25. A thin plate first grows out from the seed at the center. Note a particle of variant (2) seen in Figure 6.3(a) and 6.3(b) disappears in the configuration shown in Figure 6.3(c), and the satellite plates that grow perpendicularly out in Figure 6.3 (e) and 6.3(f) revert to the parent phase and then transform to the particles of the opposite variant. The final microstructure consists of alternating, parallel plates of the two martensite variants, in contrast to the complex microstructure that develops in the irreversible case (Figure 6.1). Figure 6.4 compares the TT curves for the two cases. The value of M_S is the same (the transformation cannot be reversed until it has begun), but the value of M_f is much higher in the reversible case; the thermal resistance to the transformation is significantly lower.

The influence of the reversible transformation during cooling decreases as R becomes smaller, and almost disappears for $R \leq 0.2$. In this case the rotation of the habits is not obvious (see Chapter 5), and the irreversible transformation generates a simple microstructure of parallel plates, so there is little need for the reverse transformation.

The reversible transformation during cooling becomes less important as the reversibility factor, f_r, decreases or the reverse frictional resistance, $\Delta G_r^{'}$, increases. When $f_r < 0.5$, the reverse transformation becomes ineffective in relieving the accumulated elastic strain. When $\Delta G_r^{'}$ becomes large ($\Delta G_r^{'} \geq 2.0$ in the dimensionless form used here), the reverse transformation does not occur to any significant degree.

It is interesting to note that the reverse transformation also becomes unimportant when there is a large frictional resistance, ΔG_r, to the forward transformation. This effect is illustrated in Figure 6.5, which compares the TT curves during cooling for three values of the forward frictional resistance, given $f_f = f_r = 1$ and $\Delta G_r^{'} = 0$. Increasing the frictional resistance to the forward transformation, ΔG_r, not only decreases M_S, but also increases

the thermal resistance, $\Delta M = M_s - M_f$, until it approaches the value of the irreversible transformation. The reason is that, as ΔG_r is increased, the chemical driving force, $|\Delta G_v|$, for the martensitic transformation must also be increased to bring it about. The chemical driving force opposes the reverse transformation. As ΔG_r increases the reverse transformation becomes more and more difficult until, eventually, the transformation becomes effectively irreversible.

6.3.3. Reverse Transformation of a Constrained Crystal during Heating

A. Reverse transformation with full reversibility of elastic energy

Assume that a constrained crystal has been cooled to below M_f to complete the martensitic transformation. Let it then be heated to reverse the transformation. Let us first consider the reversion in the absence of the relaxation of elastic energy and frictional resistance ($f_f = f_r = 1$, $\Delta G_r = \Delta G_r^{'} = 0$). As an example, we use the case illustrated in Figure 6.3. The microstructure before reversion is shown in Figure 6.3(h). Figure 6.6(a) to Figure 6.6(h) show the development of the transformation as the sample is heated. Comparing with Figure 6.3(a) to Figure 6.3(g), one can easily see that the transformation path is not the reverse of that followed on cooling.

Figure 6.6(a) is taken near the beginning of the reverse transformation, and has the same number of martensite particles as in Figure 6.3(g). The two configurations are not exactly the same, but they are very similar. The elementary cells that transformed last during cooling have very high elastic energy, and revert most easily when the sample is heated. As temperature is increased, however, the pattern of the reverse transformation diverges from that taken during cooling. Comparing Figure 6(b), 6(c) and 6(d) with Figure 6.3(f), 6.3(e) and 6.3(d) reveals the qualitative difference in the pattern. During cooling, the crystal transforms by the sequential growth of martensite plates, while during

heating many plates thin simultaneously. Figure 6.6(e) to 6.6(h) show the completion of the reverse transformation through the shrinkage of the last two plates. The plate that reverses last (Figure 6.6(h)) is the plate that transformed first on cooling (Figure 6.3(a)) although its shrinkage is not exactly the reverse of its growth.

The reason for the path difference during cooling and heating in the simulation is straightforward, and is due to the fact that many distinct plates form during the forward transformation which takes place in a constrained crystal. The criterion of the transformation or reversion used in the simulation is the *minimum energy path*.. The minimum energy path selects the parent cell to transform which introduces the minimum elastic energy increase during cooling; it selects the martensite particle to reverse which causes maximum elastic energy reduction during heating. If we ignore the last stages of the transformation, which are nearly reversible, the forward transformation occurs through plate growth and thickening into the matrix. New plates nucleate and grow to compensate the matrix strain from the plates that have already formed (see Chapter 5). As a consequence, the plate interiors in the fully transformed microstructure have relatively low elastic energy; the high-energy sites are along the boundaries where plates impinge on one another. When the transformation is reversed during heating, these high-energy sites transform first, and all plates thin and shrink almost simultaneously, resulting in a very different path from the forward path. The two paths resemble one another only at the beginning and the end. The first few cells to reverse are the last to form, since these have very high elastic energy. The last cells to reverse are the first to form; when there is only one plate left to be transformed, the energetics of the forward and reverse transformations are nearly the same. If the seed is irreversible, the particle which reverses last is usually the one which transformed first and is adjacent to the seed. When the seed is allowed to reverse, the particle which reverses last is not necessarily the one that is adjacent to the seed. But the plate which disappears last is still one which forms first because of its largest size. In reality, seeds of martensite are pre-existing defects and are normally irreversible.

Figure 6.7 is the TT curve of the reversible transformation for both cooling and heating processes. There are three important features of this curve: (1) the existence of a hysteresis, (2) the position of A_s, above M_f, and (3) the position of A_f, below T_0 (where $\Delta G_v = 0$). The essential coincidence of A_s and M_f is due to the fact that the last particle transforms when the temperature is just sufficiently low to make its total free energy negative. Since, in the absence of elastic relaxation, the reversion of this particle recovers the elastic energy needed to form it, the free energy for the reverse reaction becomes negative when the temperature is raised incrementally above M_f. The TT curve of heating cannot be the same as that of cooling, because the paths of the forward and reverse transformations are not exactly reversed, and the elastic energy changes of the transformation and reversion are different. The elastic relaxation must contribute to the hysteresis, as it does to the irreversible transformation path. More detailed discussions about fundamental reason of the hysteresis in the TT curve and the position of T_0 relative to A_f will appear in the discussion section.

B. The influence of reversibility and reverse frictional resistance

When the reversibility factor, f_r, is less than 1, A_s is raised above M_f and the thermal hysteresis is increased. The effect is illustrated in Figure 6.8, which compares the TT curves for four values of the reversibility factor. The reason for this behavior is straightforward. As f_r decreases, less elastic energy is available to drive the reverse transformation. In the limit $f_r = 0$, no elastic energy is recovered; the transformation is driven entirely by the chemical energy, and, in the absence of frictional resistance, occurs at T_0.

Figure 6.9(a) through Figure 6.9(h) show the sequence of the reverse transformation during heating when the reversibility, f_r, is 0.2. The reversibility factor, f_r, affects the reverse transformation during cooling, therefore, the microstructural evolution

and the final martensite configuration at the transformation completion temperature, M_f, are different from those obtained when f_r =1. As a consequence, the microstructural evolution shown in Figure 6.9 is not the same as that shown in Figure 6.6. But one characteristic is preserved: all martensite plates thin and shrink almost simultaneously, starting from the boundaries of the martensite plates.

When the reverse frictional resistance, $\Delta G_r'$, is not zero, the reverse transformation become more difficult. The effect is to raise A_S and A_f, so the hysteresis is increased. Figure 6.10(a) and 6.10(b) compare the TT curves with different values of the reverse frictional resistance during heating for two values of the reversibility (f_r = 1 and f_r = 0.5) assuming the forward frictional resistance ΔG_r is zero.

The influence of the reversibility and reverse frictional resistance is illustrated in Figure 6.11, which includes plots of A_S and A_f (in chemical energy unit) as a function of $\Delta G_r'$ for different values of the reversibility factor, f_r. The M_S for the frictionless forward transformation (ΔG_r = 0) is also shown in the figure for comparison. A_S and A_f change almost linearly with $\Delta G_r'$. The reversibility of the elastic energy has dramatic effects on A_S but very little influence on A_f. As shown in Figure 6.11(a), A_S can be below or above M_S, and below or above T_0, depending on the reversibility and the value of reverse frictional resistance. As discussed above, frictional resistance to the forward transformation decreases M_S and M_f, and, hence, also affects the relative positions of A_S, M_S and T_0.

Table 6.1. The effects of reversibility and transformation resistance on M_S, M_f, A_S and A_f temperatures

Variables		M_S	M_f	A_S	A_f
fr	↓	N	↓	↑	↑
ΔGr	↑	↓	↓	/	/
$\Delta G_r'$	↑	N	↓	↑	↑

↑ -- increase, ↓ -- decrease, N -- no effect, / -- no direct effect

Table 6.1 summarizes the effects of the reversibility of elastic energy (f_r), and forward and reverse frictional resistance on the characteristic temperatures, M_s, M_f, A_s and A_f.

6.3.4. Interrupted Transformations of a Constrained Crystal

To study the reverse transformation of a partially transformed microstructure, simulations were done in which the temperature was decreased to T_l, where $M_s > T_l > M_f$, and then increased until the martensite was completely reversed to the parent phase. To study the effect of partially reversed transformations, the temperature was decreased to T_l, then increased to T_h, where $A_f > T_h > T_l$, and then decreased again until the martensite transformation is complete. Let T_a denotes the temperature where the reverse transformation starts during heating from T_l, and T_b denotes the temperature where the forward transformation starts during cooling from T_h.

Figure 6.12 includes TT curves for partial transformed cycles for three combinations of the reversibility and the values of forward and reverse frictional resistance. Note that the reverse transformation of a sample cooled to T_l completes at A_f, whatever the value of T_l is. The reason is that the last plate to reverse is always the same, so the last stage of the reverse transformation is independent of T_l. The temperature, T_a, where the reversion begins is always above A_s. These results reproduce experimental observations on thermoelastic alloys [39]. If A_s is below M_s (Figure 6.12(a)), when T_l is above the A_s, the reversion starts as soon as heating begins. After a small amount of reversion, the TT curve merges into the TT curve for the reversion of fully transformed materials, and overlaps with it at all higher temperatures.

Figure 6.13 compares TT curves of samples that are partially transformed by cooling to T_l, heating to T_h (which must be greater that Ta to initiate reversion), and then cooled to complete the martensitic transformation. The effect depends on the extent of

reversion, that is, on the difference, $T_h - T_a$. When the extent of reversion is small (< 1% of the transformed particles), there is little or no effect on the transformation path when transformation resumes, and there is little or no hysteresis in the TT curve between T_l and T_h (Figure 6.13(a)). As the extent of reversion increases (for example, the case shown in Figure 6.13(b) involves about 15% reversion), thermal hysteresis becomes apparent in the cycle T_l -> T_h -> T_l, and the shape of the TT curve between T_l and M_f is also changed. The final configuration is also affected.

6.3.5. Transformation and Reverse of an Unconstrained Crystal during a Thermal Cycle

The results presented above are obtained from simulation of the transformations of a constrained crystal. The results from the transformations of an unconstrained crystal are illustrated in Figure 6.14 through Figure 6.16. For the purpose of comparison, the configurations in Figure 6.14 and Figure 6.15 are plotted such that the number of cells of the parent phase (blank) in each configuration of Figure 6.15 is the same as the number of martensite particles in each corresponding configuration of Figure 6.14. As shown in Figure 6.14, the martensitic transformation occurs through the growth of a single plate from the pre-existing seed, which then thickens to transform the whole crystal. The reverse transformation, as illustrated in Figure 6.15, is exactly the same: a plate of austenite grows out from the seed, which is selected at random, and thickens until the parent phase is restored. The habit of the parent phase in the martensite phase is exactly the same as that of the martensite phase in the parent phase. (Note the sequences in Figure 6.14 and Figure 6.15 are not identical, since a martensite particle of variant (2) appears in the beginning of transformation (Figure 6.14(a)) and then disappears later because the transformation is reversible.) The TT curves for the transformation and reversion are illustrated in Figure 6.16. In these results, the growth from the initial seed leads to complete transformation; the M_s and M_f temperatures are essentially the same, so are the A_s and A_f temperatures.

The frictional resistance, ΔG_r and $\Delta G_r^{'}$, which are positive make the transformation and reversion more difficult, and hence decrease M_s and increase A_s (broaden the hysteresis loop). If frictional resistance is the same for both transformation and reversion, the equilibrium temperature, T_0, lies midway between M_s and A_s (Eq.(6.1)) when the effects of f_f and f_r are not considered ($f_f = f_r = 1$). If ΔG_r is different from $\Delta G_r^{'}$, M_s and A_s are asymmetric about T_0 to a degree that is linearly proportional to the difference between ΔG_r and $\Delta G_r^{'}$.

Figure 6.17 plots the total energy versus the fraction of martensite during forward and reverse transformations. It shows that the total elastic energy in the transforming crystal initially increases, then decreases, and vanishes when the transformation is complete. The total elastic energy in the final transformed, single variant body is zero since the martensite is fully relaxed. The change of the total energy during the reverse transformation is the same as that of the forward transformation, because when a martensite particle reverses to the parent phase, it causes a elastic strain field which is exactly the same as that created by a martensite particle in a parent matrix. Since the reverse transformation starts from a strain-free crystal and the elastic energy is not the part of the driving force for the reverse transformation, the transformation is non-thermoelastic.

This result has clarified the situations in which the Eq.(6.1) will be satisfied -- when the transformed martensite phase is fully relaxed and no elastic energy is stored in the solid, or the elastic energy stored during forward transformation cannot be reversed, and the values of frictional resistance for the transformation and reversion are the same.

6.4. Discussion and Conclusions

6.4.1. Thermal Hysteresis and Dissipative Effect

The most important result of the simulation is that the thermal hysteresis exists even when the elastic energy is fully reversible (no plastic deformation) and the frictional resistance is absent. Frictional resistance and plastic relaxation can add substantially to the magnitude of the hysteresis, but they are not the fundamental sources of it. To eliminate the contribution of the irreversible transformation path to the hysteresis, transformations in which the reversion of martensite during heating is forced to follow the exactly reversed path during cooling ("exactly reversed path" in short) were investigated. The following are the results of the investigation.

Consider that the reversibility factor, f_r, is 1 and the value of frictional resistance is zero, then from Eqs. (6.2) and (6.3), the criterion for the forward transformation is

$$\Delta G(T, p, \mathbf{R}) = \upsilon \Delta G_{\upsilon}(T) + \Delta G_e(p, \mathbf{R}) \leq 0 \tag{6.6}$$

and for the reverse transformation

$$\Delta G'(T', p, R) = \upsilon \Delta G'_{\upsilon}(T') + \Delta G'_e(p, \mathbf{R}) \leq 0 \tag{6.7}$$

Since $\Delta G'_{\upsilon}(T') = -\Delta G_{\upsilon}(T')$, and because of the exactly reversed path, when the volume fraction of martensite during the reversion is the same as that during the forward transformation, then

$$\Delta G'_e(p, \mathbf{R}) = -\Delta G_e(p, \mathbf{R}) \tag{6.8}$$

therefore, for any given martensite volume fraction, we obtain

$$- \upsilon \, \Delta G_{\upsilon}(T') \leq \Delta G_e(p,\mathbf{R}) \leq -\upsilon \Delta G_{\upsilon}(T) \tag{6.9}$$

Eq. (6.9) clearly tells us that, at each step of the transformation, the elastic energy increment, $\Delta G_e(p,\mathbf{R})$, generated during the cooling process must be bounded between the TT curves of cooling and heating. The TT curves are the plots of fraction of martensite versus the negative of the chemical energy change during cooling and heating, $-\Delta G_{\upsilon}(T)$ and $-\Delta G_{\upsilon}(T')$. Figure 6.18 shows the results of the TT curves and $\Delta G_e(p,\mathbf{R})$ curve from the simulation using the exactly reversed path. The reverse transformation was not allowed during cooling to avoid complications in the simulation.

The physical meaning of Eq. (6.9) and Figure 6.18 is very clear. The driving force must be greater or equal to the transformation resistance for both forward and reverse transformations. During cooling, the driving force for the forward transformation of a martensite particle of variant p at location **R** is $-\Delta G_{\upsilon}(T) = |\Delta G_{\upsilon}(T)|$, and the resistance is $\Delta G_e(p,\mathbf{R})$. During heating, the elastic energy $\Delta G_e(p,\mathbf{R})$ becomes the driving force for the reverse transformation of the martensite particle, and the resistance comes from the chemical free energy increment $-\Delta G_{\upsilon}(T')$. Therefore, in Figure 6.18 the driving forces are always on the right side of the resistance.

As shown in Figure 6.18, the elastic energy increment does not monotonically increase with the fraction of martensite. Because of that, the transformation is not always in thermoelastic equilibrium where $\upsilon \Delta G_{\upsilon}(T) + \Delta G_e(p,\mathbf{R}) = 0$. Only when near the completion of the transformation, does thermoelastic equilibrium hold and the two TT curves overlap.

These results demonstrate that the thermal hysteresis generated when the transformation and reversion follow the exactly reversed path is due to non-equilibrium effects between the chemical driving force and the elastic energy resistance. The size of the

hysteresis loop, or A_f, is determined by the smallest elastic energy increment, $(\Delta G_e)_{min}$, during cooling. In other words, the size of the hysteresis is determined by the amount of the elastic relaxation. The greater the elastic relaxation, the larger the hysteresis. If $(\Delta G_e)_{min} > 0$, $A_f < T_0$; if $(\Delta G_e)_{min} < 0$, $A_f > T_0$. Figure 6.18 is an example of the later case.

If we set $T' = T$ in Eq. (6.9), then the hysteresis disappears when the TT curves for cooling and heating overlap, and

$$- \upsilon \, \Delta G_\upsilon(T) = \Delta G_e(p,R) \tag{6.10}$$

holds for any given martensite fraction. If $\Delta G_e(p,R)$ increases monotonically with martensite fraction, Eq. (6.10) remains equal with decreasing T. In the other word, if the thermoelastic equilibrium always holds during the forward transformation, no thermal hysteresis should exists.

Figure 6.19 compares the TT curves from the exactly reversed path and the minimum energy path. The TT curve during heating from the minimum energy path is in between the TT curve during cooling and the TT curve during heating from the exactly reversed path, resulting in a smaller hysteresis loop. This shows that the minimum energy path requires a less superheating and is energetically favored. It also indicates that the thermoelastic equilibrium is only a sufficient condition, not a necessary condition for the disappearance of the thermal hysteresis. Since the thermal hysteresis from the minimum energy path is always smaller than that from the exactly reversed path, under the condition of Eq. (6.10), the minimum energy path is the same as the exactly reversed path, and the TT curves of both paths overlap.

In general, $\Delta G_e(p,R)$ does not always increase monotonically with martensite fraction, because of the microstructural relaxation of the elastic energy that develops during the transformation. The elastic relaxation comes from not only the elastic strain

accommodations of martensite plates of different variants, but also from the interaction of martensite particles of same variants. To understand this, we need to see how the elastic energy increment varies with the growth of martensite plates.

In a constrained crystal, as the first thin layer of martensite of the single variant grows in its length direction the elastic energy increment decreases despite increasing total elastic energy. This is because when the transformation strain is invariant, the formation of a thin plate relaxes and minimizes the elastic energy of the system, as it has been shown in Chapter 4 and Chapter 5. Once the thin layer reaches the constrained boundary and is forced to thicken, the elastic energy increment increases abruptly, and then decreases again with the growth of the new layer of martensite. The formation of plates with the second variant is another source of elastic relaxation. As a consequence, the elastic energy increment alternates with the increase of martensite volume fraction. On the other hand, the chemical driving force is constant for every particle that transforms at a given temperature. The transformation starts at the initial driving force (M_S), and no additional chemical driving force needs to be added until the point when the accumulated elastic energy in the system is so large that the elastic energy increment for an additional particle to transform exceeds its chemical driving force, that is, a thermoelastic equilibrium is reached. The transformation continues after the temperature is lowered. The elastic energy increment again varies with the development of the martensitic transformation, but soon reaches the thermoelastic equilibrium again because of the substantial amount of elastic energy accumulated in the system. Temperature must be lowered again in order to allow the transformation to continue, and the transformation is only completed when M_f is reached.

When the transformation takes place in an unconstrained crystal, it starts at M_S,and continues to its completion without reaching the thermoelastic equilibrium (exception occurs for some values of the dilation ratio, R, where a slight increase of chemical free energy is needed). As an example, in Figure 6.20, the TT curve is a vertical line ($M_S = M_f$ or $A_S = A_f$), and the elastic energy increment alternates between negative and positive

values when the martensite plate grows and thickens. The peaks of the elastic energy increment curve which have negative values are where the transformation of a thin layer is completed; the peaks with positive values are where the thickening of the existing martensite plate starts by transforming a cell of a new layer adjacent to the plate.

It is because of the lack of equilibrium between the chemical driving force and the elastic energy increment, that there is excess energy which then changes into heat and dissipates.

The above discussion clarifies that: (1) The essence of the thermal hysteresis, which exists even when plastic relaxation and frictional resistance are absent, is the absence of equilibrium between the chemical driving force and elastic energy resistance; such non-equilibrium transformation is due to the elastic relaxation caused by the elastic interaction between martensite particles of the same or different variants, and is the source of the energy dissipation. (2) The burst phenomenon in the martensitic transformation, which is reflected as a vertical segment in TT curves, is a consequence of the non-equilibrium transformation. It is not an indication that no elastic energy is involved in the transformation as claimed by Deng and Ansell [26].

Although thermal hysteresis is observed in the most thermoelastic transformations, it is not a criterion for a thermoelastic transformation. On the contrary, the existence of thermal hysteresis indicates that thermoelastic equilibrium does not always exist. For the convenience in the following discussion , we define an *ideal thermoelastic transformation*, in which the elastic energy is fully reversible (no effect of plastic deformation) and the frictional resistance is absent; thermoelastic equilibrium is achieved at every step of the martensitic transformation, so that $A_s = M_f$, $A_f = M_s$, and the thermal hysteresis does not exists.

6.4.2. *The position of T_0 relative to M_s, M_f, A_s, and A_f*

From the simulation results and the discussion of thermal hysteresis, the answer to this question is straight forward. When the martensitic transformation leads to a fully relaxed microstructure, as in the case of the unconstrained transformation of a single crystal or a transformation that is fully relaxed by plastic deformation, then the forward and reverse transformations should be approximately symmetric about the equilibrium temperature, T_0, which will lie half-way between M_s and A_s (Eq. (6.1)). In a constrained crystal, the accumulated elastic strain facilitates the reverse transformation. If the transformation is ideally thermoelastic, $A_s = M_f$ and $A_f = M_s$; if the transformation is not ideally thermoelastic, and no plastic relaxation or the frictional resistance exist, then $A_s = M_f$ and $A_f > M_s$, and A_f can be below T_0 or above T_0 depending on the paths of reverse transformation and the amount of elastic relaxation, or the minimum elastic energy increment generated during cooling. When plastic relaxation and frictional resistance are important, A_s and A_f have no necessary relation to M_s, M_f and T_0 beyond the thermodynamic requirement that $A_s \geq M_f$ and $A_f \geq M_s$.

6.4.3. *The Irreversibility of Transformation Path*

The martensitic transformation path is only strictly reversible, that is, the transformation and reversion sequences are exactly reversed, when the reversion of an element of martensite releases precisely the mechanical energy that was needed to create it. The simulation suggests that this is rarely the case, even in the absence of friction and plastic relaxation. The reason is the elastic relaxation during the transformation, as discussed in Section 6.4.1. When the transformation takes place in a constrained crystal, thermoelastic equilibrium occurs in the very last stages of the transformation where the transforming elements are highly strained. These elements are readily reversed when the

temperature is increased above M_f, and the transformation path is reversible in the early stages of the reverse transformation. In this case, the constraint is essential.

Using the minimum energy path as the transformation criterion, the computer simulation model generates the irreversible transformation path. The similarity of the characteristics of the martensite morphologies during cooling and heating produced by the computer simulation (see Figure 6.3 and Figure 6.6) to that of experimental observations [25] demonstrates that the minimum energy path criterion does have its physical basis. The minimum energy path results in a smaller thermal hysteresis compared with the exactly reversed path, and requires less superheating and is thermodynamically favored.

6.4.4. The Influence of Reversibility on the Martensitic Transformation

One of very interesting results of this investigation is the significant influence of reversibility on the thermal resistance, $\Delta M = M_s - M_f$, and on the microstructure produced by athermal martensitic transformations in constrained crystals. The growth and impingement of multiple martensite plates creates local regions of high elastic energy. If reversion is possible, these regions can be eliminated by reverse transformation, which allows the microstructure to rearrange itself into a simpler configuration in which the elastic energy is significantly reduced. The result is a more regular microstructure and a smaller thermal resistance ΔM (a higher value of M_f). This microstructural relaxation is opposed by any factor that makes reversion more difficult. Hence the final microstructure is more complex, and ΔM is increased, if the reversibility factor, f_r, is less than 1 or if the frictional resistance, ΔG_r is relatively large.

Since the elastic energy stored in the system acts as a driving force for the reverse transformation when it is released during heating, the reversibility factor of the elastic energy, f_r, has a strong influence on the starting temperature of the reverse transformation, A_s. When f_r is zero during heating, the reverse transformation from martensite to the

parent phase can happen only when the temperature is above or at T_0 depending on whether there is elastic or frictional resistance for the reverse transformation, and the transformation is not thermoelastic.

From the above discussion, it is reasonable to state that the reversibility of the elastic energy is a unique factor which determines the thermoelasticity of a material.

6.4.5. Thermoelasticity

Thermoelasticity is characterized by the transformation and growth of martensite plates upon cooling and reversion and shrinkage of the martensite plates upon heating. Non-thermoelastic transformation is distinguished from the thermoelastic transformation by the function of the elastic energy during the reverse transformation. The thermoelastic transformation is triggered by strain-induced reversion of martensite plates, and the elastic energy acts as a driving force for the reverse transformation. Non-thermoelastic transformation is triggered by the independent nucleation of the high-temperature phase, and no elastic energy assists the reverse transformation. Any effect which tends to reduce the loss of elastic energy, and therefore, the loss of the reversibility of the elastic energy, should be regarded as promoting thermoelasticity. The simulation suggests that plastic deformation and frictional resistance reduce the thermoelasticity and have their effect in different ways. Plastic deformation relaxes the elastic energy and changes it into an irreversible form, and therefore, decreases the reversibility of the elastic energy. Frictional resistance, which includes the effects from boundary friction, surface energy, and plastic deformation, is essentially irreversible energy. The transformation by independent nucleation can occur before strain-induced reversion of martensite does, if the value of frictional resistance is substantially large (since high A_S and A_f temperatures). The characteristics observed in many thermoelastic transformations, such as, a small chemical driving force, a small transformation shape deformation, and a matrix with a high flow

stress (or the critical resolved shear stress) [5,25,34], are not defining features for thermoelastic behavior. They are, however, the conditions under which plastic deformation will not or at least less likely to occur during the transformation, hence the elastic energy loss is minimum and the thermoelastic transformation is more likely to be preserved. The reversibility of the elastic energy and frictional resistance vary with composition, transformation strains, transformation mechanism and material properties (e.g.,the critical resolved shear stress), etc., and can change with processing history. This is the reason that some alloys exhibit large thermoelasticity and others small, and why some alloys traditionally considered to be non-thermoelastic show thermoelastic features under certain conditions [35-44]. It is not surprising that some systems do not meets the strict conditions for either thermoelasticity or non-thermoelasticity and have mixed features.

In most so called thermoelastic transformations, thermoelastic equilibrium is not always achieved, as it has been concluded in section 6.4.1. The constraint is essential for the transformation to reach the thermoelastic equilibrium. It is only in the ideal thermoelastic transformation that thermoelastic equilibrium is obtained at every step of the transformation and thermal hysteresis disappears.

CHAPTER 7

COMPUTER SIMULATION OF REVERSIBLE MARTENSITIC TRANSFORMATIONS -- PART II: PSEUDOELASTICITY AND THE SHAPE MEMORY EFFECT

In this chapter, the simulation of reversible martensitic transformation is extended to include external stresses, and the results of an investigation of pseudoelasticity and the shape memory effect are presented.

7.1. Introduction

Pseudoelastic behavior is a mechanical analog to the thermoelastic transformation. The martensite transforms continuously with increasing applied stress, and reverses continuously when the stress is decreased. The "plastic" strain is caused by the shape strain accompanying the formation of martensite and recovers when the transformation is reversed. The total strain may or may not be completely recovered depending on whether irreversible deformation occurs or not, or whether there is a transformation resistance. Figure 7.1 is the schematic drawing of an experimental stress-strain curve first published by Burkart and Read [45] for indium-thallium alloys in 1953. The experimental temperature was fixed at a value greater than that of the reverse completion temperature A_f. A hysteresis exists in a stress-strain curve under such conditions. In Figure 7.1, σ_{c1} is the stress where the induced transformation from parent phase to martensite phase starts during loading, σ_{c2} is the stress where the transformation is completed, and σ_{c3} is the stress where the reverse transformation from martensite phase to parent phase starts during unloading. The stress-strain curve, and hence the hysteresis was found as a function of testing temperature and crystal orientation [46,47].

Pseudoelasticity can be obtained not only by stress-induced martensitic transformation, but also by variant-reorientation [48-51] when external stress is applied on a crystal consisting of martensite. This type of pseudoelasticity can be compared to the elastic twinning and untwinning in crystals [52]. In this case, σ_{c1} is the stress where the variant-reorientation starts during loading. Wasilewski [53] concluded that if the martensite is stressed between M_f and A_d ($A_d < M_f$), where A_d is the lowest temperature at which the stress-assisted reorientation can occur, the reversion from martensite to austenite is only a transient intermediate step, which is followed by the immediate and also stress-assisted transformation of this austenite to another martensite variant with a different orientation from that of the original martensite. Although it is difficult to make Wasilewski's two-step mechanism visible experimentally, there are indications [27] that this two-step mechanism can occur on an atomic scale.

Pseudoelasticity can also be caused by the combination of transformation and reorientation of martensite. For an example, the transformation is first induced by applying external stress, then the reorientation takes place when this stress-induced martensite is further stressed. The multiple plateaus observed in some stress-strain curves was considered as a consequence of such combined effect [50].

Similar to the thermal hysteresis, the origin of the stress-strain hysteresis as well as its related dissipating effect is not well understood. In Chapter 6, it was concluded from our investigation that the fundamental source of the thermal hysteresis is the absence of equilibrium between the chemical driving force and the elastic resistance. It is my belief that the explanation of the stress-strain hysteresis is similar to that of the thermal hysteresis, and the only difference is that, in this case, the driving force includes chemical energy and/or external stress.

The shape memory effect often occurs if a macroscopic deformation is accompanied by a martensitic transformation under an applied stress, and is not reversed by removing the applied stress, but by heating after the removal of the applied stress. There are very

close interrelations between thermoelasticity, pseudoelasticity and the shape memory effect. Wayman and Shimizu concluded [54] that the shape memory effect can be universally correlated with a martensitic transformation that is thermoelastic in nature. Delaey et al. [55] pointed out that if the reverse transformation is incomplete when the applied stress is reduced to zero in the pseudoelastic case, the residual martensite can be reversed by heating, resulting in the shape memory effect. The experimental work by Guilemany and Gil [56] show that the recovered strain after releasing the applied stress also changes with loading cycle. The first cycle produces a higher residual strain or lower recovery of the shape change than the subsequent cycles, resulting in a training effect under stress. Guilemany and Gil believe that such a training effect is due to interactions between martensite plates which cause localized plastic strain and/or irreversible martensite pinned by defects. There is a lack of experimental and theoretical evidence which can prove this explanation.

In this chapter, the simulation results will be presented to show how the stress-strain curve and the amount of strain which can recover vary with loading temperature and loading cycles, how the reversibility of the elastic energy and reverse frictional resistance affect the strain recovery after the applied stress is released, and how they affect the reverse transformation of the remaining martensite by heating after the stress is released, reproducing the shape memory effect. The evidence form the simulation will also be presented to show that the essence of stress-strain hysteresis is the exact analogy of the thermal hysteresis -- the free energy change due to the applied stress is not always in equilibrium with the elastic energy increment due to the martensitic transformation.

7.2. Computer Simulation Model

The computer model for simulating the reversible transformation under external stress has been described in Chapter 3. The transformation in an constrained crystal is

simulated. The total Gibbs free energy changes for the transformation and reversion of an element (p,R) under an external stress, σ^e, at a fixed temperature, T, are shown in Eqs. (3.17) and (3.18). For simplicity, the effects of the relaxation factor, f_f, and forward frictional resistance, ΔG_r, are neglected ($f_f = 1$, $\Delta G_r = 0$):

$$\Delta G(T, p,R) = \upsilon \Delta G_\upsilon(T) + \Delta G_e(p,R) + \Delta G_i(\sigma^e,p) \tag{7.1}$$

$$\Delta G'(T, p,R) = \upsilon \Delta G'_\upsilon(T) + f_r (\Delta G'_e(p,R) + \Delta G'_i(\sigma^e,p)) + \Delta G'_r \tag{7.2}$$

To plot stress-strain curves which are generated from the simulation, the macroscopic strain induced by the transformation must be calculated. From Eq. (3.14), when a uniaxial stress is imposed at the y-direction of a transforming body, the macroscopic strain induced by the transformation at the y-direction is

$$\bar{\varepsilon}_y = \bar{\varepsilon}_{22} = \sum_p \zeta_p \varepsilon^0_{22}(p) \tag{7.3}$$

where $\varepsilon^0_{22}(p)$ is the transformation strain component of a martensite particle of variant p, and ζ_p is the volume fraction of variant p martensite. Substituting $\varepsilon^0_{22}(1) = \varepsilon_s(R - 1)$, $\varepsilon^0_{22}(2) = \varepsilon_s(R + 1)$, $\zeta_1 = N_1/N$ and $\zeta_2 = N_2/N$ into Eq. (7.3), we have

$$\bar{\varepsilon}_y = \bar{\varepsilon}_{22} = \varepsilon_s \frac{N_2 - N_1}{N} + \varepsilon_s R \frac{N_2 + N_1}{N} \tag{7.4}$$

where N_1 and N_2 are the numbers of martensite particles of variant (1) and (2) respectively, and N is the total number of cells. If we measure the stress in units of $\mu\varepsilon_s$, $\sigma^e_{22} = \sigma^* \mu\varepsilon_s$, the relation of σ^* versus $\bar{\varepsilon}_y/\varepsilon_s$ qualitatively reflects features of a stress-strain curve produced by the martensitic transformation. If the second term at the right side of Eq. (7.4) is omitted, we obtain a simpler expression

$$\varepsilon_y = \bar{\varepsilon}_y / \varepsilon_s = \frac{N_2 - N_1}{N} \tag{7.5}$$

If $\varepsilon_y = 1$, the completely transformed body consists of only martensite particles of variant (2); if $\varepsilon_y = 0$, the body consists of either no martensite particles or has an equal number of martensite particles of both variants.

The stress-strain curves can be qualitatively represented by σ^*-$\bar{\varepsilon}_y$, or σ^*-ε_y, where $\sigma^* = \sigma^e_{22}/\mu\varepsilon_s$, $\bar{\varepsilon}_y$ and ε_y are described in Eq. (7.4) and Eq. (7.5) respectively.

The forward and reverse transformations are allowed during both loading and unloading processes, unless otherwise indicated. The transformation directly from one variant of martensite to the second variant of martensite is not considered.

7.3. Results and Discussion

7.3.1. Reversible Transformation under External Stress -- Pseudoelasticity

A. The Influence of Loading Temperature and Loading Cycle on Stress-Strain Relation

The simulations were conducted for different values of chemical driving force, ΔG_υ, corresponding to different temperatures, and a uniaxial stress that was cycled between $\sigma^* = 3.0$ and 0. A dilation ratio of 0.2 (R = 0.2) is assumed in the transformation strain. From the temperature-transformation (TT) curve during a thermal cycle for R = 0.2, $f_r = 1$ and $\Delta G_r^{'} = 0$, the values of the chemical free energy corresponding to M_s, M_f, A_s, and A_f can be found: $-\Delta G_\upsilon(M_s) = 1.25$, $-\Delta G_\upsilon(M_f) = -\Delta G_\upsilon(A_s) = 1.96$, and $-\Delta G_\upsilon(A_f) = 0$ Hence, the values of $-\Delta G_\upsilon$ are chosen ranging from -0.5 ($T > M_s$) to 3.5 ($T < M_f$). When $T > M_s$, the initial body is the parent phase, and there is a single martensite particle of variant (2) as a seed. When $M_s > T > M_f$, the initial body contains a fraction of martensite

transformed thermally at that temperature. When $T < M_f$, the initial body contains only martensite particles with two variants transformed thermally.

Since the second term in Eq. (7.4) only adds a constant to ε_y and does not change the shape of stress-strain relations, in the following, all stress-strain curves are presented by σ^*-ε_y.

Figure 7.2(a) to (h) are σ^*-ε_y curves from the simulation at eight different temperatures. Figure 7.2(a) and 7.2(b) show only the first cycle of σ^*-ε_y curve, since the curves of the higher cycle are identical to that of the first one. Figure 7.2(c) through 7.2(h) plot the σ^*-ε_y curves of the first and the second cycle. The σ^*-ε_y curve during unloading of the second cycle overlaps the unloading section of the first one. The σ^*-ε_y curves of the third and higher cycles are identical to that of the second cycle.

The following are the observations from Figure 7.2. (1) When loading temperature $T > M_s$, the stress, σ_{c1}, where the martensite transformation starts, decreases with decreasing temperature ((a) through (d)). (2) When loading temperature $T < M_f$, the stress, σ_{c1}, is where the reorientation or change of the martensite variant occurs (Note: it is actually the stress where the reverse transformation of martensite to the parent phase during loading begins since the direct transformation from one variant to the other is not allowed). At this temperature range, σ_{c1} increases with decreasing temperature ((f) through (h)). (3) The stress, σ_{c2}, where the transformation or reorientation completes during loading, increases with decreasing temperature. (4) The stress where the reverse transformation starts during unloading decreases with decreasing temperature. (5) At the end of the first cycle, the remaining strain increases with decreasing temperature. In other words, the net recovered strain decreases after the stress is released with decreasing temperature. (6) At the end of the second, or higher cycle, the strain (refer to the starting point of the second cycle) is completely recovered. (7) The hysteresis widens with decreasing temperature because of increasing σ_{c2} and decreasing σ_{c3}.

The above observations from Figure 7.2 have obvious physical reasons: When loading temperature $T > M_S$, the parent phase is thermodynamically favored. The higher the temperature, the more difficult the martensitic transformation is. Therefore, the stress at which the induced transformation starts increases with temperature. When loading temperature $T < M_f$, martensite is thermodynamically favored. The degree of difficulty of the reverse transformation from the martensite to the parent phase increases with decreasing temperature. Therefore, the stress at which the reorientation starts during loading increases with decreasing temperature, and the stress where the reverse transformation starts during unloading decreases with decreasing temperature.

Strictly speaking, pseudoelasticity is realized when loading temperature is equal or above A_f. The σ^*-ε_y curves of such type are shown in Figure 7.2 (a) and 7.2 (b), where the transformation-induced strain is completely recovered at the end of the first loading cycle. When some or all transformation-induced strain remains after the removal of the applied stress, as shown in Figure 7.2 (c) to 7.2 (h), the phenomenon is called *pseudoplasticity* since the remaining strain resembles that created by plastic deformation.

B. The Influence of Loading Temperature and Loading Cycle on Microstructure

When loading temperature is above or close to A_f, (see the σ^*-ε_y curves in Figure 2 (a) and (b)), the stress-induced martensite consists of entirely or almost entirely variant (2) particles. The martensite particles reverse to the parent phase completely when the applied stress is released to zero. Figure 7.3 shows an example of the configurations at eight different stresses in the first loading-unloading cycle when $-\Delta G\upsilon = -0.5$ ($T > A_f$). The whole body transforms into variant (2) martensite ($\varepsilon_y = 1$) before reaching the maximum stress. The σ^*-ε_y curve shows a vertical segment after the completion of the transformation since the pure elastic strain caused by the Young's modulus is not shown in the relation. If the maximum applied stress is lower, e.g., $\sigma^* = 1.0$, the final transformed

configuration looks like that shown in Figure 7.3 (b) and the reversion starts from that point if the applied stress is reduced. As the loading and unloading cycles, the shape change induced by the martensitic transformation and reversion repeats just like a rubber band.

When the loading temperature is relatively low but still above M_s (see σ^*-ε_y curves in Figure 7.2 (c) and 7.2(d)), the martensite particles induced by the initial load contain both variants, but with higher fraction of variant (2). Subsequential increase of the load causes the reversion of variant (1) and the transformation of variant (2). When the load is decreased from its maximum, the amount of particles of variant (2) decreases, and at the same time the amount of particles of variant (1) increases. After the load is reduced to zero, the partial martensite particles of both variants remain and do not reverse to the parent phase. Since the number of particles of two variants are not the same, the net strain is not zero. Figure 7.4 shows the configurations at different stresses during the first loading-unloading cycle when $-\Delta G\upsilon = 1.0$. At this temperature ($A_f > T > M_s$), a thin plate with variant (2) particles forms at $\sigma^* = 0.15$. At $\sigma^* = 0.3$, about 91% of the total cells have transformed into martensite of both variants (Figure 7.4 (a)). Figure 7.4(b) through 7.4(d) show the configurations at the other three different applied stresses ($\sigma^* = 0.6$, 1.05 and 1.5) during the loading of the first cycle. When $\sigma^* = 1.65$ or higher, all variant (1) particles are reversed into the parent phase and then transformed into variant (2) particles. During the unloading of the first cycle, the reversion does not start until the applied stress is reduced to $\sigma^* = 0.9$ at which some of variant (2) particles are reversed to the parent phase (Figure 7.4(e)). Figure 7.4(f) through 7.4(h) show the configurations at three different applied stresses ($\sigma^* = 0.6$, 0.3 and 0) during the unloading of the first cycle. Since the martensite is not completely reversed at zero stress, the morphologies generated during loading of the second cycle are different from those in the first cycle and, therefore, the σ^*-ε_y curve during the loading of the second cycle is different from that of the first one. Figure 7.5(a) through 7.5(d) show configurations at four different applied stresses ($\sigma^* =$

0.45, 0.9, 1.35 and 1.65) during the loading of the second cycle. When σ^* is higher than 1.65 only the particles of variant (2) exist.

When the loading temperature is lower than M_f (see the σ^*-ε_y curves in Figure 7.2 (e) through 7.2(g)), a martensite particle of variant (1) is reversed to the parent phase and then immediately transformed to variant (2) particle. This reversion-transformation process starts and proceeds at the boundaries of martensite plates of two variants. The macroscopic effect is the movement of twin boundaries. During unloading, the number of martensite particles of variant (2) which reverse to the parent phase and subsequently transform to variant (1) reduces with decreasing temperature. Figure 7.6 shows configurations during the loading ((a)-(d)) and unloading ((e)-(f)) in the first cycle when $-\Delta G\upsilon = 2.0$, a temperature just below the M_f. The initial configuration at zero stress consists two variants with almost even volume fraction (Figure 7.6(a)). Before the applied stress, σ^*, reaches the maximum, all variant (1) particles have transformed back to the parent phase and then to variant (2) (at $\sigma^* = 2.1$). During unloading, the number of martensite particles of variant (2) which reverse to the parent phase and then transform into variant (1) increases with decreasing load. At the end of the first cycle, more than 70% of the strain is recovered and the configuration at that point is shown in Figure 7.6(d). When the loading temperature is much lower that M_f ($-\Delta G\upsilon = 3.5$), less than 10% of martensite particles are still variant (1) at the maximum load. Figure 7.7 shows the configurations at four different stresses during loading. Unloading has almost no effect on the σ^*-ε_y curve and configuration, as shown in Figure 7.7 (d). There is no recovered strain at zero load.

Figure 7.8 is the plot of the recovered strain after the applied stress is released at the end of the first cycle versus the loading temperature ($-\Delta G\upsilon$). The recovery of the strain is complete when $T \geq A_f$, and decreases drastically with decreasing temperature when $T < M_f$.

C. The Influence of Maximum Stress

Since the maximum stress used for generating the results shown in Figure 7.2 is high ($\sigma^* = 3.0$), all the particles are variant (2) at the maximum stress regardless of loading temperatures and of the number of cycles. Therefore, the morphologies and σ^*-ε_y curves produced in the higher cycles are exactly the same as those produced in the second cycle, since in our simulation the elastic energy change is determined by the configuration only. In reality, an energy fluctuation may occur and the morphologies and stress-strain curves of different cycles may not coincide. If the stress reaches the maximum and the transformed body consists both variants, the σ^*-ε_y curves do not overlap even at higher cycles because the morphologies are not identical at the same load. Figure 7.9 shows the TT curve of such case when the maximum stress, σ^*, is 2.0 and $-\Delta G\upsilon = 2.0$. The net fraction of variant (2) does not reaches 1.0 until the end of loading in the second cycle, and the remaining strain at the end of second cycle is negative (with respect to the strain at the starting point of the second cycle). The σ^*-ε_y curve of the third cycle does not coincide with that of the second cycle since the initial configurations at zero stress of the two cycles are different.

D. The Influence of Reversibility of Elastic Energy and Frictional Resistance

Figure 7.10 shows the σ^*-ε_y curve when the reversibility, f_r, is reduced to 0.5 and the frictional resistance, $\Delta G_r'$, is still zero for a maximum stress 3.0 and $-\Delta G\upsilon = 1.0$ ($A_f > T > M_s$). Comparing this with Figure 7.2(d) which shows the σ^*-ε_y curve for $f_r = 1$, we can see that lowering the reversibility increases the stress, σ_{c2}, under which all particles transform or reorientate to variant (2), decreases the stress, σ_{c3}, where the reverse transformation starts during unloading, and decreases the strain recovered after the stress is released to zero. Figure 7.11 shows the σ^*-ε_y curves when $f_r = 1$ and $\Delta G_r' = 1.0$ (a) and 2.0 (b) respectively. The effect of $\Delta G_r'$ on the σ^*-ε_y curve is the same as that of lowering

reversibility, and when $\Delta G_r^{'} = 1.0$, the σ^*-ε_y curve is almost the same as that shown in Figure 7.10 where $f_r = 0.5$. When $\Delta G_r^{'} = 2.0$ (Figure 7.11 (b))., the recovered strain after the stress is released is less than 0.2. While when $\Delta G_r^{'} = 0$ (Figure 7.2 (d)), the recovered strain is more than 0.8.

The smaller the reversibility, f_r, or the larger the reverse frictional resistance, $\Delta G_r^{'}$, the closer the microstructure produced by the reversible transformation is to that in the irreversible case.

7.3.2. The Strain Recovery After Unloading -- Shape Memory Effect

To simulate the shape memory effect, the stress-induced transformation must show pseudoplasticity at the end of a loading cycle. Then the temperature ($-\Delta G\upsilon$) is increased gradually until all martensite particles are reversed to the parent phase. Three cases are selected: (1) $T < M_f$ ($-\Delta G\upsilon = 3.0$), $f_r = 1$, $\Delta G_r^{'} = 0$; (2) $M_s < T < A_f$ ($-\Delta G\upsilon = 1.0$), $f_r = 0.5$, $\Delta G_r^{'} = 0$; (3) $M_s < T < A_f$ ($-\Delta G\upsilon = 1.0$), $f_r = 1.0$, $\Delta G_r^{'} = 1.0$. The σ^*-ε_y curves of these cases have been shown in Figure 7.2 (g), Figure 7.10 and Figure 7.11 (a) respectively. The top portions in Figure 7.12(a) through 7.12(c) are the σ^*-ε_y curves of the first loading cycle of these three cases; the bottom parts in Figure 7.12(a) through 7.12(c) are the temperature-transformation (TT) curves and temperature-strain relations obtained after unloading.

Figure 7.12 (a) (case 1) shows that if the loading and unloading are done at the fixed temperature ($-\Delta G\upsilon = 3.0$) below M_f, about 20% of the strain is recovered after the unloading, while no martensite is reversed to the parent phase. The strain recovery is due to the variant-reorientation, that is, variant (2) particles transform to variant (1) particles through the reversion to the parent phase first. After unloading, then subsequent increases in temperature causes the recovery of the strain and reversion of martensite. Although both strain and volume fraction of martensite decrease with increasing temperature, the rates of

decreasing are different at different temperature ranges. As shown in Figure 7.12 (a), there are three temperature regions. In the first region, where $T < M_f$, the strain increases drastically but the change of the fraction of martensite is zero. In the second region, where $M_f < T < M_s$, the rate of the strain recovery is decreased to about a half of that of the first region, and a little martensite is reversed to the parent phase. In the third region, the rate of the strain recovery is the same as that of the second region, but the fraction of martensite decreases dramatically with the increasing temperature until the reversion is complete near A_f. The microstructure shows that, in the first region, the recovered strain is due to the variant-reorientation. In the third region, the remaining strain is recovered mainly by the reverse transformation of the martensite to the parent phase. The reverse transformation completes at or a little below the A_f which is below T_0 (see Chapter 6).

Figure 7.12 (b) (case 2) and 7.12 (c) (case 3) compare the effects of the reversibility of the elastic energy and reverse frictional resistance on strain recovery. In both cases, the reversion and strain recovery are complete at their reverse transformation completion temperature, A_f. The completion of reverse transformation for the case 3 requires much higher temperature since the existence of reverse transformation resistance has shifted A_f up (see Chapter 6). At this loading temperature, the martensitic transformation is induced by the applied stress (since $T > M_s$) and the strain recovered during unloading is due to mainly the variant-reorientation. As shown in Figure 7.12 (b) and 7.12(c), about 98% of the particles are martensite after the stress is released to zero.

7.4. Discussion and Conclusion

7.4.1. The Source of Stress-Strain Hysteresis of Pseudoelasticity

From Figure 7.2 it can be seen that a stress-strain hysteresis exists even when the temperature is higher than A_f and that the strain is completely recovered after the stress is

released. In Chapter 6 it has been shown the thermal hysteresis is due to the absence of thermoelastic equilibrium. To show this is also true for the stress-strain hysteresis, the reverse transformation during unloading that follows exactly the reverse sequence of the forward transformation during loading ("exactly reversed path" for short) was simulated.

Using the same procedure employed in Chapter 6, the following relation can be obtained from Eqs. (7.1) and (7.2) (when $f_r = 1$ and $\Delta G_r^{'} = 0$) for the exactly reversed path

$$- \upsilon \Delta G_{\upsilon}(T) - \Delta G_i(\sigma^{e'}, p) \leq \Delta G_e(p,\mathbf{R}) \leq -\upsilon \Delta G_{\upsilon}(T) - \Delta G_i(\sigma^{e}, p) \qquad (7.6)$$

The above relation shows that the elastic energy increment, $\Delta G_e(p,\mathbf{R})$, of the loading process for any given martensite volume fraction must be bounded between the Stress-Transformation (ST) curves of the loading and unloading. The ST curves are the plots of fraction of martensite particles versus the negative of the free energy change caused by the applied stress plus the chemical free energy change during loading and unloading, $-(\upsilon \Delta G_{\upsilon}(T) + \Delta G_i(\sigma^{e}, p))$ and $-(\upsilon \Delta G_{\upsilon}(T) + \Delta G_i(\sigma^{e'}, p))$. Since temperature is fixed, the effect of chemical energy on both transformation and reversion is the same. Figure 7.13 illustrates the ST curves and $\Delta G_e(p,\mathbf{R})$ curve from the simulation of the exactly reversed path. Again as in the thermoelastic transformation (Chapter 6), the reverse transformation is not allowed during loading to avoid complication of the simulation. Figure 7.13 shows that the elastic energy increment, $\Delta G_e(p,\mathbf{R})$, does not monotonically increase with the fraction of martensite particles. However, since the free energy caused by the applied stress is proportional to the net fraction of martensite particles of variant (2), which is favored in the tension, the equilibrium condition, where $\upsilon \Delta G_{\upsilon}(T) + \Delta G_e(p,\mathbf{R}) + \Delta G_i(\sigma^{e}, p) = 0$, does not always exist.

Figure 7.14 compares the ST curves from the exactly reversed path and minimum energy path. The ST curve generated from the minimum energy path produces a smaller hysteresis loop.

Setting $\sigma^{e'} = \sigma^{e}$ in Eq. (7.8), then only the equation

$$-\upsilon \Delta G_{\upsilon}(T) - \Delta G_{i}(\sigma^{e},p) = \Delta G_{e}(p,R) \qquad (7.7)$$

holds for any volume fraction of martensite. This means, if the equilibrium always holds during loading. no stress-strain hysteresis should exists and the minimum energy path is the same as the exactly reversed path.

7.4.2. Training Effect under Stress

At certain temperatures and applied stresses, the strain produced in the second or higher loading cycles is completely recovered after the stress is released, while there is remaining strain in the first cycle. The conditions under which the Figure 7.2 is generated exclude any effects caused by dislocation structures since no plastic deformation or any frictional resistance is considered. The reason for the training effect found in the simulation is that, after a complete loading cycle one martensite variant is favored. At a certain loading temperature and maximum applied stress, all particles transform into variant (2) when the maximum stress is reached. During unloading, the amount of particles of variant (2) which can reverse to the parent phase and then transform to variant (1) is determined by loading temperature. The lower the loading temperature, the lower the stability of the parent phase and the possibility of the reversion from the martensite phase to the parent phase. At one extreme, as shown in Figure 2 (h), when the loading temperature is much lower that M_f, no particles can reverse after the stress is released, and the retained martensite is mostly variant (2).

7.4.3. The Shape Memory Effect

The shape memory effect can be realized only when materials show pseudoplasticity and are thermoelastic in nature. It can be utilized most effectively when deformation (or loading) temperature is below the M_f, so that the strain induced by the martensitic transformation and reorientation is at its maximum when the applied stress is released. During the heating process which follows the removal of the applied stress, the strain recovery is mainly due to the martensite reorientation when temperature is below M_f.

CHAPTER 8

COMPUTER SIMULATION OF MARTENSITIC TRANSFORMATIONS OF CUBIC TO MONOCLINIC STRUCTURE

8.1. Introduction

The computer simulations in previous chapters were done in an ideal crystal, and the system was considered isotropic. In this chapter the computer simulation model is applied to partial-stabilized-zirconia systems to simulate the martensitic transformation from a cubic to a monoclinic structure as an approximation of the transformation from a tetragonal to a monoclinic structure.

Twinning occurs in small particles which are embedded in cubic zirconia matrix during the transformation from tetragnal to monoclinic structure. This phase transformation increases the fracture toughness of the material [8]. The twinning, however, cannot be explained by the crystallographic theory since no invariant plane is found in the twinned monoclinic structure [20]. One explanation for the twinning is the constraint imposed by untransformed cubic matrix, because the formation of twins reduces the total shape change under the constraint [20]. To my knowledge, however, so far there is no theoretical study or computer simulation that has been done to conclusively determine the source of such twinning. It has been shown in Chapter 4 through Chapter 7 that the constrained boundary imposed by untransformed matrix promotes the twining in a two-dimensional space. In the following sections, the simulation results of the martensitic transformation in three-dimensional space under the stress-free and constrained condition are presented, and the role of the constraint for the twinning is discussed.

8.2. Computer Simulation Model

The simulation is done in a cubic system of three-dimensional space without external stresses. The driving force is provided by chemical free energy (undercooling). The model used here is essentially the same as that described in Chapter 3 except that the transformation strain is monoclinic, and the elastic system is cubic (non-isotropic). These differences are elaborated in the following.

For simplicity the parent phase is assumed to be a cubic structure, instead of tetragonal structure. Due to the crystallographic symmetry, there are total 12 variants of monoclinic transformation strain. For the purpose of this work, it is adequate to choose 4 variants in the simulation:

$$\varepsilon(1)=\begin{bmatrix}\varepsilon_1 & 0 & \gamma\\ 0 & \varepsilon_2 & 0\\ \gamma & 0 & \varepsilon_3\end{bmatrix} \qquad \varepsilon(2)=\begin{bmatrix}\varepsilon_1 & 0 & -\gamma\\ 0 & \varepsilon_2 & 0\\ -\gamma & 0 & \varepsilon_3\end{bmatrix}$$

$$\varepsilon(3)=\begin{bmatrix}\varepsilon_2 & 0 & 0\\ 0 & \varepsilon_1 & \gamma\\ 0 & \gamma & \varepsilon_3\end{bmatrix} \qquad \varepsilon(4)=\begin{bmatrix}\varepsilon_2 & 0 & 0\\ 0 & \varepsilon_1 & -\gamma\\ 0 & -\gamma & \varepsilon_3\end{bmatrix} \tag{8.1}$$

Two sets of values of the transformation strain are used in the simulation. These values along with the references are listed in Table 8.1. The elastic constants obtained from a cubic yttria-stabilized zirconia system [57] are used in the elastic energy calculation (units = 10^{12} dyn/cm^2): $c_{11} = 3.94$, $c_{12} = 0.91$ and $c_{44} = 0.56$.

Table 8.1. The values of the transformation strain

set	ε_{11}	ε_{22}	ε_{33}	γ	Reference
1	- 0.0054	0.0125	0.0387	0.0753	58
2	0.00997	0.02594	0.02622	0.08133	59

8.3. Simulation Results

When the transformation takes place in an unconstrained crystal, the simulations using the two sets of values of the transformation strain produce different microstructures. Figure 8.1 is a three-dimensional configuration generated by the first set of the values listed in Table 8.1. Initially, a seed of variant (1) is placed in the center of the cube. Although the four variants compete with each other in the simulation, the final configuration consists of two variants (variant (1) and variant (2)) of monoclinic martensite phase in a twinned structure. Figure 8.2 is a schematic drawing of the final configuration showing the shape change. For the second set of the values of the transformation strain, the final configuration consists of all four variants (Figure 8.3). If only two variants (variant (1) and variant (2)) are used in the simulation, the final configuration is a fine twinned structure (Figure 8.4).

When the transforming crystal is constrained by untransformed matrix, the simulation using the first set of the transformation strain generates a fine twinned structure, as shown in Figure 8.5. Figure 8.6 shows the configurations of two different cuboids generated by applying different amount of the constraint in three directions, when only the two variants are used. The twinned monoclinic structures have {001} twin planes. The constraint has little effect on the final configurations when the simulation is done by using the second set of the transformation strain, and the configurations are similar to those shown in Figure 8.3 and Figure 8.4.

8.4. Disscusions and Conclusion

As discussed in Chapter 2, a strain is dyadic if, and only if, one of its principal strains vanishes and the other two are opposite in sign. In order to use this criterion to determine a dyadic strain or a composite dyadic strain, the transformation strain presented

in Eq. (8.1) is diagonalized, and the values listed in Table 8.1 are used to find the principal strains. Table 8.2 lists the principal strains of the two sets of transformation strains for variant (1)s. The principal strains of variant(2)s can be obtained by exchanging the values of ε_1 and ε_3 of variant (1)s.

Table 8.2. The principal strains

set	ε_1	ε_2	ε_3	Reference
1	0.0951	0.0125	-0.0618	58
2	0.0998	0.0259	-0.0636	59

First, it is very simple to determine that the transformation strain of each set is not dyadic, since none of its three principal strains is zero. Second, using the condition provided in Chapter 2, it is clear that a composite dyadic strain cannot be achieved by combining variant (1) and variant (2) in Eq. (8.1), since $|\varepsilon_3| < |\varepsilon_1|$ (or $|\varepsilon_1| < |\varepsilon_3|$ for variant (2)s) and $\varepsilon_1 + \varepsilon_3$ has the same sign as ε_2.

It can be concluded that the transformation strains in Eq. (8.1) with the values in Table 8.1 fall into the category of non-dyadic strain where a transformation strain is not dyadic and cannot be made so by creating a composite strain. The non-dyadic transformation strain produces a multivariant microstructure to minimize the net elastic strains.

The experimental observations and the simulation results presented in Figures 8.1 through 8.6 show that the volume fraction of each of the variants in the twinned structure is about 0.5. Taking a average strain of variant (1) and variant (2) in Eq. (8.1), we obtain

$$\varepsilon = \frac{1}{2}\varepsilon(1) + \frac{1}{2}\varepsilon(2) = \begin{bmatrix} \varepsilon_1 & 0 & 0 \\ 0 & \varepsilon_2 & 0 \\ 0 & 0 & \varepsilon_3 \end{bmatrix} \tag{8.2}$$

which cancels the shear components, γ, and becomes an orthorhombic strain. But since none of the strain components in Eq. (8.2) is zero, the net strain is not a dyadic, or an invariant strain. Therefore, the twinning in this case is not to achieve an invariant plane strain, as concluded by Kelly and Ball [20] after their applying the crystallographic theory, but to relieve the partial elastic strain energy by canceling the shear components.

These simulation results illustrate that the microstructures are determined by the transformation strains and boundary conditions. The constraint imposed by an untransformed matrix promotes the twinning.

The two sets transformation strains produce different microstructures, as shown in Figure 8.1 and Figure 8.3, although both are non-dyadic strains. The second set has a larger volume expansion than the first one, but it is not clear whether this is the reason for the difference. Further investigation needs to be done to clarify this issue.

CHAPTER 9

SUMMARY

9.1. The Computer Simulation Model

This dissertation reports a computer simulation of martensitic transformations. To study the development of microstructure, a finite-element computer simulation model was constructed to mimic the transformation process. The transformation is athermal and simulated at each incremental step by transforming the cell which maximizes the decrease in the free energy. To determine the free energy change, the elastic energy developed during martensite growth is calculated from the theory of linear elasticity for elastically homogeneous media, and updated as the transformation proceeds. The model separates the effects of elastic resistance, relaxation and reversibility of elastic strain, frictional resistance, geometric constraint and external stress on the thermal resistance, microstructure and stress-strain relations during martensitic transformation and reversion.

The model is simple but very fruitful in increasing our understanding of the martensitic transformation and its related phenomena. It successfully produces the preferred microstructures of martensite, which can be predicted analytically from the linear elastic theory. It also generates unusual microstructures, such as "butterfly martensite" which have been observed experimentally. It illustrates the increased accuracy obtained by using the finite volume of the elementary cell instead of a point approximation and clarifies the physics of studies that are conducted by simulation in two dimensions. It reveals the characteristics of thermal resistance of the transformation and produces complex, multivariant microstructures when the transformation is constrained by an untransformed matrix on which external stresses are or are not present. The model simulates the reversible martensitic transformation and has expanded our understanding of thermal and stress-strain hysteresis as well as the features of thermoelasticity, pseudoelasticity and the shape

memory effect. When plastic deformation and frictional resistance are absent, thermal hysteresis exists because of the absence of equilibrium between the chemical free energy and the elastic energy during transformation at any volume fraction of martensite. This non-equilibrium effect is due to the elastic relaxation caused by elastic interaction and accommodation between martensite particles of same and different variants, and which is also the source of energy dissipation. Applied to the partially-stabilized-zirconia systems, the model simulates the transformation from cubic to monoclinic structure and generates twinned microstructures that have {100} habit planes. It has verified that, the twinning in small particles that are embedded in cubic zirconia matrix is not to achieve an invariant plane, but to reduce the transformation shape change and minimize the elastic energy.

The success and excitement of this model should not only to be judged by how close to experimental observations the martensite morphologies from the simulation are, but also by the amount of insight on martensitic transformations it provides to the broader understanding of unsolved problems.

9.2. Extensions of the Model

The model is not limited to the study of martensitic transformations, but is useful for any transformations which are primarily controlled by elastic strain energy. The model can be easily extended to study coherent precipitations and ordering-disordering reactions which are primarily dominated by elastic energy arising during the transformations. With necessary modification, the model can be used even to study plastic deformation. Traditional studies of plastic deformation are based on dislocation theories. The new approach proposed here views plastic deformation from a different perspective. When a part of a crystal is plastically deformed, it can be treated as if it undergoes a martensitic transformation with its transformation strain being equal to the plastic strain. The stress and strain distributions caused by the localized plastic strain are treated as those due to a

misfit inclusion in an elastic media. This idea was first suggested by Eshelby [9,10]. But to my knowledge, there has been no research work reported in the literature on applying this model.

9.2. Possible Changes to the Model

Several possible changes to the model might be useful in increasing understanding of elastic strain induced transformations.

First, the effects of transformation criteria other than the *minimum energy path* can be easily obtained by changing the transformation criterion in the model. The examples of the criteria are (1) the *negative energy* criterion in which the transformation is permitted to all elements that give a negative free energy change once they are transformed, and (2) the *X percentage* criterion in which X percent (randomly picked) of all elements that give a negative free energy change is allowed to transformed at each step. Since the elastic energy change at each step depends on the number of existing transformed particles and the interactions between them and is a function of the morphology of the transformation product, the change of transformation criteria will alter the morphology at each transformation step. It is interesting to see how microstructures change with the change of the criteria and what additional information can be obtained from difference criteria.

Secondly, in Chapter 6 and Chapter 7, the reverse transformation is confined to the transformation from martensite to parent phase only. The reverse transformation from one variant to the other can be added into the model without too much difficulty. This will reveal an additional possible transformation path and give us an idea which path, the martensite-parent transformation or the variant-variant transformation, is more realistic or more energetically favored.

Thirdly, matrix plasticity can be incorporated into the model in the conjunction of the simulation of plastic deformation. The elastic energy controlled transformation and the plastic deformation will co-exist in simulation, which is closer to reality.

Finally, the difference in elastic constants between the martensite and the matrix has been ignored in the model. The heterogeneity of elastic modulus changes both the two-particle elastic interaction and the interaction with the external stress. Its ultimate effect is similar to that of the transformation strain [10] and will be reflected in microstructural changes (e.g., habit changes). It is, however, very difficult to incorporate such a modulus effect into the model because it depends on the shape of the transformed region. The features of the modulus effect may be revealed by using approximations of the elastic heterogeneity.

REFERENCES

[1] M. Cohen, G.B. Olson and P.C. Clapp, Proceeding of International Conference on Martensitic Transformations (ICOMAT-79), Cambridge, Mass., 1979, p. 1.

[2] E.C. Bain, Trans. AIME., 1924, vol. 70, p. 25

[3] M.S. Wechsler, D.S. Lieberman, and T.A. Read, *Trans. AIME J. Metals*, 1953, vol. 197, p. 1503.

[4] J.S. Bowles and J.K. Mackenzie, *Acta Metall.*, 1954, pp. 129-137.

[5] J.W. Christian, *The Theory of Transformation in Metals and Alloys*, 2nd ed., Pergamon Press, New York, NY, 1975

[6] C.M. Wayman, *Introduction to the Crystallography of Martensitic Transformation*, Macmillan Series in Material Science, New York, NY, 1964.

[7] Z. Nishiyama, *Martensitic Transformation*, Academic Press, New York, NY, 1978.

[8] D.L. Porter and A.H. Heuer, *J. Amer. Ceram. Soc.*, 1977, 60, p.183.

[9] J.D. Eshelby, *Proc. Roy. Soc. A.*, 1957, vol. 241, p. 376.

[10] J.D. Eshelby, *Proc. Roy. Soc. A.*, 1959, vol. 252, p. 561.

[11] A.G. Khachaturyan, *Soviet Physics - Solid State*, 1967, vol. 8, p. 2163.

[12] A.G. Khachaturyan and G.A. Shatalov, *Sov. Phys. JETP*, 1969, vol. 29, p. 557.

[13] A.G. Khachaturyan, *Theory of Structural Transformations in Solids*, Wiley, New York, NY, 1983.

[14] A.L. Roitburd, *Crystallography - Solid State*, 1968, vol.12, No.4, p. 499.

[15] A.L. Roitburd, *Soviet Physics - Solid State*, 1969, vol.10, No.12, p. 2870.

[16] A.G. Khachaturyan, S.V. Semenovskaya and J.W. Morris Jr.,*Acta Metall.* 1988, vol.1, p. 1563.

[17] S. Wen, A.G. Khachaturyan and J.W. Morris, Jr., *Proc. Int. Conf. Martensitic Trans.*, MIT, Cambridge, Mass., 1979, p. 94.

[18] S. Chen (Wen), Ph.D. Dissertation, Unversity of California, Berkeley, 1979.

[19] T. Maki, S. Shimooka, M. Umemoto and I. Tamura, *Trans. Jpn. Inst. Met.*, 1972, vol. 13, p. 400.

[20] P.M. Kelly and C.J. Ball, *J. Amer. Ceram. Soc.*, 1986, 69, p. 259.

[21] J.R. Patel and M. Cohen, *Acta Metall.* 1953, vol.1, p. 531.

[22] Z. Mei and J.W. Morris, Jr.,*Metall. Trans.. A,* 1990, vol. 21, p. 3137.

[23] G.V. Kurdjumov and L.C. Khandros, *Dokl. Akad. Nauk. SSSR*, 1949, vol. 66, p.211.

[24] G.V. Kurdjumov, *Zhurnal tekhnicheskoi fiziki (Tech. Phys. U.S.S.R.)*, 1948, vol. 18, p.999.

[25] D.P. Dunne and C.M. Wayman, *Metall. Trans.. A*, 1973, vol. 4, p.137.

[26] Y. Deng and G.S. Ansell, *Acta Metall.*, 1991, vol. 39, p.1995.

[27] R.V. Krishnan, L. Delaey, H. Tas and H. Warlimont, *J. of Materials Science*, 1974, vol. 9, p.1536.

[28] J. Ortin and A. Planes, *Acta Metall.*, 1988, vol. 36, p.1873.

[29] G.B. Olson and M. Cohen, *Scripta Metall.*, 1977, vol. 11, p.345.

[30] J. Ortin and A. Planes, *European Symposium on Martensitic Transformation and Shape Memory Properties*, Aussois, France, 1991, p.C4-13.

[31] L. Kaufman and M. Cohen, *Prog. Met. Phys.*, 1958, vol. 7, p.165.

[32] H.C. Tong and C.M. Wayman, *Acta Metall.*, 1974, vol. 22, p.887.

[33] G.B. Olson and M. Cohen, *Scripta Metall.*, 1975, vol. 9, p.1247.

[34] H.C. Ling and W.S. Owen, *Acta Metall.*, 1981, vol. 29, p.1721.

[35] K. Enami, A. Nagasawa and S. Nenno, *Scripta Metall.*, 1975, vol. 9, p.941.

[36] A. Sato, E. Chishima, K. Soma, and T. Mori,*Acta Metall.*, 1982, vol. 30, p.1177.

[37] A. Sato, E. Chishiam, Y. Yamaji, and T. Mori, *Acta Metall.*, 1984, vol. 32, p.539.

[38] A. Sato, Y. Yamaji, and T. Mori, *Acta Metall.*, 1986, vol. 34, p.287.

[39] J.S. Robinson and P.G. McCormick, *Scripta Metall.*, 1989, vol. 23, p.1975.

[40] Tan Shiming, Lao Jinhai and Yang Shiwei, *Scripta Metall.*, 1991, vol. 25, p.1119.

[41] Y. Tomota, W. Nakagawara, K. Tsuzaki, and T. Maki, *Scripta Metall.*, 1992, vol. 26, p.1571.

[42] X.X. Wang and L.C. Zhao, *Scripta Metall.*, 1992, vol. 26, p.303.

[43] J.H. Yang, H.Chen, and C.M. Wayman, *Metall. Trans.. A*, 1992, vol. 23A, p.1431.

[44] Yu.N. Koval and G.E. Monastyrsky, *Scripta Metall.*, 1993, vol. 28, p.41.

[45] M.W. Burkart and T.A. Read, *Trans. Met. Soc. AIME*, 1953, vol. 197, p.1516.

[46] H. Pops, *Metall. Trans.*, 1970, Vol 1, p.251.

[47] R.V. Krishnan and L.C. Brown, *Metall. Trans.*, 1973, Vol 4, p.423.

[48] H.K. Birnbaum and T.A. Read, *Trans. Met. Soc. AIME*, 1960, vol. 218, p.662.

[49] Z.S. Basinski and J.W. Christian, *Acta Met.*, 1954, vol. 2, p.148.

[50] R.E. Busch, R.T. Luedeman and P.M. Cross, U.S. Army Material Research Report, AD 629726 (1966).

[51] A. Nagasawa, *Phys. Stat. Sol. (a)*, 1971, vol. 8, p.531.

[52] K. Sumino, *Phys. Stat. Sol.*, 1969, vol 33, p.327.

[53] R. J. Wasilewski, *Metall. Trans.*, 1971, vol 2., p.2973.

[54] C.M. Wayman and K. Shimizu, *Metal Science Journal,* 1972, vol. 8, p.175.

[55] L. Delaey, R.V. Krishnan, H. Tas and H. Warlimont, *J. of Materials Science,* 1974, vol. 9, p.1521.

[56] J.M. Guilemany and F.J. Gil, *J. of Materials Science*, 1992, vol. 27, p. 3211.

[57] J.M. Farley, J.S. Thorp, J.S. Ross and G.A. Saunders, *J. of Mater. Sci.*, vol. 7, p. 475.

[58] M. Hayakawa and M. Oka, *Mater. Sci. Forum.*, 1990, Vols. 56-58, p. 383.

[59] D.L. Porter, A.G. Evans and A.H. Heuer, *Acta. Metall.*, 1979, vol. 27, p.1649.

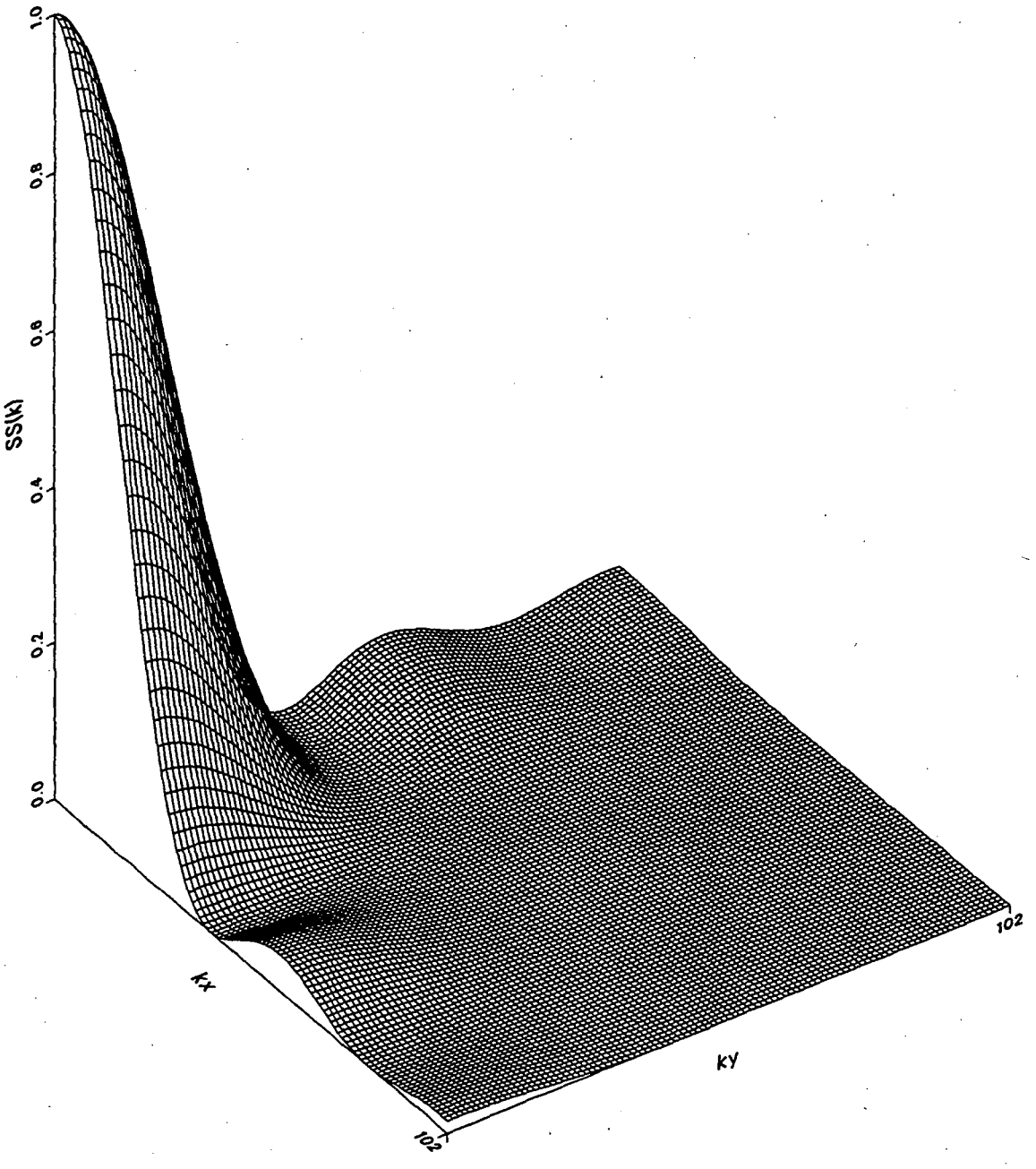

Fig. 3.1 A plot of a quadrant of shape function, $|\eta_0(\mathbf{k})|^2$, extended into 5th Brillouin zone in a two-dimensional space.

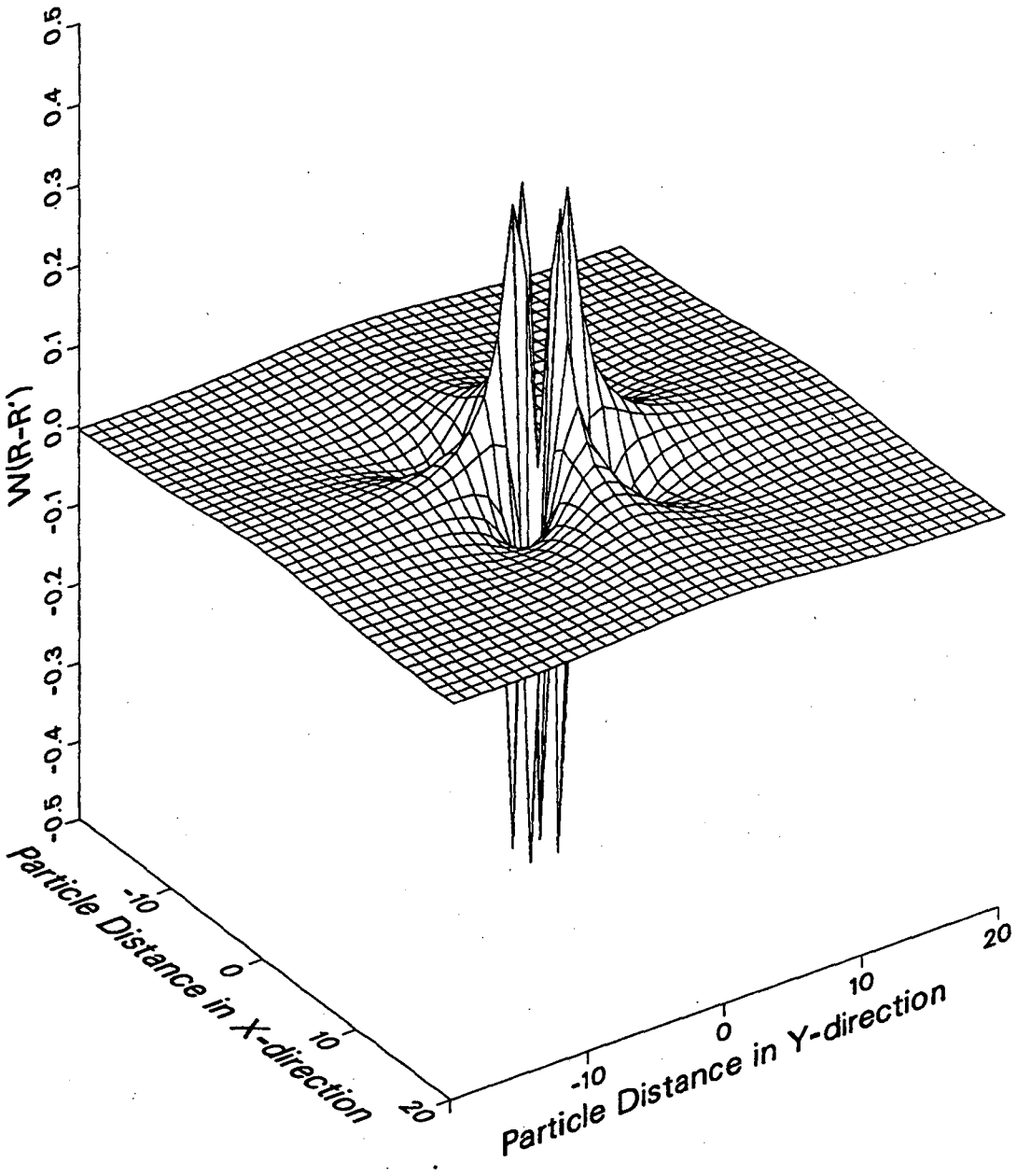

Fig. 3.2(a) The two-body interaction, $W_{11}(\mathbf{R}\text{-}\mathbf{R}')$, between like variants in a two-dimensional transformation with a pure shear transformation strain(the plot with blanking).

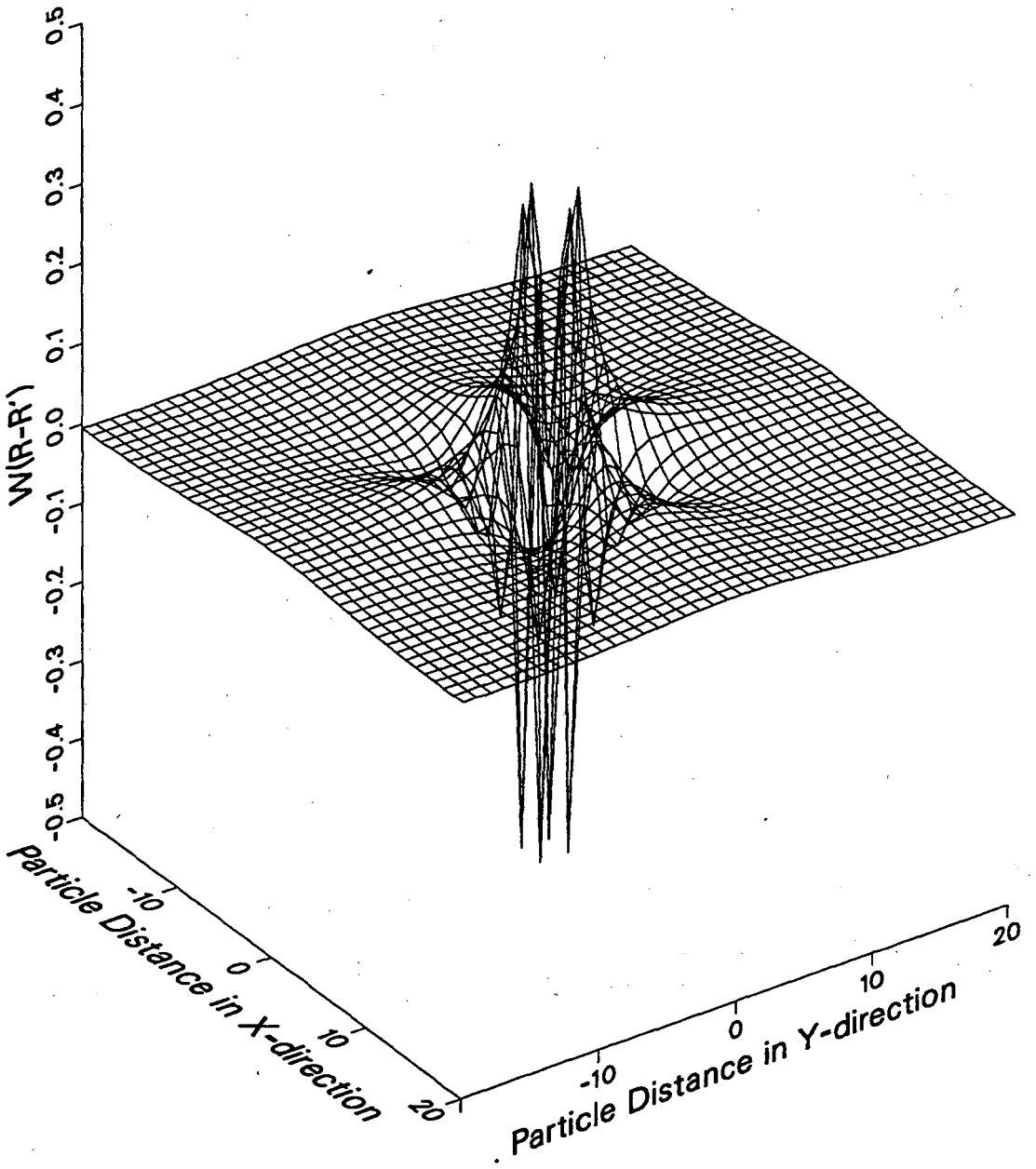

Fig. 3.2(b) The two-body interaction, $W_{11}(\mathbf{R}\text{-}\mathbf{R}')$, between like variants in a two-dimensional transformation with a pure shear transformation strain (the plot without blanking).

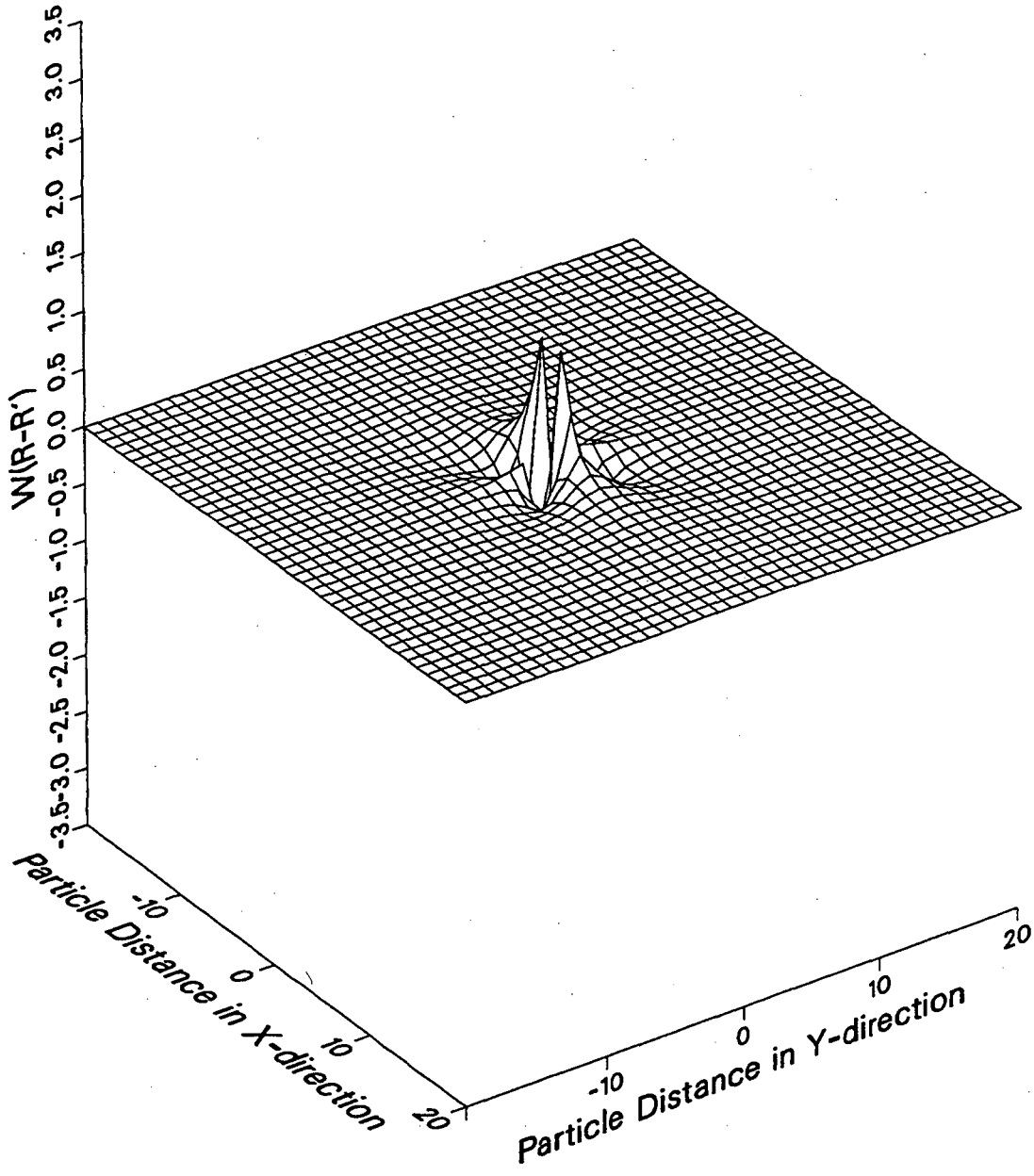

Fig. 3.3(a) The two-body interaction, $W_{11}(\mathbf{R}\text{-}\mathbf{R}')$, between like variants in a two-dimensional transformation with a non-zero dilation (R = 0.25) transformation strain(the plot with blanking).

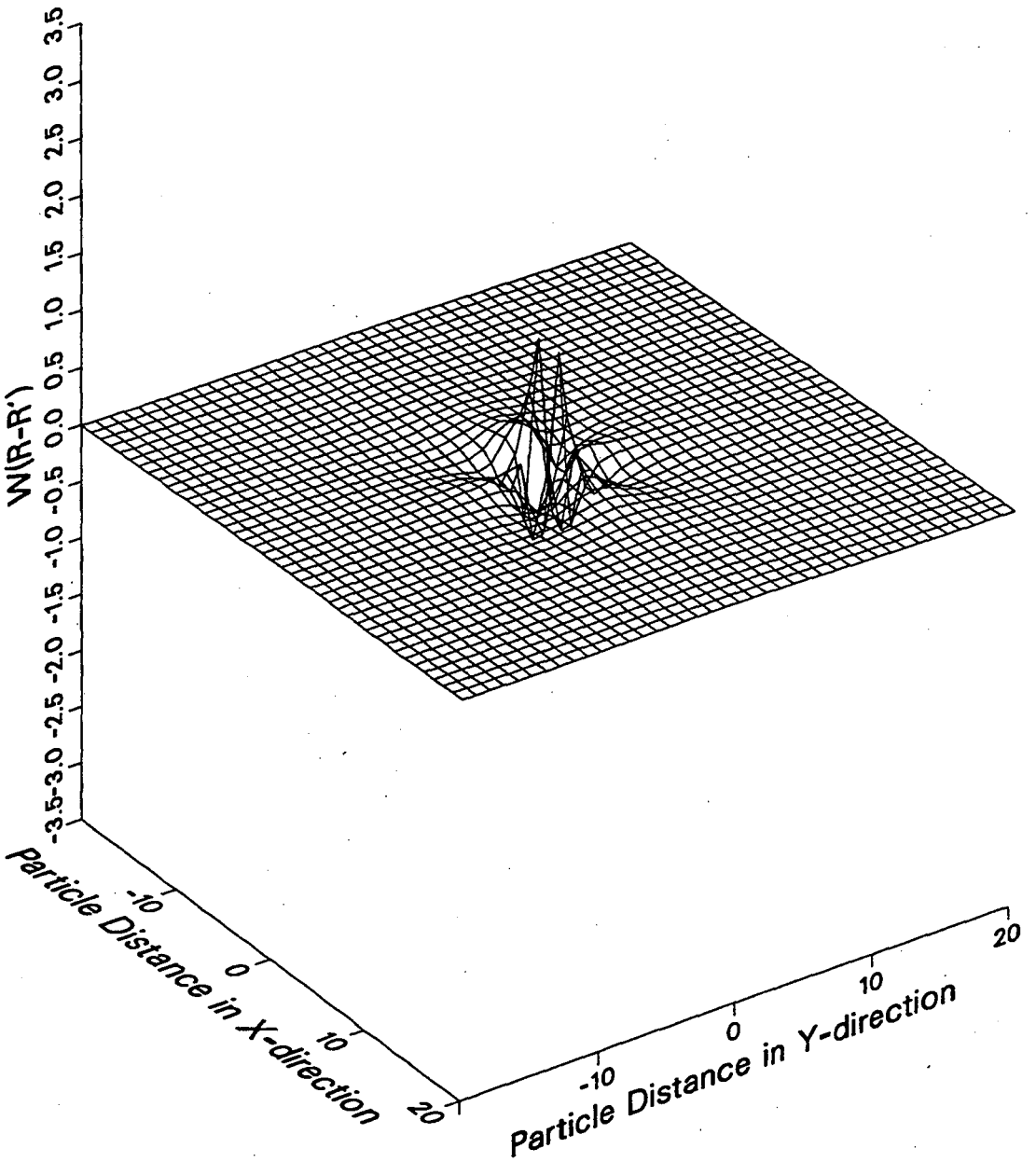

Fig. 3.3(b) The two-body interaction, $W_{11}(\mathbf{R}-\mathbf{R}')$, between like variants in a two-dimensional transformation with a non-zero dilation (R = 0.25) transformation strain(the plot without blanking).

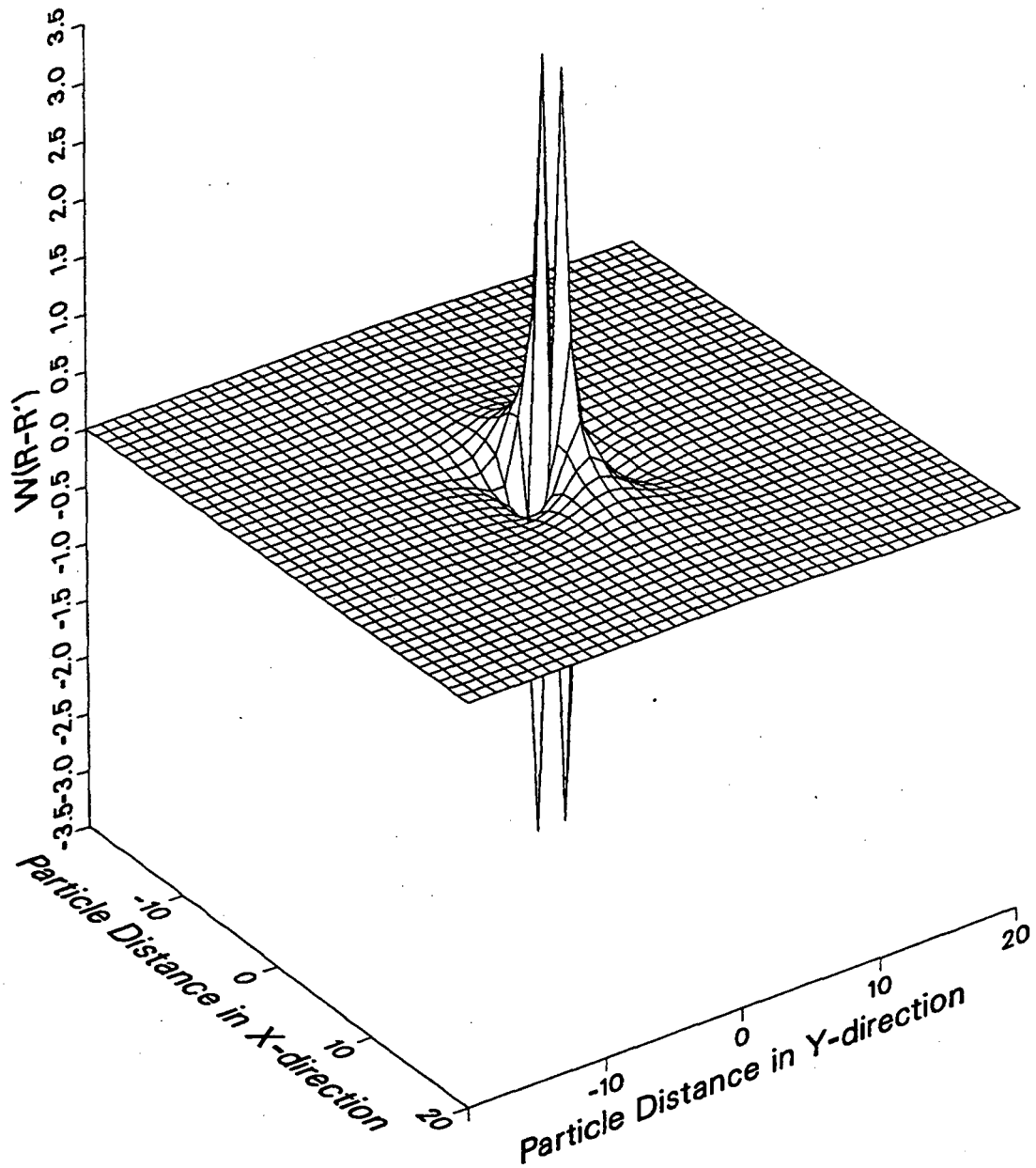

Fig. 3.4(a) The two-body interaction, $W_{11}(\mathbf{R}\text{-}\mathbf{R}')$, between like variants in a two-dimensional transformation with a non-zero dilation (R = 1.0) transformation strain.(the plot with blanking).

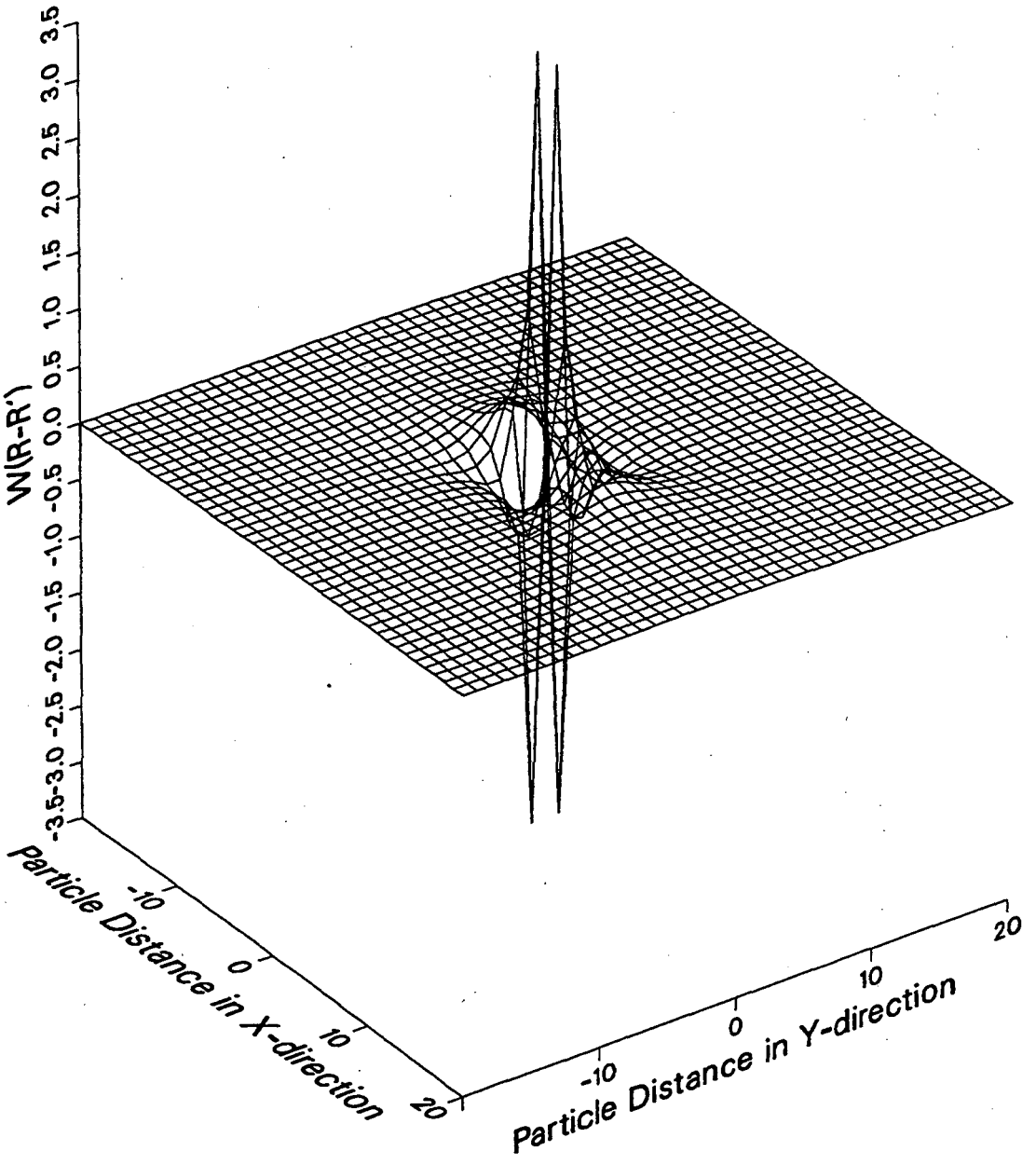

Fig. 3.4(b) The two-body interaction, $W_{11}(\mathbf{R}-\mathbf{R}')$, between like variants in a two-dimensional transformation with a non-zero dilation (R = 1.0) transformation strain(the plot without blanking).

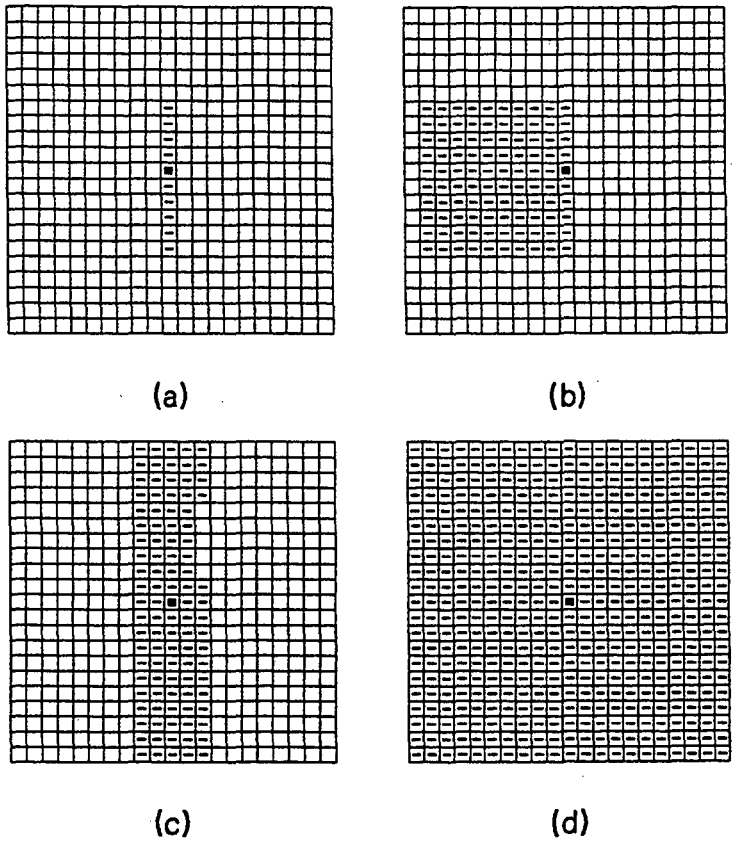

Fig. 4.1 A simulated martensitic transformation with R = 1. (001) and (010) cross-sections are shown after 50 transformation steps ((a) and (b)), and 200 steps ((c) and (d)).

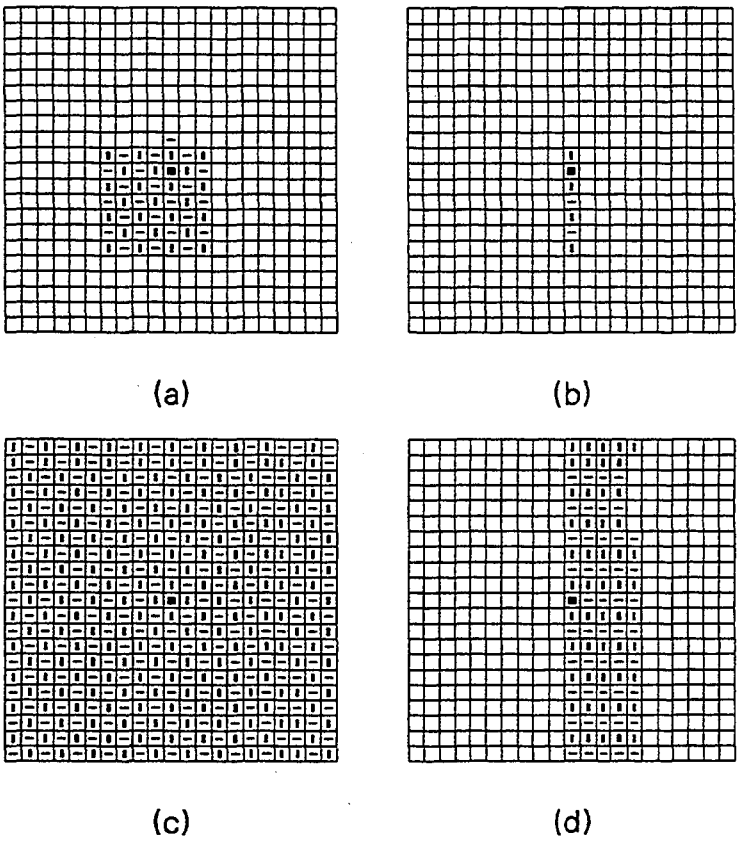

Fig. 4.2 A simulated martensitic transformation with R = -0.5. (001) and (010) cross-sections are shown after 50 transformation steps ((a) and (b)), and 200 steps ((c) and (d)). The final microstructure is shown in (e).

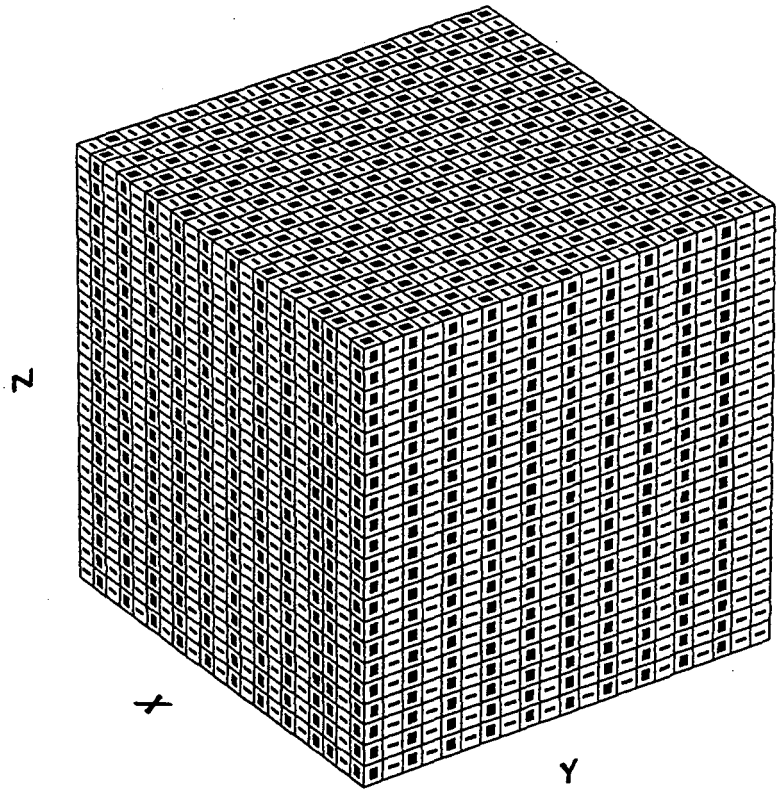

(e)

Fig. 4.2(Cont.) A simulated martensitic transformation with R = -0.5. (001) and (010) cross-sections are shown after 50 transformation steps ((a) and (b)), and 200 steps ((c) and (d)). The final microstructure is shown in (e).

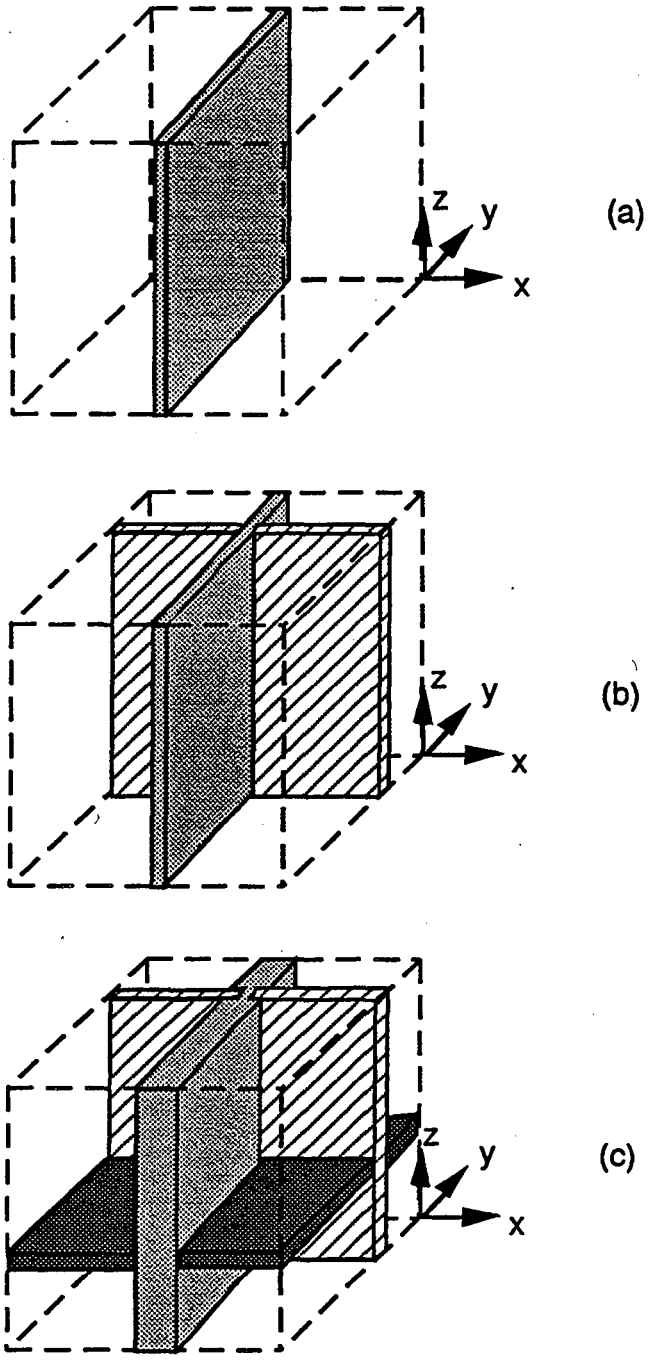

Fig. 4.3 A simulated martensitic transformation with R = 2. The transformed region is shown: (a) after a variant (1) plate forms; (b) after a variant (2) plate forms; and (c) after a variant (3) plate forms.

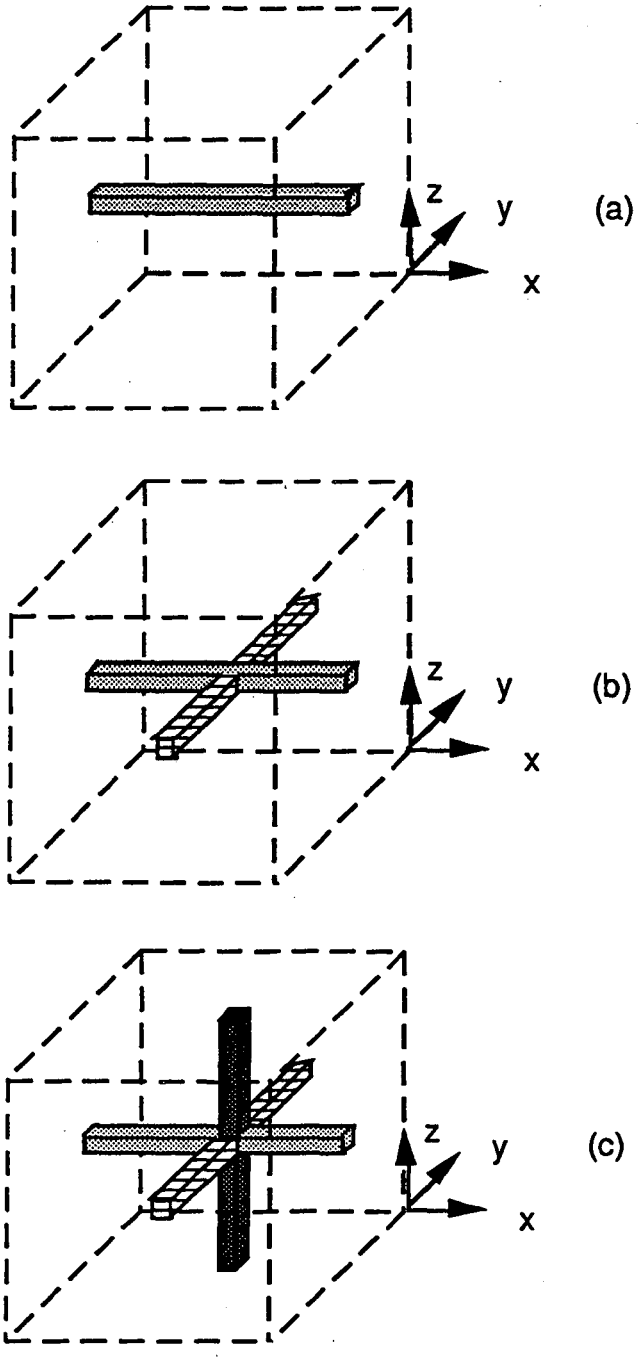

Fig. 4.4 A simulated martensitic transformation with R = - 2. The transformed region is shown: (a) after a variant (1) rod forms; (b) after a variant (2) rod forms; and (c) after a variant (3) rod forms.

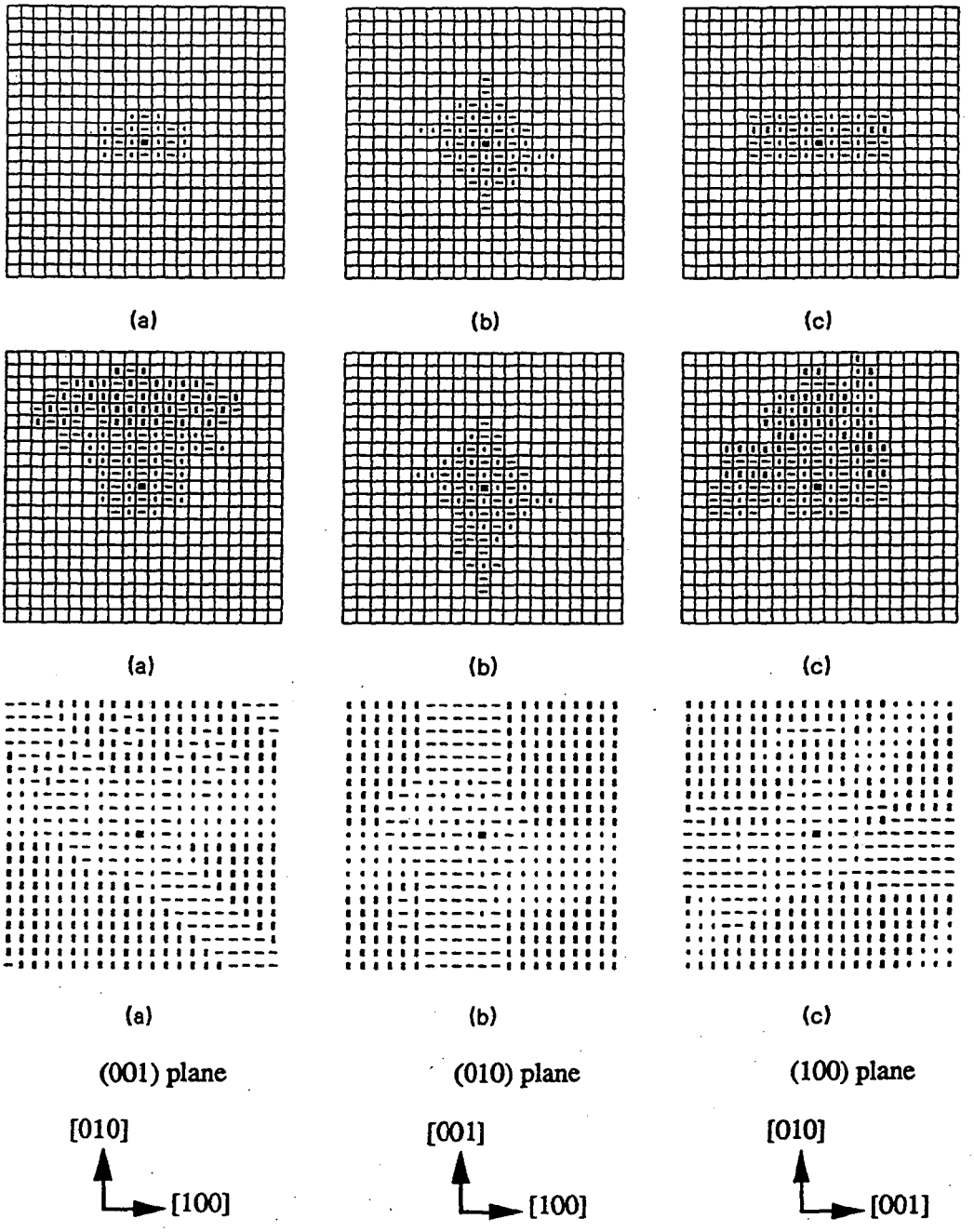

Fig. 4.5 A simulated martensitic transformation with R = 0 (pure shear). Cross-sections on the three {100} planes are shown after 200 transformation steps, 1000 steps, and completion.

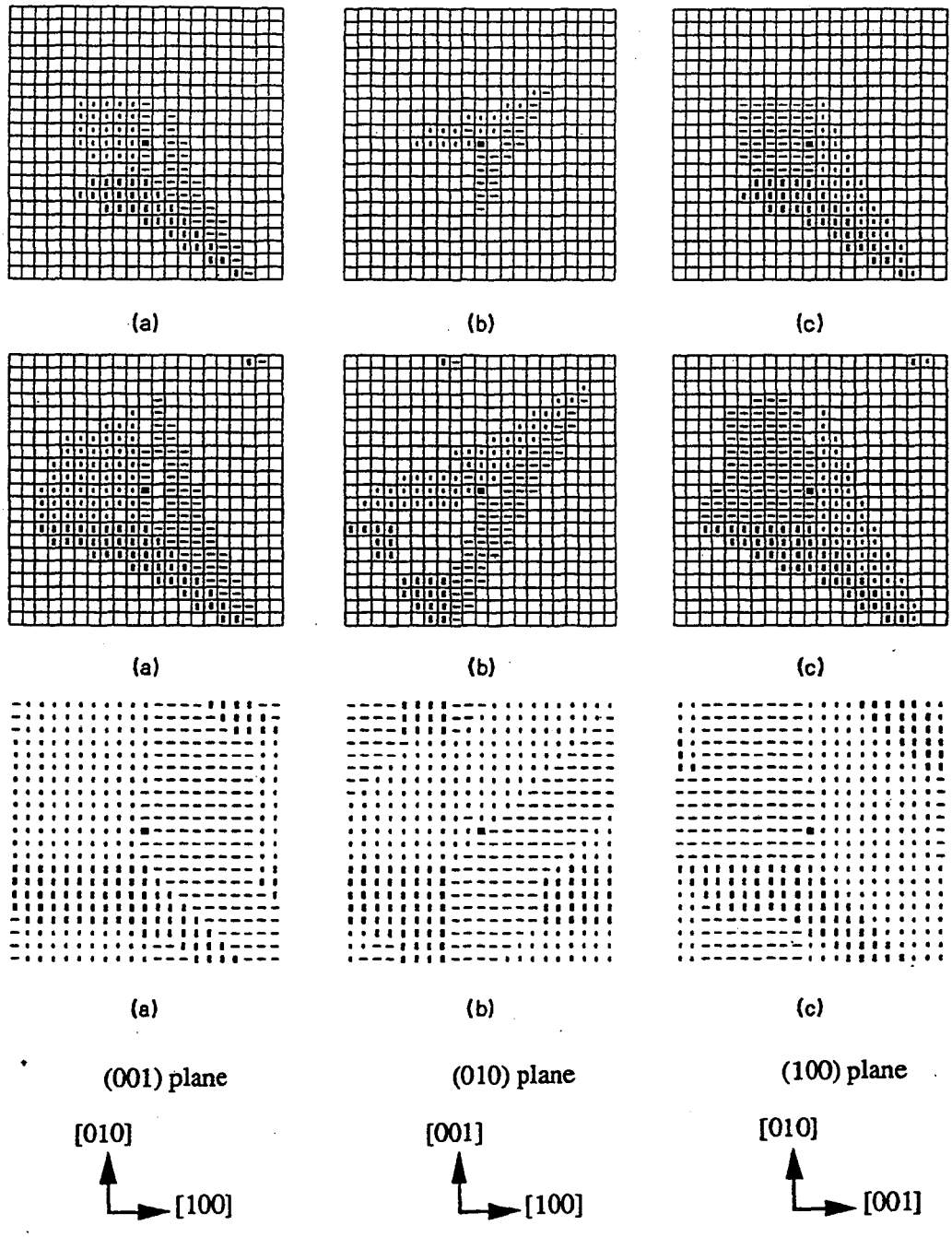

Fig. 4.6 A simulated martensitic transformation with R = 0.2. Cross-sections on the three {100} planes are shown after 1000 steps, 3000 steps and completion .

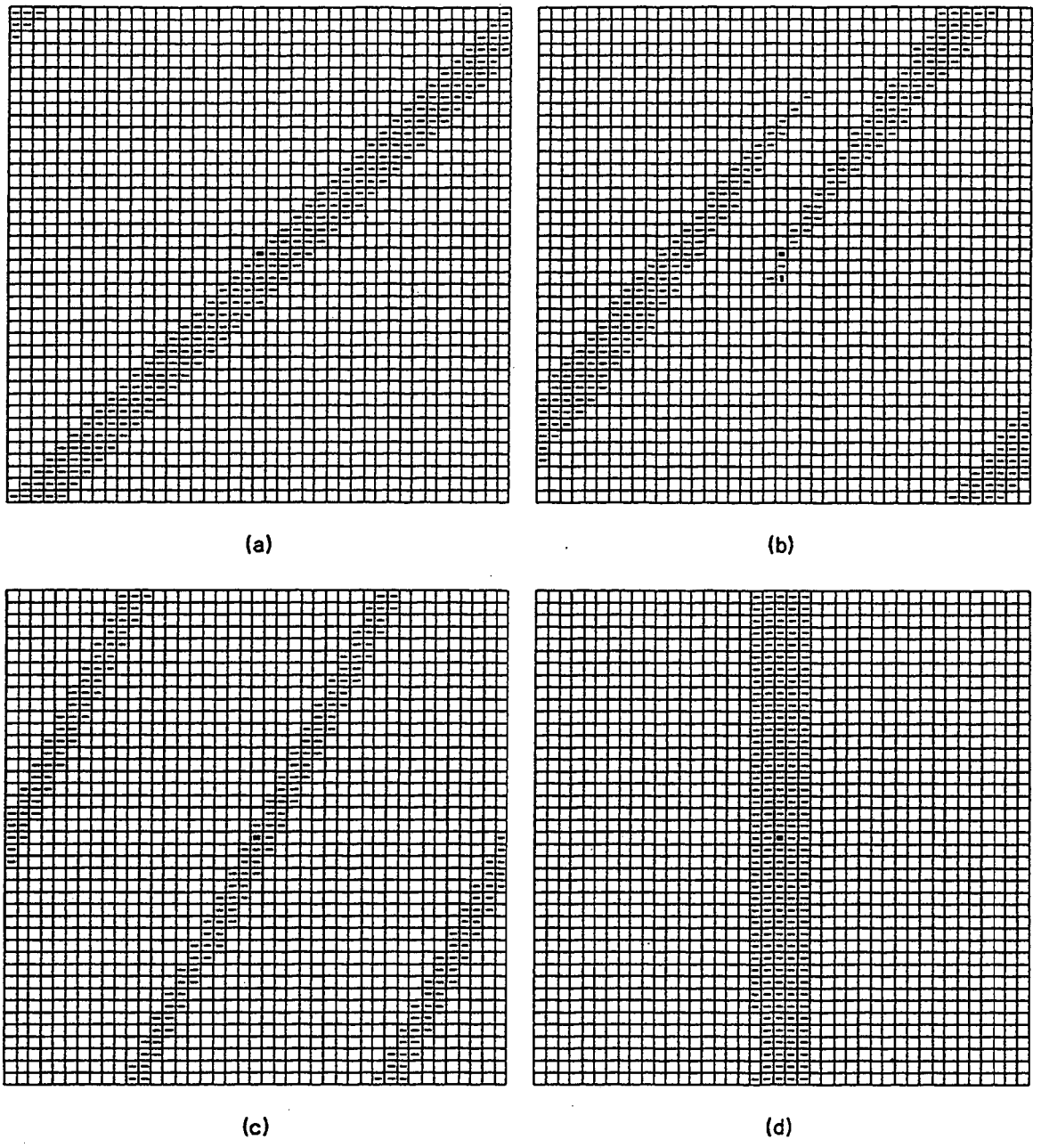

Fig. 4.7 Simulated martensitic transformations in two dimensions showing the influence of the dilation ratio (R) on the constitution and habit of the initial martensite plate: (a) R = 0, (b) R = 0.22, (c) R = 0.3, and (d) R = 1.

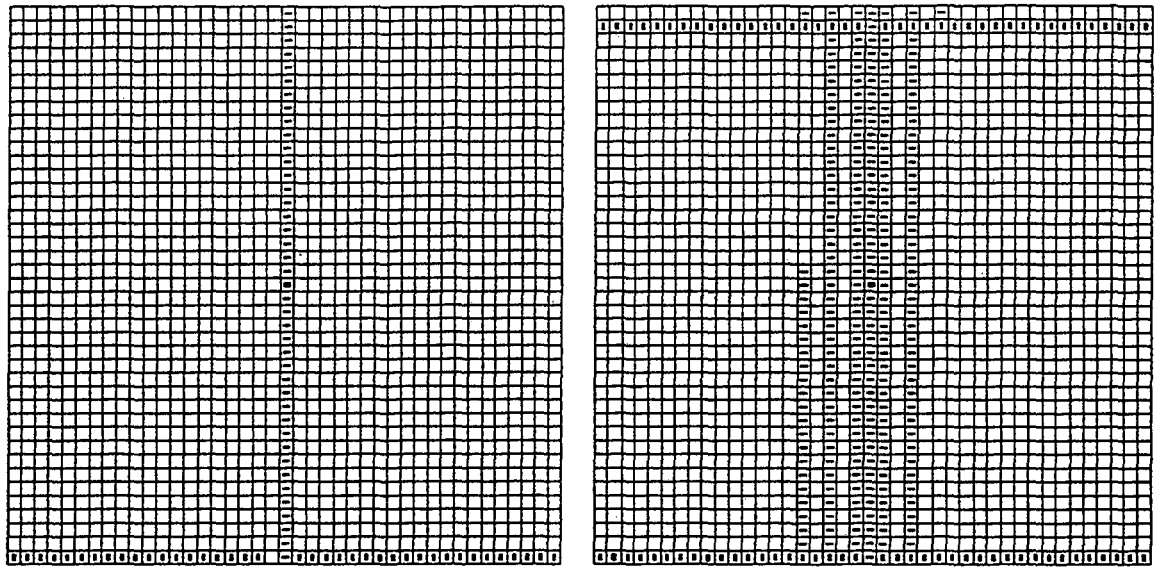

Fig. 4.8 Simulated martensitic transformation in two dimensions with R = 1.5: (a) after 80 transformation steps, (b) after 300 steps.

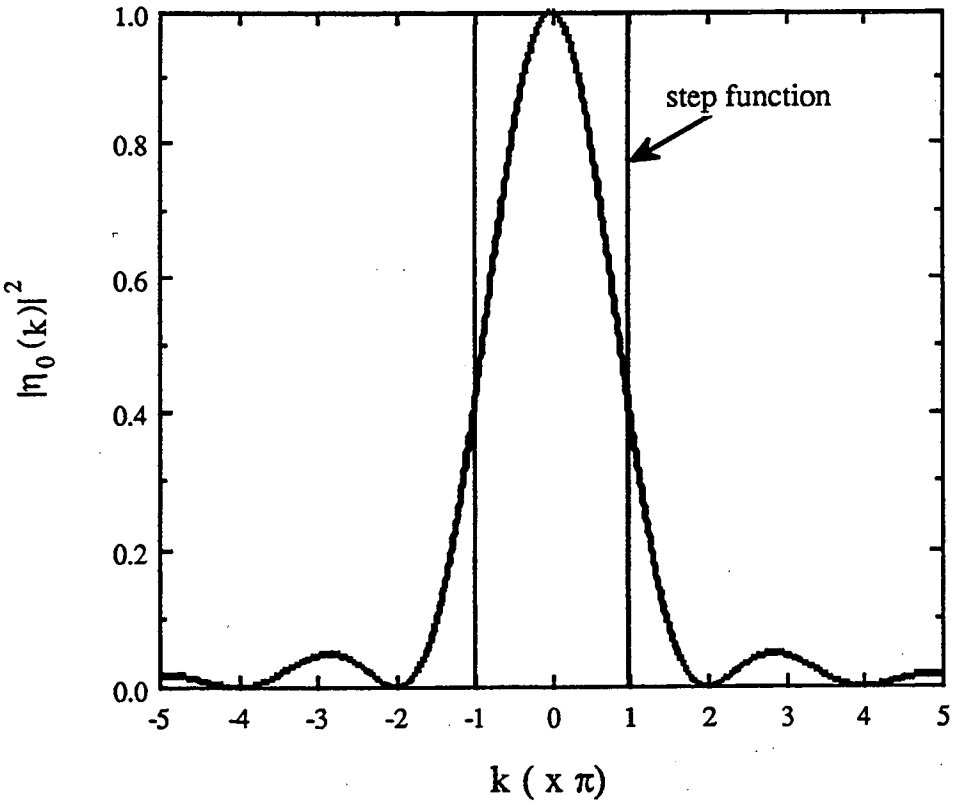

Fig. 4.9 The shape function, $|\eta_0(\mathbf{k})|^2$, and the step function of the point approximation in (10) direction of a two-dimensional space.

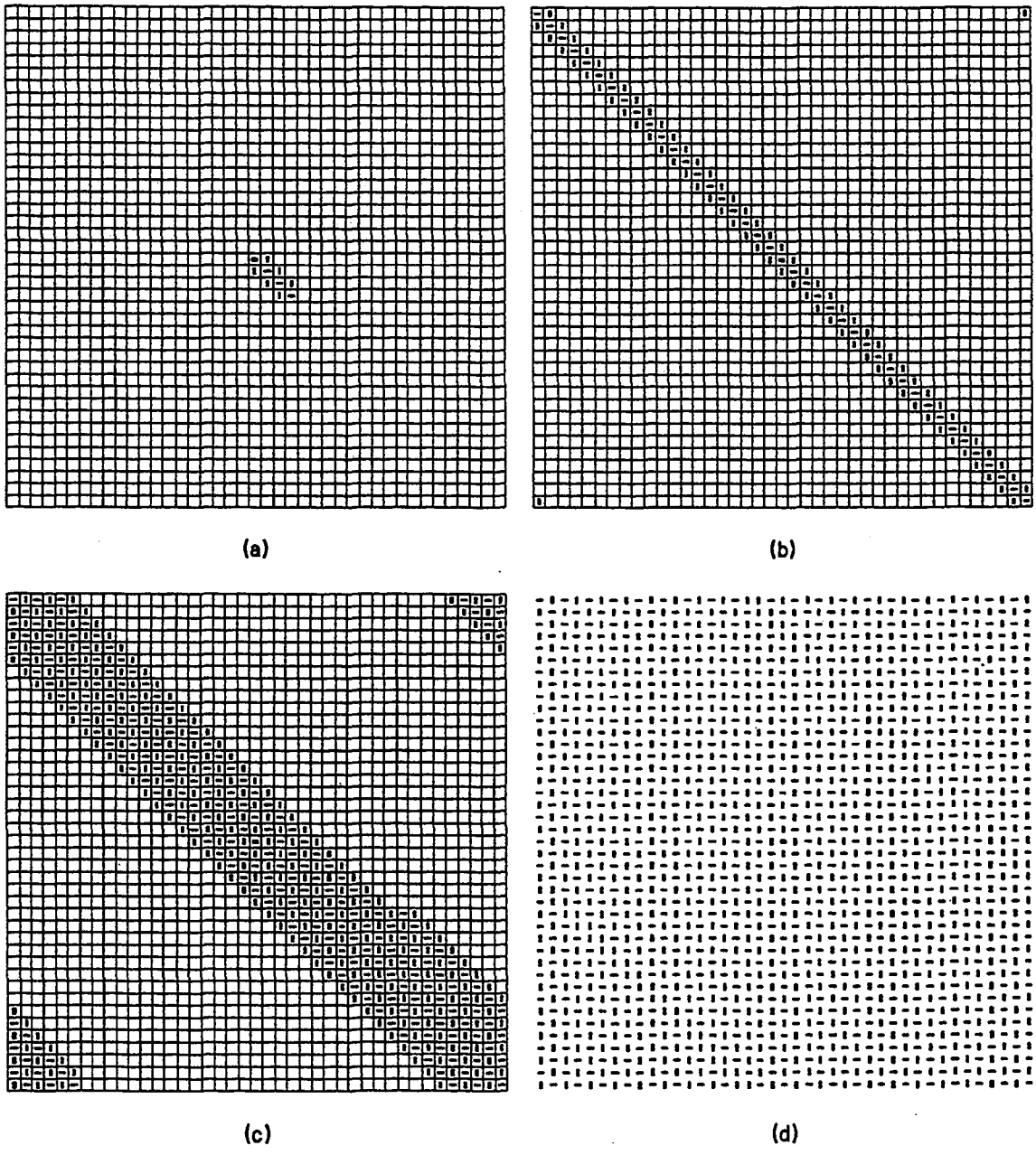

Fig. 4.10 The microstructure obtained from the simulation in two dimensions using the point approximation (R = 0).

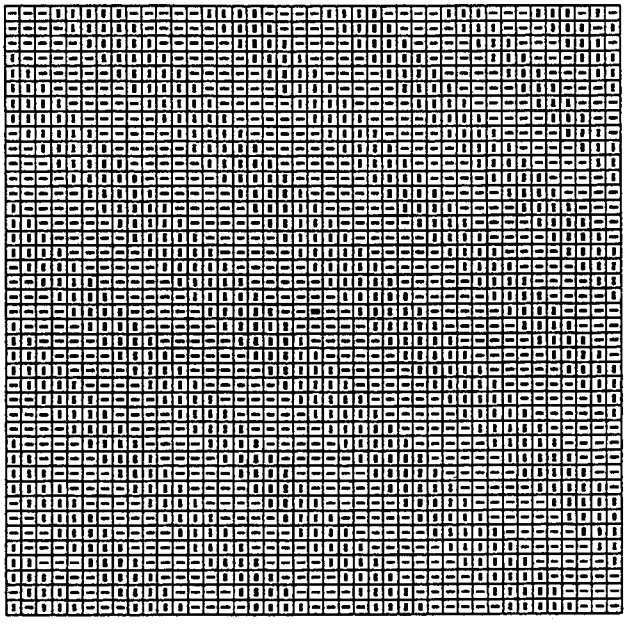

Fig. 5.1 The microstructure generated by a pure shear transformation (R = 0) in a stress-free crystal embedded in an untransformed matrix.

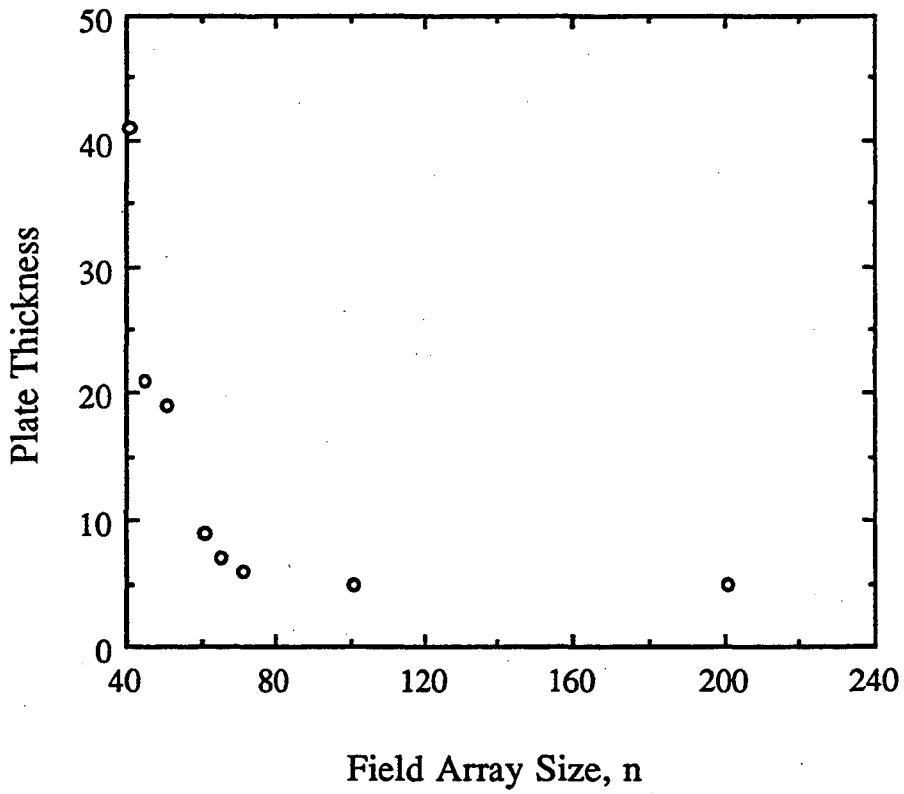

Fig. 5.2 The variation of plate thickness in a microstructure like that shown in Fig. 1 with the degree of constraint. The transformed crystal is 41 x 41; the array size is n x n.

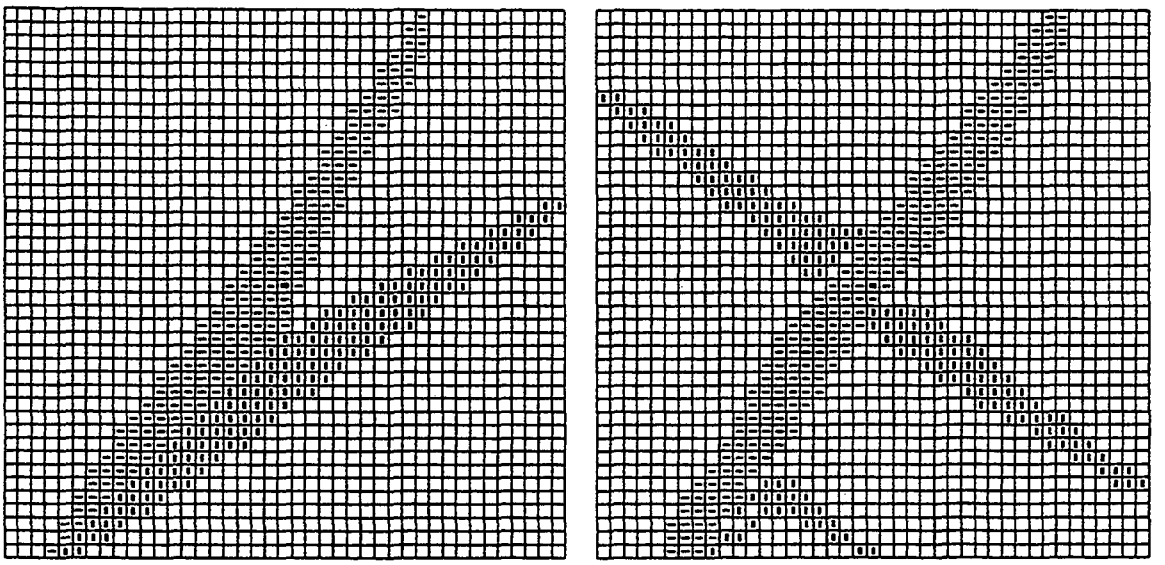

Fig. 5.3 The two common morphologies found in partially transformed crystals with $R \neq 0$: (a) the "butterfly" morphology; (b) the crossed morphology.

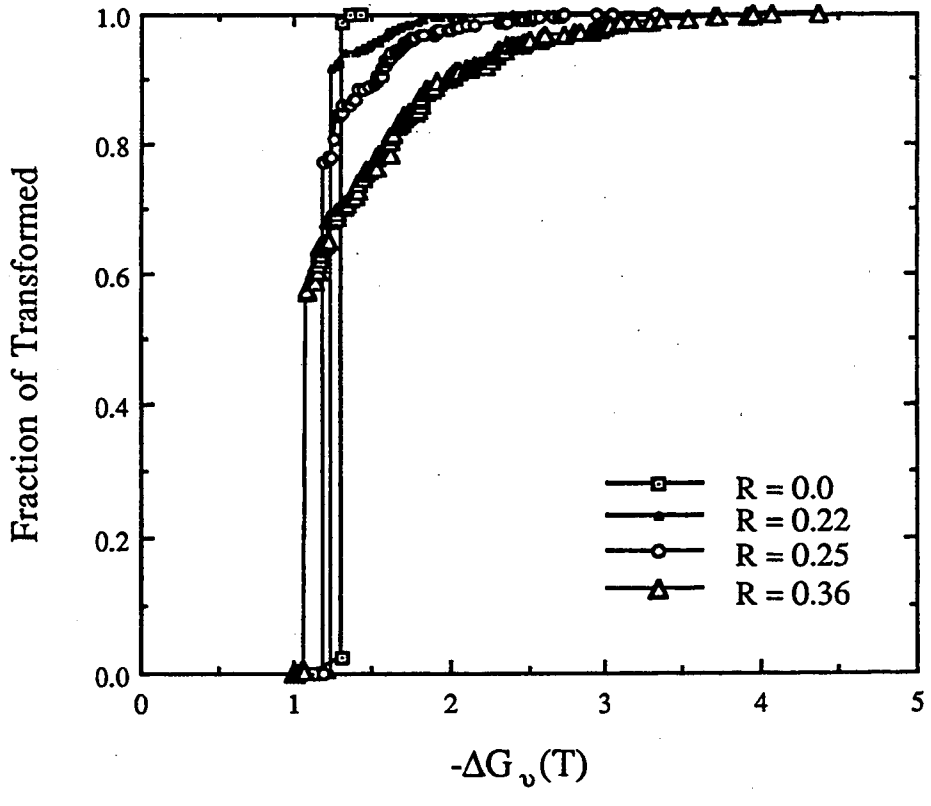

Fig. 5.4 The temperature-transformation (TT) curves for stress-free transformation at various values of the dilation ratio (R). The abscissa is plotted as ΔG_{υ}, which is approximately linear in T.

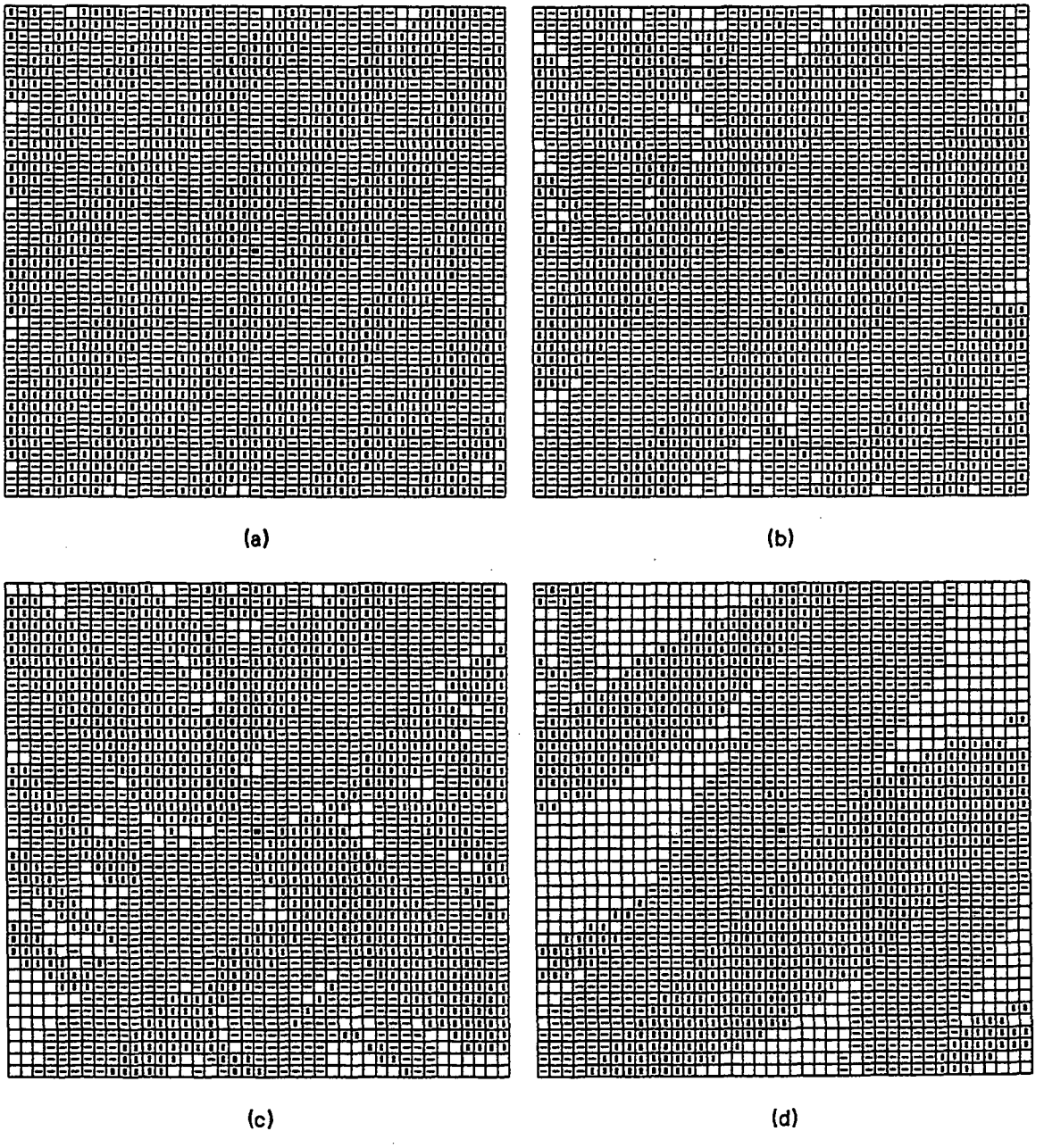

Fig. 5.5 Microstructural patterns after the burst of transformation shown in Fig. 5.4 for (a) R = 0.2, (b) R = 0.22, (c) R = 0.25, (d) R = 0.36.

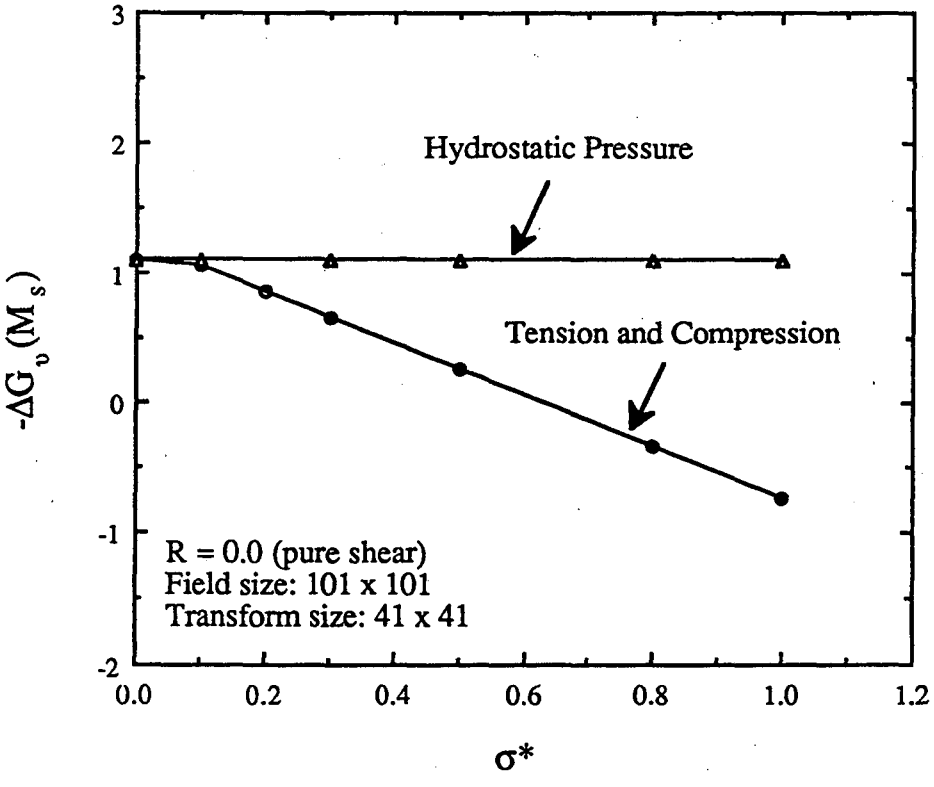

Fig. 5.6(a) The value of the driving force, ΔG_{υ}, (or, equivalently, the temperature, M_S) required to initiate transformation as a function of the dimensionless stress magnitude, σ^*, for hydrostatic stress and for uniaxial tension and compression with R = 0..

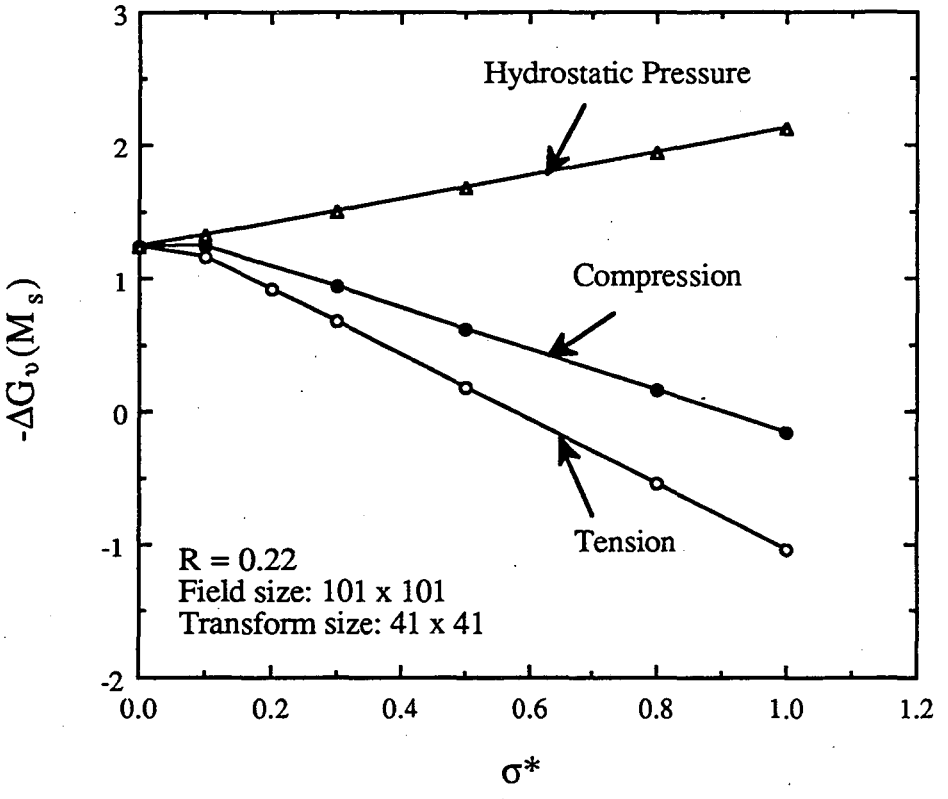

Fig. 5.6(b) The value of the driving force, ΔG_v, (or, equivalently, the temperature, M_S) required to initiate transformation as a function of the dimensionless stress magnitude, σ^*, for hydrostatic stress and for uniaxial tension and compression with R = 0.22.

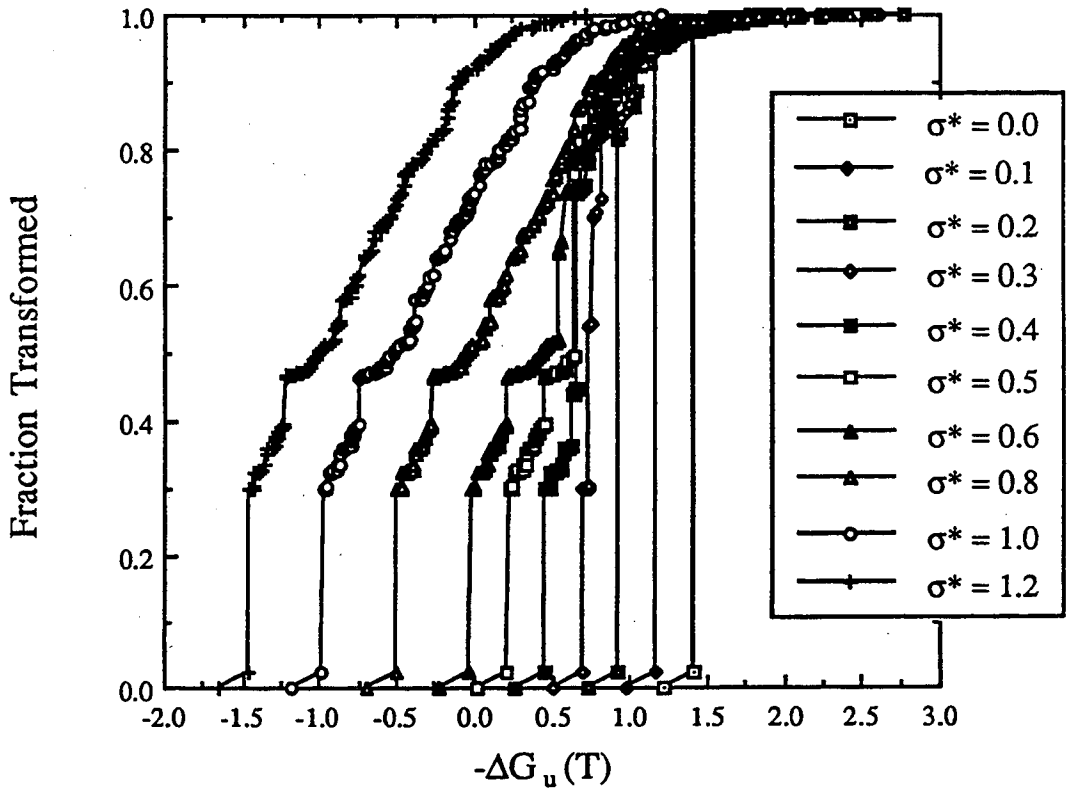

Fig. 5.7 Temperature-transformation (TT) curves for a transformation with R = 0.2 for various values of the applied stress.

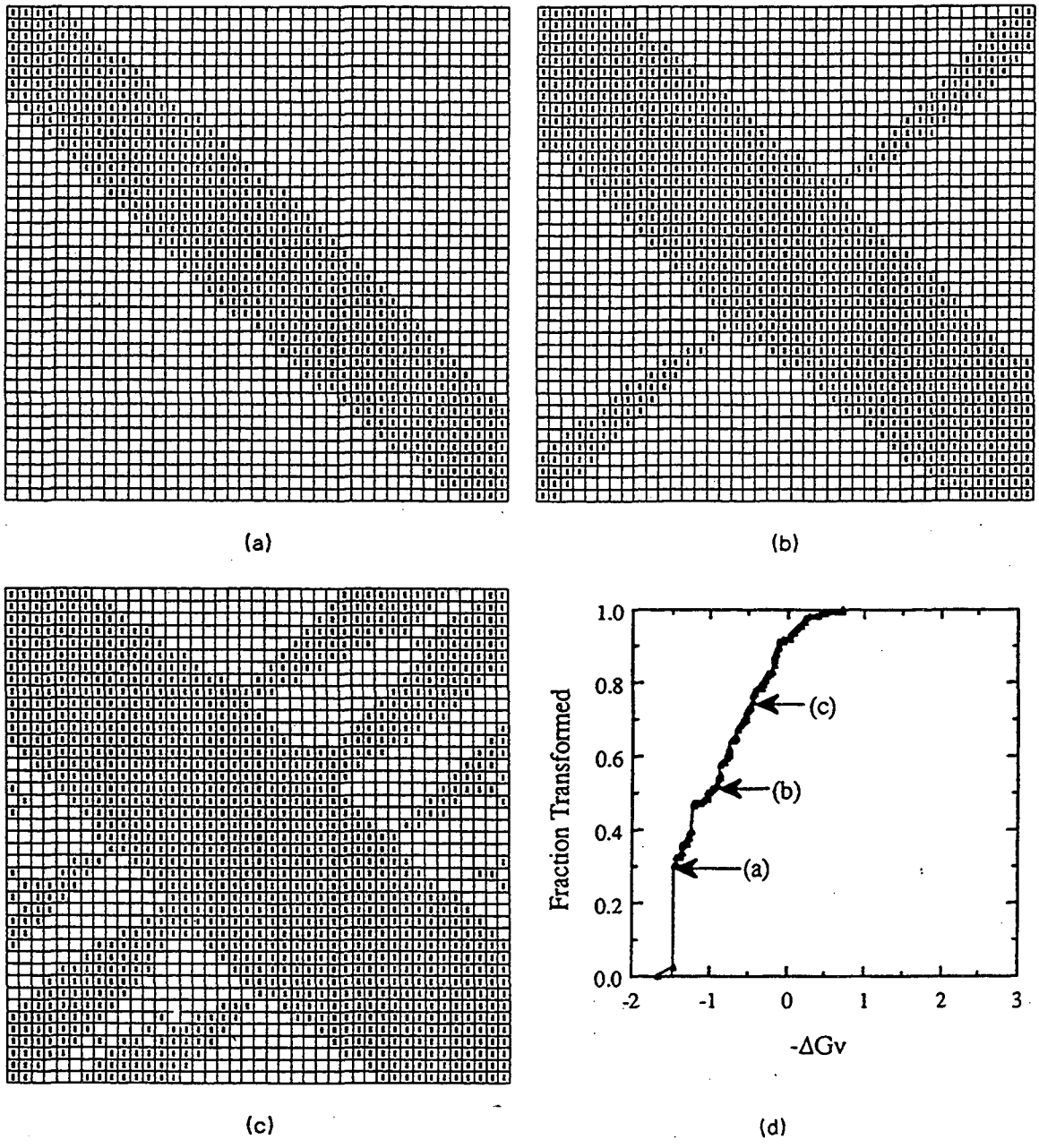

Fig. 5.8 The pattern of transformation in the high-stress limit ($\sigma^* = 1.2$) for R = 0.2. The TT curve is plotted in (d); (a) - (c) show the microstructures that correspond to the corresponding points labeled in (d).

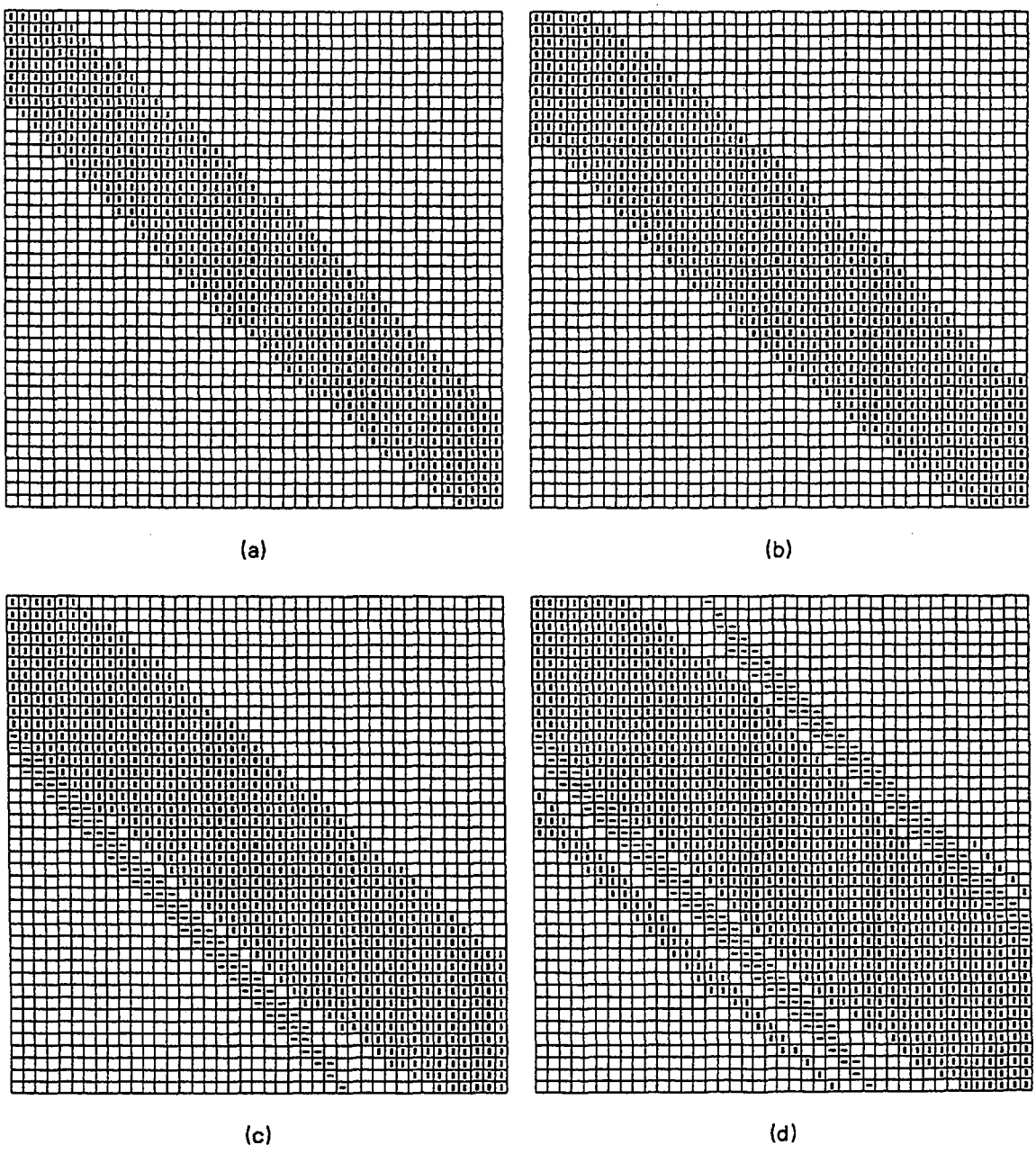

Fig. 5.9 The pattern of transformation at intermediate stress ($\sigma^* = 0.4$) for R = 0.2. The TT curve is plotted in (h); (a) - (g) show the microstructures that correspond to the corresponding points labeled in (h).

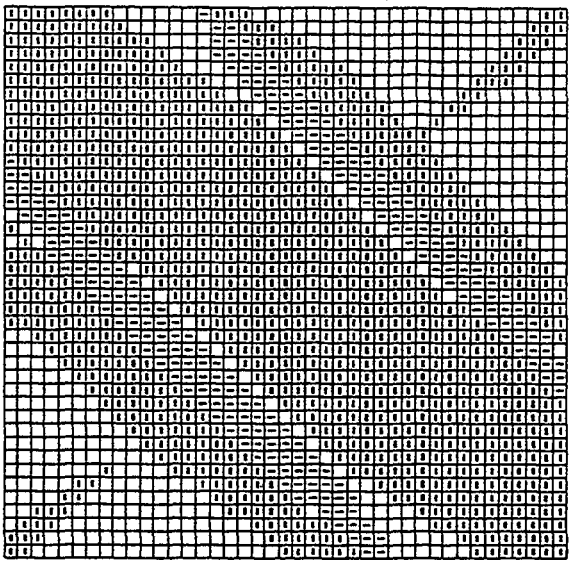

(e)

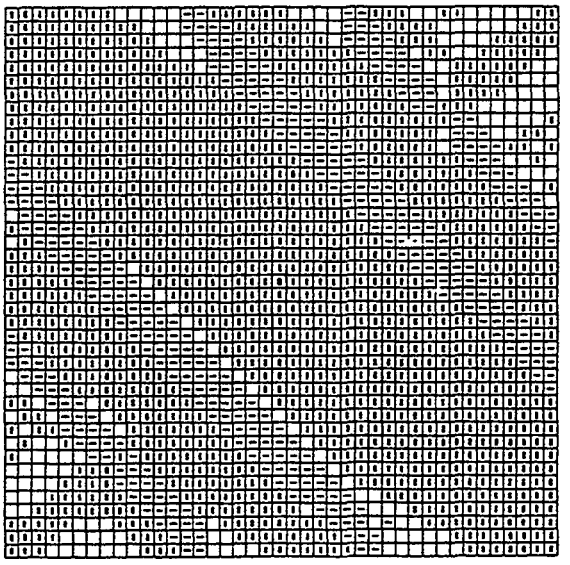

(f)

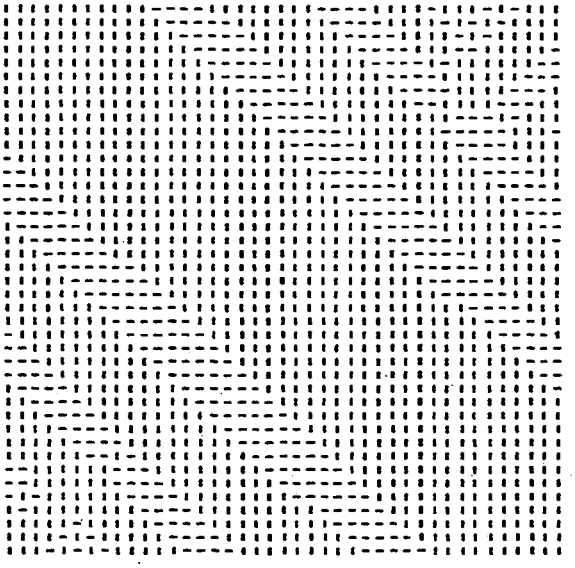

(g)

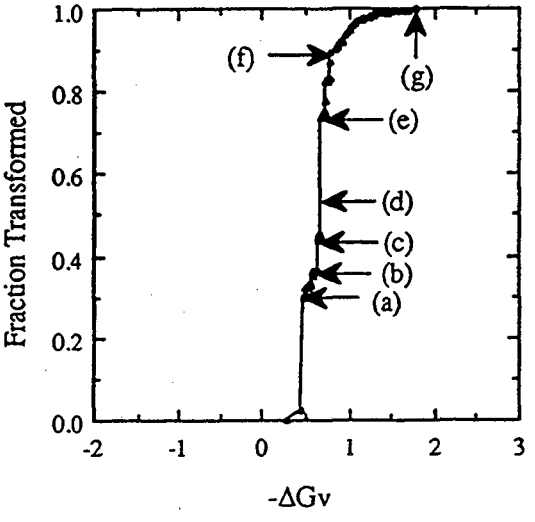

(h)

Fig. 5.9(Cont.) The pattern of transformation at intermediate stress ($\sigma^* = 0.4$) for R = 0.2. The TT curve is plotted in (h); (a) - (g) show the microstructures that correspond to the corresponding points labeled in (h).

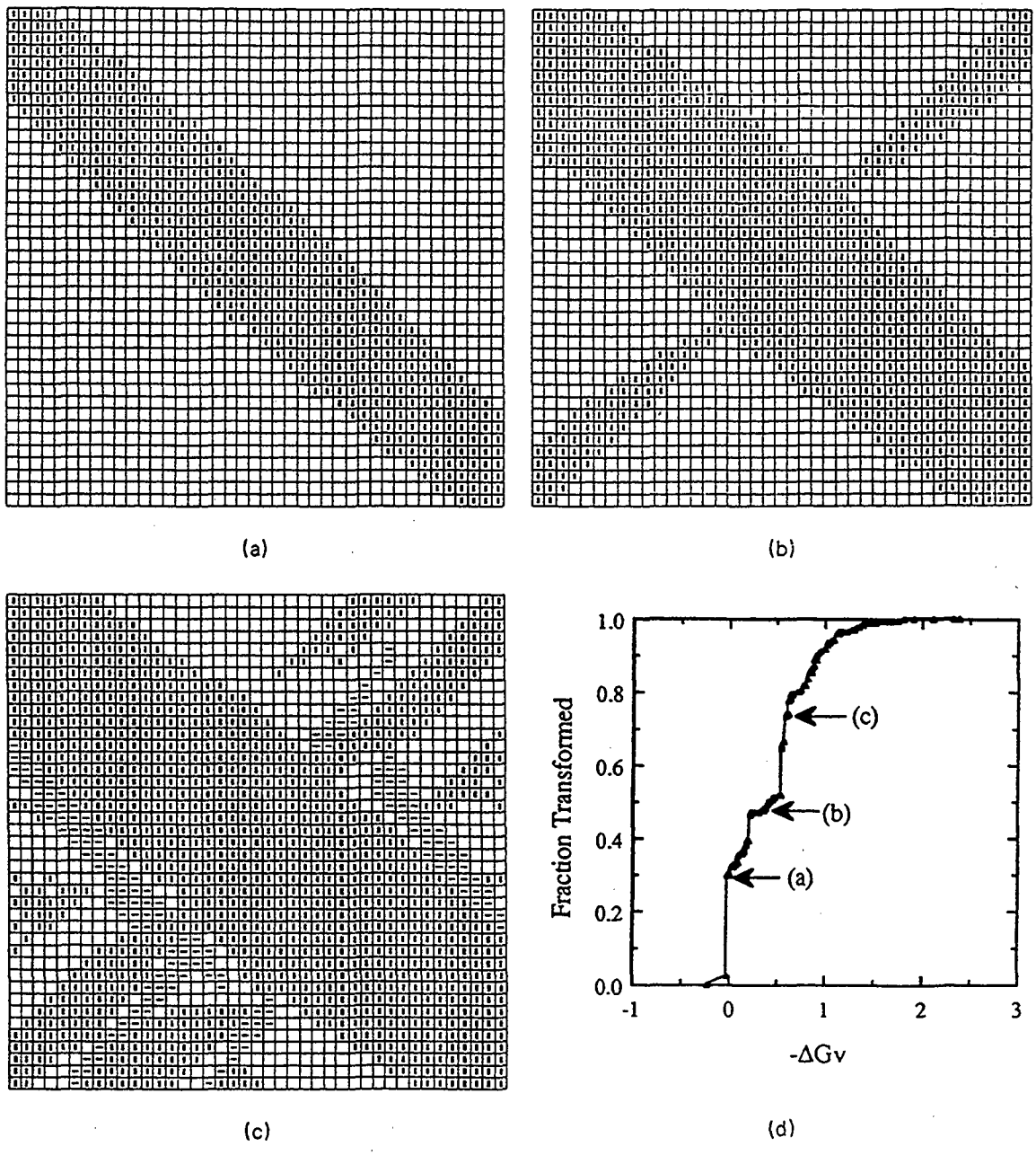

Fig. 5.10 The pattern of transformation at intermediate stress ($\sigma^* = 0.6$) for R = 0.2. The TT curve is plotted in (d); (a) - (c) show the microstructures that correspond to the corresponding points labeled in (d)

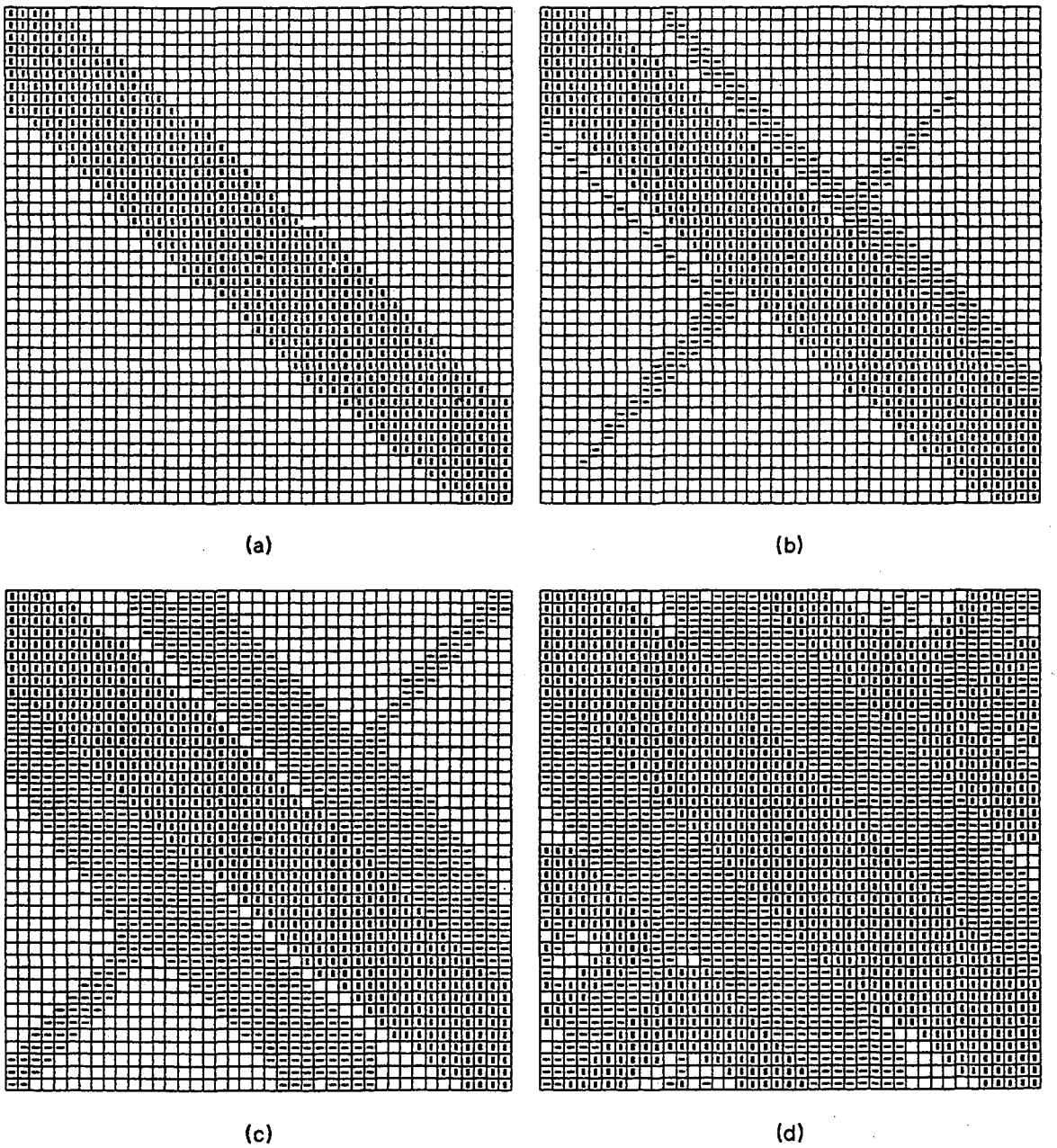

Fig. 5.11 Simulated martensitic transformation under a cyclic load with a constrained boundary condition, a fixed driving force ($\Delta G_0 = -0.265\ E_0$) and R = 0.2: (a) $\sigma^* = 0.5$ (max. load); (b) $\sigma^* = 0$; (c) $\sigma^* = -0.5$ (min. load); and (d) the final microstructure when the transformation stops after several cycles.

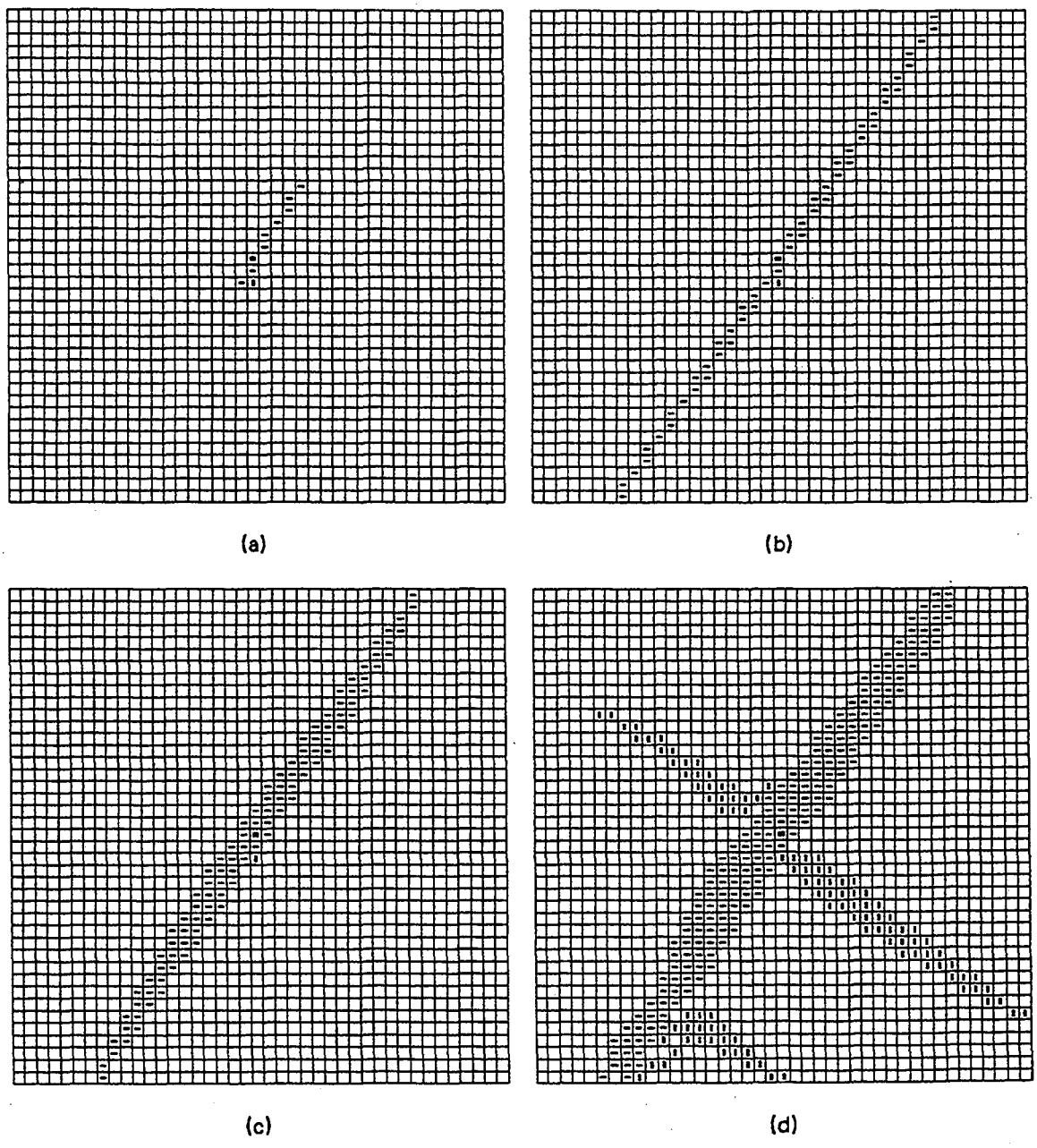

Fig. 6.1 The microstructural evolution generated by a simulated irreversible transformation (R = 0.25) during cooling process.

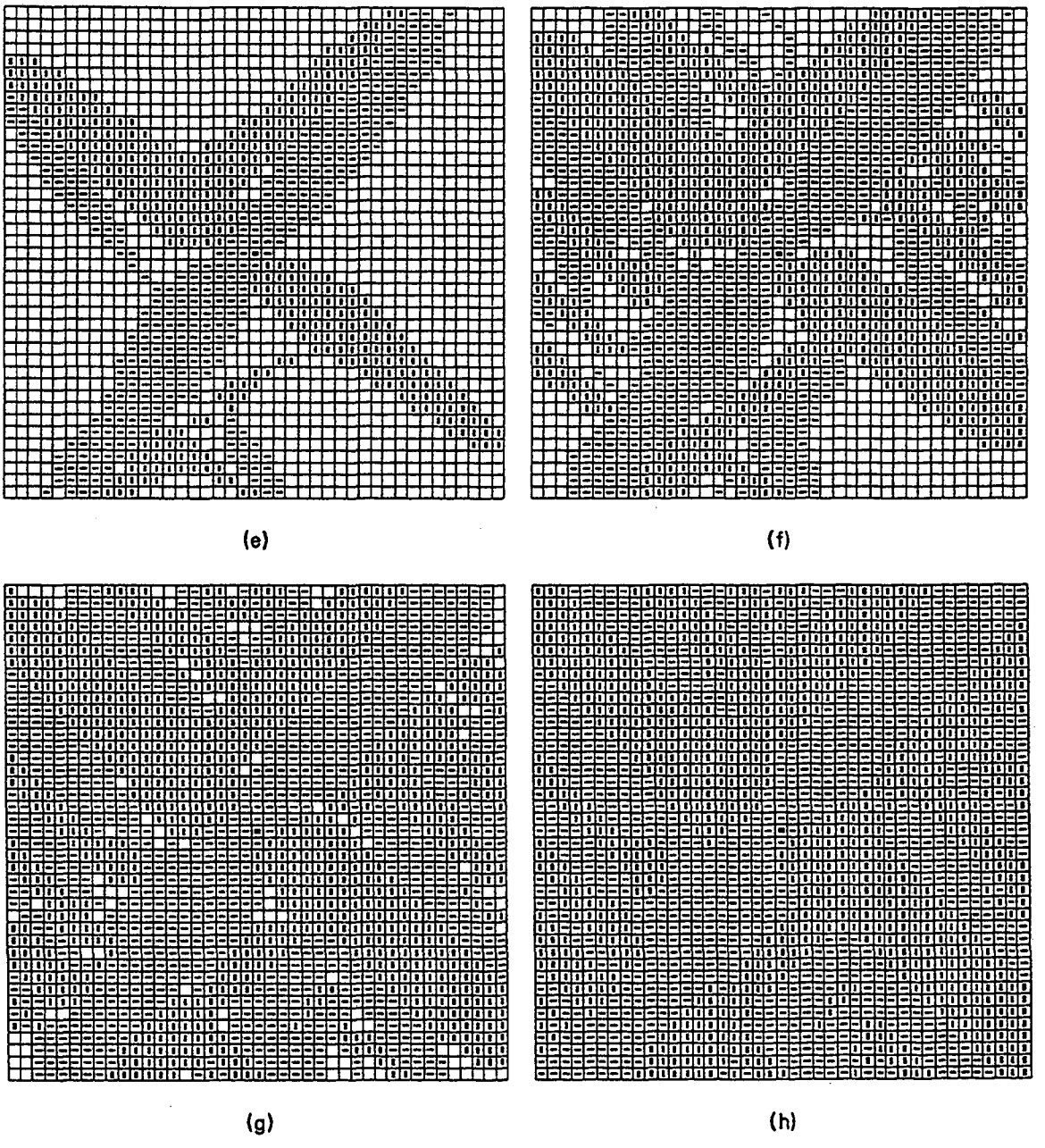

Fig. 6.1(Cont.) The microstructural evolution generated by a simulated irreversible transformation (R = 0.25) during cooling process.

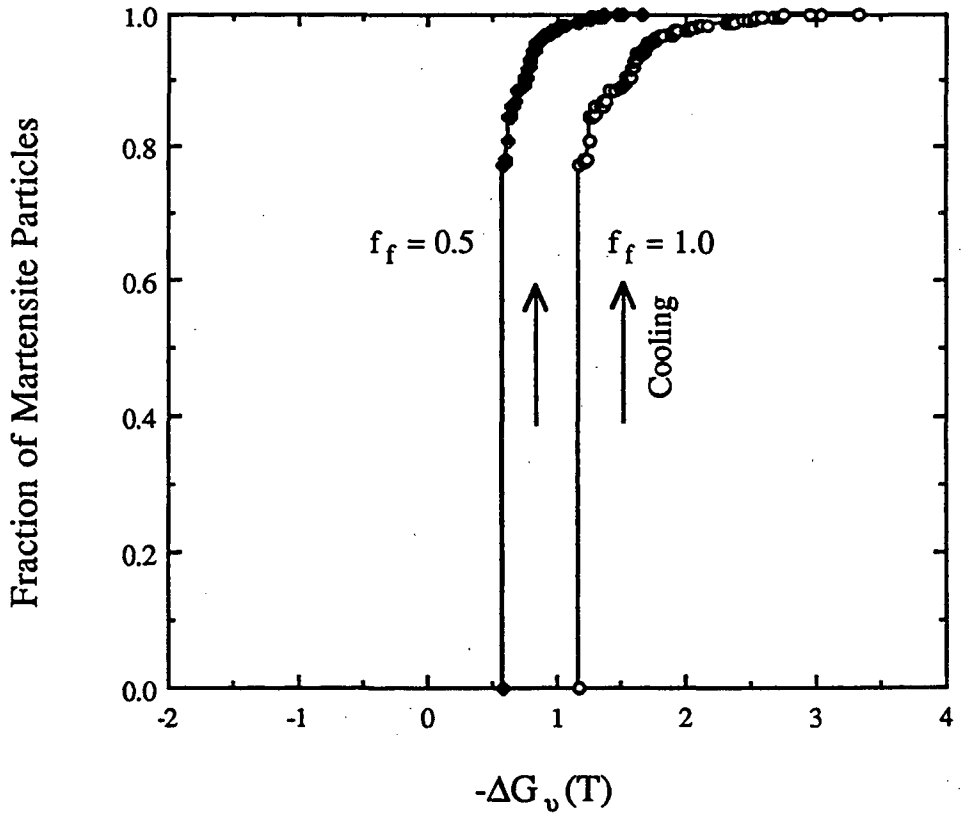

Fig. 6.2 The temperature-transformation (TT) curves of irreversible transformations (R = 0.25) with two different values of f_f.

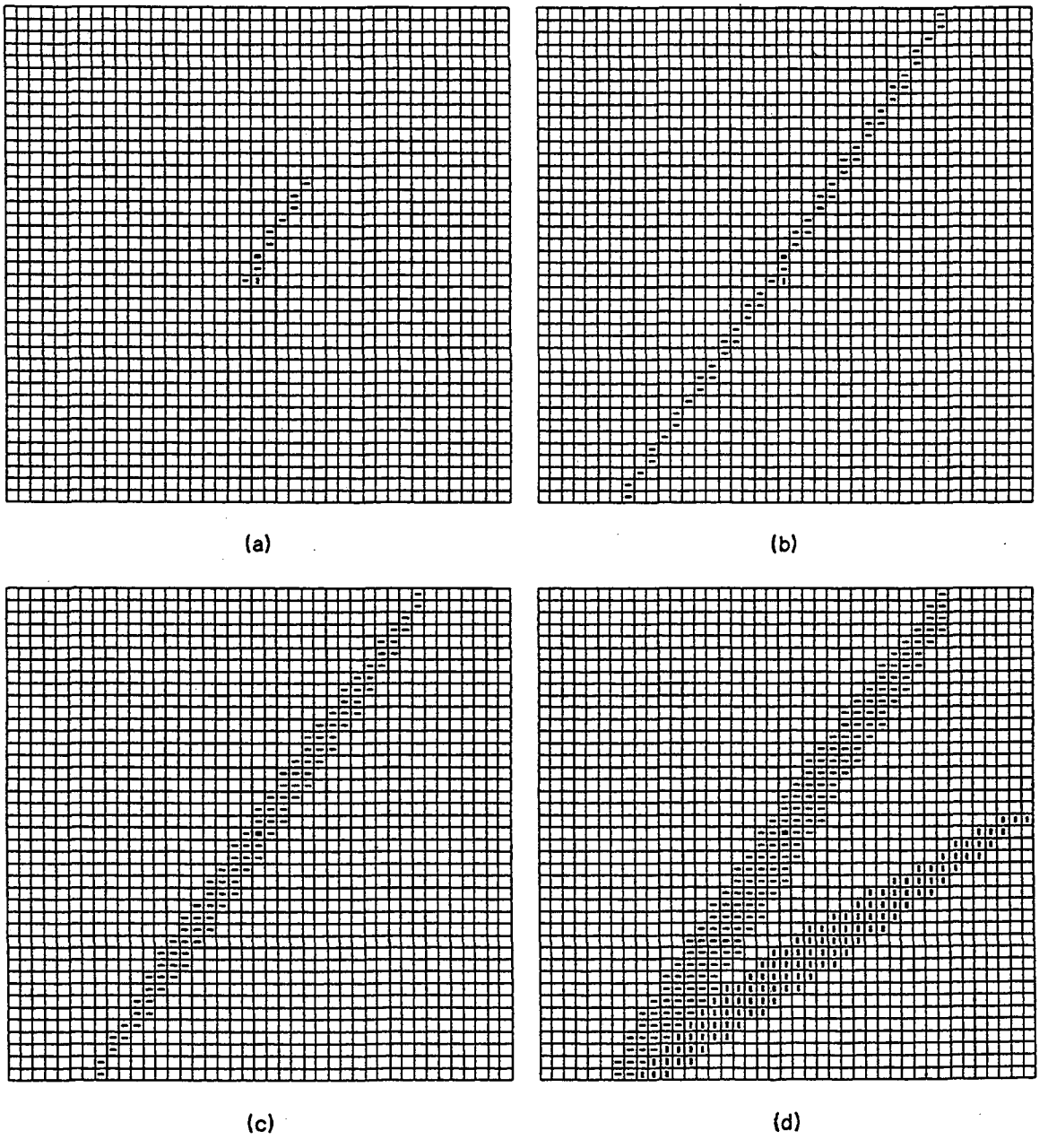

Fig. 6.3 The microstructural evolution generated by a simulated reversible transformation ($f_r = 1$, $R = 0.25$) during cooling process.

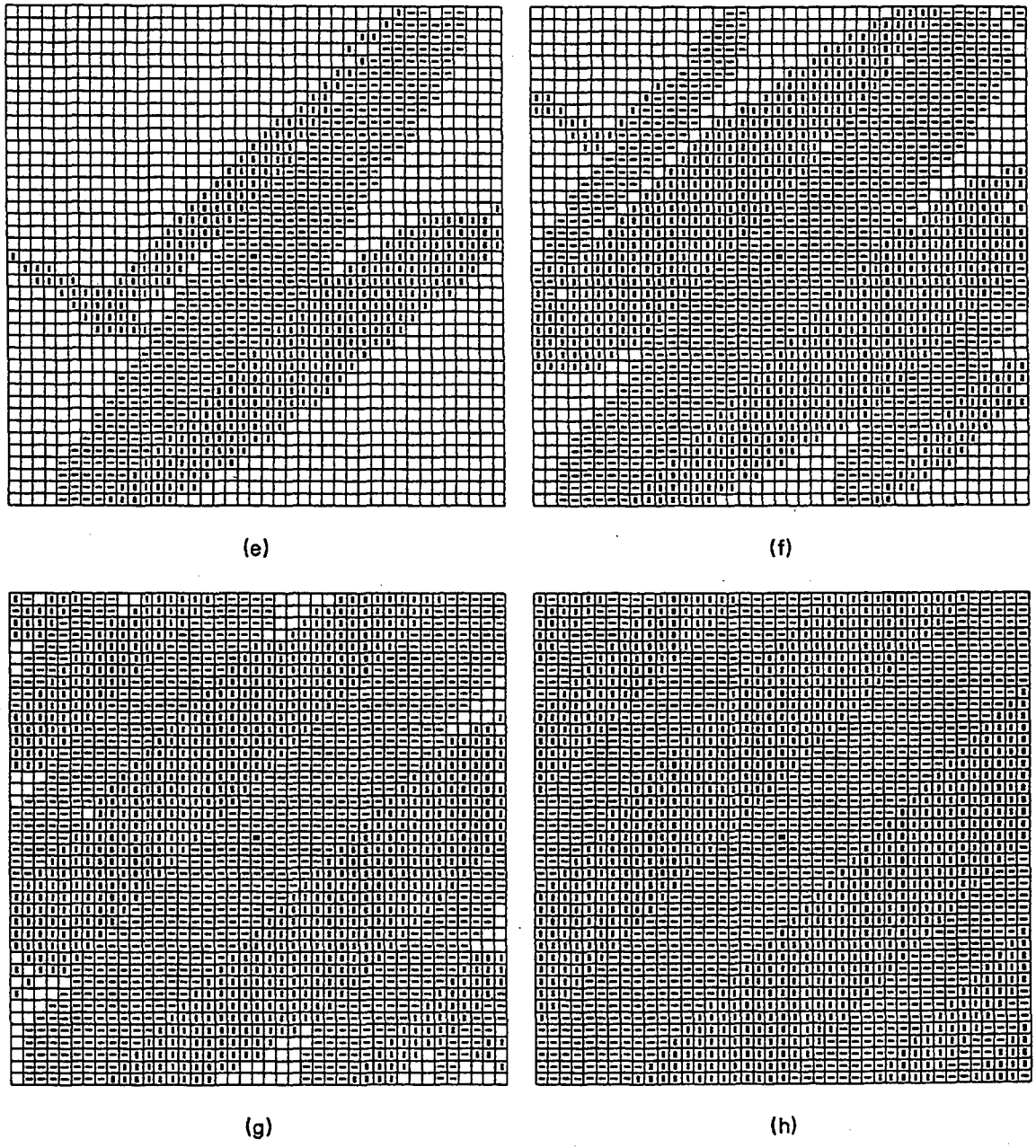

Fig. 6.3(Cont.) The microstructural evolution generated by a simulated reversible transformation ($f_r = 1$, $R = 0.25$) during cooling process.

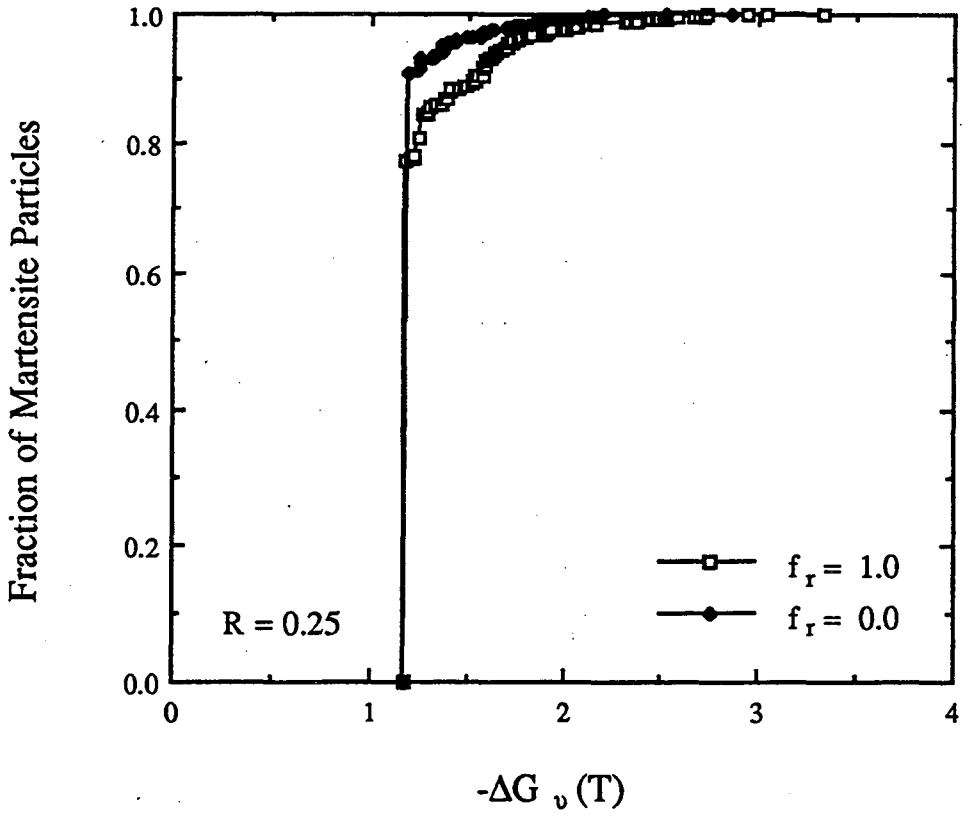

Fig. 6.4 The temperature-transformation (TT) curves for the reversible and irreversible transformations shown in Fig. 6.1 and Fig. 6.3.

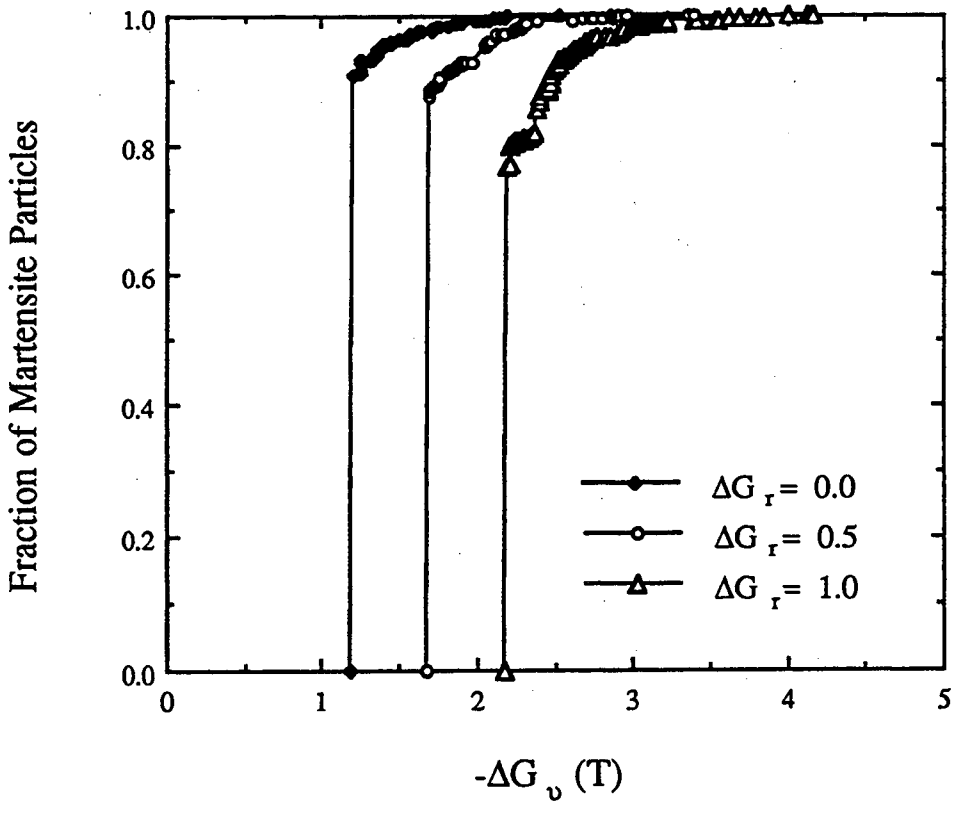

Fig. 6.5 The temperature-transformation (TT) curves for reversible transformations ($f_r = 1$, $R = 0.25$) with three different values of forward frictional resistance ΔG_r.

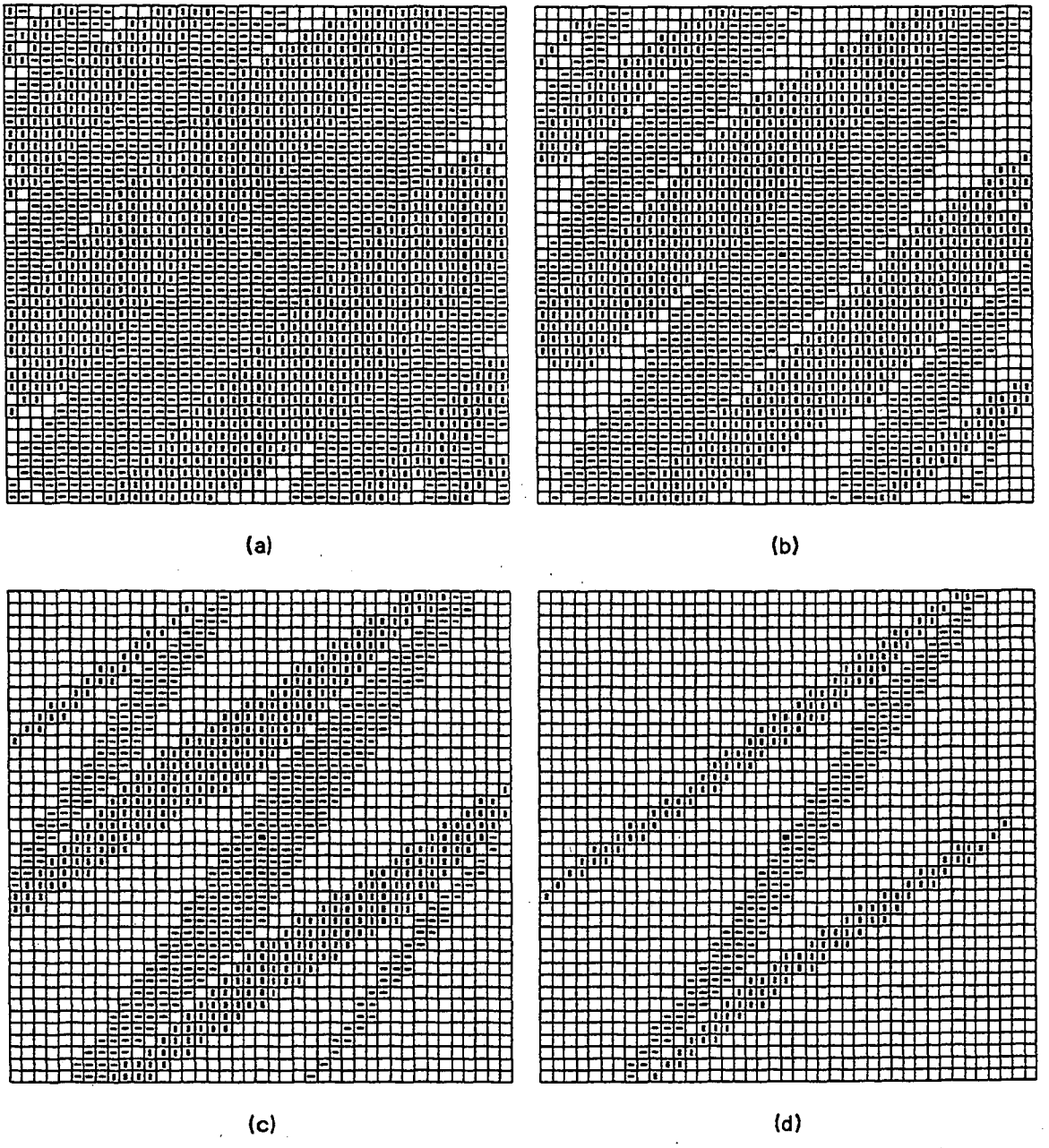

Fig. 6.6 The microstructural evolution generated by a simulated reversible transformation ($f_r = 1$, $R = 0.25$) during heating process.

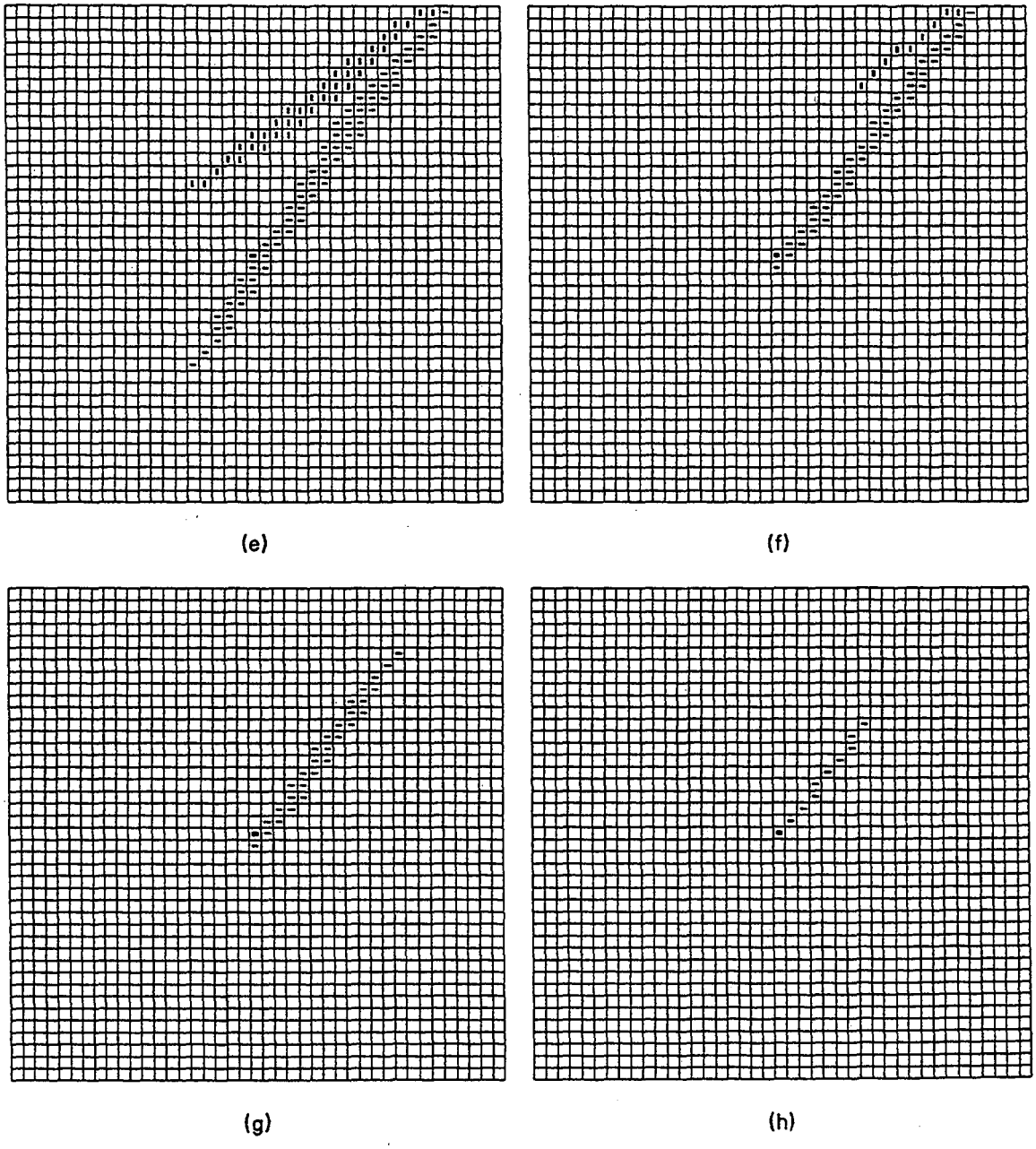

Fig. 6.6(Cont.) The microstructural evolution generated by a simulated reversible transformation ($f_r = 1$, $R = 0.25$) during heating process.

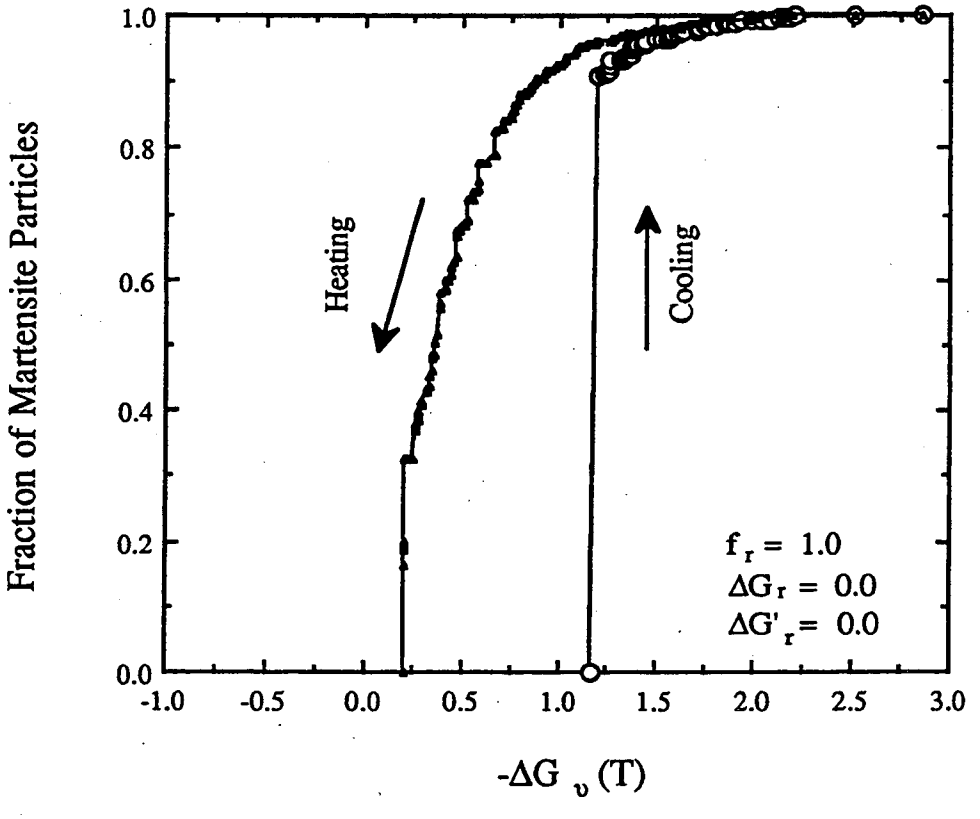

Fig. 6.7 The temperature-transformation (TT) curve of a cooling-heating cycle for a reversible transformation (R = 0.25) with $f_r = 1$.

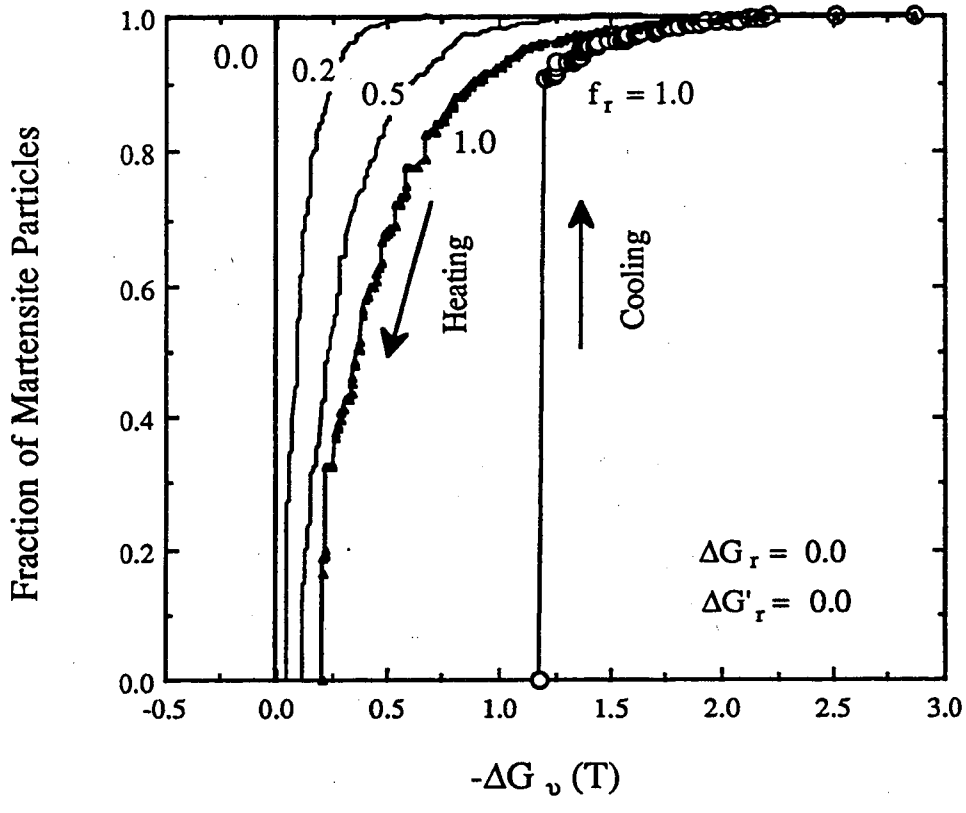

Fig. 6.8 The temperature-transformation (TT) curves of reversible transformations (R = 0.25) with different values of f_r.

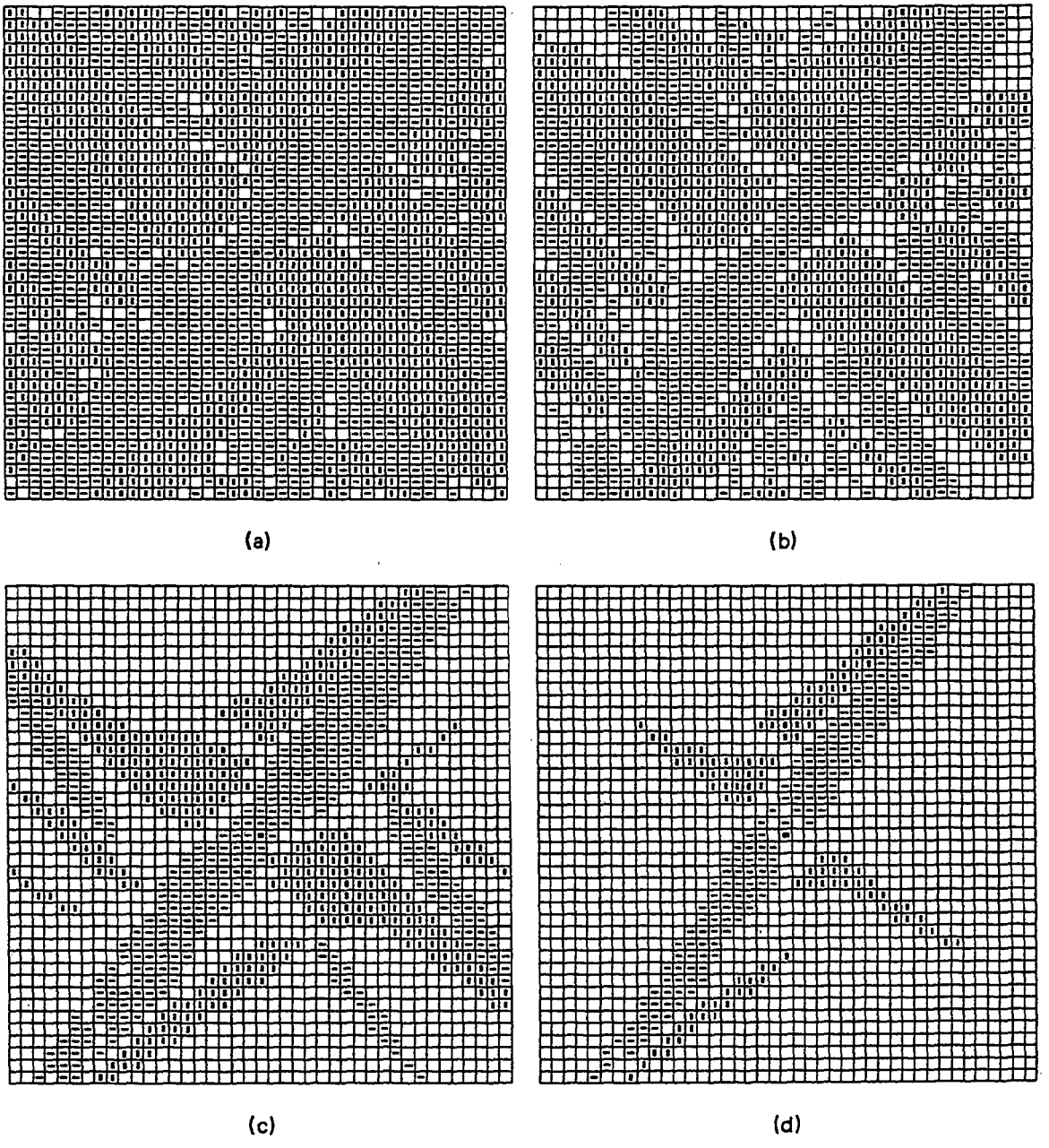

Fig. 6.9 The microstructural evolution generated by a simulated reversible transformation ($f_r = 0.2$, $R = 0.25$) during heating process.

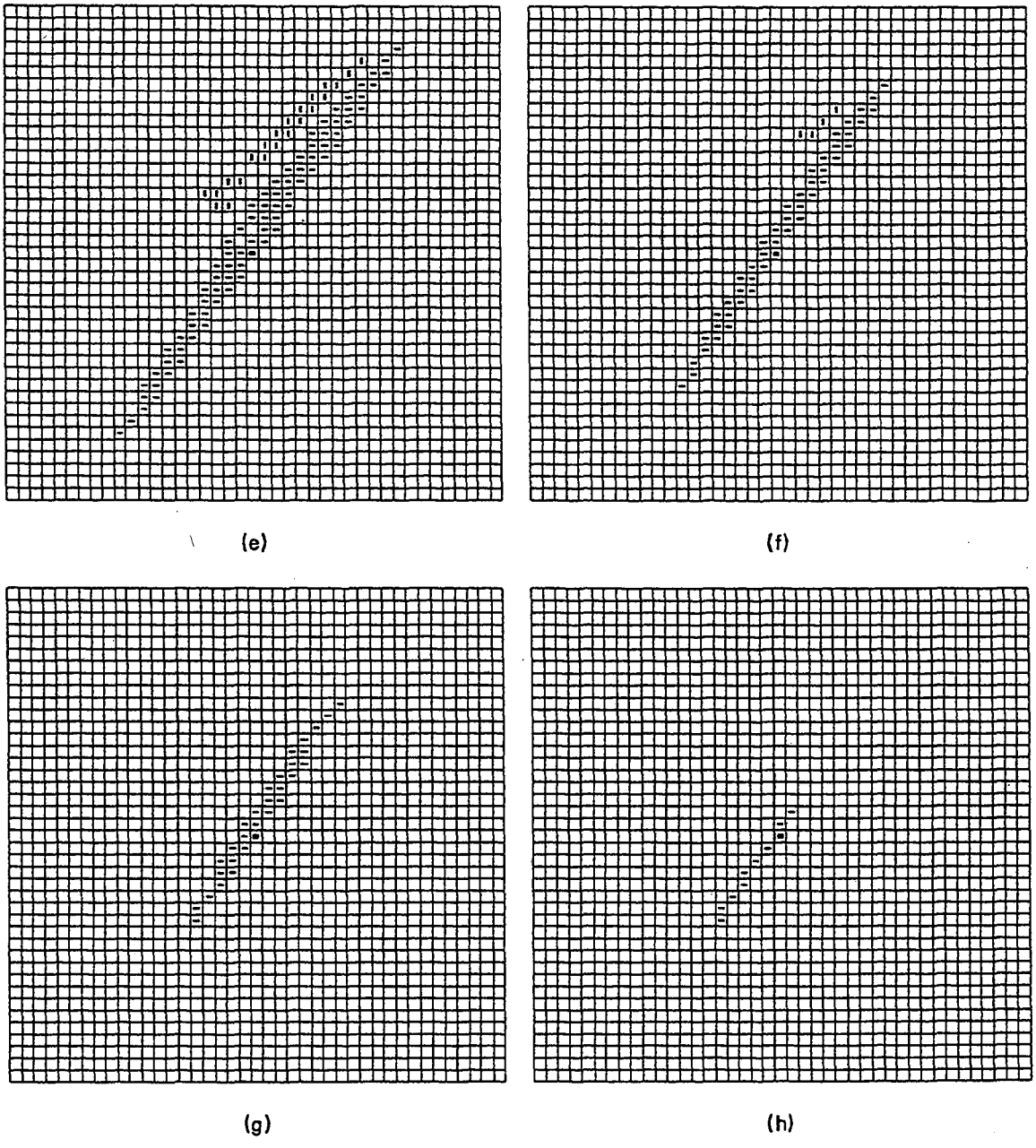

Fig. 6.9(Cont.) The microstructural evolution generated by a simulated reversible transformation ($f_r = 0.2$, $R = 0.25$) during heating process.

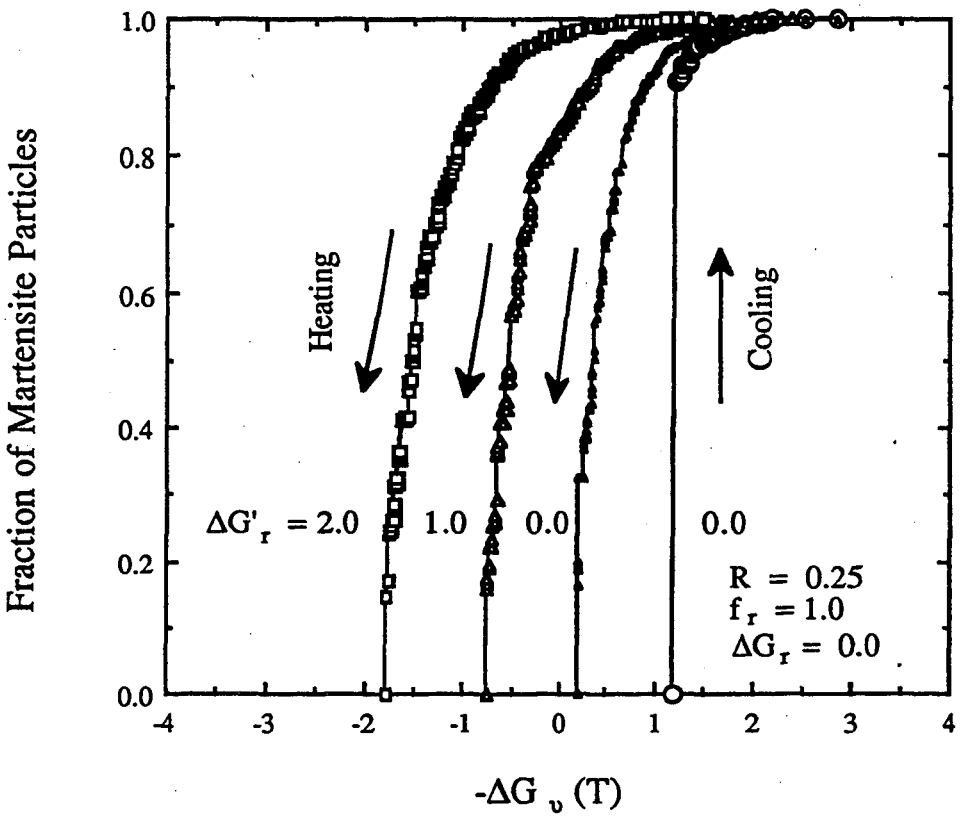

Fig. 6.10(a) The temperature-transformation (TT) curves for reversible transformations (R = 0.25) during heating with different values of reverse frictional resistance ΔG_r when $f_r = 1$.

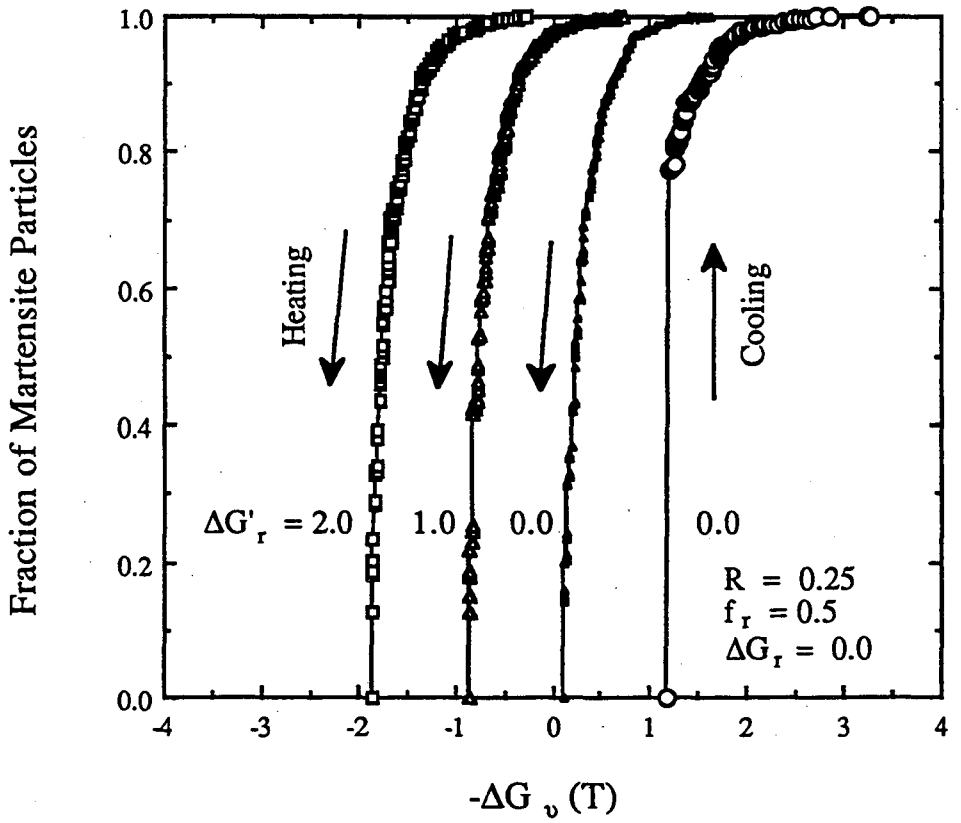

Fig. 6.10(b) The temperature-transformation (TT) curves for reversible transformations (R = 0.25) during heating with different values of reverse frictional resistance ΔG_r when $f_r = 0.5$.

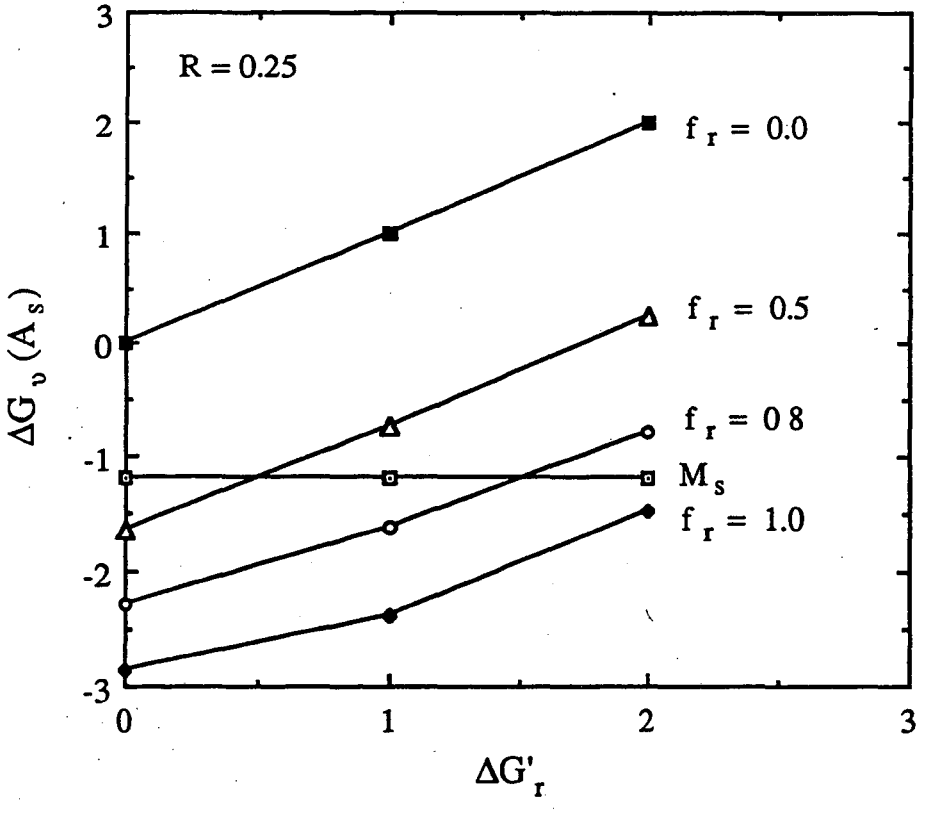

Fig. 6.11(a) The effects of the reversibility, f_r, and reverse frictional resistance, ΔG_r, on A_S, the starting temperature of the reversion of martensite.

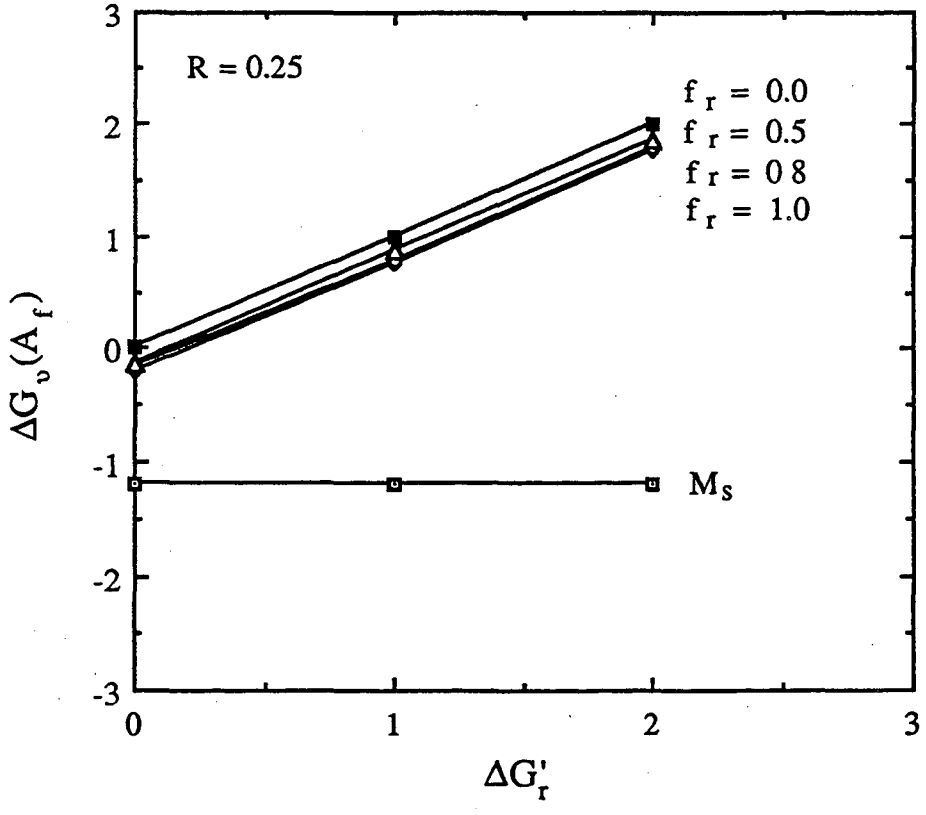

Fig. 6.11(b) The effects of the reversibility, f_r, and reverse frictional resistance, $\Delta G_r'$, on A_f, the finishing temperature of the reversion of martensite.

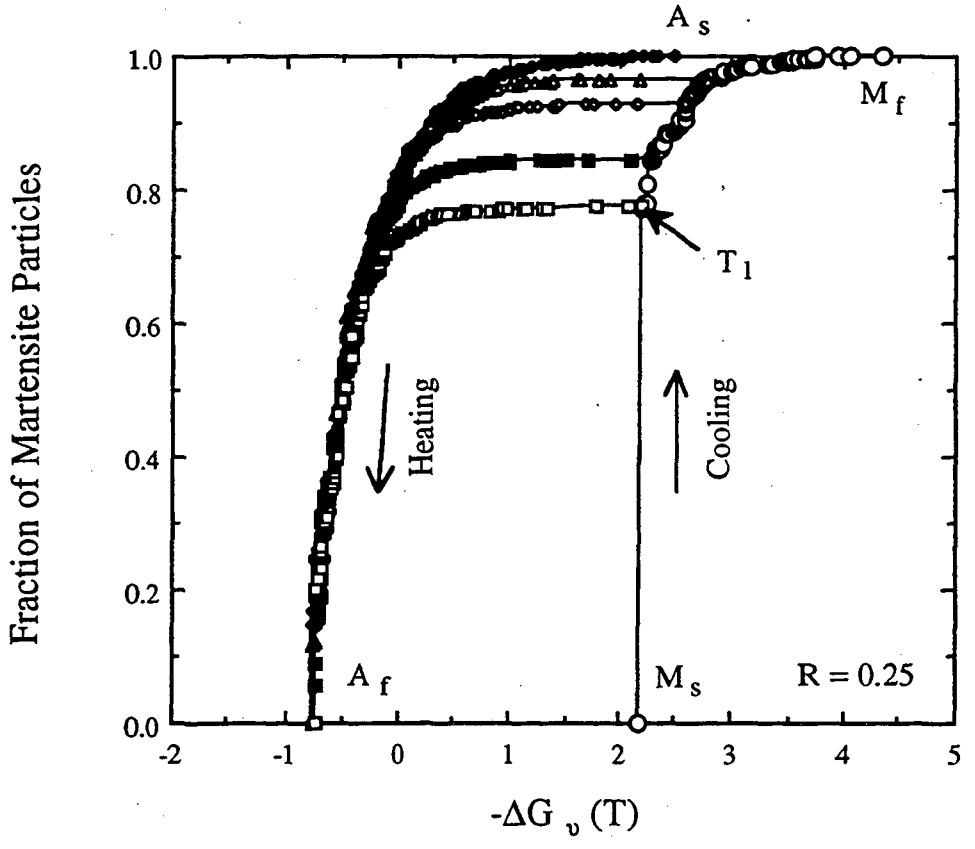

Fig. 6.12(a) The temperature-transformation (TT) curves for partial transformations (R = 0.25) with $f_r = 1$, and $\Delta G_r = \Delta G_r = 1$.

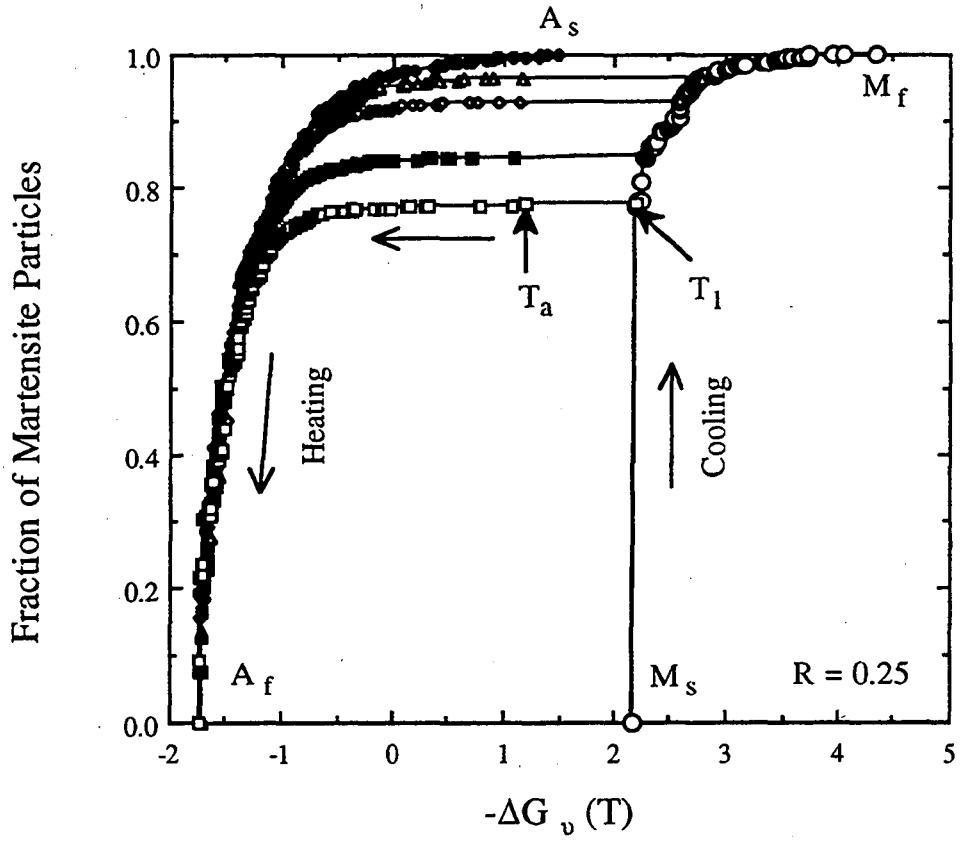

Fig. 6.12(b) The temperature-transformation (TT) curves for partial transformations (R = 0.25) with $f_r = 1$, $\Delta G_r = 1$, and $\Delta G_r' = 2.0$.

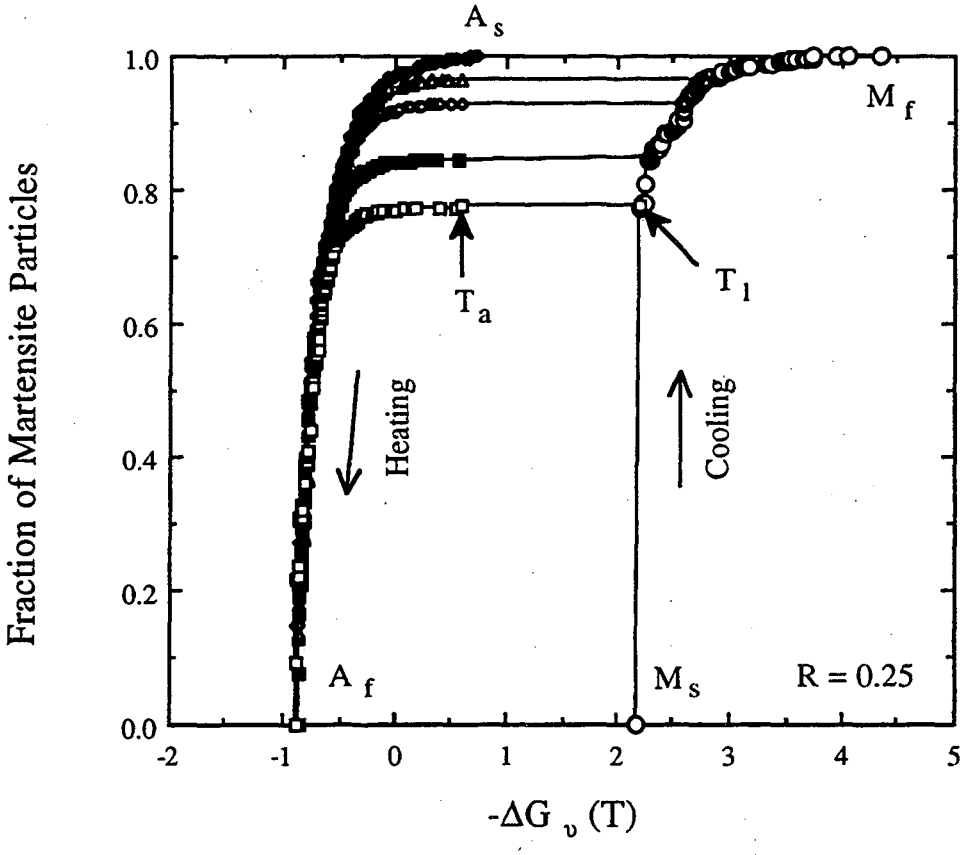

Fig. 6.12(c) The temperature-transformation (TT) curves for partial transformations (R = 0.25) with $f_r = 0.5$, and $\Delta G_r = \Delta G_r = 1$.

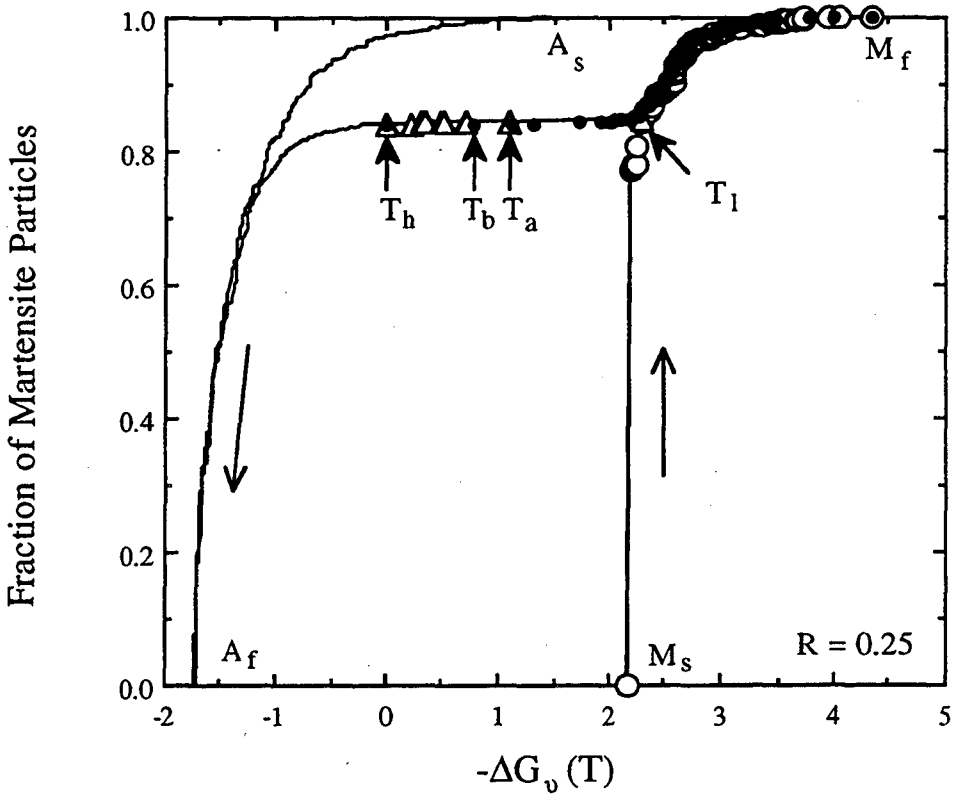

Fig. 6.13(a) The temperature-transformation (TT) curves for a partial reversion with $f_r = 1$, $\Delta G_r = 1.0$ and $\Delta G_r = 2.0$ when the amount of reversed martensite is less than 1% (R = 0.25).

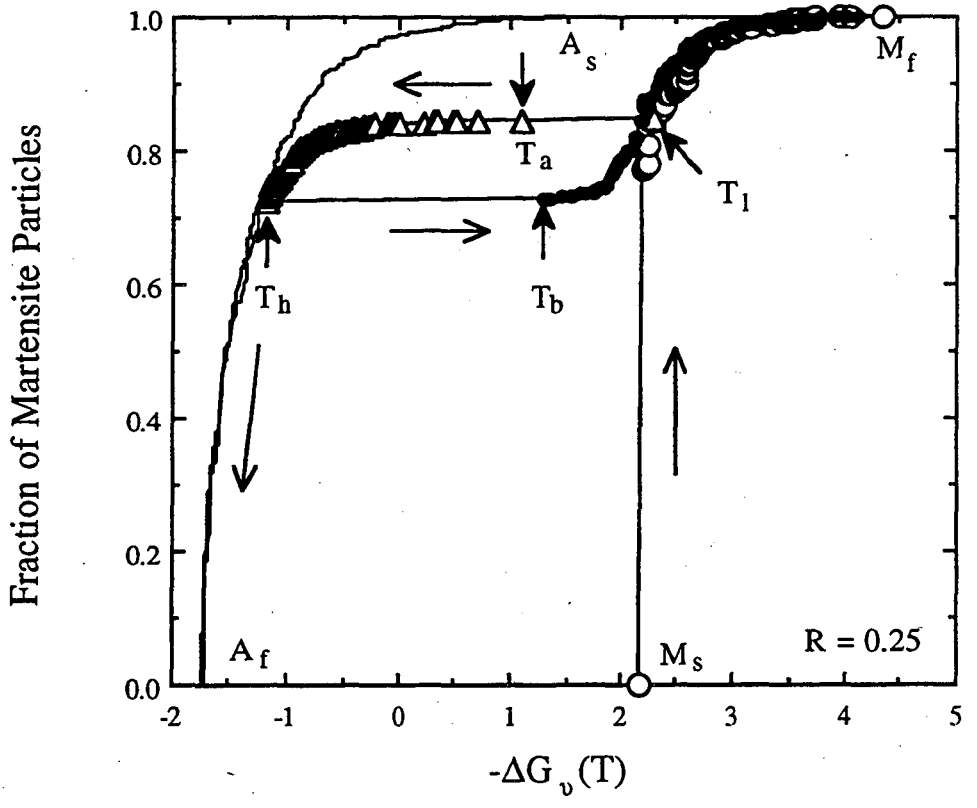

Fig. 6.13(b) The temperature-transformation (TT) curves for a partial reversion with $f_r = 1$, $\Delta G_r = 1.0$ and $\Delta G_r = 2.0$ when the amount of reversed martensite is about 15% (R = 0.25).

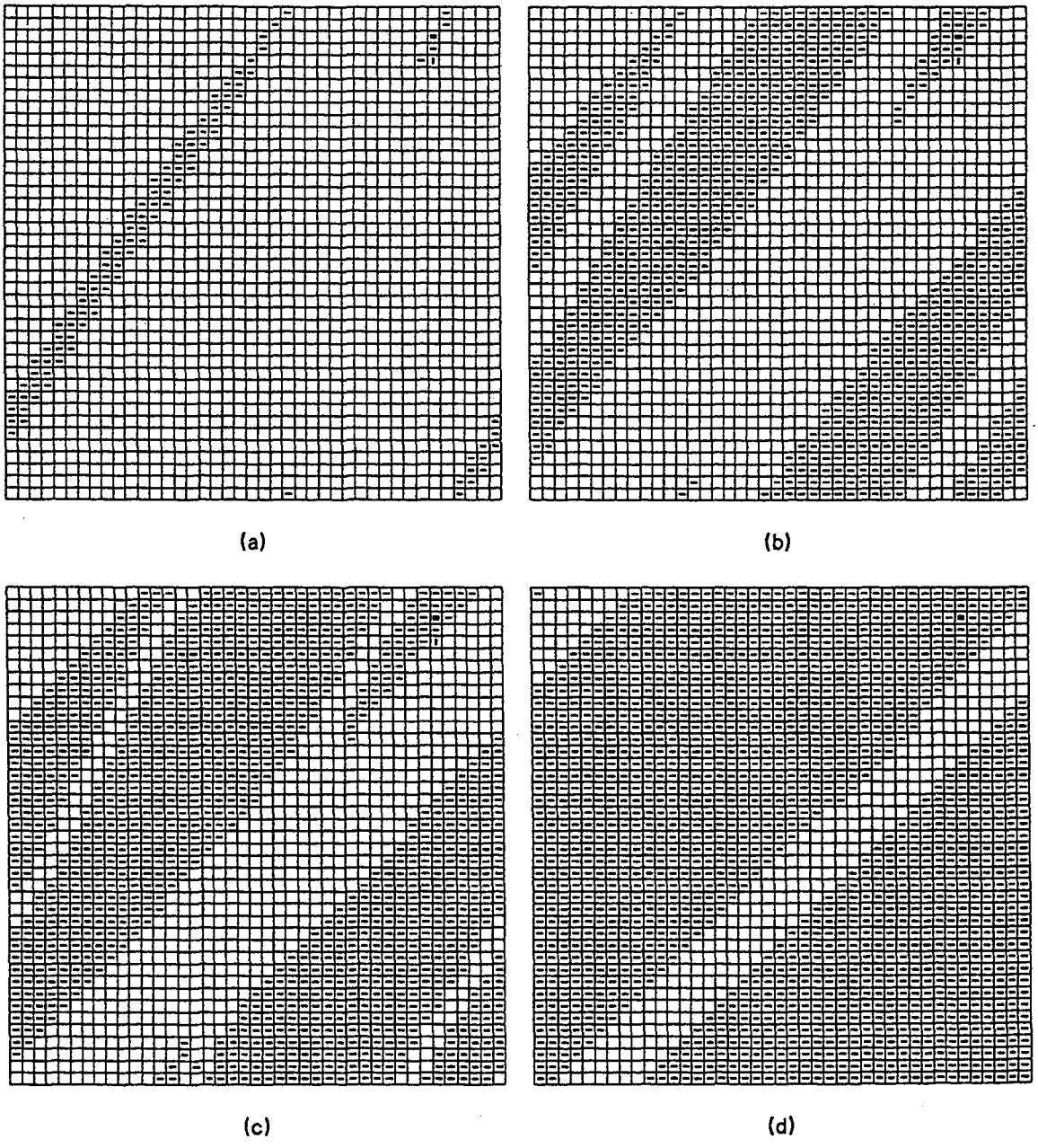

Fig. 6.14 The microstructural evolution generated by a simulated reversible transformation ($f_r = 1$, $R = 0.25$) of an unconstrained crystal during cooling process.

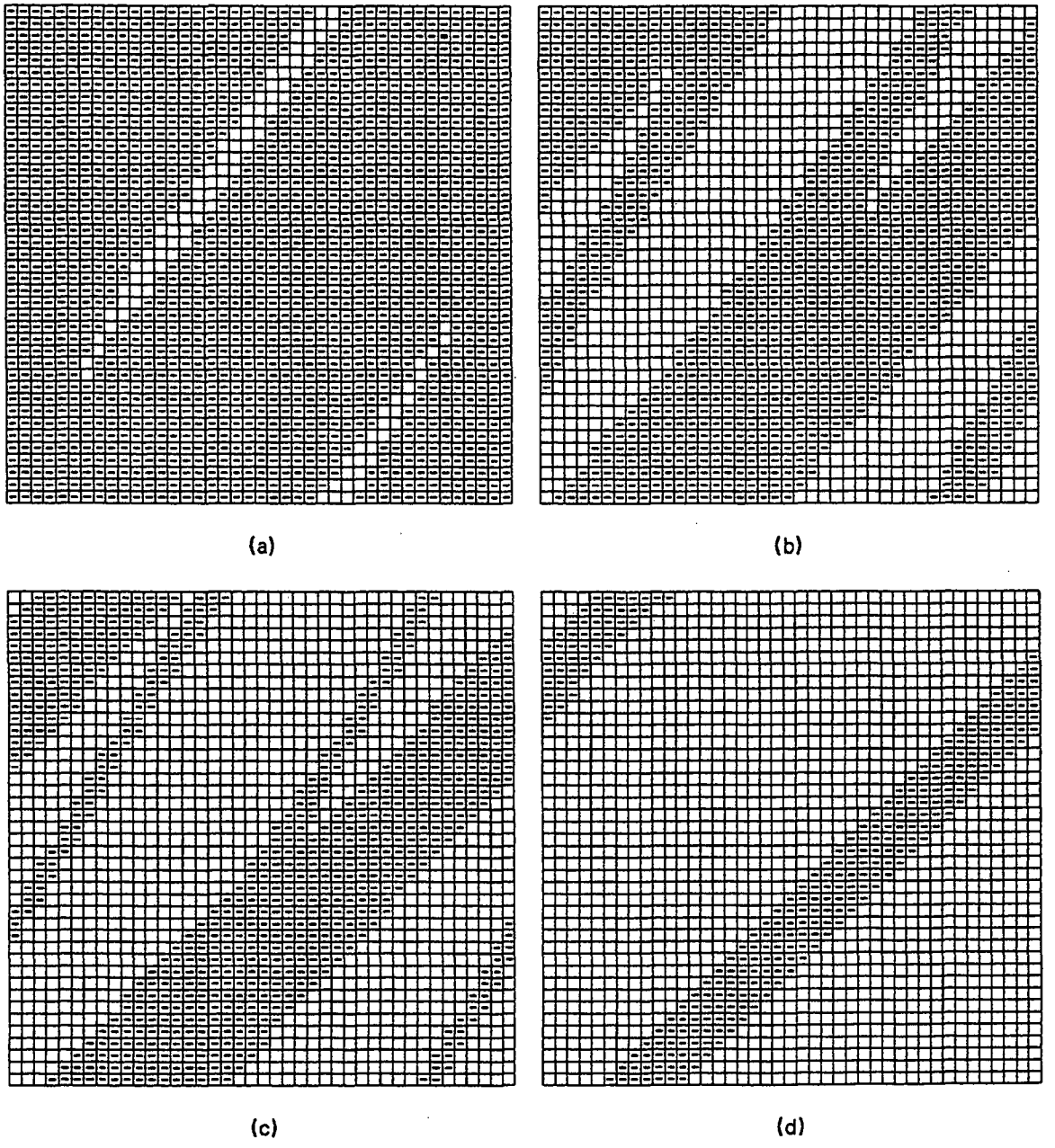

Fig. 6.15 The microstructural evolution generated by a simulated reversible transformation ($f_r = 1$, $R = 0.25$) of an unconstrained crystal during heating process.

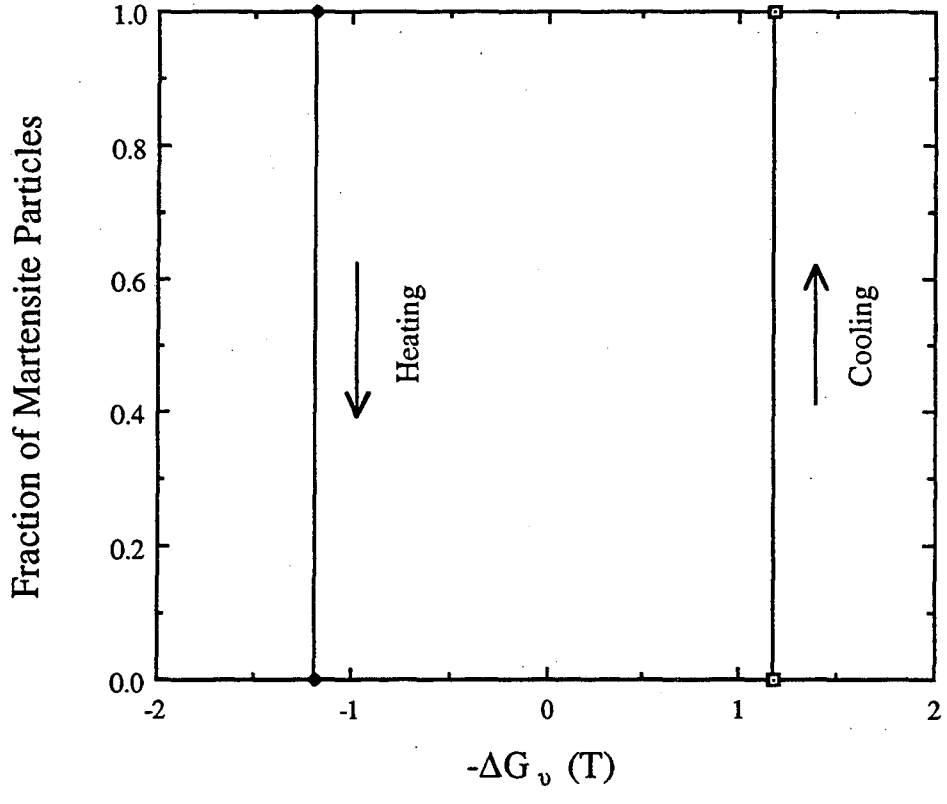

Fig. 6.16 The temperature-transformation (TT) curves for the transformations of an unconstrained crystal shown in Fig. 6.14 and Fig. 6.15

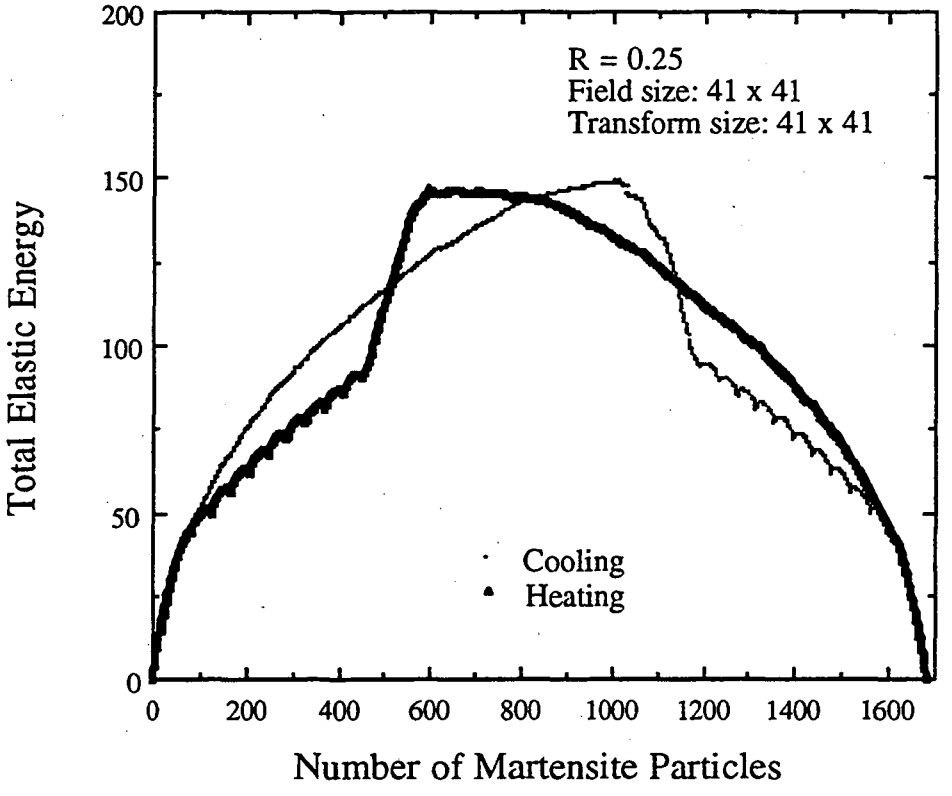

Fig. 6.17 The fraction of martensite versus total elastic energy generated during the transformation and reversion of an unconstrained crystal (R = 0.25).

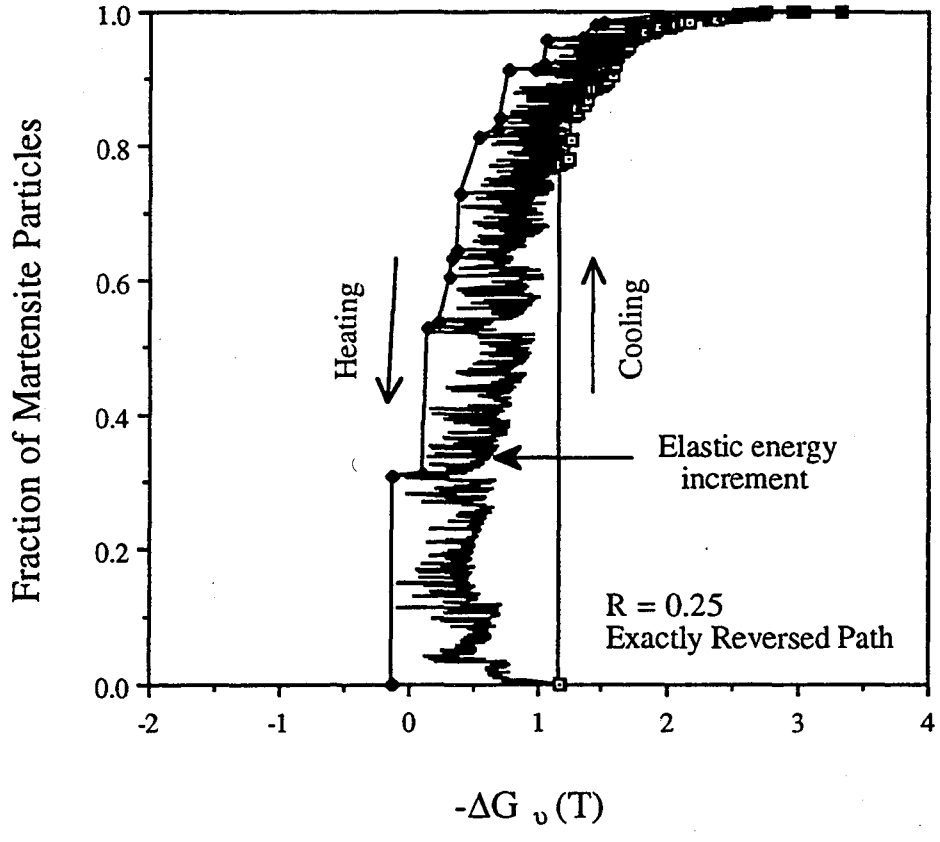

Fig. 6.18 The temperature-transformation (TT) curve and elastic energy increment curve for the exactly reversed path.

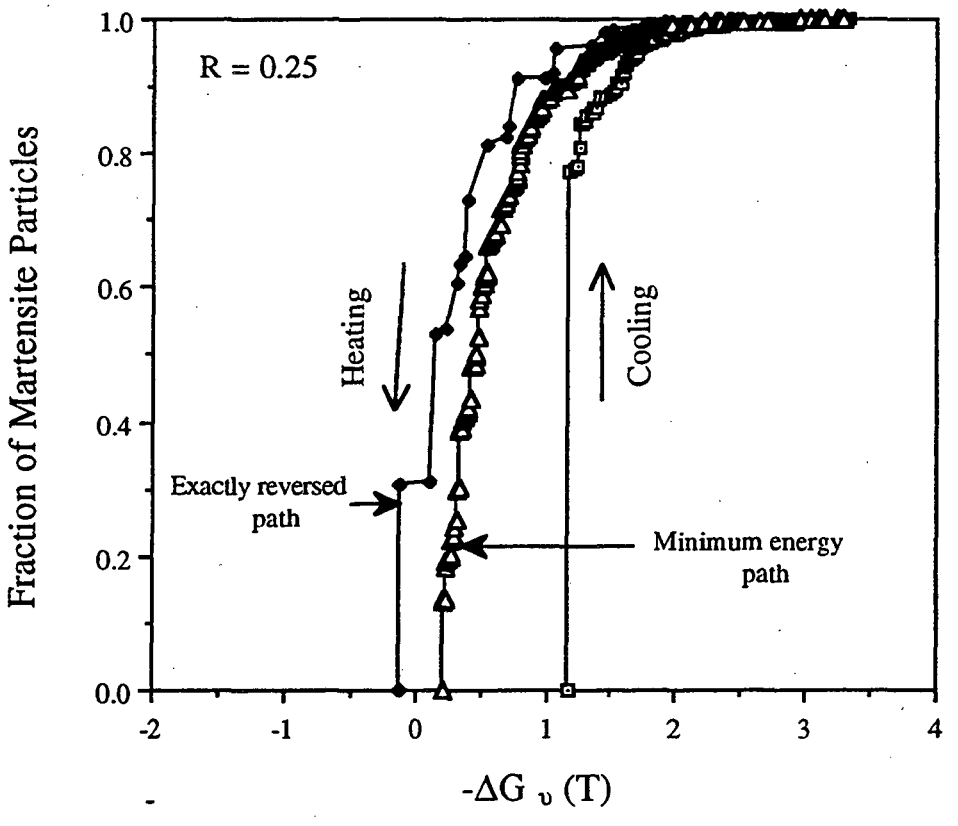

Fig. 6.19 The temperature-transformation (TT) curves for the exactly reversed path and the minimum energy path.

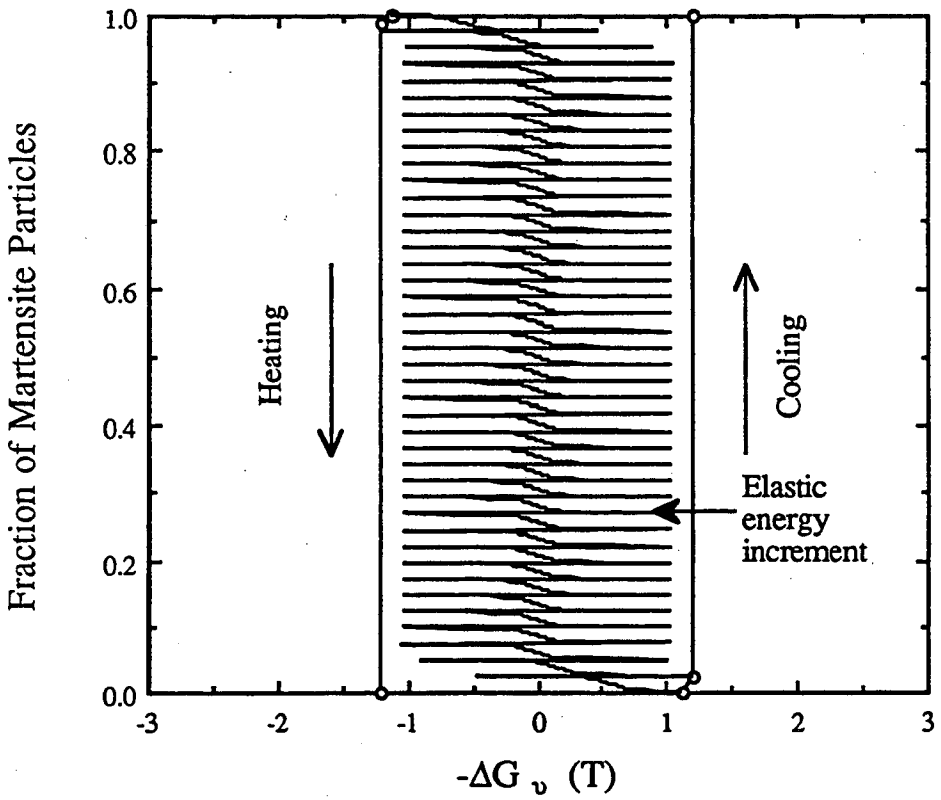

Fig. 6.20 The temperature-transformation (TT) curves for the exactly reversed path and the elastic energy increment curve from the transformation of an unconstrained crystal.

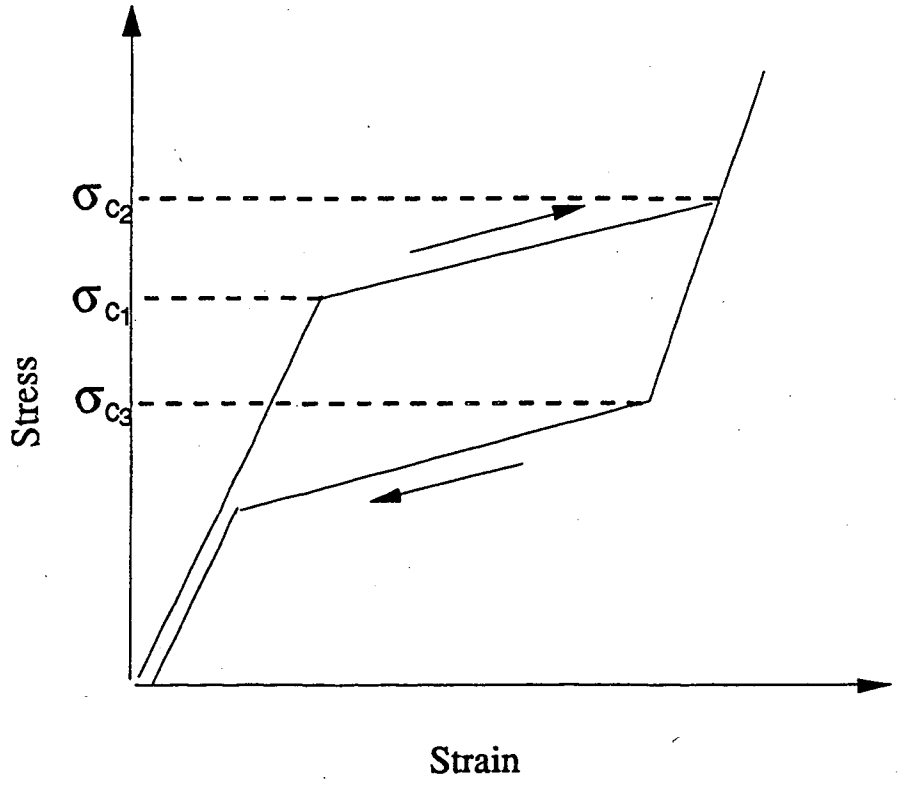

Fig. 7.1 The schematic drawing of stress-strain curve showing pseudoelasticity caused by stress-induced martensitic transformation.

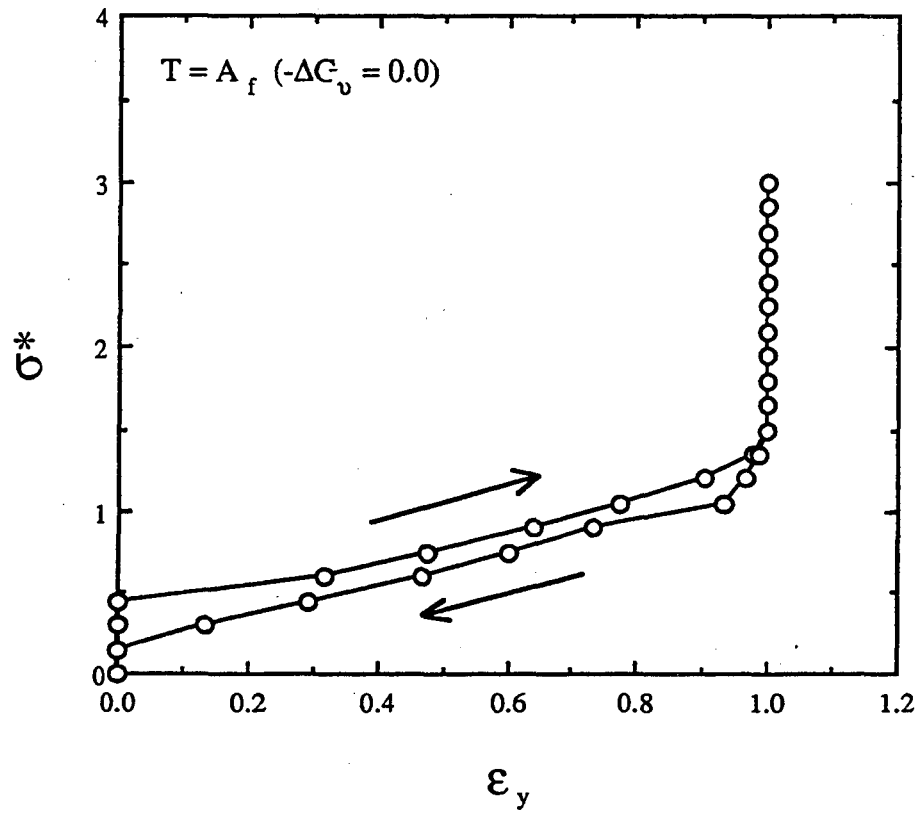

Fig. 7.2(a) The σ^* -ε_y curve of a simulated reversible transformation (f_r = 1, R = 0.2) at a loading temperature T > A_f (-$\Delta G\upsilon$ = - 0.5).

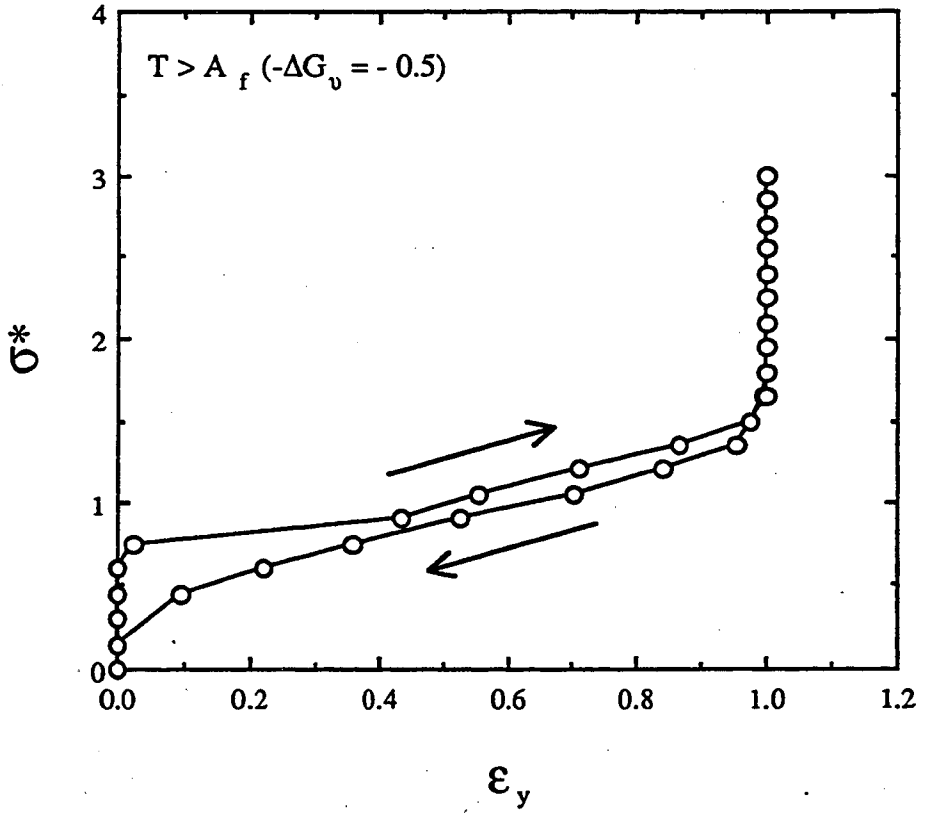

Fig. 7.2(b) The σ^* -ε_y curve of a simulated reversible transformation ($f_r = 1$, R = 0.2) at a loading temperature $T = A_f$ ($-\Delta G\upsilon = 0.0$).

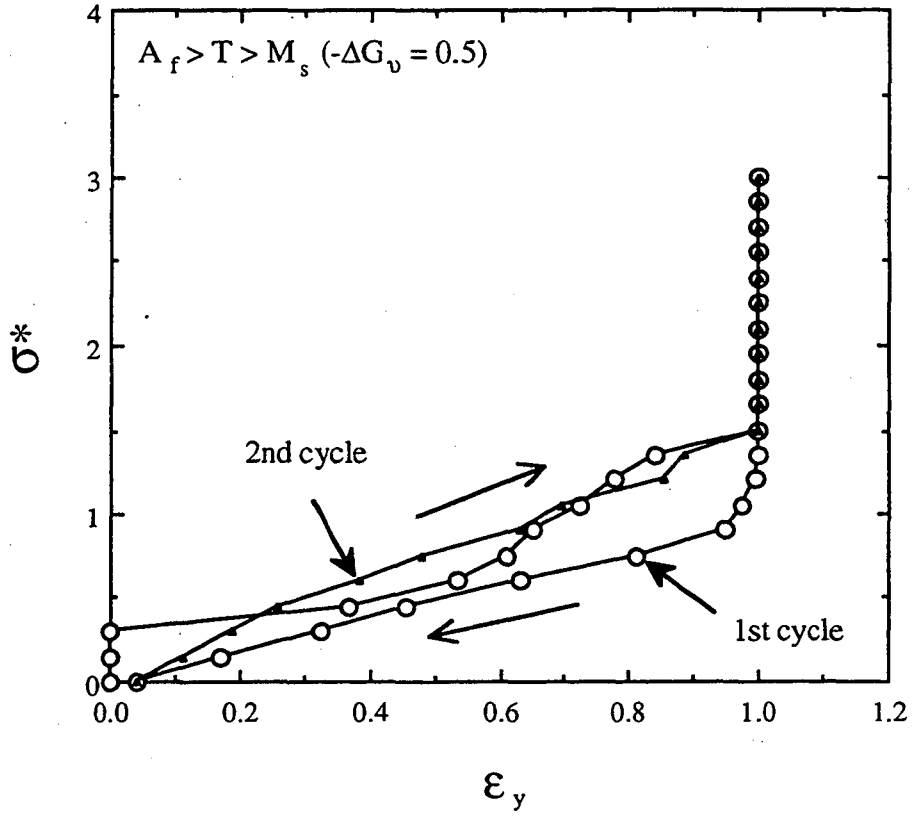

Fig. 7.2(c) The σ^* -ε_y curve of a simulated reversible transformation ($f_r = 1$, R = 0.2) at a loading temperature $A_f > T > M_S$ ($-\Delta Gv = 0.5$).

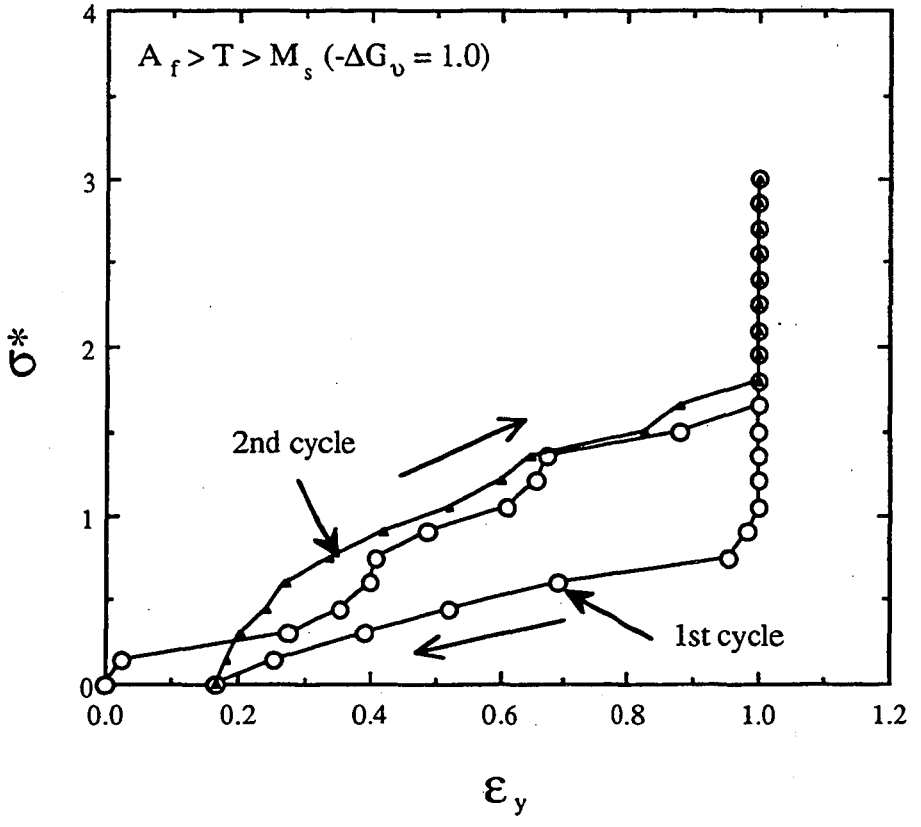

Fig. 7.2(d) The σ^* -ε_y curve of a simulated reversible transformation ($f_r = 1$, R = 0.2) at a loading temperature $A_f > T > M_s$ ($-\Delta G\upsilon = 1.0$).

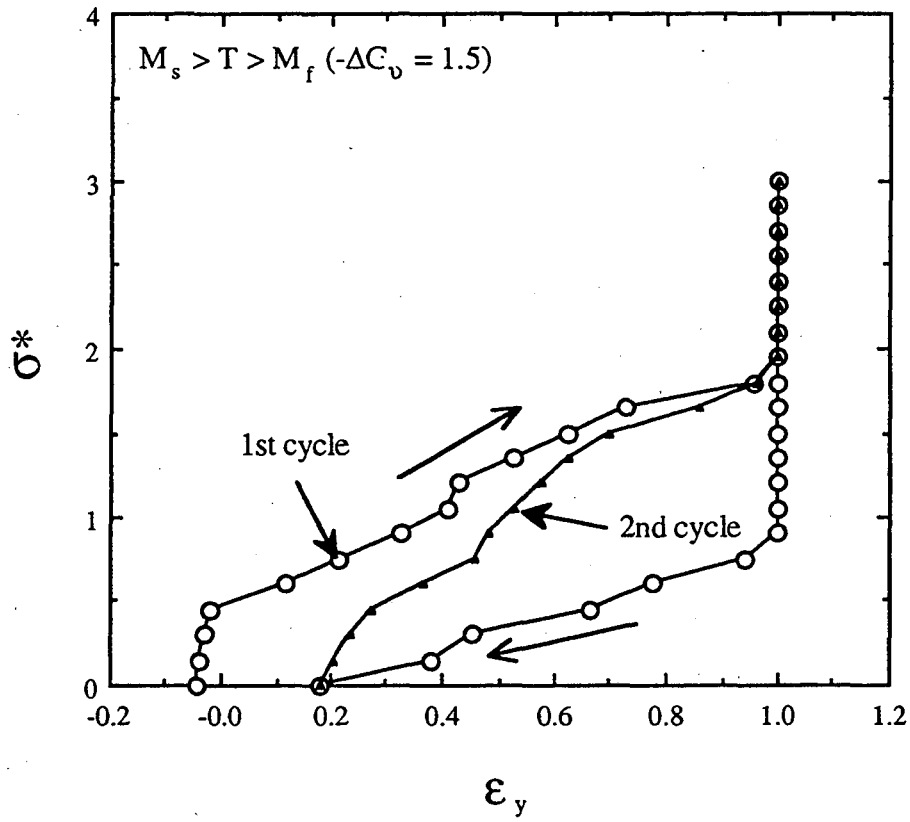

Fig. 7.2(e) The σ^* -ε_y curve of a simulated reversible transformation ($f_r = 1$, R = 0.2) at a loading temperature $M_S > T > M_f$ ($-\Delta G\upsilon = 1.5$).

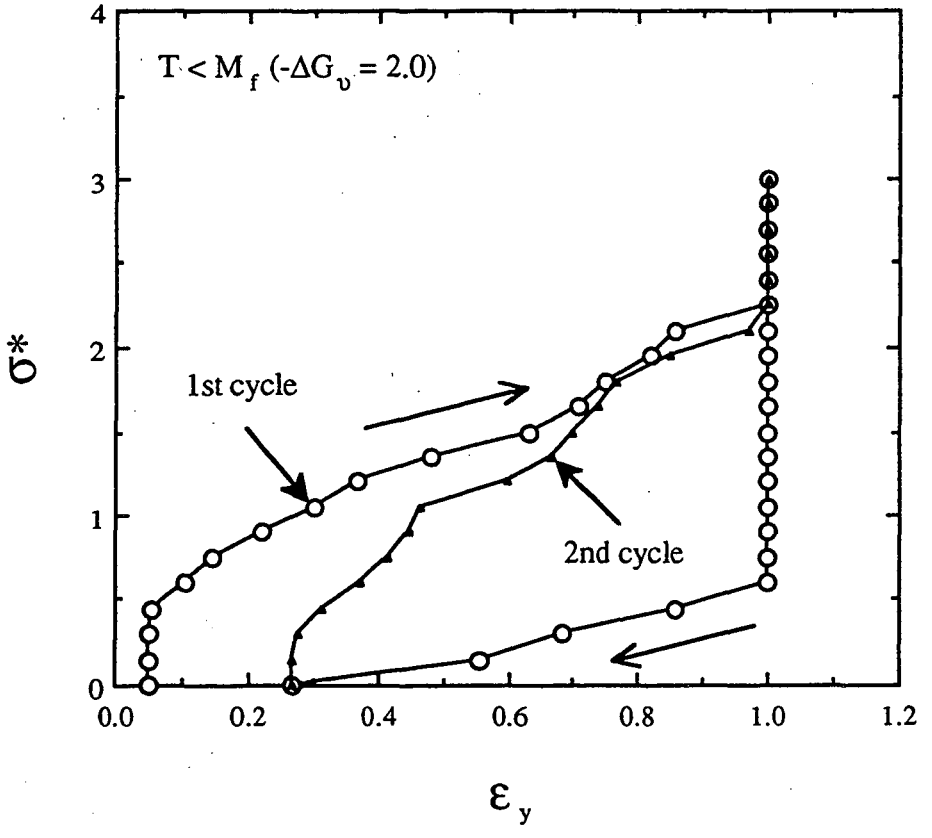

Fig. 7.2(f) The σ^* -ε_y curve of a simulated reversible transformation ($f_r = 1$, R = 0.2) at a loading temperature $T < M_f$ ($-\Delta G\upsilon = 2.0$).

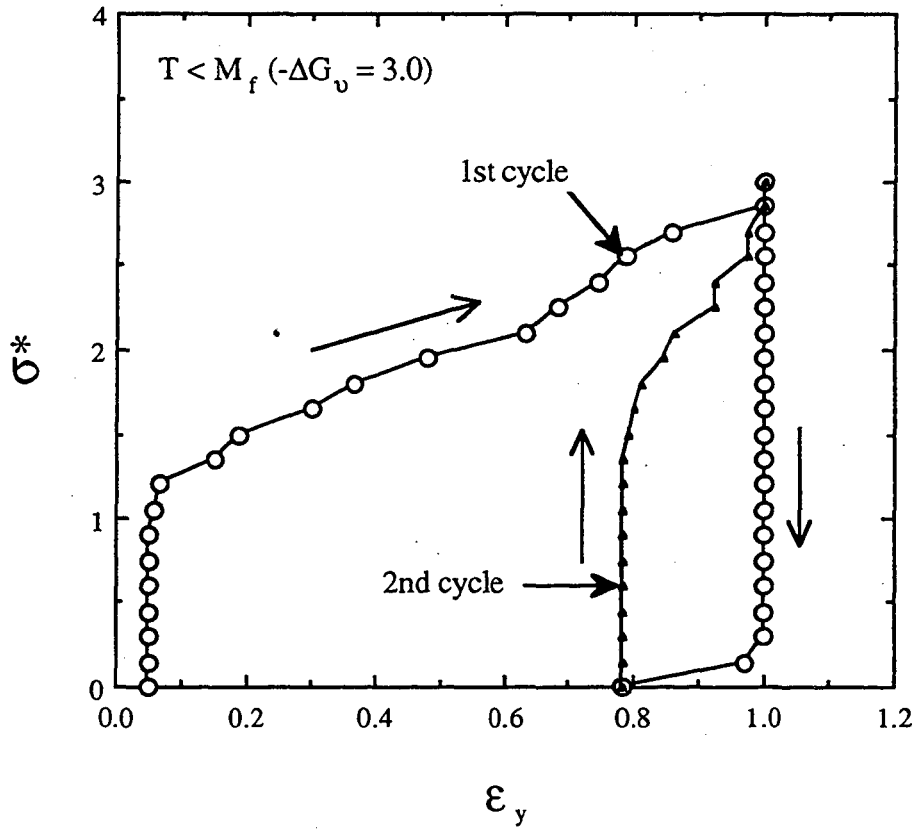

Fig. 7.2(g) The σ^* -ε_y curve of a simulated reversible transformation ($f_r = 1$, R = 0.2) at a loading temperature $T < M_f$ ($-\Delta G\upsilon = 3.0$).

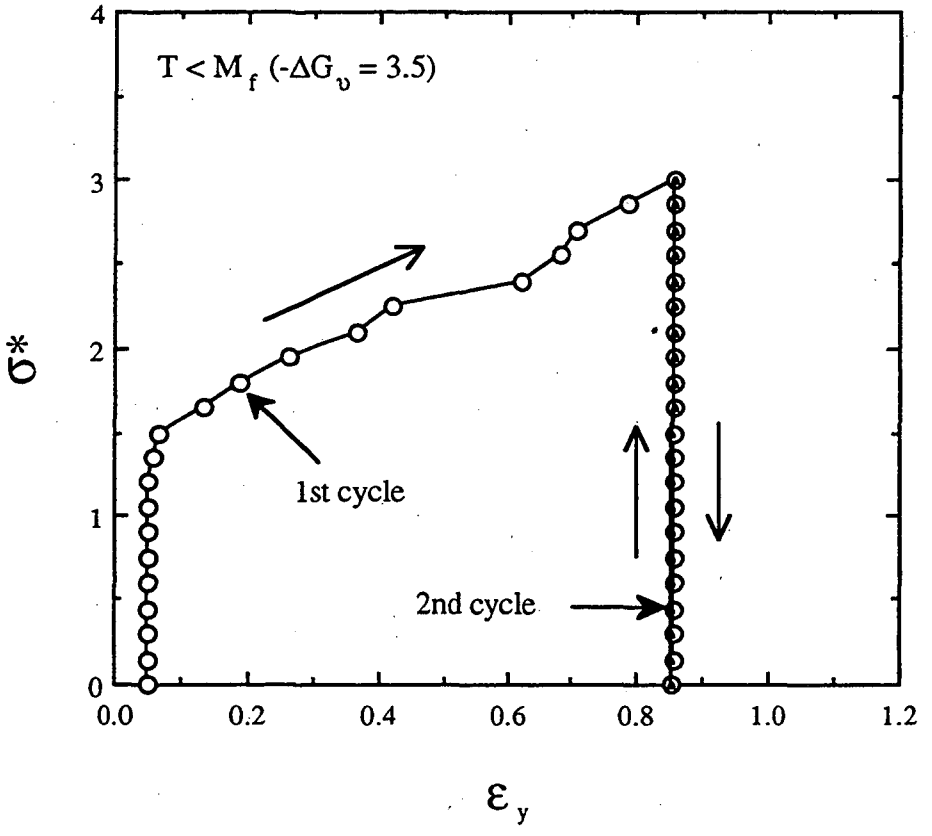

Fig. 7.2(h) The σ^* -ε_y curve of a simulated reversible transformation ($f_r = 1$, R = 0.2) at a loading temperature $T < M_f$ ($-\Delta G\upsilon = 3.5$).

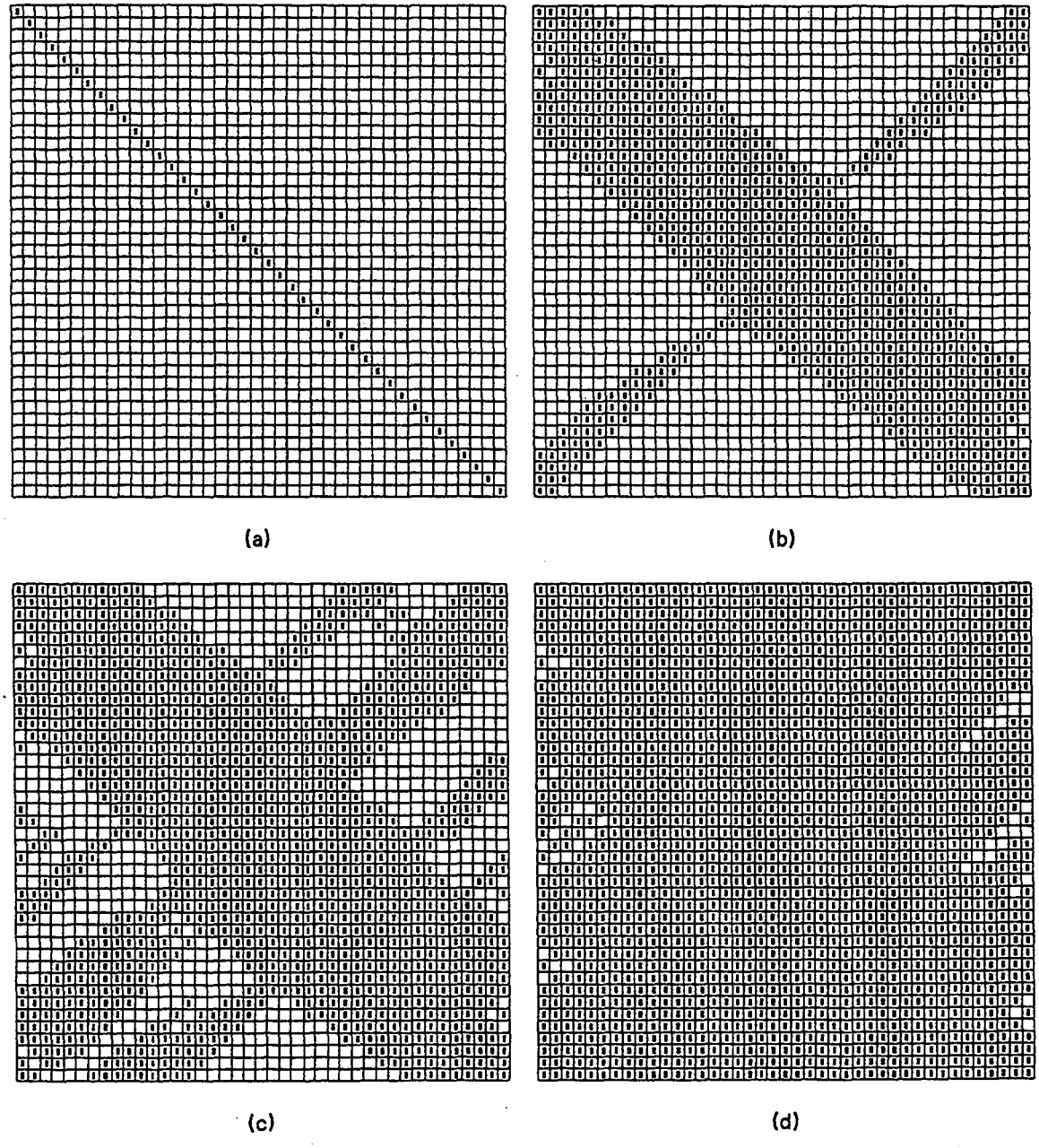

Fig. 7.3 The microstructural evolution generated by a simulated reversible transformation during the first loading-unloading cycle when $A_f < T$ ($-\Delta G_v = -0.5$): (a)-(d) loading, $\sigma^* = 0.75$, 0.9, 1.2 and 1.5; (e)-(h) unloading, $\sigma^* = 1.5$, 0.9, 0.6, and 0.45.

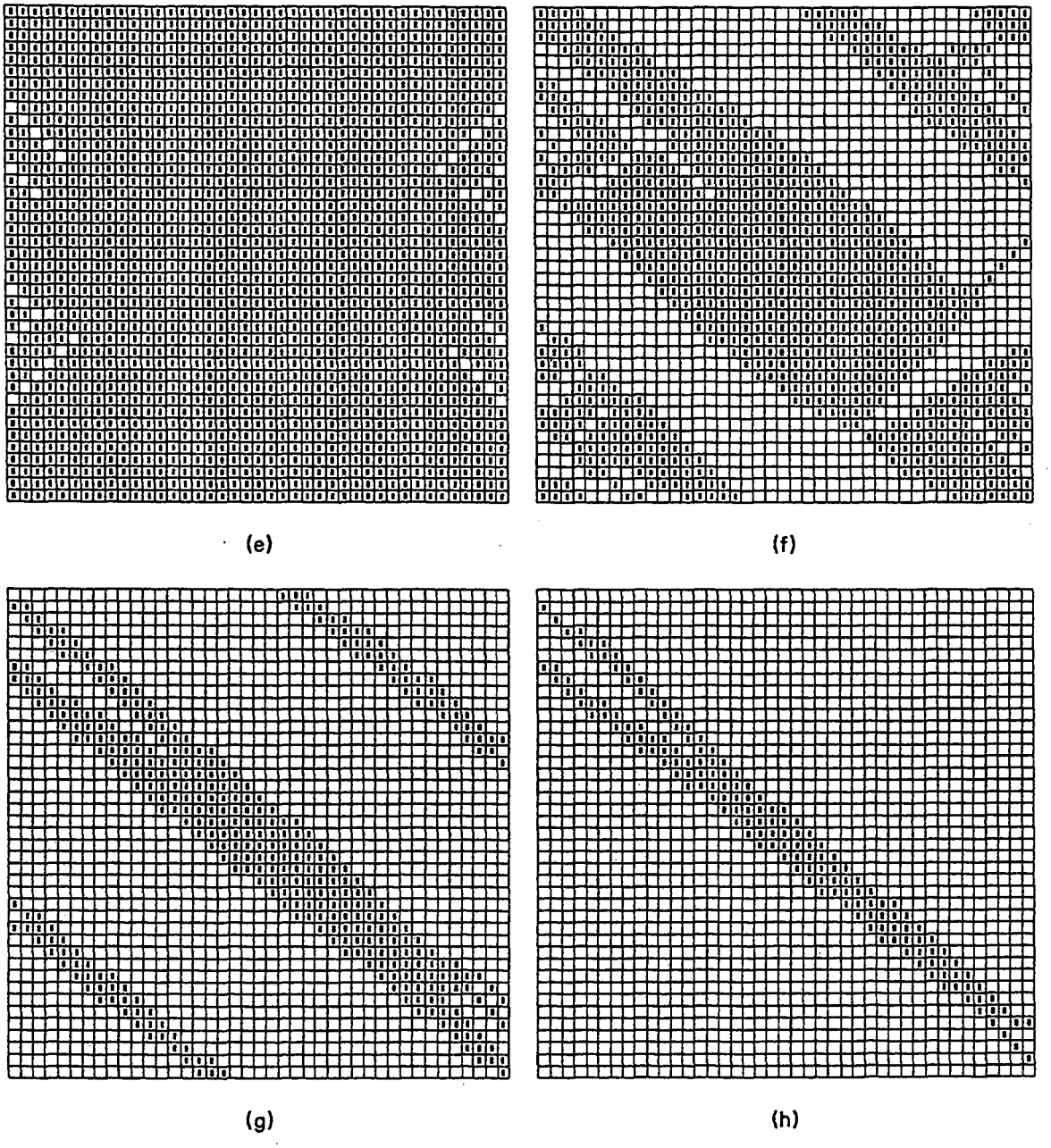

Fig. 7.3(Cont.) The microstructural evolution generated by a simulated reversible transformation during the first loading-unloading cycle when $A_f <$ T ($-\Delta G_v = -0.5$): (a)-(d) loading, $\sigma^* = 0.75, 0.9, 1.2$ and 1.5; (e)-(h) unloading, $\sigma^* = 1.5, 0.9, 0.6$, and 0.45.

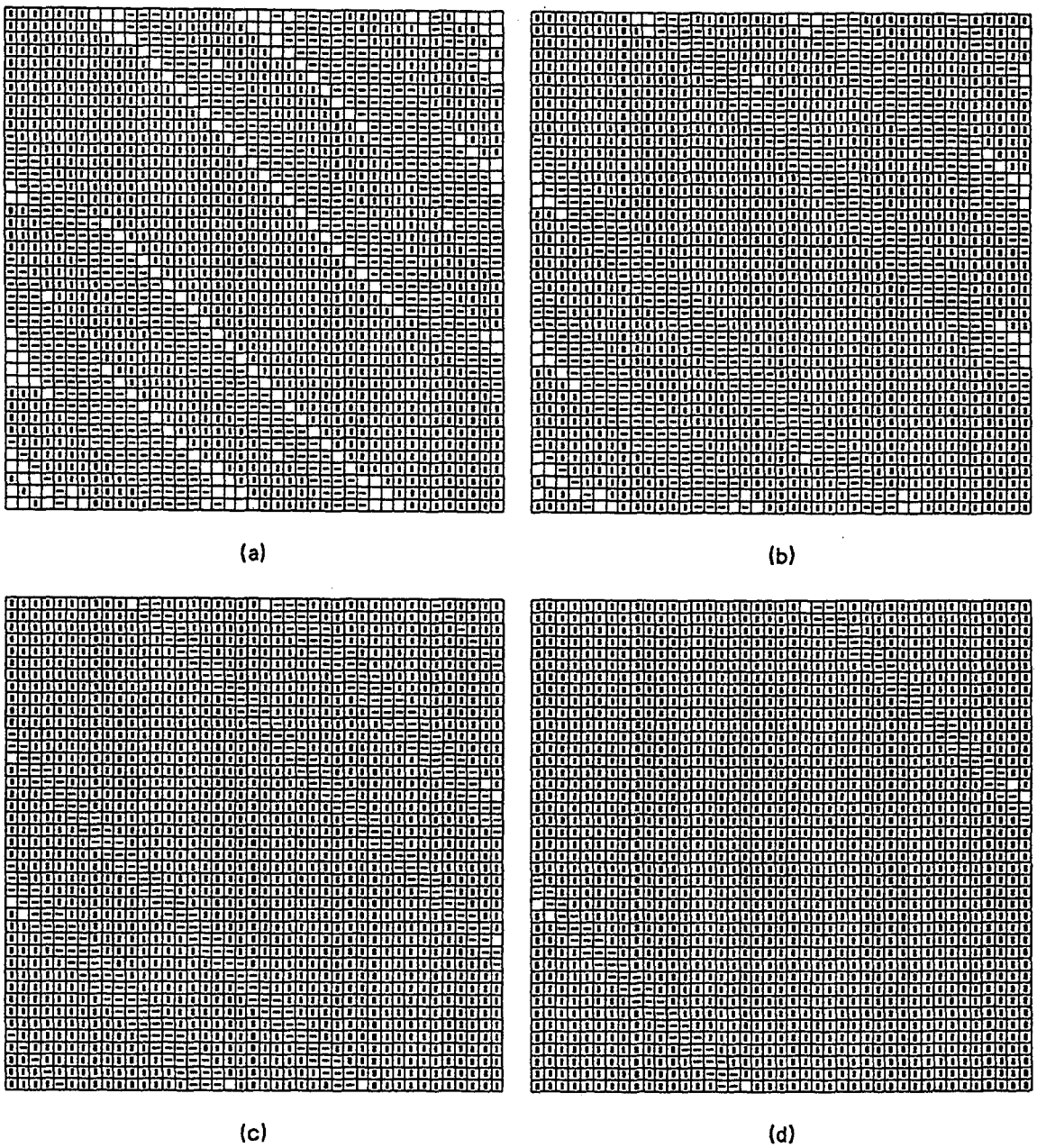

Fig. 7.4 The microstructural evolution generated by a simulated reversible transformation during the first loading-unloading cycle when $A_f > T > M_s$ ($-\Delta G_v = 1.0$): (a)-(d) loading, $\sigma^* = 0.3, 0.6, 1.05$ and 1.5; (e)-(h) unloading, $\sigma^* = 0.9, 0.6, 0.3$ and 0.0 (min.).

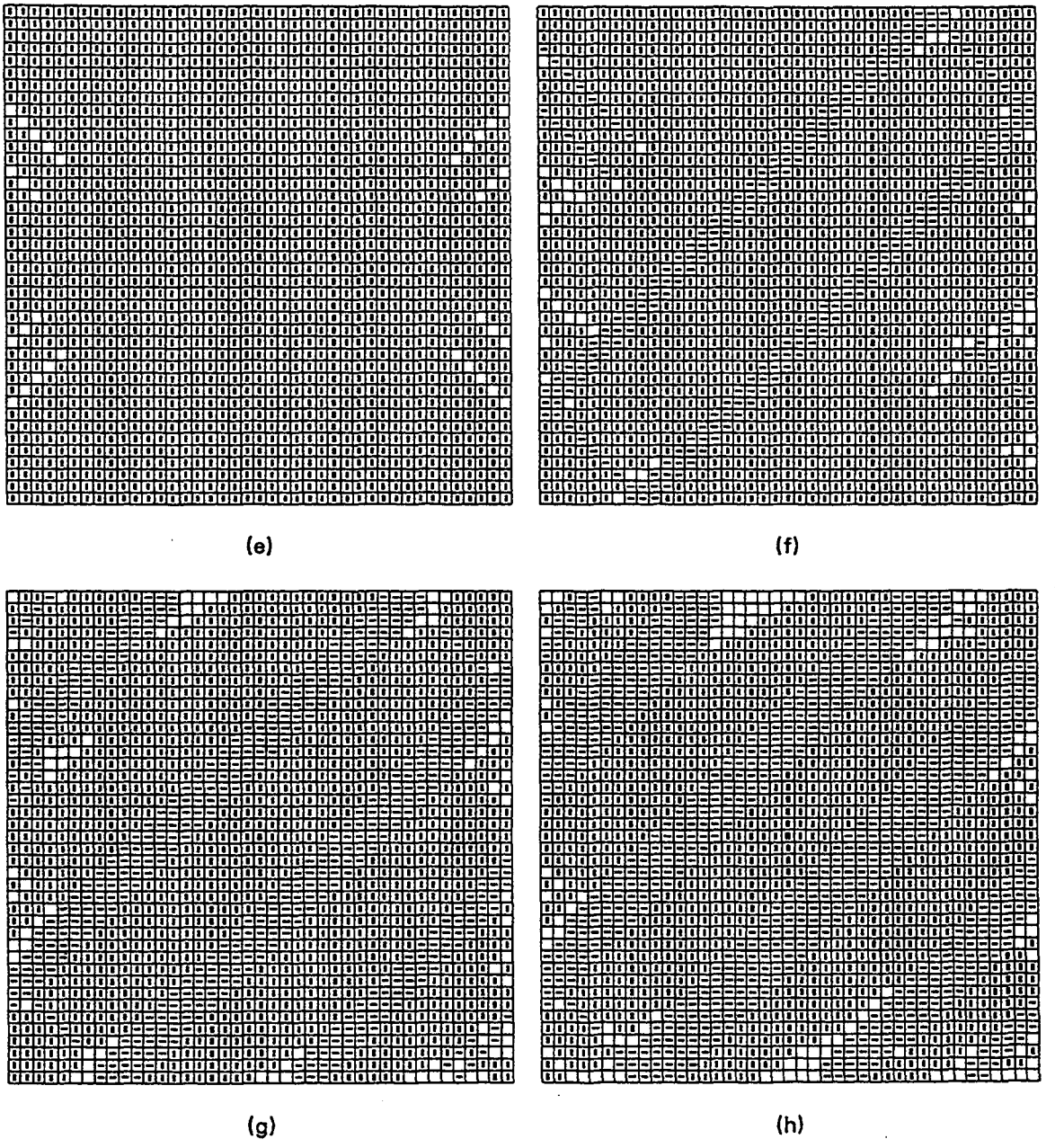

Fig. 7.4(Cont.) The microstructural evolution generated by a simulated reversible transformation during the first loading-unloading cycle when $A_f > T > M_S$ ($-\Delta G_v = 1.0$): (a)-(d) loading, $\sigma^* = 0.3$, 0.6, 1.05 and 1.5; (e)-(h) unloading, $\sigma^* = 0.9$, 0.6, 0.3 and 0.0 (min.).

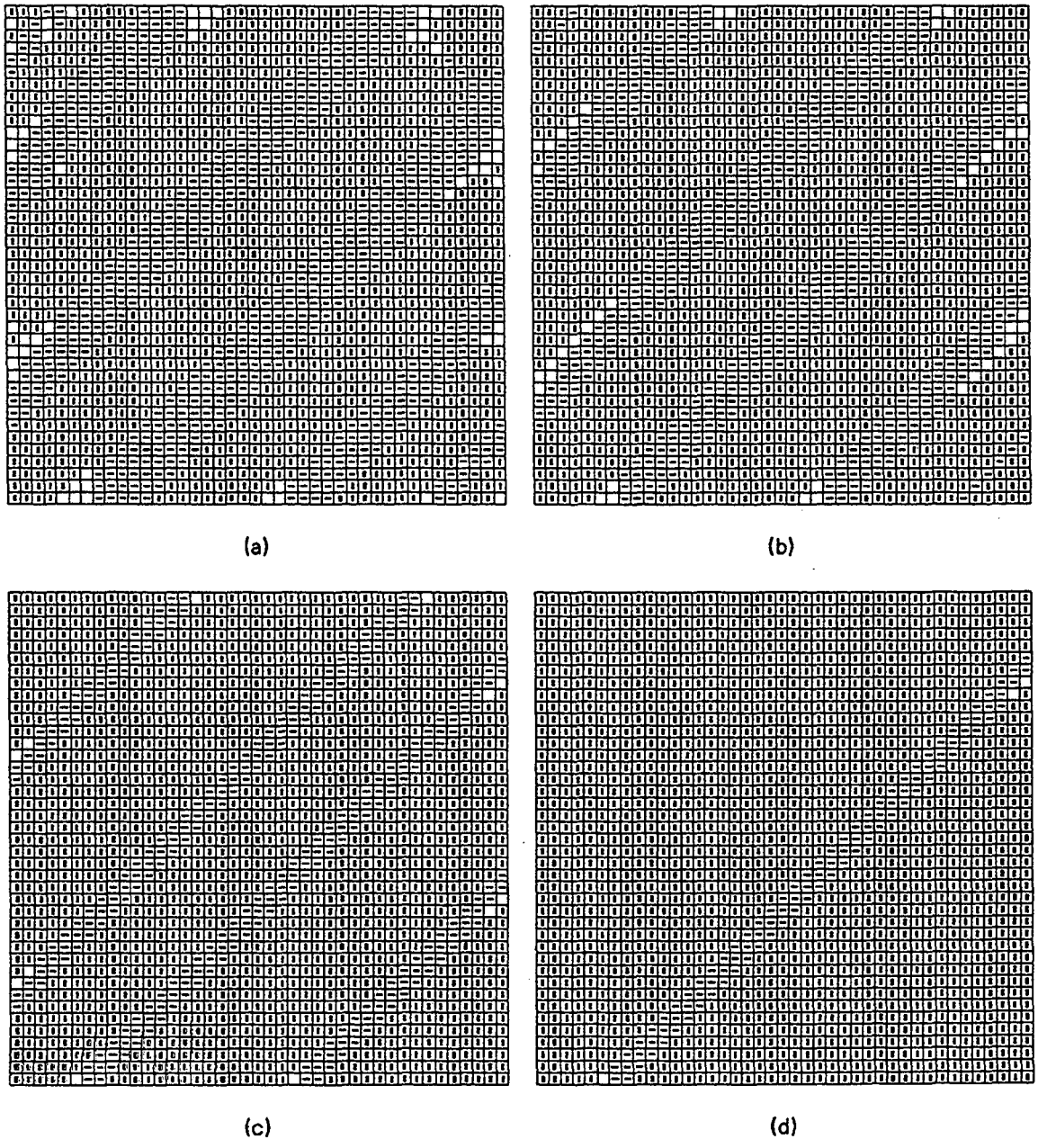

Fig. 7.5 The microstructural evolution generated by a simulated reversible transformation during loading of the second cycle when $A_f > T > M_S$ ($-\Delta G_v = 1.0$): (a)-(d) $\sigma^* = 0.45, 0.9, 1.35$, and 1.65.

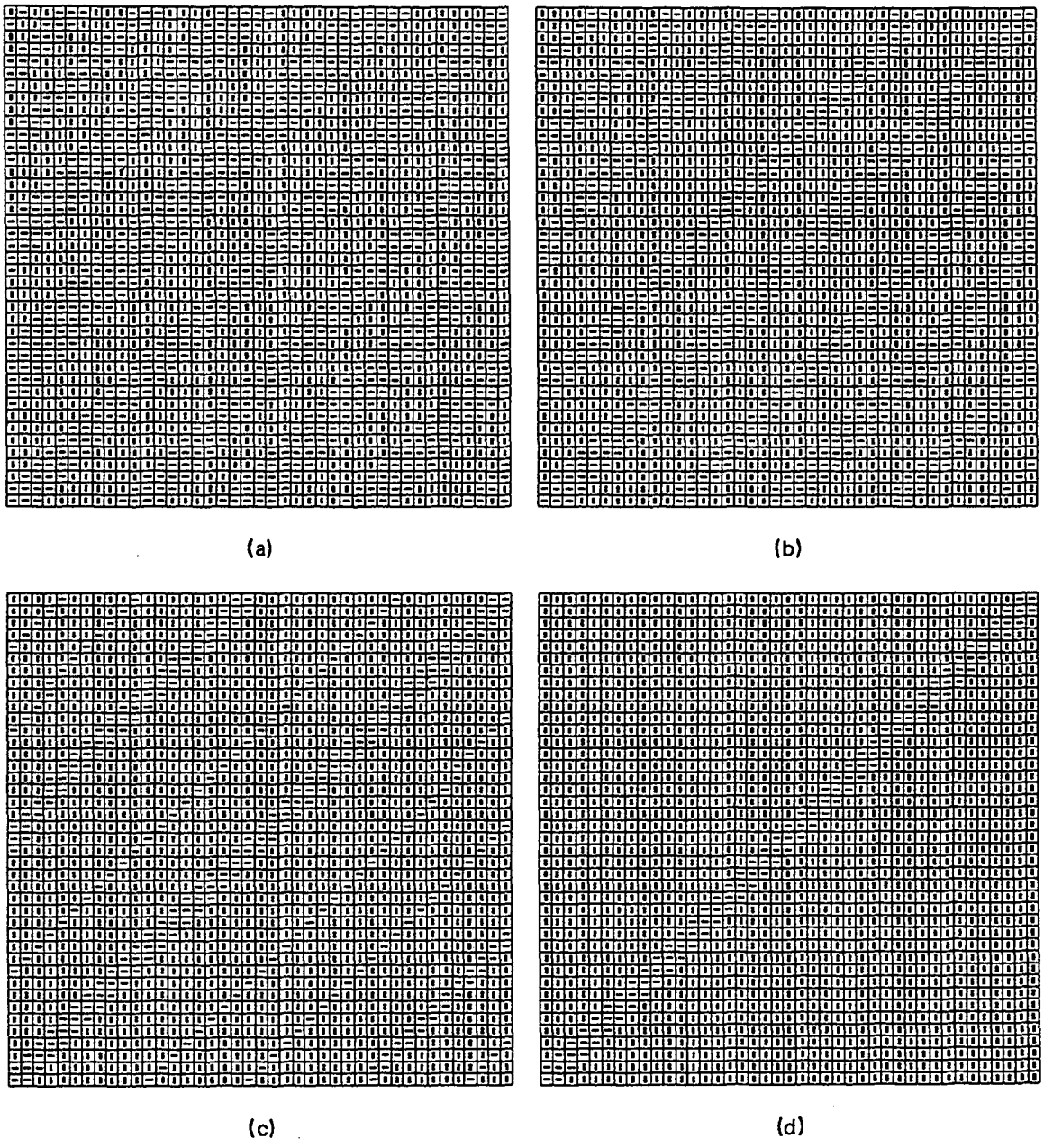

Fig. 7.6 The microstructural evolution generated by a simulated reversible transformation during the first loading-unloading cycle when $T < M_f$ ($-\Delta G_v = 2.0$): (a)-(d) loading, $\sigma^* = 0.0$ (min.), 1.05, 1.5 and 2.1; (e)-(h) unloading, $\sigma^* = 0.45$, 0.3, 0.15 and 0.0 (min.).

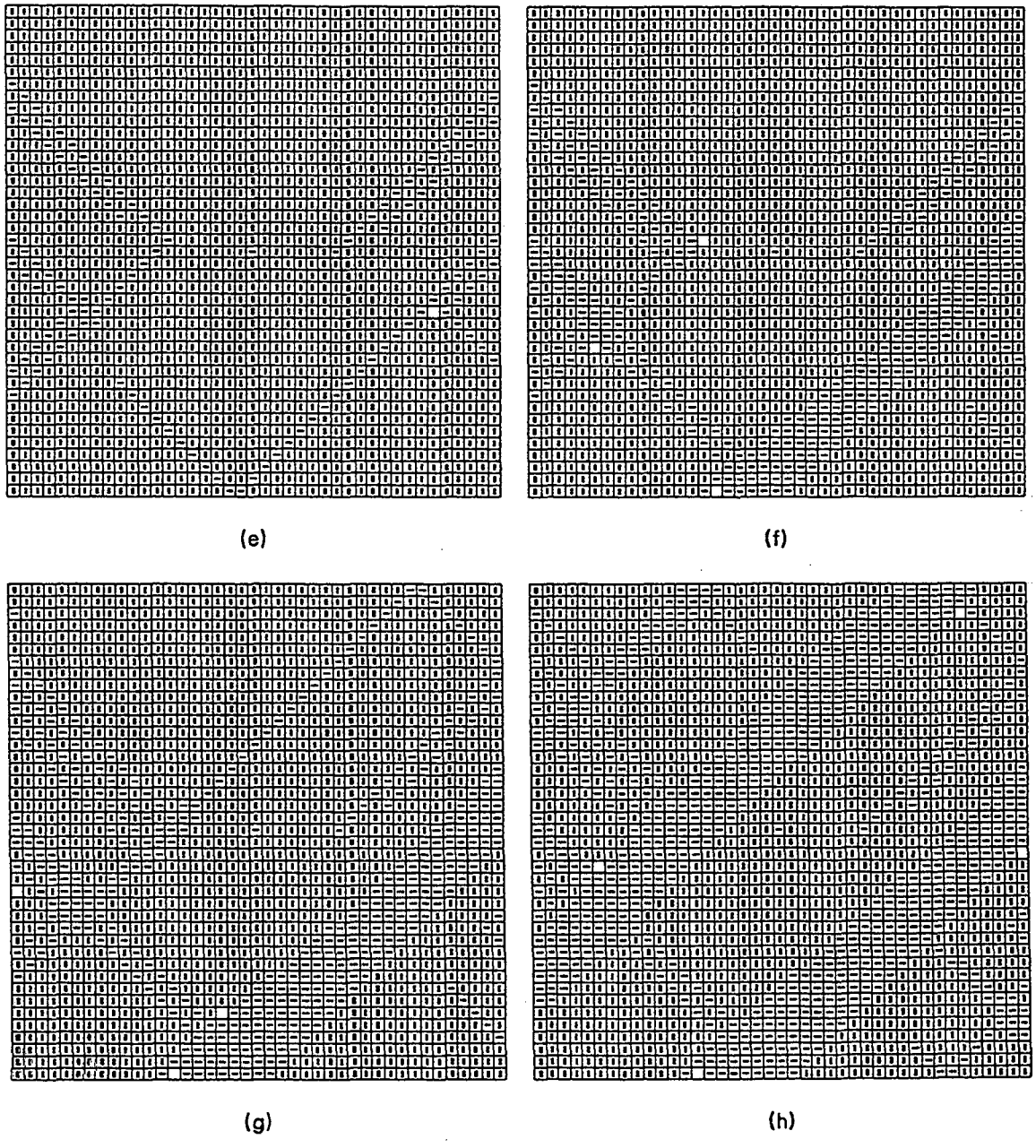

Fig. 7.6(Cont.) The microstructural evolution generated by a simulated reversible transformation during the first loading-unloading cycle when $T < M_f$ ($-\Delta G_v = 2.0$): (a)-(d) loading, $\sigma^* = 0.0$ (min.), 1.05, 1.5 and 2.1; (e)-(h) unloading, $\sigma^* = 0.45$, 0.3, 0.15 and 0.0 (min.).

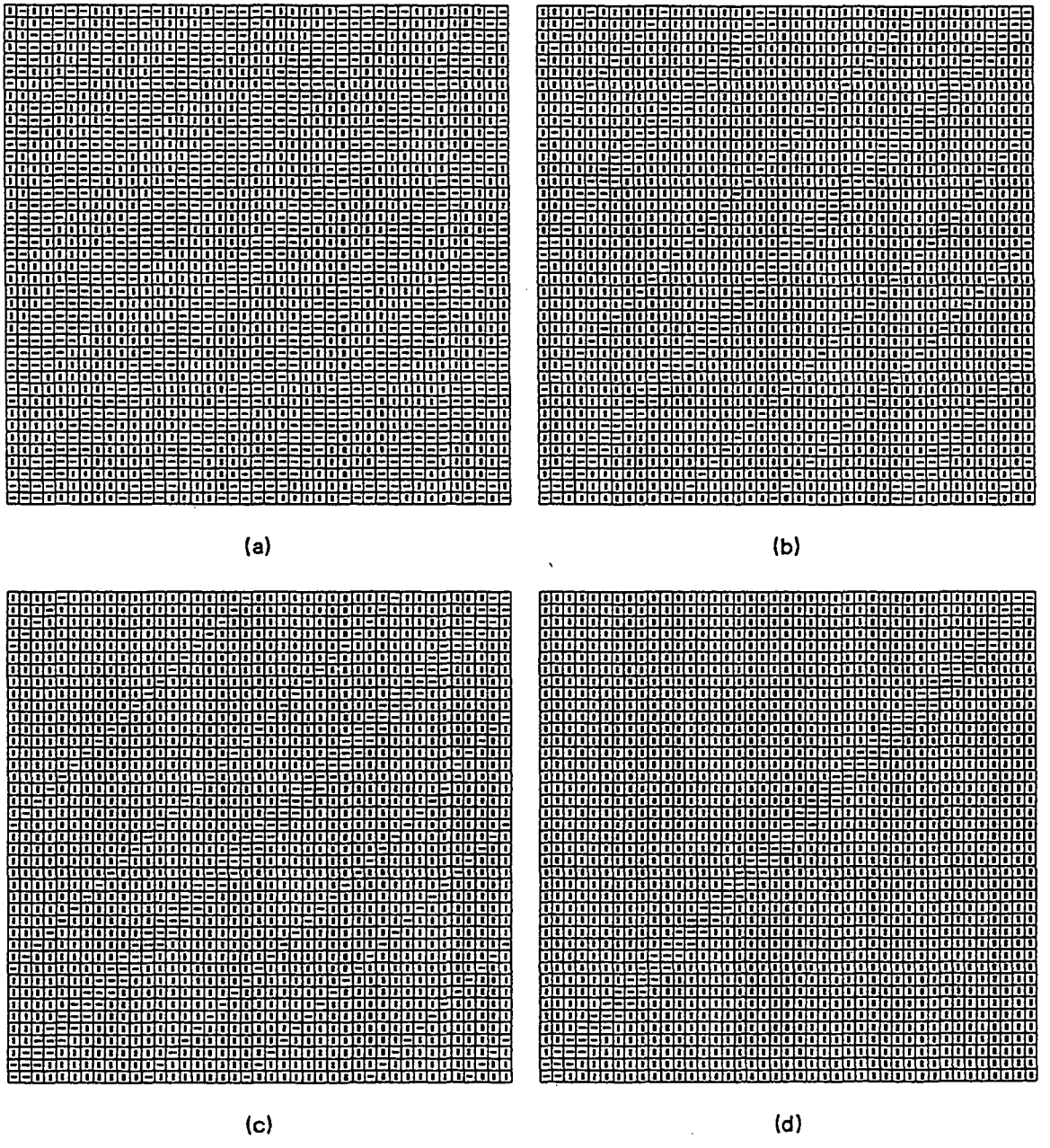

Fig. 7.7 The microstructural evolution generated by a simulated reversible transformation during loading of the second cycle when $T < M_f$ ($-\Delta G_v = 3.5$): (a)-(d) $\sigma^* = 0.0$ (min.), 2.4, 2.7, and 3.0 (max.).

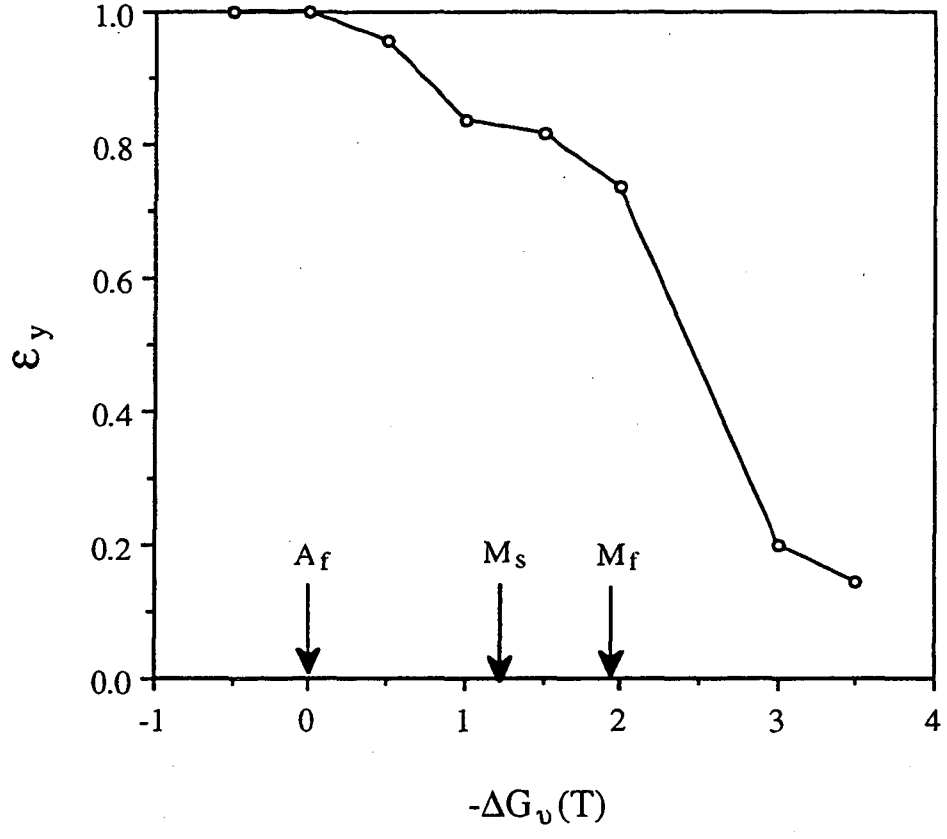

Fig. 7.8 The plot of the recovered strain, ε_y, versus $-\Delta G_v$ (loading temperature).

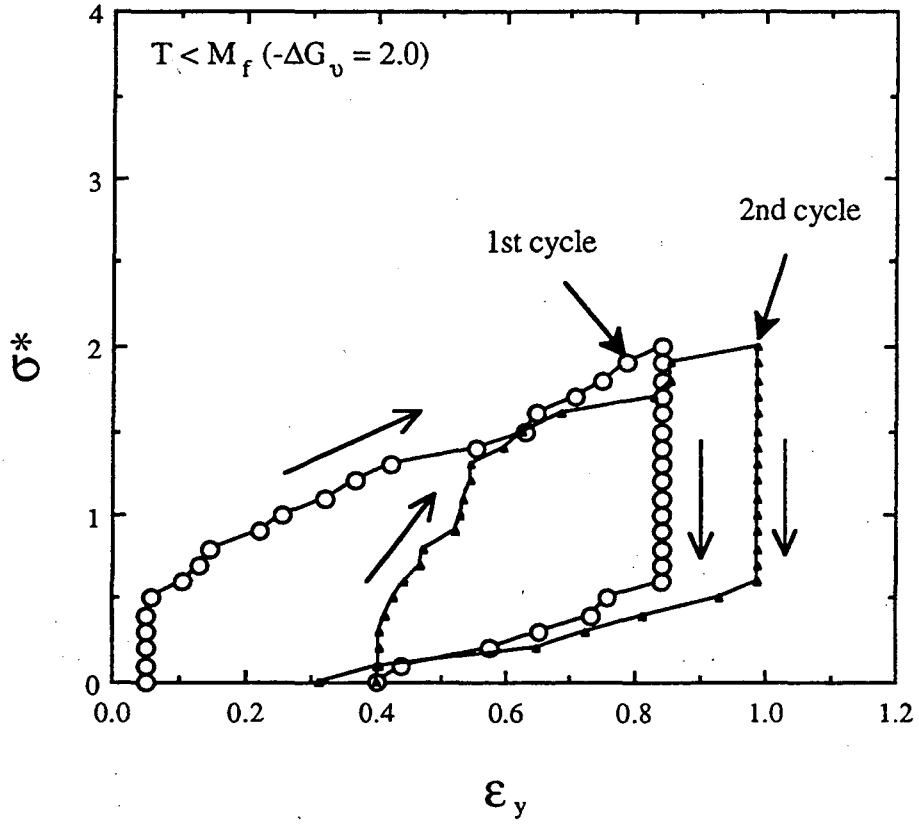

Fig. 7.9 The σ^*-ε_y curves of a simulated reversible transformation ($f_r = 1$, $R = 0.2$) at a loading temperature $T < M_f$ ($-\Delta G\upsilon = 2.0$) and a maximum stress $\sigma^* = 2.0$.

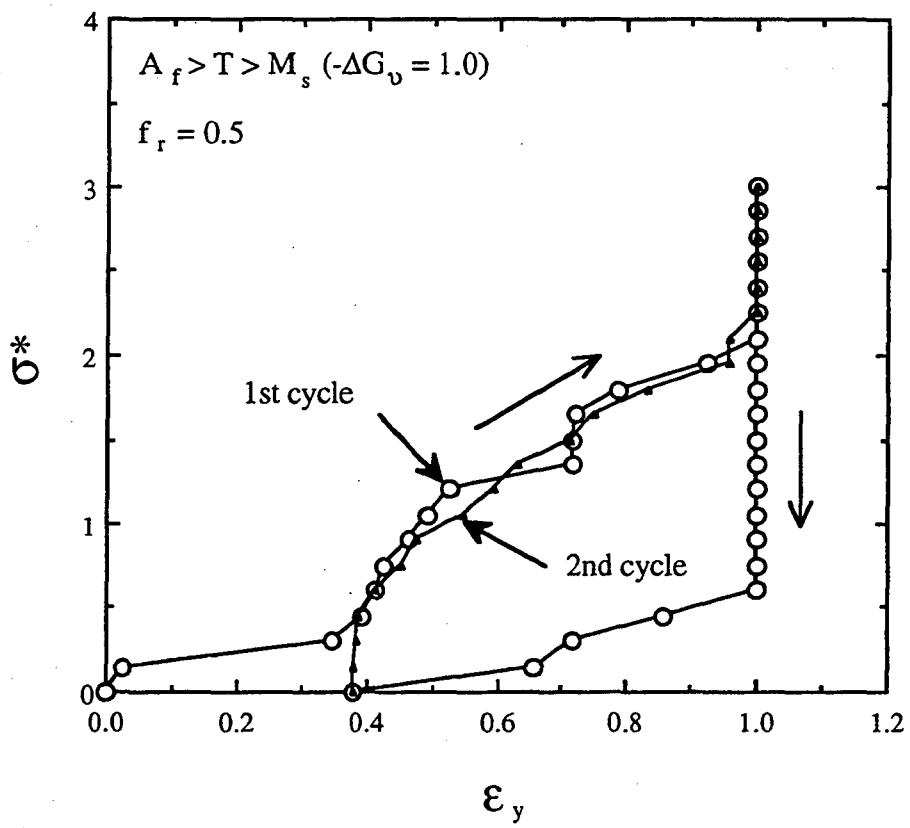

Fig. 7.10 The σ^*-ε_y curves of a simulated reversible transformation (R = 0.2) at a loading temperature $T > M_S$ ($-\Delta G\upsilon = 1.0$) with $f_r = 0.5$ and $\Delta G_r = 0$.

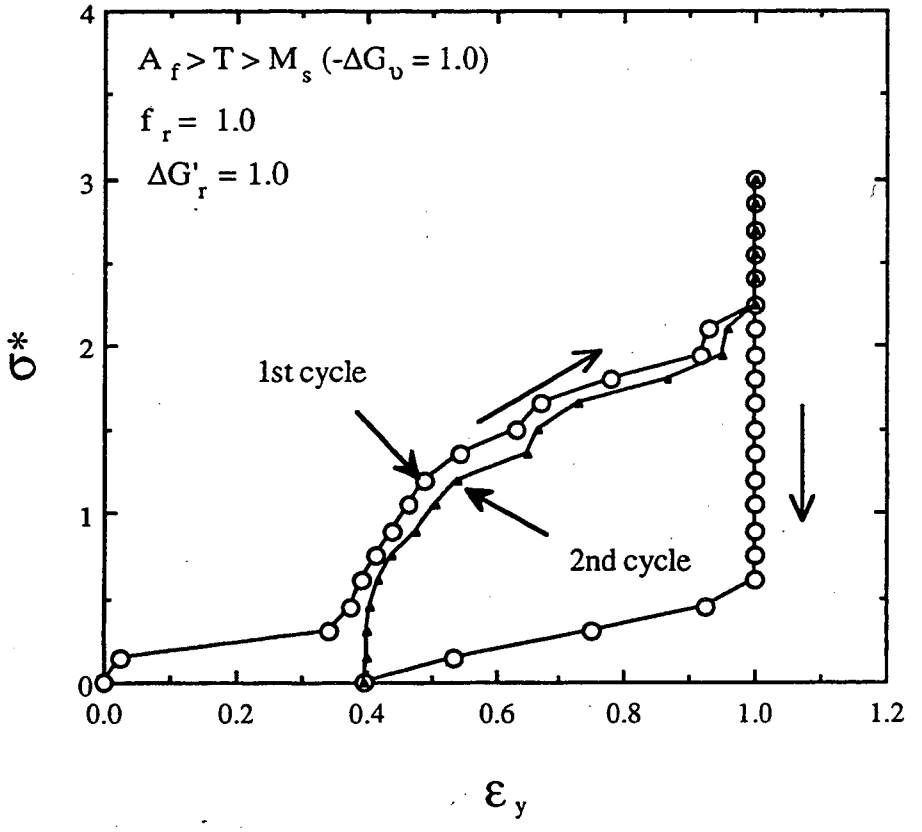

Fig. 7.11(a) The σ^*-ε_y curve of a simulated reversible transformation (R = 0.2) at a loading temperature $T > M_S$ ($-\Delta G\upsilon = 1.0$) with $f_r = 1$ and $\Delta G'_r = 1.0$.

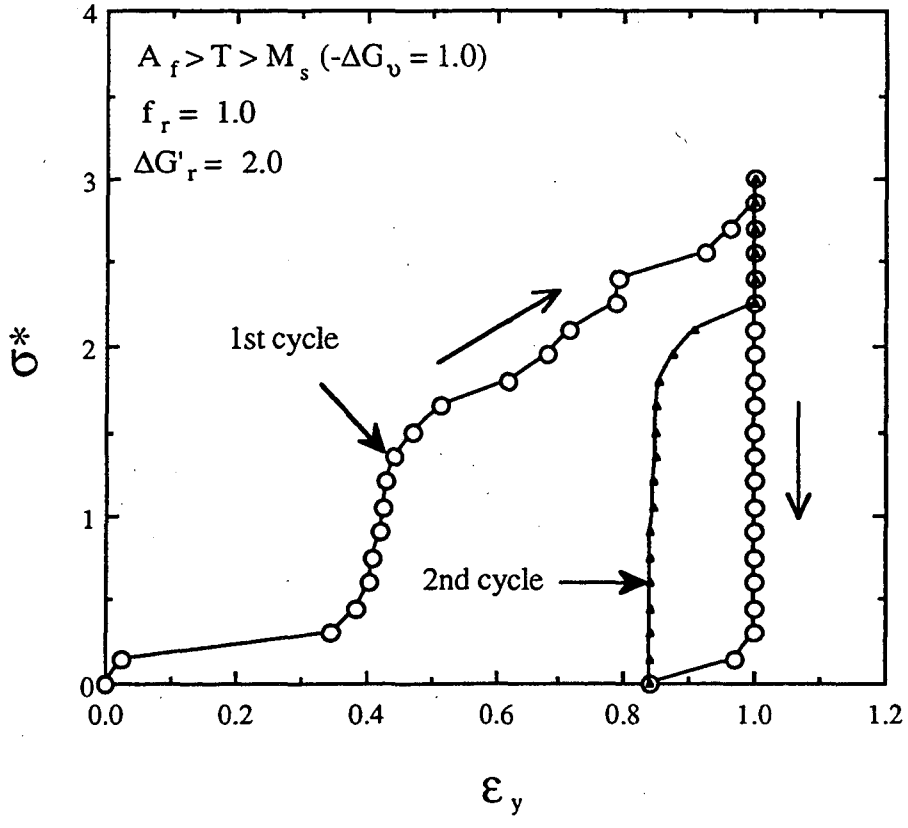

Fig. 7.11(b) The σ^*-ε_y curve of a simulated reversible transformation (R = 0.2) at a loading temperature $T > M_S$ ($-\Delta G\upsilon = 1.0$) with $f_r = 1$ and $\Delta G_r' = 2.0$.

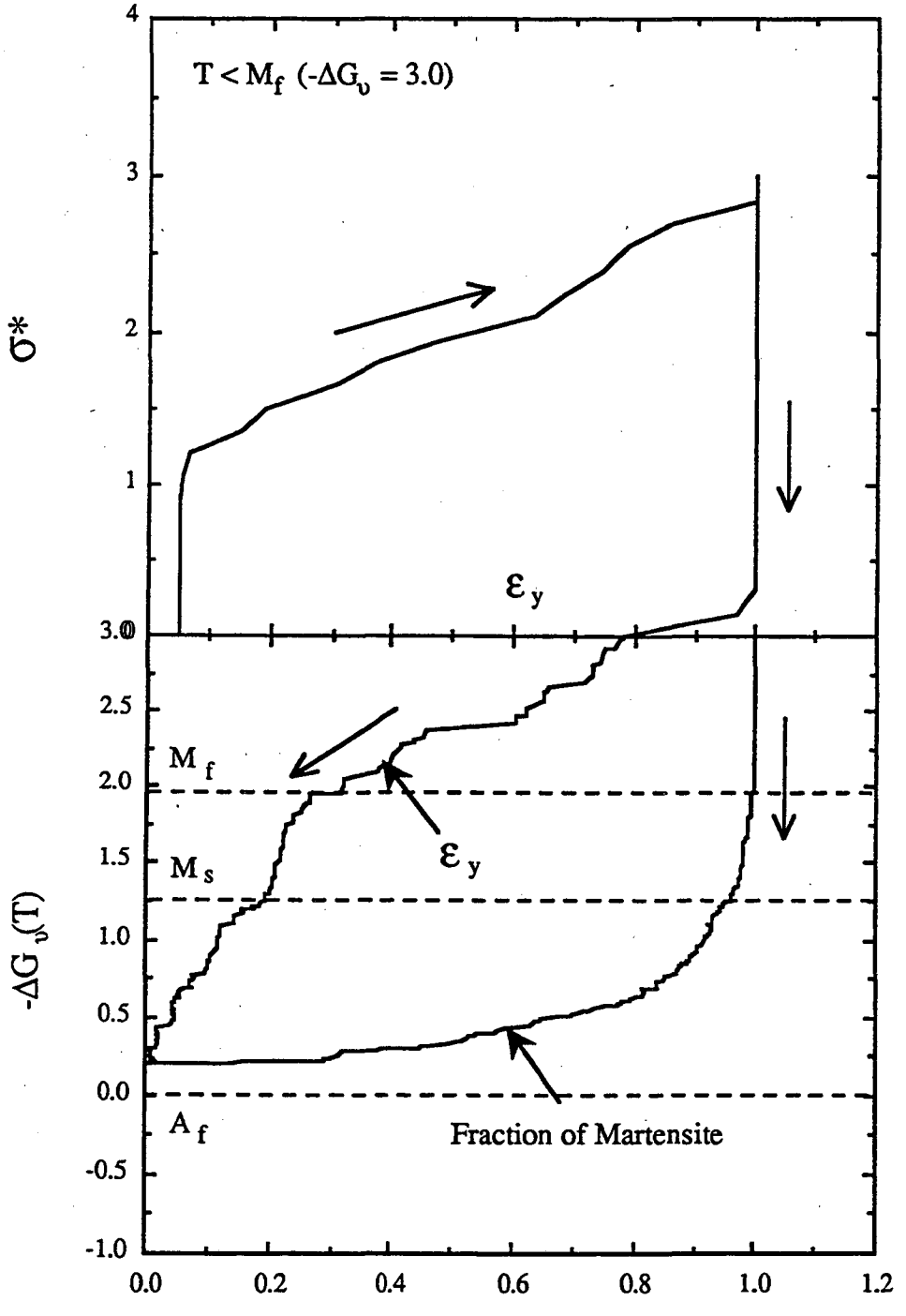

Fig. 7.12(a) The stress-strain (σ^*-ε_y), temperature-transformation (TT) and temperature-strain relation of a simulated reversible transformation (R = 0.2) showing the shape memory effect when the loading temperature $T < M_f$ ($-\Delta G_\upsilon = 3.0$), $f_r = 1$, and $\Delta G_r = 0$.

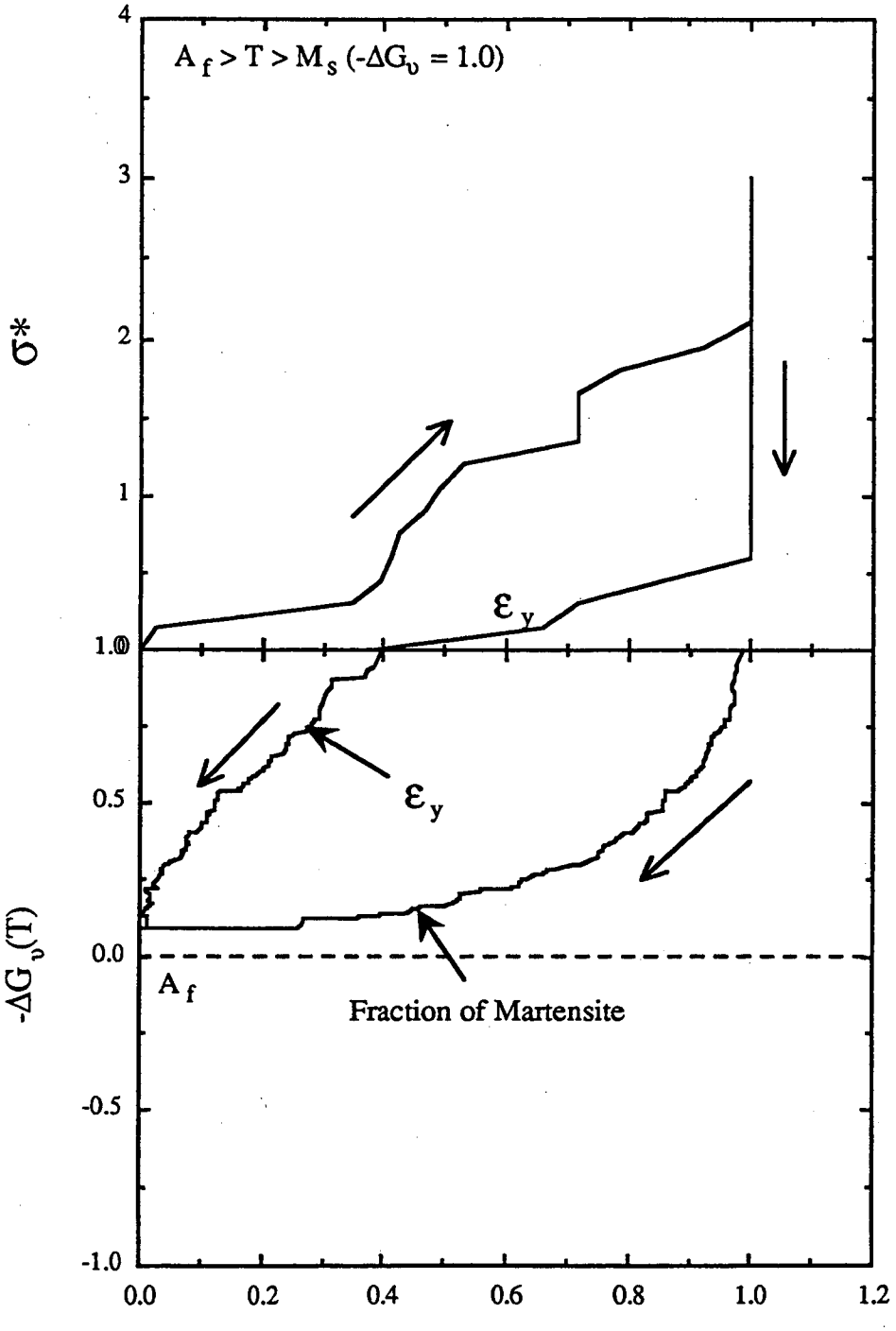

Fig. 7.12(b) The stress-strain (σ^*-ε_y), temperature-transformation (TT) and temperature-strain relation of a simulated reversible transformation (R = 0.2) showing the shape memory effect when the loading temperature $A_f > T > M_S$ ($-\Delta G_v = 1.0$), $f_r = 0.5$, and $\Delta G_r = 0$.

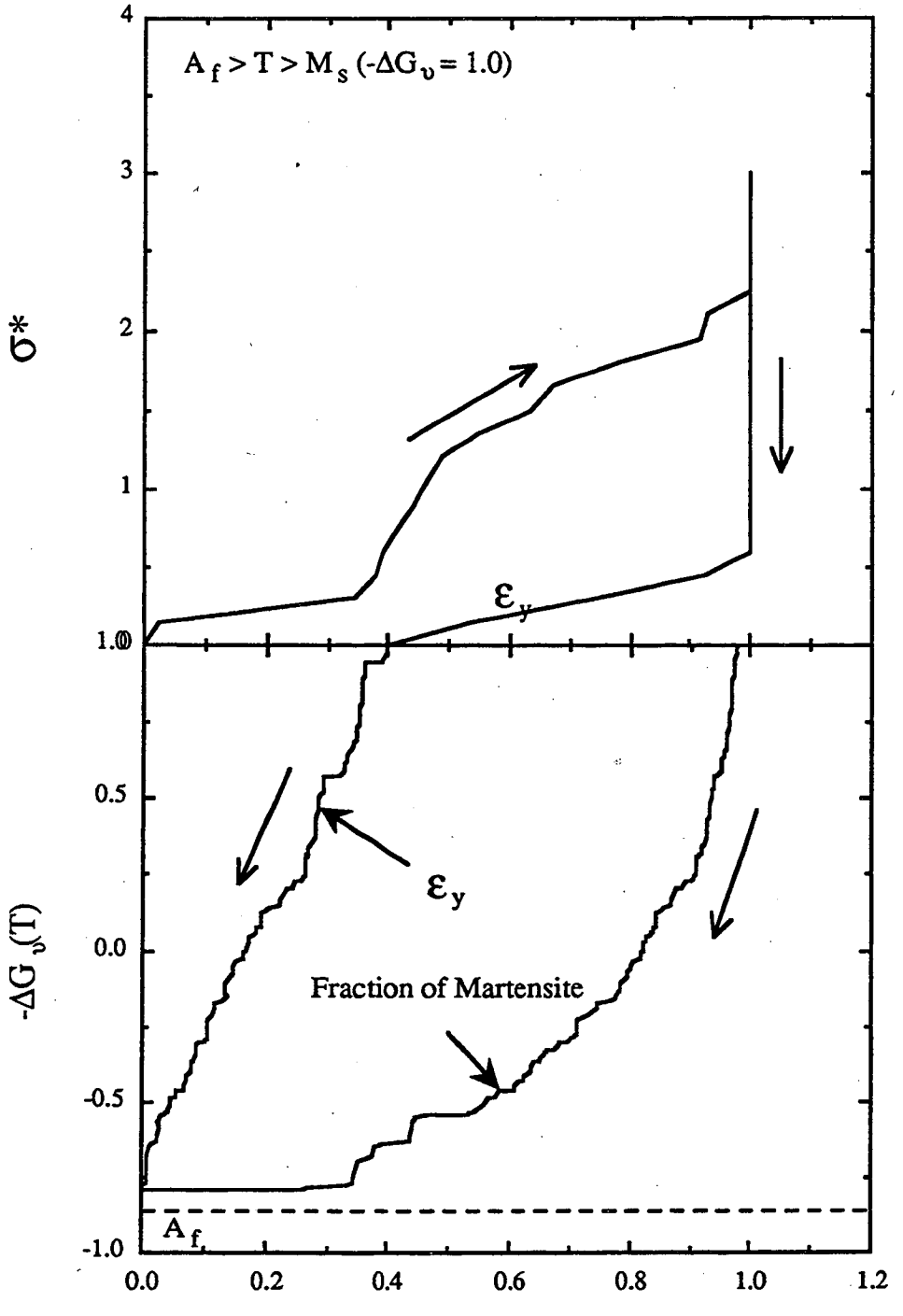

Fig. 7.12(c) The stress-strain (σ^*-ε_y), temperature-transformation (TT) and temperature-strain relation of a simulated reversible transformation (R = 0.2) showing the shape memory effect when the loading temperature $A_f > T > M_s$ ($-\Delta G_v = 1.0$), $f_r = 1$, and $\Delta G_r = 1.0$.

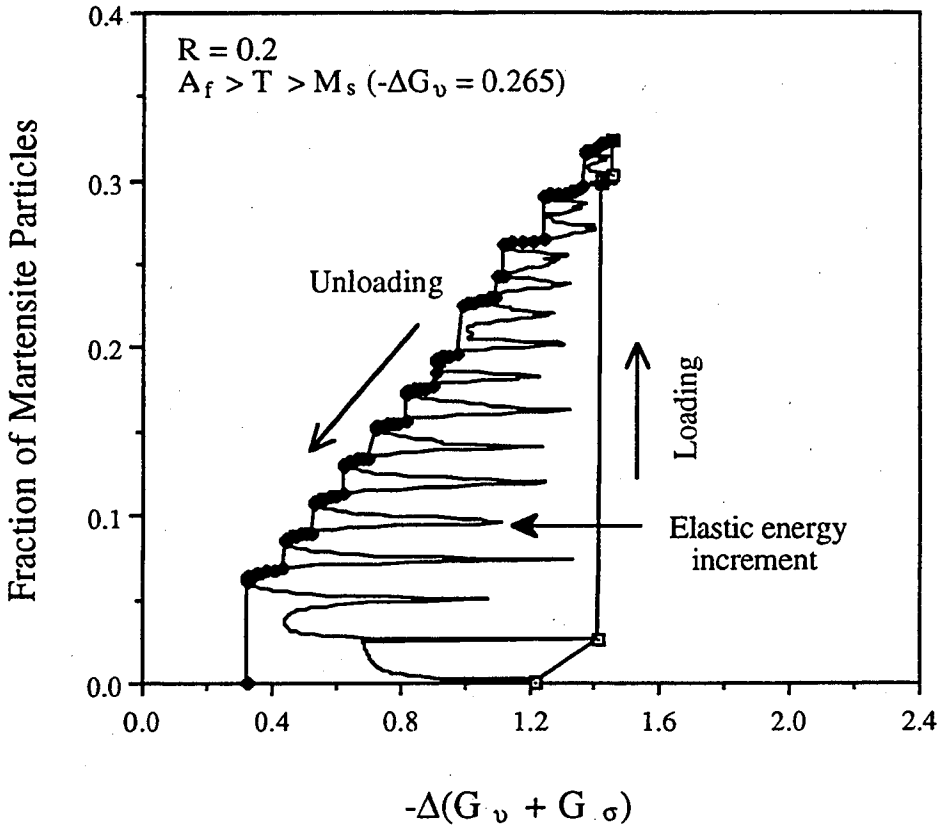

Fig. 7.13 The stress-transformation (ST) curve and the elastic energy increment curve for the exactly reversed path.

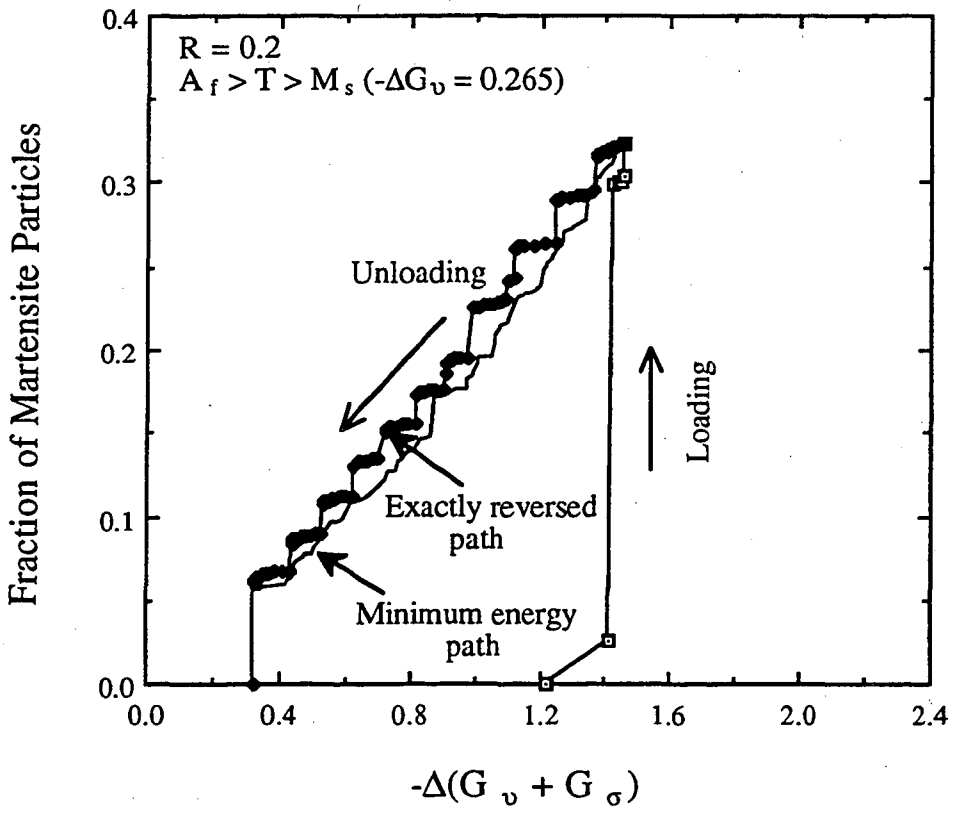

Fig. 7.14 The stress-transformation (ST) curves for the exactly reversed path and the minimum energy path.

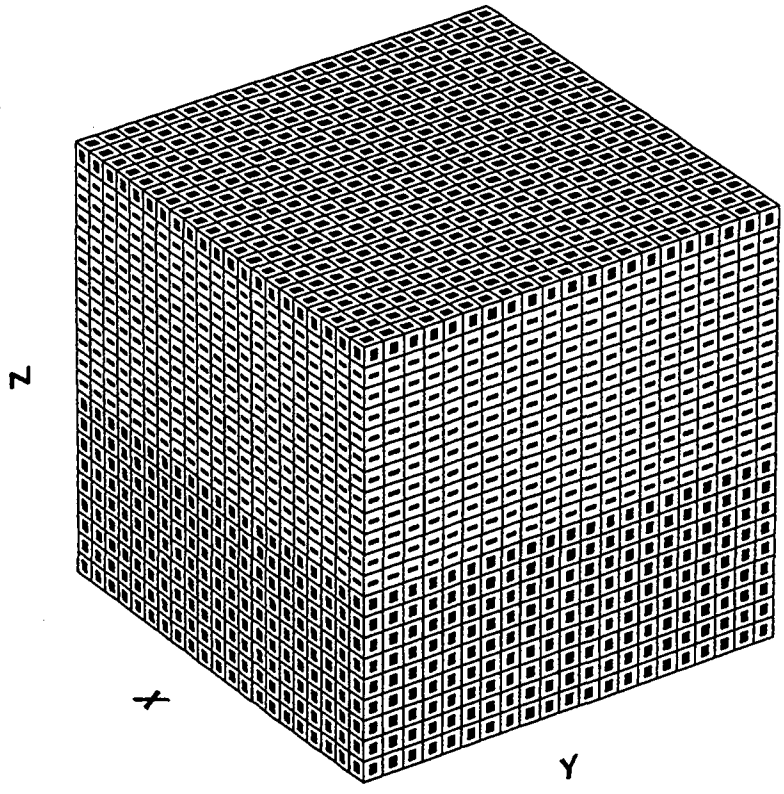

Fig. 8.1 The microstructure generated by a simulated transformation using the transformation strain value of set 1 (see the text in Chapter 8) in a stress-free cubic system.

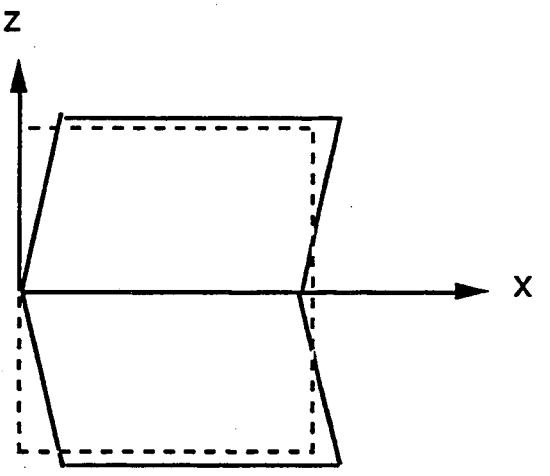

Fig. 8.2 The schematic drawing of the shape change of the transformation shown in Fig. 8.1.

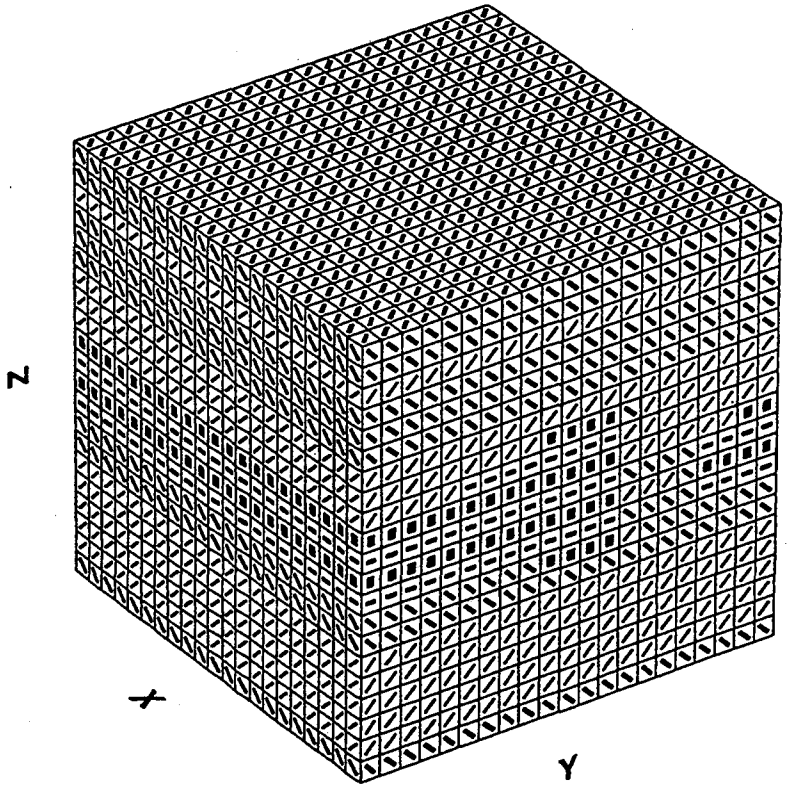

Fig. 8.3 The microstructure generated by a simulated transformation using the transformation strain value of set 2 (see the text in Chapter 8) in a stress-free cubic system.

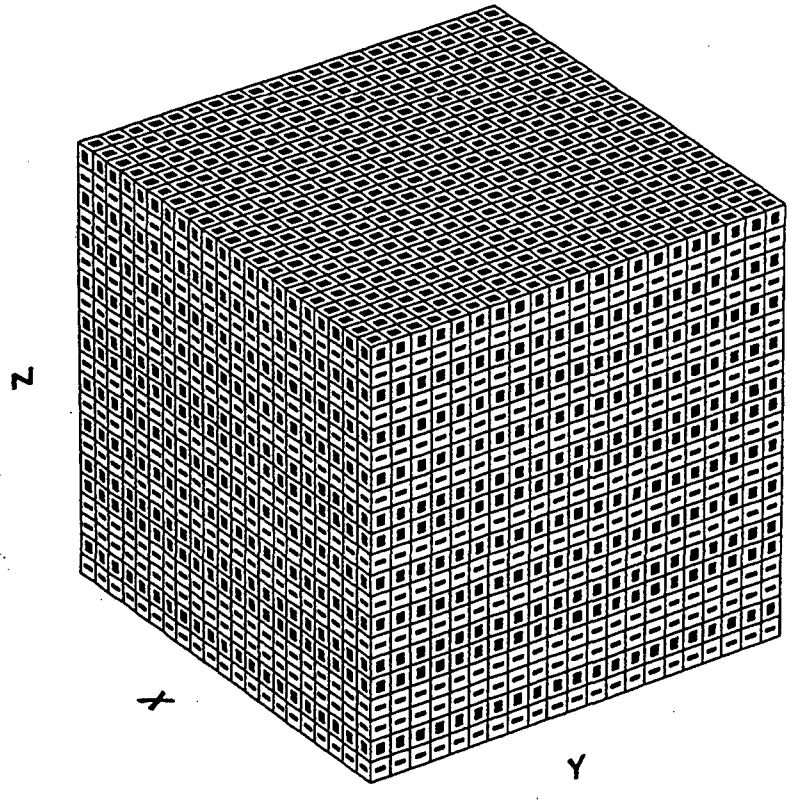

Fig. 8.4 The microstructure generated by a simulated transformation using the transformation strain value of set 2 (two variants only, see the text in Chapter 8) in a stress-free cubic system.

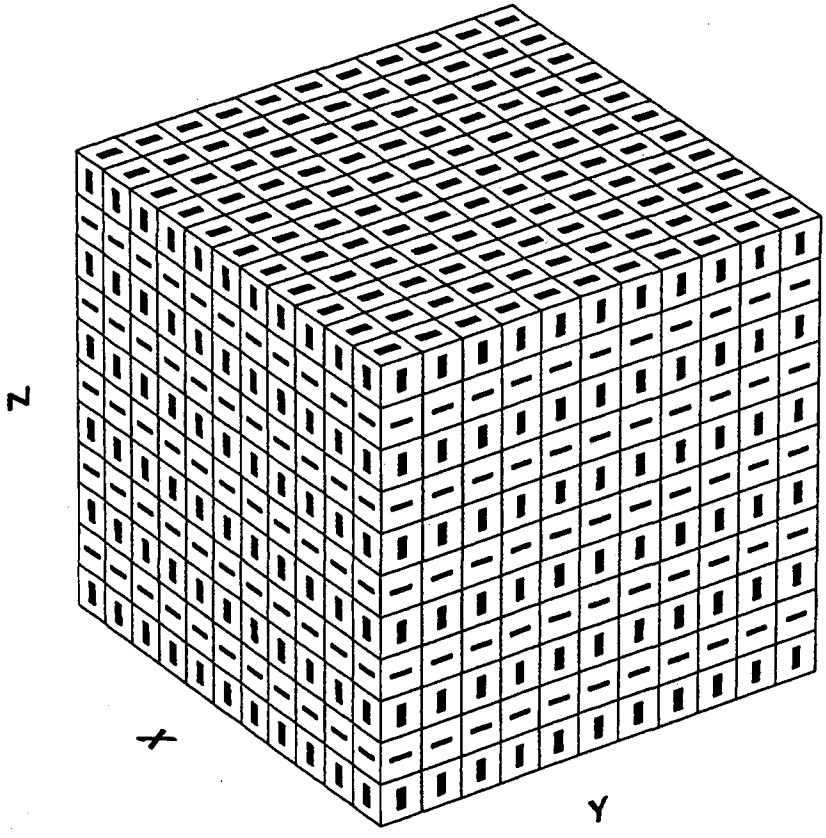

Fig. 8.5 The microstructure generated by a simulated transformation using the transformation strain value of set 1 (see the text in Chapter 8) in a cube constrained by an untransformed matrix.

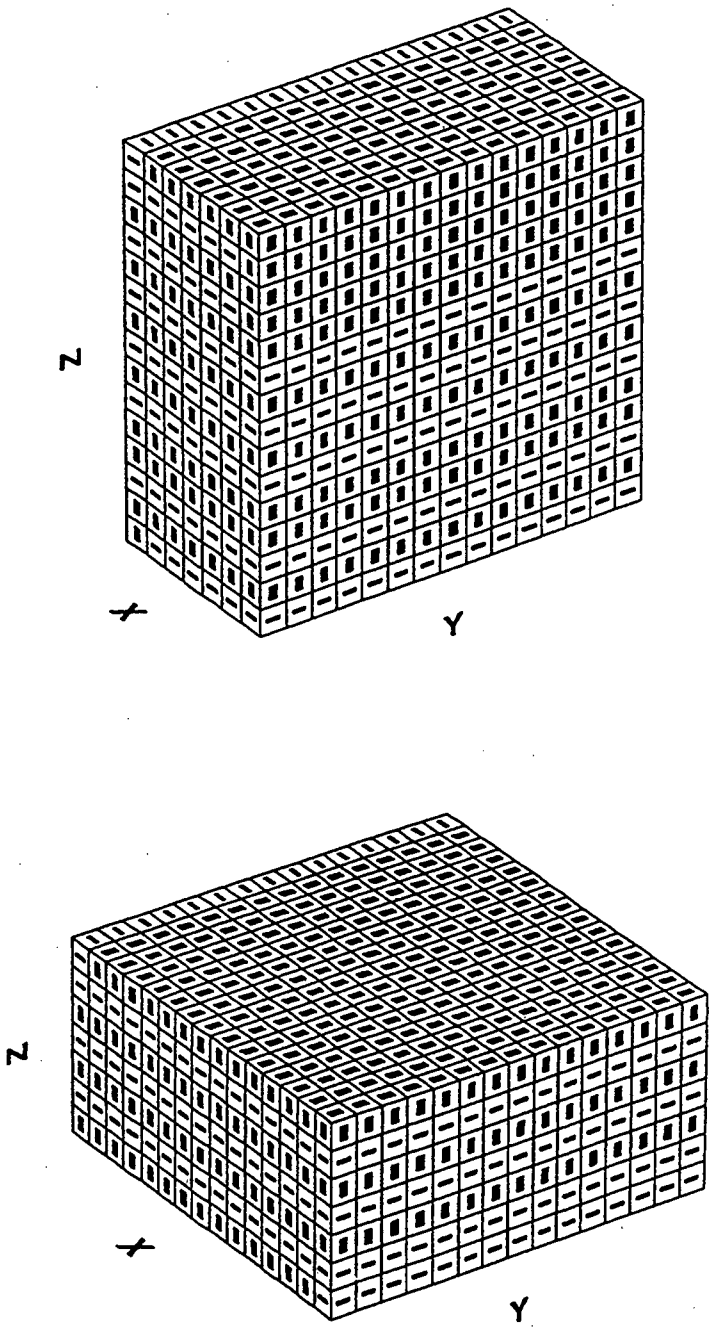

Fig. 8.6 The microstructures generated by simulated transformations using the transformation strain value of set 1(two variants only, see the text in Chapter 8) in two cuboids constrained by an untransformed matrix.

LAWRENCE BERKELEY LABORATORY
UNIVERSITY OF CALIFORNIA
TECHNICAL INFORMATION DEPARTMENT
BERKELEY, CALIFORNIA 94720